2007-08-15

CFD simulation of transport and reaction in cylindrical catalyst particles

Ertan M. Taskin
Worcester Polytechnic Institute

Repository Citation

Taskin, E. M. (2007). *CFD simulation of transport and reaction in cylindrical catalyst particles*. Retrieved from https://digitalcommons.wpi.edu/etd-dissertations/463

CFD simulation of transport and reaction in cylindrical catalyst particles

by

M. Ertan Taşkın

A Dissertation
Submitted to the Faculty
of the
WORCESTER POLYTECHNIC INSTITUTE
in partial fulfillment of the requirements for the
Degree of Doctor of Philosophy
in
Chemical Engineering

August 2007

Approved:

Prof. A.G. Dixon, Major advisor

Prof. H. Stitt, Co-Advisor, Johnson Matthey

Prof. G. Tryggvason, Committee member

Prof. J. Wilcox, Committee member

Abstract

Multitubular packed bed reactors with low tube-to-particle diameter ratios (N) are especially selected for strongly endothermic reactions such as steam reforming and propane dehydrogenation. For low N tubes, the presence of the wall causes changes in bed structure, flow patterns, transport rates and the amount of catalyst per unit volume. In particular, the particles close to the wall will behave differently to those inside the bed. The problem is that, due to the simplifying assumptions, such as uniform catalyst pellet surroundings, that are usual for the current pseudo-continuum reactor models, the effects of catalyst pellet design changes in the near-wall environment are lost. The challenge is to develop a better understanding of the interactions between flow patterns, species pellet diffusion, and the changes in catalyst activity due to the temperature fields in the near wall region for the modeling and design of these systems.

To contribute to this improved understanding, Computational Fluid Dynamics (CFD) was used to obtain detailed flow, temperature, and species fields for near-wall catalyst particles under steam reformer and propane dehydrogenation reactor inlet conditions.

As a first step, a reduced size model was generated by only considering a 120 degree segment of an N = 4 tube, and validated with a larger size complete bed model. In terms of the flow and temperature contours and profiles, the complete tubes can be represented well by the reduced size models, especially focusing on the center particles positioned in the middle of the near wall region.

The methane steam reforming heat effects were implemented by a user-defined code with the temperature-dependent sinks in the catalyst particles, near to the pellet surfaces for different activity levels. For the sinks terms, bulk phase species concentrations were used in the reaction rates, and with the reaction heat effects inclusion, significant pellet sensitivity was observed with different activity levels. Furthermore, non-symmetric temperature fields in and around the near wall particles were noticed as contrary to the conventional approach.

In order to focus on the 3D intra-pellet distributions of temperature and species, diffusion and reaction were coupled to the external flow and temperature fields by user-defined code. Strong deviations from uniformity and symmetry on the temperature and species distributions existed as a result of the strong wall heat-flux into the particles

Additionally, the pseudo-continuum type of packed bed model was created, which considers the simplified environment for the reacting particles. The results obtained by the diffusion reaction application in the 3D discrete packing model could not be re-produced by the conventional simplified pseudo-continuum approach, no matter which parameter values were chosen for the latter.

The significance of these observations is that, under the conventional assumption of symmetric particle surroundings, the tube wall temperature and reaction rates for catalyst particles can be incorrectly evaluated and important design considerations may not be well predicted, thus, negative consequences on the plant safety and efficiency may be observed.

Acknowledgments

In August 16, 2003, my one of the first days in WPI, while looking around to explore the atmosphere in the Goddard Hall, I have unintentionally met with one of the faculties of the Chemical Engineering Department that I would not know he was going to be my advisor: Prof. Anthony G. Dixon. I would like express my deepest gratitude to him for his continuing scientific, financial, and moral support during my study here.

I would also like to thank to my co-advisor Prof. Hugh Stitt as an academic liaison of Johnson Matthey Catalysts, UK. During our research, I have found a chance to get to know his strong industrial and scientific background.

I want to acknowledge Johnson Matthey Catalysts for supporting our project. Additionally, I have to thank to the Department of Chemical Engineering at WPI including all the faculty members for accepting me as a funded graduate student, and providing me a Teaching Assistantship position which helped me to know the faculty members well. My special thanks to Prof. Barbara Wyslouzil, and Prof. Nikolaos Kazantzis who were my first contacts in WPI, and I always remember their positive attitude. Further acknowledgment is made to the Donors of the American Chemical Society Petroleum Research Fund for partial support of this research.

I want to thank to Prof. Gretar Tryggvason and Prof. Jennifer Wilcox as accepting to be my committee members, and their valuable suggestions.

Besides the academic experience, there were special people who became valuable friends for me and my family. I especially want to thank my dear friend Ozgur. Our friendship has mainly started while studying the Ph.D. qualification exam, and now he is literally one of our family members. Even my son considers him as his “older” brother. I would also like to thank to Engin and Didem, for sharing so many moments together. Prior to coming USA, I have sent many e-mails to Engin, Ceylan, and Ipek to get as much information as possible. I am very grateful them for sharing their experiences. Additional thanks to all the graduate students in Chemical Engineering Department.

As our former and current administrative staff members, my special thanks to Joe, Sandy, Elaine, and Felicia.

The computational difficulties were mainly solved by Sia Najafi, I thank to him for his kindness and all the help.

Our presence in USA needed a strong moral support form the first day. We are very thankful to our parents for their positive approach and endless support.

Last, but of course not least, I want to deeply express my gratitude to my lovely wife Nuriye. I would not get this degree without her encouragement, support, and commitment. Our precious spices, my daughter Aslinur, and my son Emre, they are the meaning of our lives. I would especially thank to both of them, for their patience, and understanding during my study.

On top of everything, I am extremely grateful to God, who gave me everything.

Thanks to everybody.

Ertan

I would like to dedicate my thesis to
the memory of
Prof. Hasan Orbey
who was one of my undergraduate teachers
and inspired me
including many students
during his lifetime

Table of Contents

List of Figures

List of Tables

1. Introduction

1.1 Problem Statement

The discovery of solid catalysts and their application to chemical processes in the early years of the 20th century has led to a breakthrough of the chemical industry. Since then, this industry has diversified and grown in a spectacular way through the development of new or the rejuvenation of established processes, mostly based on the use of solid catalysts (Froment and Bischoff, 1990).

In chemical engineering processes, fixed bed reactors are frequently used catalytic systems. At present, the majority of commercial gas-phase catalytic processes are carried out in these reactors. Some of the main fixed bed catalytic processes are listed in Table 1.1 (Froment and Bischoff, 1990).

Table 1.1 Main fixed bed catalytic processes

Basic chemical industry	Petrochemical industry	Petroleum refining
Steam reforming	Ethylene oxide	Catalytic reforming
CO conversion	Vinylacetate	Isomerization
Ammonia synthesis	Maleic anhydride	Polymerization
Sulfuric acid synthesis	Phthalic anhydride	Hydrocracking
Methanol synthesis	Styrene	(Hydro) desulphurization

Fixed bed reactors are preferred because of their simpler technology and ease of operation. In the design of these devices, fluid dynamics plays an important role, since the transport of chemical species, mixing or contacting catalytic surfaces is entirely described by the fluid dynamical conservation laws. The main considerations in design of fixed bed reactors are the heat exchange, bed pressure drop, safe operating temperature range, catalyst packing, and so on.

In the fixed bed reactors, reactions take place on the catalyst particles (pellets) which are placed inside the reactor tubes either randomly or structurally. The feed is given from one end of the reactor and products are taken from the other end of it. According to the energetic nature of the reaction, the heat is either supplied to the tube wall by mostly the outside burners, or taken out by cooling jackets. The schematic illustration is given by Figure 1.1.

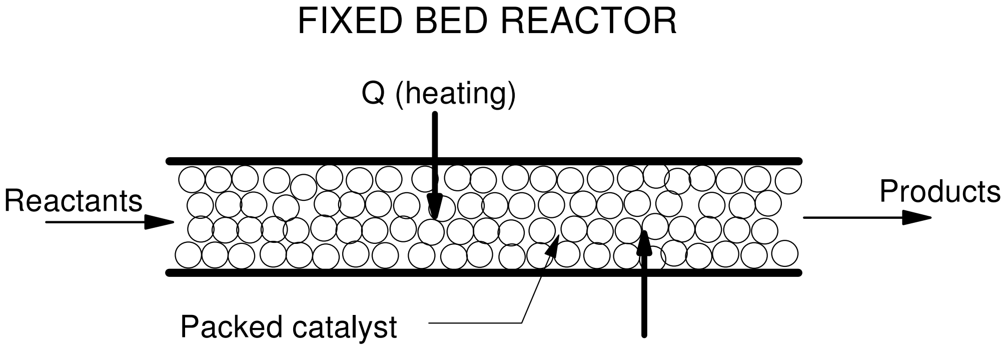

Figure 1.1 The schematic illustration of a fixed bed reactor

Since, fixed bed reactors are an essential part of the industry for almost a century, effective modeling of flow and heat transfer inside the reactor has gained importance since then.

In order to model a packed bed reactor, transport phenomena occurring in the bulk fluid, in the pellet, and at their interfaces must be considered utilizing the appropriate reaction rate expressions. These phenomena can be classified as the following;

- Heat transfer by the tube wall
- Convection of the fluid
- Heat and mass dispersion in the fluid phase
- Heat and mass transfer between bulk fluid and pellet
- Conduction in the solid phase
- Intra-particle diffusion of heat and mass

These transport phenomena have been handled based on fairly radical simplifying assumptions, such as pseudohomogeneity, the utilization of correlation-based effective transport parameters, unidirectional velocity field, uniform catalyst pellet surroundings, and reaction source terms using effectiveness factors in the conventional packed bed modeling approaches. These simplifications have been driven by a fast-disappearing need for computational savings and by complex structure of the random packed tubes.

The packed bed reactors with low tube-to-particle diameter ratios (N) are frequently selected for strongly endothermic reactions such as steam reforming and propane dehydrogenation in multitubular form. For low-N tubes, the presence of the wall causes changes in bed structure, flow patterns, transport rates and the amount of catalyst per unit volume as compared to the high-N tubes. In particular, the particles close to the wall will behave differently to those inside the bed. The problem is that, due to the mentioned simplifying assumptions, the effects of catalyst pellet design changes in the near-wall environment are lost. The challenge is to develop a better understanding of the interactions between flow patterns, species pellet diffusion, and the changes in catalyst activity due to the temperature fields in the near wall region for the modeling and design of these systems.

One of the important parameters in the design and operation of steam reformers is the tube wall temperature. The consequences of excessive temperatures on the tube are quite dramatic. Figure 1.2 shows the photographs of reformer tube banks with signatures of poor performance and tube over-heating. In Figure 1.2(a), the flame from the burner is clearly visible in the top right of the photograph. On several of the tubes, clear evidence of hot bands and hot patches can be seen with the light red color due to the temperature difference. These may be the result of local deactivation, local catalyst voids, or flow channeling. In Figure 1.2(b), several of the tubes can be seen as overheated through their entire length as a most probable result of low flow. This emphasizes the thermally aggressive environment to which the reformer tube is exposed.

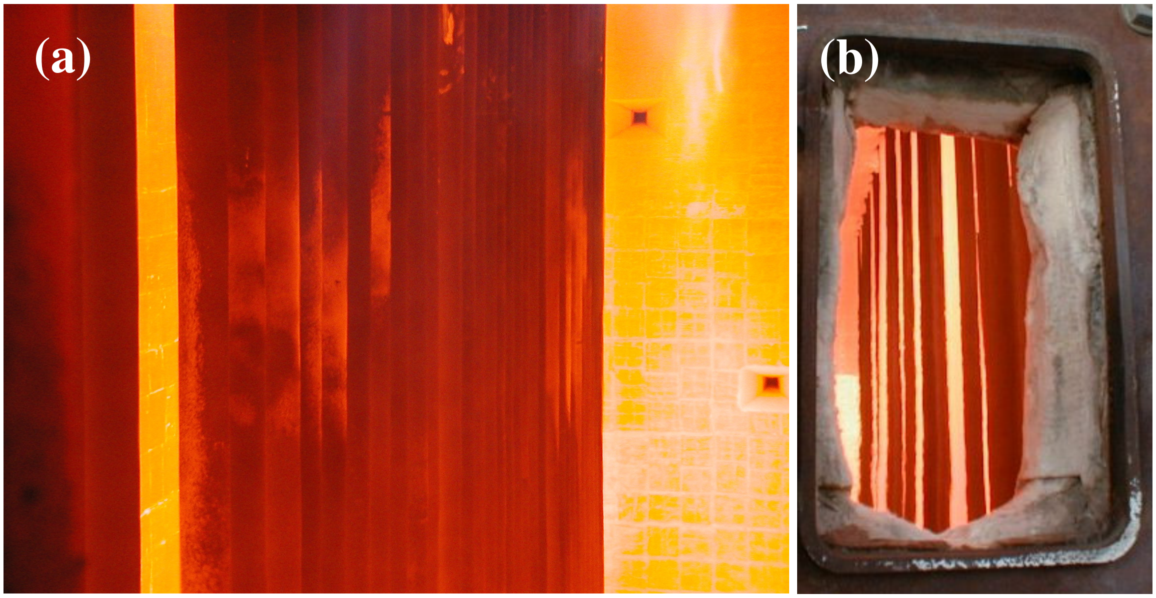

Figure 1.2 Photographs of primary steam reformer tube banks showing high tube wall temperature features: (a) showing bands and hot patches and (b) showing the entire tubes that have overheated. Source: Johnson Matthey Catalysts.

As a consequence of poor heat transfer, the damaged tube photographs are given in Figure 1.3. The excessive tube wall temperature, as shown in Figure 1.2(a), causes the cracked sections on the tubes as in Figure 1.3(a). On the other hand, the bent tubes, shown in Figure 1.3(b), occur as a result of unequal heating of the two sides, which is another heat transfer problem in steam reformer tubes.

It has been discussed by Dixon et al. (2005) that, from the Larson-Miller analysis, due to the effects of sustained high temperature, the tube life is drastically affected; a 20°C increase of tube wall temperature will foreshorten the tube life by 50%.

Considering the damages on the tubes or the reduction in tube life, replacing the tubes becomes a necessity to continue the production. Regarding the updated cost of a typical reformer tube as USD 15000, and 300-400 tubes in the reformer, the cost of complete re-tube becomes in the range of USD 10-15 million taking the on-site expenditures into account.

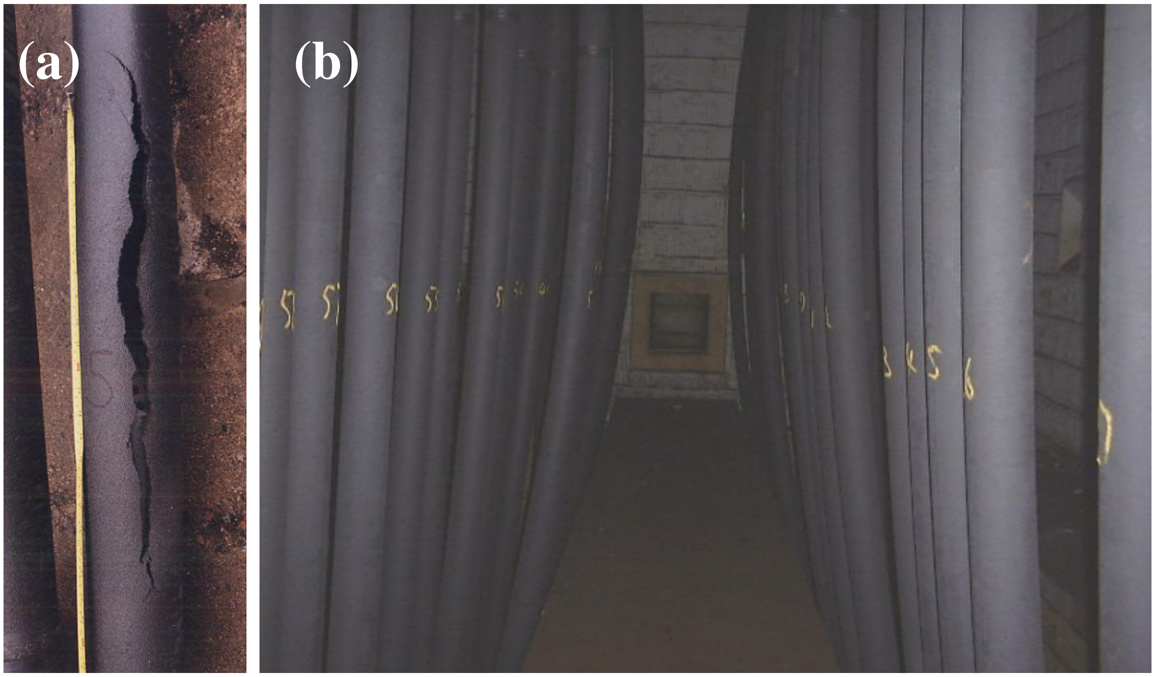

Figure 1.3 Photographs of consequences of poor heat transfer on primary steam reformer tubes: (a) showing the cracked tube and (b) showing the bent tubes. Source: Johnson Matthey Catalysts.

By these examples of consequences of poor heat transfer, the significance of near wall effects of low-N tubes, and importance of proper modeling of the transport processes taking place inside of the tubes can be understood. By the traditional modeling approaches with simplifications, these types of effects of transport processes might not be captured.

In these days, with the increasing computational capabilities, Computational Fluid Dynamics (CFD) has became a quite robust modeling tool not only for fixed bed reactor systems, but also for a lot of different kind of reacting or non-reacting systems in chemical engineering such as stirred tanks, extruders, and separation towers. CFD can provide us with detailed information on flow processes and heat and mass transfer processes. This is a tremendous advantage over traditional methods of obtaining flow and heat transfer data in fixed beds, which are usually limited to few sampling points and are mostly intrusive.

In earlier studies it has been shown that CFD is an accurate, reliable, and non-intrusive method that can provide a wealth of data in fixed beds. The detailed CFD applications on fixed bed reactors can be found in Chapter 2.

Regarding the expressed introductory information up to here, the main goal of this research would be described as to combine the methodologies of CFD and reaction engineering, to obtain better understanding and modeling approaches for low-N fixed bed reactors for the highly endothermic reactions such as methane steam reforming (MSR) and propane dehydrogenation (PDH). To date, CFD codes have not been developed to include the reaction inside the solid catalysts, and therefore the interaction between the chemistry taking place inside the catalyst particles, and the transport processes surrounding them have not been investigated. For that reason, coupling the flow convection to heat conduction, mass diffusion, and reaction inside the catalyst particles via CFD would be an efficient method to evaluate the reaction inside the particles under the correct conditions, especially in the near wall region where the transport processes are strongly influenced by the presence of the wall and by the heat transfer through the wall.

1.2 Computational Fluid Dynamics

With CFD, the Engineer can build a model to investigate the flow, turbulence, and heat and mass transfer characteristics of reactors or other process equipment in detail. For systems at high temperatures or pressures, or having high corrosiveness or a high degree of hazard, CFD models may well be the only good tools available for studying the fluid dynamics.

CFD involves the numerical solution of conservation equations for mass, momentum and energy in the flow geometry of interest, together with additional sets of equations reflecting the problem in hand.

1.2.1 Introduction

The equations that form the theoretical foundation for the whole science of fluid mechanics were derived more than one century ago by Navier (1827) on the basis of molecular hypothesis. Later the same equations were derived by Stokes (1845) without using such hypothesis. These equations are commonly referred to as the Navier-Stokes equations. Despite the fact that these equations have been known for more than a century, no general analytical solution of the Navier-Stokes equations is known. This state of the art is due to the complex mathematical nature of these equations (Kuipers and Van Swaaij, 1998).

During the first half of the nineteenth century a spectacular development in boundary layer theory took place that was driven mainly by the needs of the aerodynamics community. However, until 1970 the storage capacity and speed of digital computers were not sufficient to enable efficient calculation of full three-dimensional flow fields around airplanes. This situation has by now definitely changed with the available great computational capabilities.

Nowadays, CFD is truly interdisciplinary since it cuts across all disciplines where the analysis of fluid flow and associated phenomena is of importance.

1.2.2 Theory

CFD involves the analysis of fluid flow and related phenomena such as heat and/or mass transfer, mixing, and chemical reaction using numerical solution methods. Commercially available CFD codes use one of the three basic spatial discritization methods: finite differences (FD), finite volumes (FV), or finite elements (FE). Earlier CFD codes used FD and FV method. The mostly addressed CFD method is FV method. In this method, the domain of interest is divided into a large number of control volumes (or computational cells or elements) which have a relatively small size in comparison with the macroscopic volume of the domain of interest. For each control volume, a discrete representation of the relevant conservation equations is made after which an iterative solution procedure is invoked to obtain the solution of the nonlinear equations. The FV and FE methods support both structured and unstructured grids, and therefore it can be applied to more complex geometries. However, FD method is limited to structured grids, which are hard to apply to complex geometries (Dixon et al., 2006). The unstructured grid can consist of elements in a variety of shapes such as quadrilaterals and triangles for 2D simulations, and hexahedra, tetrahedra, polyhedra, prisms and pyramids for 3D simulations. The more detail can be found in section 1.2.3.

During the last decade, another CFD method, known as lattice-Boltzman method (LBM), has been frequently applied to fluid flow problems in highly complex geometries. The basic idea of the LBM is the numerical simulation of simplified molecular dynamics of the fluid. This is done by evaluating a time- and space- discrete equation. Macroscopic values like pressure and velocity can be obtained from the automata fluid density distributions. The numbers of researchers prefer LBM than the FV methods. Because in the latter one, the disretized macroscopic equations are directly solved which are usually nonlinear, and therefore it is relatively difficult to solve those equations. Whereas, in the LBM, an analogy with the kinetic theory of the gases is considered, which forms the kinetic (lattice Boltzmann) equation, and the differential term of this equation is in simple linear form. Therefore, for the complex fluid flows problems, LBM is thought to be preferable. On the other hand, there are some limitations of the LBM, such as the turbulence simulations are more expensive than the FV methods, and it is difficult to include heat transfer.

The laminar and turbulent flow equations, and FV methods used to solve them have been extensively presented in the literature (Patankar, 1980; Ranade, 2002; Fluent 2005).

In this study the commercial grid generation software GAMBIT, and CFD solver FLUENT have been used. The aspects of iterative FV CFD application regarding the implementation for our purposes will be summarized in the following section.

1.2.2.1 Fluid Flow Fundamentals

The numerical solution of the discretized forms of highly nonlinear mass and momentum conservation equations for each control volume is achieved by an iterative solution procedure in order to obtain the solution. The generalized balances that are used in FLUENT are the Navier-Stokes equations for conservation of mass and momentum. To describe the turbulent features of the flow, additional equations can be used.

1.2.2.1.1 Navier-Stokes Equations

The general equation used for the conservation of mass (the continuity equation) is defined as follows:

$$\frac{\partial \rho}{\partial t} + \frac{\partial(\rho u_i)}{\partial x_i} = S_m \qquad (1.1)$$

The source term S_m contains the mass added through phase changes or user-defined sources. In general, and in the simulations described here, the source term was equal to zero.

The equation for conservation of momentum in direction i and in a non-accelerating reference frame is given by:

$$\frac{\partial(\rho u_i)}{\partial t} + \frac{\partial(\rho u_i u_j)}{\partial x_j} = -\frac{\partial p}{\partial x_i} + \frac{\partial \tau_{ij}}{\partial x_j} + \rho g_i + F_i \qquad (1.2)$$

In this balance p is static pressure, τ_{ij} is the stress tensor, and ρg_i is the gravitational body force. F_i is an external body forces component; it can include forces from interaction between phases, centrifugal forces, Coriolis forces, and user-defined forces. For single-phase flow through packed tubes it is usually zero. The stress tensor τ_{ij} for a Newtonian fluid is defined by:

$$\tau_{ij} = \left[\mu \left(\frac{\partial u_i}{\partial x_j} + \frac{\partial u_j}{\partial x_i} \right) \right] - \frac{2}{3} \mu \frac{\partial u_1}{\partial x_1} \delta_{ij} \qquad (1.3)$$

Here μ is the molecular viscosity; the second term on the right-hand side of the equation is the effect of volume dilation.

1.2.2.1.2 Turbulence models

The fluctuating velocity fields are the characteristics of the turbulent flows which results in fluctuations for transported quantities of momentum, energy, and species concentrations. Since these fluctuations can be of small scale and high frequency, they are computationally very expensive to simulate directly in practical calculations. In order to solve the turbulence, separate models composed of set of equations must be considered. Unfortunately no single turbulence model is universally accepted as being superior for all classes of problems. The choice of turbulence model depends on considerations such as the physics encompassed in the flow, the established practice for a specific class of problem, the level of accuracy required, the available computational resources, and the amount of time available for the simulation (Fluent, 2005).

Two methods have been developed to transform the Navier-Stokes equations so that the small-scale turbulent fluctuations do not have to be directly simulated. These are Reynolds averaging (RANS) and filtering or Large-Eddy simulation (LES). Both methods introduce additional terms in the governing equations that need to be modeled in order to achieve sufficient number of equations for all the unknowns.

LES provides a capability to compute large eddies in a time dependent simulation that uses a set of filtered equations. Filtering is essentially a manipulation of the exact Navier-Stokes equations to remove the smaller eddies than the mesh size. LES has not been applied to complex geometries as used in packed-tube modeling because of the requirement for the large computer resources to resolve energy-containing turbulent eddies in the highly turbulent flows.

RANS approach is generally adopted for practical engineering calculations, and uses models such as Spalart-Allmaras, κ-ε and its variants, κ-ω and its variants, and Reynolds Stress Model (RSM).

With RANS the solution variables in the Navier-Stokes equations are decomposed into mean, $\overline{u_i}$, and fluctuating u_i' components, and integrated over an interval of time large compared to the small-scale fluctuations as shown below:

$$u_i = \overline{u_i} + u_i' \tag{1.4}$$

When this is applied to the Navier-Stokes equations (equations 1.2-1.4), the result is:

$$\frac{\partial(\rho u_i)}{\partial t} + \frac{\partial(\rho u_i u_j)}{\partial x_j} = -\frac{\partial p}{\partial x_i} + \frac{\partial}{\partial x_j}\left[\mu\left(\frac{\partial u_i}{\partial x_j} + \frac{\partial u_j}{\partial x_i}\right) - \frac{2}{3}\mu\frac{\partial u_1}{\partial x_1}\right] + \frac{\partial(-\rho\overline{u_i'u_j'})}{\partial x_j} \tag{1.5}$$

The velocities and other solution variables are now represented by Reynolds-averaged values, and the effects of turbulence are represented by the "Reynolds stresses", $(-\rho\overline{u_i'u_j'})$ that are modeled by the Boussinesq hypothesis:

$$(-\rho\overline{u_i'u_j'}) = \mu_t\left(\frac{\partial u_i}{\partial x_j} + \frac{\partial u_j}{\partial x_i}\right) - \frac{2}{3}\left(\rho k + \mu_t\frac{\partial u_i}{\partial x_i}\right)\delta_{ij} \tag{1.6}$$

The k-ε turbulence model was developed and described by Launder and Spalding (1972). The turbulent viscosity, μ_t, is defined in terms of the turbulent kinetic energy, κ, and its rate of dissipation, ε.

$$\mu_t = \rho C_\mu \frac{\kappa^2}{\varepsilon} \tag{1.7}$$

The turbulent kinetic energy and its dissipation rate are obtained from the adopted transport equations:

$$\frac{\partial(\rho\kappa)}{\partial t} + \frac{\partial(\rho u_i \kappa)}{\partial x_i} = \frac{\partial}{\partial x_i}\left[\left(\mu + \frac{\mu_t}{\sigma_\kappa}\right)\frac{\partial\kappa}{\partial x_i}\right] + G_\kappa + G_b - \rho\varepsilon \tag{1.8}$$

$$\frac{\partial(\rho\varepsilon)}{\partial t}+\frac{\partial(\rho u_i\varepsilon)}{\partial x_i}=\frac{\partial}{\partial x_i}\left[\left(\mu+\frac{\mu_t}{\sigma_\varepsilon}\right)\frac{\partial\varepsilon}{\partial x_i}\right]+C_{1\varepsilon}\frac{\varepsilon}{\kappa}\{G_\kappa+(1-C_{3\varepsilon})G_b\}-C_{2\varepsilon}\rho\frac{\varepsilon^2}{\kappa}$$

(1.9)

In these equations, G_κ is the generation of turbulent kinetic energy, κ, due to the turbulent stress, and is defined by:

$$G_\kappa=-\rho\overline{u_i'u_j'}\frac{\partial u_j}{\partial x_i} \quad (1.10)$$

G_b is the generation of turbulent kinetic energy, κ, due to buoyancy:

$$G_b=\beta g_i\frac{\mu_t}{\mathrm{Pr}_t}\frac{\partial T}{\partial x_i} \quad (1.11)$$

Here, Pr_t is the turbulent Prandtl number for temperature or enthalpy and β is the thermal expansion coefficient:

$$\beta=\frac{1}{\rho}\left(\frac{\partial\rho}{\partial T}\right)_p \quad (1.12)$$

The default values of the constants have been established from experimental work with air and water, and have been found to work well for a wide range of wall-bounded and free shear flows (Launder and Spalding, 1972).These values are:

$C_{1\varepsilon}= 1.44$, $C_{2\varepsilon}= 1.92$, $C_\mu = 0.09$, $\sigma_k = 1.0$, $\sigma_\varepsilon = 1.3$, and $\mathrm{Pr}_t = 0.85$

The Renormalization Group (RNG) based k-ε turbulence model is derived from the instantaneous Navier-Stokes equations, using a mathematical technique called “renormalization group” methods (Yakhot and Orzag, 1986). The major differences, in application, from the standard κ-ε model are different empirical constants in the κ and ε balances, and extra terms in the turbulent dissipation balance. The RNG methods are a general methodology of model building based on the stepwise coarsening of a problem.

The main idea is that the RNG theory is applicable to scale-invariant phenomena that do not have externally imposed characteristic length and time scales. In the case of turbulence, the RNG theory is applicable to the small-scale eddies, which are independent of the larger scale phenomena that create them.

The RNG theory as applied to turbulence reduces the Reynolds number to an effective Reynolds number (Re_{eff}) by increasing an effective viscosity (μ_{eff}). Through this process the small-scale eddies are eliminated, which reduces computational demand considerably. The algebraic form of the new effective viscosity equation is as follows:

$$\mu_{eff} = \mu_{mol}\left[1+\sqrt{\frac{C_\mu}{\mu_{mol}}}\frac{\kappa}{\sqrt{\varepsilon}}\right]^2 \qquad (1.13)$$

The differential form of this equation is used in calculating the effective viscosity in the RNG κ-ε model. This method allows varying the effective viscosity with the effective Reynolds number to accurately extend the model to low-Reynolds-number and near-wall flows.

The form of main transport equations for the momentum, the turbulent kinetic energy, κ, and the turbulence dissipation, ε, in the RNG κ-ε model are again defined similar to the standard κ-ε model, now utilizing the effective viscosity defined through the RNG theory. Alternately, a mean strain rate, S, is used instead of the separate turbulence source terms. The κ and ε equations are as follows:

$$\frac{\partial(\rho\kappa)}{\partial t}+\frac{\partial(\rho u_i\kappa)}{\partial x_i}=\frac{\partial}{\partial x_i}\left[\alpha_\kappa\mu_{eff}\frac{\partial\kappa}{\partial x_i}\right]+\mu_t S^2-\rho\varepsilon \qquad (1.14)$$

$$\frac{\partial(\rho\varepsilon)}{\partial t}+\frac{\partial(\rho u_i\varepsilon)}{\partial x_i}=\frac{\partial}{\partial x_i}\left[\alpha_\varepsilon\mu_{eff}\frac{\partial\varepsilon}{\partial x_i}\right]+C_{1\varepsilon}\frac{\varepsilon}{\kappa}\mu_t S^2-C_{2\varepsilon}\rho\frac{\varepsilon^2}{\kappa}-R \qquad (1.15)$$

where α_κ and α_ε are the inverse effective Prandtl numbers for κ and ε, respectively. These variables are determined by the RNG theory through the analytically derived formula:

$$\left|\frac{\alpha - 1.3929}{\alpha_0 - 1.3929}\right|^{0.6321} \left|\frac{\alpha + 2.3929}{\alpha_0 + 2.3929}\right|^{0..3679} = \frac{\mu_{mol}}{\mu_{eff}} \qquad (1.16)$$

where $\alpha_0 = 1.0$. In the high Reynolds number limit ($\mu_{mol}/\mu_{eff} << 1$), $\alpha_\kappa = \alpha_\varepsilon \approx 1.393$.

S in equation (1.14) is the modulus of the mean rate-of-strain tensor, S_{ij}, which is defined as:

$$S = \sqrt{2S_{ij}S_{ij}} \qquad (1.17)$$

and R in equation (1.16) is given by

$$R = \frac{C_\mu \rho \eta^3 (1 - \eta/\eta_0)}{1 + \beta\eta^3} \frac{\varepsilon^2}{\kappa} \qquad (1.18)$$

where $\eta \equiv S\kappa/\varepsilon$, $\eta_0 \approx 4.38$, $\beta = 0.012$.

The model constants $C_{1\varepsilon}$ and $C_{2\varepsilon}$ from equation (1.15) are derived analytically through the RNG theory and are respectively 1.42 and 1.68.

The major difference in the RNG κ-ε model from the standard κ-ε model can be found in the ε balance where a new source term appears in the R term as described in equation (1.18). This term is a function of both κ and ε. The effect of the R term can be best illustrated when equation (1.16) is rewritten when the last two terms are combined:

$$\frac{\partial(\rho\varepsilon)}{\partial t} + \frac{\partial(\rho u_i \varepsilon)}{\partial x_i} = \frac{\partial}{\partial x_i}\left[\alpha_\varepsilon \mu_{eff} \frac{\partial \varepsilon}{\partial x_i}\right] + C_{1\varepsilon}\frac{\varepsilon}{\kappa}\mu_t S^2 - C^*_{2\varepsilon}\rho\frac{\varepsilon^2}{\kappa} \qquad (1.19)$$

where $C^*_{2\varepsilon}$ is given by:

$$C^*_{2\varepsilon} = C_{2\varepsilon} + \frac{C_\mu \eta^3 (1 - \eta/\eta_0)}{1 + \beta\eta^3} \qquad (1.20)$$

The contribution of this factor as a function of the strain rate, η can be seen here. In areas where $\eta < \eta_0$ (where $\eta_0 \approx 4.38$, as mentioned above), the R term makes a positive contribution and $C^*_{2\varepsilon}$ becomes larger than 1.68. When we look, for example, in the logarithmic layer, where $\eta \approx 3.0$, it results in a $C^*_{2\varepsilon} \approx 2.0$, which is close to the value of

$C_{2\varepsilon}$ for the standard κ-ε model, 1.92. We conclude that, for moderately strained flows the RNG model gives results comparable to the standard κ-ε model.

Alternatively, in the areas of high strain rate , $\eta > \eta_0$, the R term makes a negative contribution, reducing the value of $C^*_{2\varepsilon}$ to less than $C_{2\varepsilon}$. This means that compared to the standard κ-ε model, the RNG model has a smaller reduction of ε, augmenting the value of ε resulting in a reduced κ and eventually the effective viscosity. The RNG model yields a lower turbulent viscosity in the high strain flows than the standard κ-ε model.

The R term in the RNG κ-ε model makes the turbulence in this model sensitive to the main rate of strain. The result is a model that responds to the effect of strain and the effect of streamline curvature, a feature that is nonexistent in the standard κ-ε model. The inclusion of this effect makes the RNG κ-ε model more suitable for complex flows. Therefore, we have selected this model in our work regarding the complex flow structure of the packed bed reactors.

The details of the other turbulence models can be found in many sources such as Fluent (2005).

1.2.2.2 Energy Balance Fundamentals

The flow of thermal energy from or through a media can be in the forms of conduction, convection, and radiation depending on the problem in hand. In packed bed reactor, generally the conduction and the convection take place between the flowing fluid, the solid catalyst particles and the tube wall.

The generalized form of the energy balance equation in the direction of *i* is as follows:

$$\frac{\partial(\rho E)}{\partial t}+\frac{\partial}{\partial x_i}\left(u_i(\rho E+p)\right)=\frac{\partial}{\partial x_i}\left(k_{eff}\frac{\partial T}{\partial x_i}-\sum_j h_j\overrightarrow{J_j}+(\overline{\overline{\tau_{eff}}}u_i)\right)+S_h \qquad (1.21)$$

where k_{eff} is the effective conductivity ($k_{eff} = k + k_t$, where k_t is the turbulent thermal conductivity, defined according to the turbulence model being used), and $\overrightarrow{J_j}$ is the diffusion flux of species *j*. The first three terms on the right hand side of equation (1.21) represent the energy transfer due to the conduction, species diffusion, and viscous dissipation, respectively. S_h includes the heat of chemical reaction, or any volumetric heat source that can be defined.

In equation (1.21) E is defined as:

$$E = h - \frac{p}{\rho} + \frac{u_i^2}{2} \tag{1.22}$$

For ideal gases, sensible enthalpy, h, is defined as adding all the terms of multiplied mass fractions and enthalpies for each species.

In the solid sections, the energy balance equation is quite similar to the one given as equation (1.21).

$$\frac{\partial(\rho h)}{\partial t} + \frac{\partial}{\partial x_i}\left(u_i \rho h\right) = \frac{\partial}{\partial x_i}\left(k \frac{\partial T}{\partial x_i}\right) + S_h \tag{1.23}$$

where k is the thermal conductivity of solid media.

The RNG turbulence model provides its own energy balance, which is based on the energy balance of the standard κ-ε model with similar changes as were seen in the κ and ε balances. The RNG κ-ε model energy balance is defined as a transport equation for enthalpy. There are four contributions to the total change of enthalpy: the temperature gradient, the total pressure differential, the internal stress, and the source term. In the traditional turbulent heat transfer model, the Prandtl number is fixed and user-defined; the RNG model treats it as a variable dependent on the turbulent viscosity.

1.2.2.3 Species Transport Equations

When the conservation equations for chemical species wanted to be solved, the following equation can be considered:

$$\frac{\partial(\rho Y_i)}{\partial t} + \nabla \cdot (\rho \vec{v} Y_i) = -\nabla \cdot \vec{J}_i + R_i + S_i \tag{1.24}$$

where $\vec{J}_i$ is the diffusion flux of species *i*, R_i is the rate of production of species *i* by chemical reaction, and S_i is the rate of creation by addition from the dispersed phase plus any user-defined sources. In our work we used user-defined codes to define the reaction, so the R_i term is considered in S_i term. Y_i represents the mass fractions of each species.

For species transport calculations, there are two ways to model the diffusion of chemical species: the Fickian diffusion and the full multicomponent diffusion. The full multicomponent diffusion model considers Maxwell-Stefan equations to obtain diffusion coefficients, and accordingly the diffusive mass flux. Since, this method requires the computation of N^2 co-factor determinants of size of (N-1) x (N-1), and one determinant of size N x N, where N is the number of chemical species, it brings additional computational complexities. Therefore, in our work we have selected the Fickian diffusion model.

The mass diffion based on the Fick's law in turbulent flows can be defined in the following form:

$$J_i = -\left(\rho D_{i.m} + \frac{\mu_t}{Sc_t}\right)\nabla Y_i - D_{T,i}\frac{\nabla T}{T} \qquad (1.25)$$

where $D_{i,m}$ is the mass diffusion coefficient for species *i* in the mixture, Sc_t is the effective Schmidt number for the turbulent flow ($Sc_t = \mu_t/\rho D_t$, D_t is the effective mass diffusion coefficient due to turbulence), and D_T is the thermal diffusion coefficient. Equation (1.25) is mostly applied for the approximation of the dilute mixtures when $Y_i \ll 1$, for all *i* except the carrier gas. Mass diffusion coefficients can be defined in two different methods: dilute approximation and multicomponent. When dilute approximation is selected, the $D_{i,m}$ parameters can be pre-calculated and defined.

In the multi-component diffusion model (M-C), the $D_{i,m}$ parameters are calculated by FLUENT with the defined binary diffusivities as the following:

$$D_{i,m} = \frac{1 - X_i}{\sum_{j,j\neq i}(X_j / D_{ij})} \qquad (1.26)$$

where X is the mole fraction, and D_{ij} is the binary mass diffusion coefficient (Fluent, 2005).

1.2.2.4 Near-Wall Treatment

Turbulent flows in packed tubes are strongly influenced by the solid surfaces, both the tube wall and the surface of the packing. Collectively, solid surfaces are referred to as “walls” in the CFD literature, and in this section we will continue that tradition. Besides the no-slip boundary condition on the velocity components that has to be satisfied, the turbulence is also changed by the presence of the wall. Very close to the wall, the tangential velocity fluctuations are reduced by viscous damping and the normal fluctuations are reduced by the kinematic blocking. In the outer part of the near-wall region, in contrast, turbulence is increased by the production of turbulence kinetic energy due to the large gradients in the mean velocity.

The near-wall region is conceptually subdivided into three layers, based on the experimental evidence. The innermost layer is the viscous sublayer in which the flow is almost laminar, and the molecular viscosity plays a dominant role. The outer layer is considered to be fully turbulent. The buffer layer lies in between the viscous sublayer and the fully turbulent layer, and the effects of molecular viscosity and turbulence are equally important. To numerically resolve a solution in the sublayer requires a very fine mesh, since the sublayer is thin and gradients are large. In order to save the computational effort, high-Reynolds number models, such as RNG κ-ε model, are coupled with an approach in which the viscosity-affected inner region (viscous sublayer and buffer layer) are not resolved. Instead, semi-empirical formulas called “wall functions” are used to bridge the viscosity-affected region between the wall and the fully turbulent region. The two approaches to the sublayer problem are depicted schematically in Figure 1.4 (Fluent, 2005).

In most high-Reynolds-number flows, the wall function approach substantially saves computational resources, because the viscosity-affected near-wall region, in which the solution variables change most rapidly, does not need to be resolved. The wall function approach is popular because it is economical, robust, and reasonably accurate. It is a practical option for the near-wall treatments for industrial flow simulations.

The wall function approach, however, is inadequate in situations where the low-Reynolds-number effects are pervasive in the flow domain in question, and the hypotheses underlying the wall functions cease to be valid. Such situations require near-wall models that are valid in the viscosity-affected region and accordingly integrable all the way to the wall.

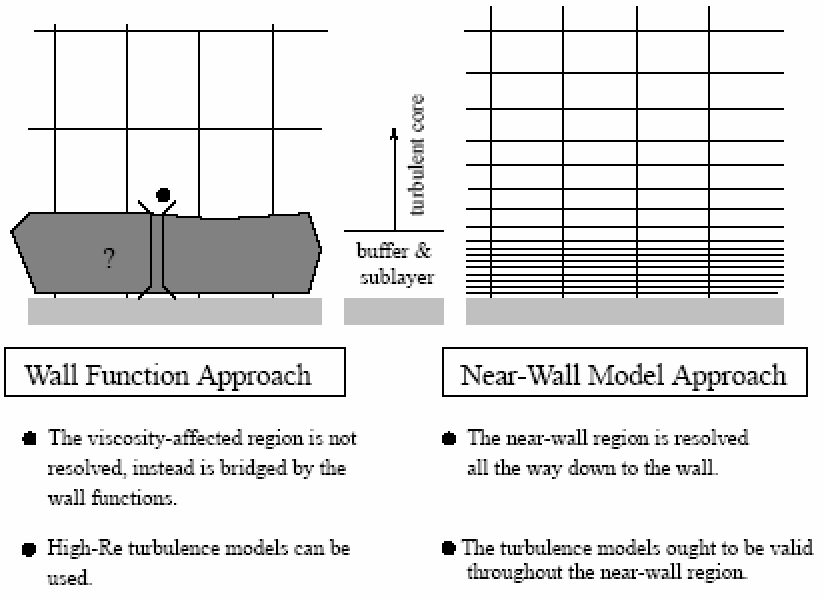

Figure 1.4 Near-wall treatments

The standard wall function (Launder and Spalding, 1974) has been widely used for industrial flows. The wall function is based on the assumption that the velocity obeys the log law-of-the-wall:

$$U^* = \frac{1}{k}\ln(Ey^*) \tag{1.27}$$

where

$$U^* \equiv \frac{U_p C_\mu^{1/4} k_p^{1/2}}{\tau_w / \rho} \tag{1.28}$$

$$y^* \equiv \frac{C_\mu^{1/4} k_p^{1/2} y_p}{\nu} \tag{1.29}$$

and k and E are universal constants, and U_p is the mean velocity at P, the centroid of the cell next to the wall, and y_p is the distance of point P from the wall. We shall follow the original reference and present the wall functions in terms of y^* and U^*, although the usual notation in the turbulent field is to use:

$$y^+ \equiv \frac{\sqrt{\tau_w / \rho}}{\nu} y_p \qquad U^+ \equiv \frac{U_p}{\sqrt{\tau_w / \rho}} \tag{1.30}$$

It is important to place the first near-wall grid node far enough away from the wall at y_p to be in the fully turbulent inner region, where log law-of-the wall is valid. This usually means that we need $y^* > 30\text{-}60$ for the wall-adjacent cells, for the use of wall functions to be valid. If the first mesh point is unavoidably located in the viscous sublayer , then one simple approach (Fluent, 2005) is to extend the log-law region down to $y^* = 11.225$ and to apply the laminar stress-strain relationship: $U^* = y^*$ for $y^* < 11.225$. Results from near-wall meshes that are very fine using wall functions are not reliable.

The heat flux to the wall and the wall temperature are related through a wall function:

$$\frac{(T_w - T_p)\rho c_p C_\mu^{0.25} k_p^{0.5}}{\dot{q}''_w} = \Pr_t [\frac{1}{k}\ln(Ey^*) + P] + \frac{1}{2}\rho \Pr \frac{C_\mu^{0.25} k_p^{0.5}}{\dot{q}''_w} \{\Pr_t U_p^2 + (\Pr - \Pr_t) U_c^2\} \tag{1.31}$$

where P can be computed using (Lauder and Spalding, 1974):

$$P = \frac{\pi/4}{\sin(\pi/4)} \left(\frac{A}{k}\right)^{0.5} \left(\frac{\Pr}{\Pr_t} - 1\right) \left(\frac{\Pr_t}{\Pr}\right)^{0.24} \tag{1.32}$$

where T_p is the temperature at the cell adjacent to the wall, T_w is the temperature at the wall, $\dot{q}''_w$ is the wall heat flux, $\Pr_t$ is the turbulent Prandtl number, U_c is the mean velocity magnitude at the edge of the thermal conduction layer, and A, k and E are universal constants.

An analogous approach is used for species transport:

$$\frac{(Y_{i,w} - Y_i)\rho C_\mu^{0.25} k_p^{0.5}}{J_{i,w}} = Sc_t [\frac{1}{k} \ln(Ey^*) + P_c] \quad (1.33)$$

where Y_i is the local species mass fraction, Sc_t is the turbulent Schmidt number, and $J_{i,w}$ is the diffusion flux of species *i* at the wall. Here, P_c is calculated in a similar was as P with a difference being that the Prandtl numbers are always replaced by the Schmidt numbers.

If the near-wall mesh is fine enough to be able to resolve the laminar sublayer (typically $y^+ \approx 1$), instead of standard wall functions, another method, called "Enhanced Wall Treatment", (EWT), which uses blending functions to obtain a single equation valid for all three near-wall layers may be selected (Fluent, 2005):

$$u^+ = e^\Gamma u^+_{lam} + e^{1/\Gamma} u^+_{turb} \quad (1.34)$$

where the blending function is given by:

$$\Gamma = -\frac{a(y^+)^4}{1+by^+},\ a = 0.01c,\ b = \frac{5}{c},\ c = \exp\left(\frac{E}{E''} - 1.0\right) \quad (1.35)$$

where $E = 9.793$ and E'' is equal to E/f_r, where f_r is a roughness function.

EWT thermal and species functions follow the same approach developed for the profile of u^+, as changing u^+ parameters with T^+ and Y_i^+ respectively. Also, in the blending function, Prandtl and Schmidt numbers appear as a multiplier of y^+ both in nominator and denominator for thermal and species functions, respectively.

1.2.2.5 Numerical Solutions

The governing partial differential equations for the conservation of momentum and scalars such as mass, energy, species and turbulence are solved in the integral form. The commercial CFD software, FLUENT, that we use in our work, uses control-volume basis technique, which consists of three basic steps:

- Division of the domain into discrete control volumes using a computational grid.
- Integration of the governing equations on the individual control volumes to construct algebraic equations for unknowns such as velocities, pressure, temperature, and conserved scalars.
- Linearization of the discretized equations and solution of the resultant linear equation system.

FLUENT allows us to choose either segregated or coupled numerical methods. Both methods employ a similar discretization process, but the approach used to linearize and solve the discretized equations is different. In short, the segregated approach solves for a single variable field (e.g., u) by considering all cells at the same time. It then solves for the next variable field by again considering all cells at the same time, and then returns back. As its nature, there is no explicit option for the segregated solver. On the other hand, in coupled solver both implicit and explicit options are available. The coupled implicit approach solves for all variables (p, u, v, w, T) in all cells at the same time, whereas the explicit one solves for all variables one cell at a time.

In our work, we have selected the segregated approach regarding our highly nonlinear computational domain. The solution loop of the segregated solver consists of six steps as illustrated in Figure 1.5:

1. Fluid properties are updated, based on the current solution. (If the calculation has just begun, the fluid properties will be updated based on the initialized solution.)
2. The u, v, and w momentum equations are each solved in turn using current values for pressure and face mass fluxes, in order to update the velocity field.
3. Since the velocities obtained in Step 2 may not satisfy the continuity equation locally, a "Poisson-type" equation for the pressure correction is derived from the continuity equation and the linearized momentum equations. This pressure

correction equation is then solved to obtain the necessary corrections to the pressure and velocity fields and the face mass fluxes such that continuity is satisfied.

4. Where appropriate, equations for scalars such as turbulence, energy, species, and radiation are solved using the previously updated values of the other variables.
5. When interphase coupling is to be included, the source terms in the appropriate continuous phase equations may be updated with a discrete phase trajectory calculation.
6. A check for convergence of the equation set is made. If the convergence is not reached to within the specific tolerance, the process is repeated from step 1.

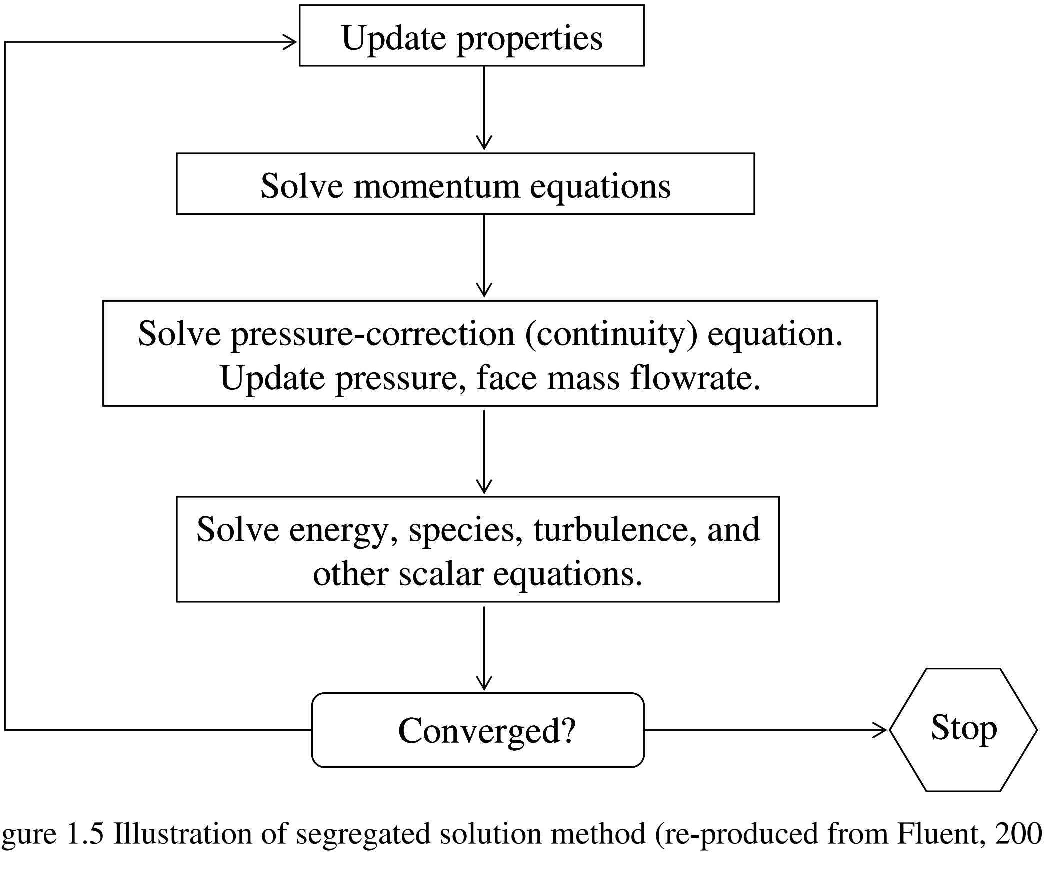

Figure 1.5 Illustration of segregated solution method (re-produced from Fluent, 2005)

1.2.2.6 Discretization

In control-volume based CFD methods, the governing differential equations are converted into algebraic equations to solve them numerically. This technique consists of integrating the governing equations about each control volume, yielding discrete equations that conserve each quantity on a control-volume basis.

Discretization of the governing equations can be illustrated most easily by considering the steady-state conservation equation for transport of a scalar quantity, ϕ. This is demonstrated by the following equation written in integral form for an arbitrary control volume V as follows:

$$\oint \rho\phi\vec{v}\cdot d\vec{A} = \oint \Gamma_\phi \nabla\phi \cdot d\vec{A} + \int_V S_\phi dV \qquad (1.36)$$

where ρ is density, $\vec{v}$ is velocity vector (= $ui + uj$ in 2D), $\vec{A}$ is surface area vector, Γ_ϕ is diffusion coefficient for ϕ, $\nabla\phi$ is the gradient of ϕ (= $(\partial\phi/\partial x)i + (\partial\phi/\partial y)j$ in 2D), and S_ϕ is the source of ϕ per unit volume.

Equation (1.36) is applied to each control volume, or cell, in the computational domain. The two-dimensional, triangular cell shown in Figure 1.6 is an example of such a control volume. Discretization of equation (1.36) on a given cell yields:

$$\sum_{f}^{N_{faces}} \rho_f \vec{v}_f \phi_f \cdot \vec{A}_f = \sum_{f}^{N_{faces}} \Gamma_\phi (\nabla\phi)_n \cdot \vec{A}_f + S_\phi V \qquad (1.37)$$

where N_{faces} is number of faces enclosing cell, ϕ_f is the value of ϕ convected through face f, $\rho_f \vec{v}_f \cdot \vec{A}_f$ is the mass flux through the face, $\vec{A}_f$ is the area of face, $(\nabla\phi)_n$ is the magnitude of $\nabla\phi$ normal to face f, and V is the cell volume.

By default, FLUENT stores discrete values of the scalar, ϕ, at the cell centers (c_0 and c_1 in Figure 1.6). However, face values, ϕ_f, are required for the convection terms in equation (1.37) and must be interpolated from the cell center values. This is accomplished using an upwind scheme. Upwinding means that the face value ϕ_f is derived from quantities in the cell upstream, or "upwind," relative to the direction of the normal velocity. There are several upwind schemes available: first-order upwind, second-order upwind, power law, and QUICK. The diffusion terms in equation (1.37) are always second-order accurate. Regarding our computationally expensive models, to keep the CPU time in a reasonable range, we have selected first-order upwind scheme in our work.

In the first-order upwind scheme quantities at cell faces are determined by assuming that the cell-center values on any field variable represent a cell-average value and hold throughout the entire cell. That means, the cell face quantities are identical to the cell-center quantities.

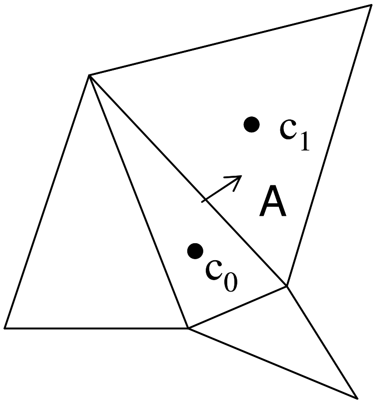

Figure 1.6 Illustrated 2D control volumes for discretization

1.2.2.6.1 Pressure-Velocity Coupling

The integrated continuity equation over the control volume will be in the form of the following discrete equation:

$$\sum_{f}^{N_{faces}} J_f \cdot \vec{A}_f \qquad (1.38)$$

where J_f is a face flux($\rho\vec{v}$). As stated before, momentum and continuity equations are solved sequentially in the segregated solver. In this sequential procedure, the continuity equation is used as an equation for pressure, which does not appear explicitly in the equation. Instead, a Semi-Implicit Method for Pressure-Linked Equations (SIMPLE) is used for introducing pressure into the continuity equation. If the momentum equation is solved with a guessed pressure field, p^*, the resulting face flux, $J_f{}^*$, can be expressed as:

$$J_f^* = \hat{J}_j^* + d_f\,(p_{c0}^* - p_{c1}^*) \tag{1.39}$$

where the term d_f is a function of the momentum equation linearization coefficients for the cell on either side of face *f*. Since equation (1.39) does not satisfy the continuity equation, a correction J'_j is added to the face flux so that the corrected face flux, J_f, can be expressed as $J_f = J_f^* + J'_f$, which satisfies the continuity equation. The SIMPLE algorithm postulates that, J'_j can be rewritten as:

$$J'_f = d_f\,(p'_{c0} - p'_{c1}) \tag{1.40}$$

where p' is the cell pressure correction. Once a solution is obtained, the cell pressure and the face flux are corrected using the following expressions:

$$p = p^* + \alpha_p p' \tag{1.41}$$

$$J_f = J_j^* + d_f\,(p'_{c0} - p'_{c1}) \tag{1.42}$$

Here the α_p is the under-relaxation factor (URF) for pressure. This factor is introduced for any scalar variable regarding the nonlinearity of the set of the equations. In order to control the change in these scalar variables, URF's are used which reduces the change of the scalar variable produced during each iteration. In a general form, the new value of the variable ϕ within a cell depends upon the old value ϕ_{old}, the computed change inϕ , $\Delta\phi$, and the URF, α, can be expressed as follows:

$$\phi = \phi_{old} + \alpha\Delta\phi \tag{1.43}$$

Commercial codes, such as FLUENT, will typically recommend values for the URF that work well with a wide range of flows. For packed bed simulations we usually used the default unity values. Some simulations, however, did not converge until very small values, of the order 0.1 or lower, were used at the beginning until the residuals have leveled out. Then, they are gradually increased up to the unity.

To determine when a solution is converged usually involves examining the residual values. The residual value is a measure of the imbalance in the discretized equation, summed over all the computational cells in the domain. Residuals can be obtained for continuity, velocity components, turbulence variables, and energy. In addition, it is a good idea to monitor other measures of convergence besides the residuals, such as pressure drop and/or an averaged wall shear stress or exit temperature (Guardo et al., 2005; Gunjal et al., 2005). We have seen apparently level residuals while the pressure drop slowly changed, and a substantial different final flow field was eventually obtained, often after several thousand iterations. Following apparent convergence, it is essential to check both mass and energy balances, as well as performing grid independence studies and comparing to experimental results, to have convergence in the solution. Just because a simulation has converged, does not mean that it is necessarily reliable.

1.2.3 Mesh generation

The mesh generation is an important part of CFD for complex geometries such as fixed beds. The accuracy of the simulation is strongly affected by the mesh structure. The mesh density has to be chosen fine enough to describe the process accurately. To find the optimal density, models can be created with different mesh sizes and/or with different grid structures, according to the available computational resources, and comparing the simulation results within each other and/or with any realistic evidence. Once the optimal density has been achieved, refining the mesh will increase the model size without capturing more details in simulations. Therefore, intelligent gridding is a key step in mesh generation, and usually this task consumes the largest amount of user time for a designer.

As stated before, the two main types of mesh are structured and unstructured. In a structured mesh, there are families of grid lines following the constraint that grid lines of the same family do not cross each other and cross each member of the other families only once. Although, the structured grid can be used to develop efficient solutions, the major disadvantage is the difficulty in controlling the grid distribution. To eliminate this disadvantage, a block-structured grid is used. In a block-structured grid the domain is divided onto a number of blocks which may or may not overlap. By this way a structured grid can be defined within each block. For very complex geometries, unstructured grids, which can fit an arbitrary domain, are used. In this case, there is no restriction on the shape of the control volume and the neighboring nodes. In 3D domains, tetrahedral cells are widely used. A local refinement flexibility that can be applied to any particular place of interest makes the unstructured grid applicable for many complex domains (Ranade, 2002). Examples of structured and unstructured grids are shown in Figure 1.7 for a typical catalyst particle with an internal hole.

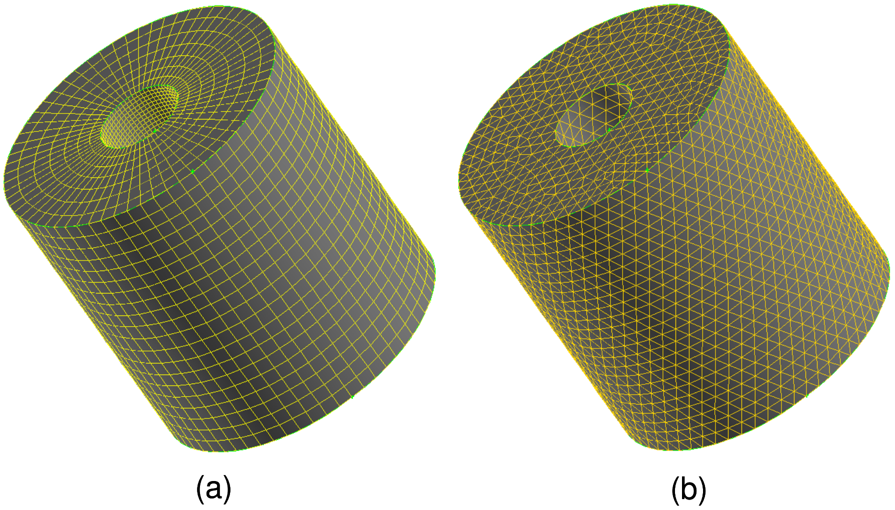

Figure 1.7 Examples of structured and unstructured grids.

For turbulent flow modeling, the preferred range for the thickness of the near-wall cell layer is $y^+ > 30$, as mentioned in the description of standard wall functions. However, this is difficult to achieve in packed beds. Because, the cell sizes are constrained by the need to fit in between the gaps and/or narrow spaces between particles, so they can not be too large. This can result in the y^+ values being too small for proper application of wall functions. The alternative to use small enough cells to resolve the boundary layer ($y^+ \approx 1$) increases the computational cost unacceptably (Dixon, 2006).

Considering these constraints, implementation of several layers of prismatic cells on the solid walls, by which $y^+ \approx 1$ can be obtained, and application of the unstructured tetrahedral elements for the rest of the domain was selected to solve the domain by many workers (Calis et al, 2001) including us. In this case the computational cost can be kept lower as opposed to creating the entire domain with very fine mesh. In Figure 1.8(a), a typical unstructured grid application for one of our packed bed models is shown. In Figure 1.8(b), a prism layer implementation on to the tube and pellet walls is shown for the bottom plane of a model represented in Figure 1.8(a). With an enlarged view of an arbitrary place, the prism layers and the unstructured grid structure with triangular face elements can be seen.

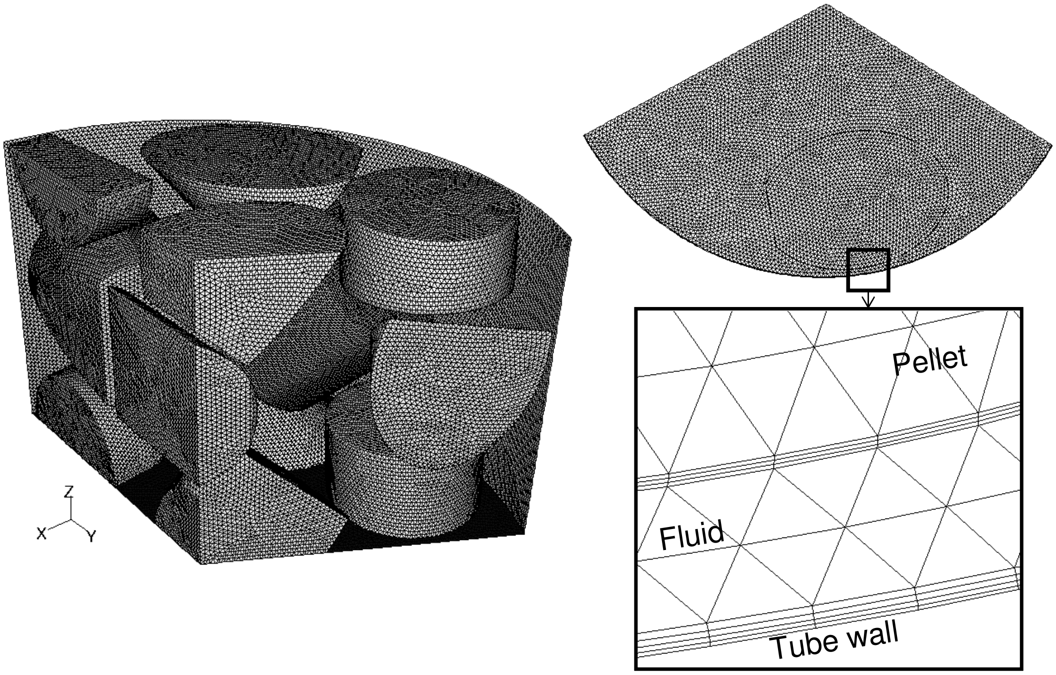

(a) (b)

Figure 1.8 (a) An example of an unstructured grid in one of our packed bed models, (b) Prism layer implementation with an enlarged view in an arbitrary place.

1.3 Use of CFD in Chemical Reaction Engineering

By the very nature of the profession, the chemical engineer has to deal frequently with chemically reactive flows in various types of single-phase and multiphase reactors. Before the advent of CFD, he or she typically had to use highly idealized and approximate solution strategies supplemented with empirical information to obtain solutions for practical problems. Recently, CFD based strategies have replaced those strategies.

In many processes encountered in industrial practice, different types of multiphase flow may exist. They can be classified basically as gas-liquid, liquid-liquid, and fluid-solid systems.

Gas-liquid systems of particular interest to the chemical engineer are encountered in bubble columns, spray columns, air lift, falling film, and stirred tank reactors. Usually the form of these reactors corresponds to that of vessels or columns. From the perspective of the chemical engineer, who is concerned with the conversion and selectivity of chemical transformations, it is of utmost importance that an intensive contact between a gas and a liquid be achieved and therefore very often one phase is continuous whereas the other is disperse. Therefore, the interfacial area and the size of the disperse phase elements constitute very important aspects of CFD modeling of these types of systems.

Liquid-liquid systems are encountered in many practical applications involving physical separations of which extraction processes performed in both sieve-tray and packed columns are well known applications. As an example, by implementing CFD on these particular cases, the theoretically computed droplet sizes were found in good agreement with the experimental values (Ohta et al., 1995). In addition to that, complex free surface flows, and systems involving droplet interactions were analyzed quite expensively by CFD.

Fluid-solid systems, especially in situations where the fluid is a gas, are very frequently encountered in various important industrial processes such as fluidized bed reactors and fixed-bed reactors.

CFD analysis clearly revealed that many important key properties of bubbling fluidized beds, such as, solid mixing and segregation, bed expansion and bubble dynamics can be predicted satisfactorily (Owoyemi et al., 2007).

The analysis of fluid flow, heat transfer processes and coupled chemical conversion in fixed bed reactors has traditionally received considerable attention from chemical engineers. For that reason, for nearly a half of a century, engineers aimed to having better insight into the reactor system. To achieve that, CFD has been considered as a suitable tool for many researchers including us, and application of CFD is rapidly becoming increased (Dixon et al., 2006).

Although the use of CFD to simulate such geometrically complex flows is too expensive and impractical currently for routine design and control of fixed-bed reactors, the real contribution of CFD in this area is to provide more fundamental understanding of the transport and reaction phenomena in such reactors. CFD can supply detailed three-dimensional velocity, species and temperature fields that are needed to improve engineering approaches. The details about the CFD application on fixed bed reactors are given in the Chapter 2.

1.4 Modeling of Fixed Bed Reactors

While designing the fixed bed reactor, the objective is to arrive at the set of system parameters that result in optimal operation. In the case of fixed bed reactors these parameters are temperature, pressure, composition, flow rate, and the reactor tube and catalyst pellet dimensions. In order to obtain the desired conversion with the specified selectivity, system of equations need to be used to relate the outlet concentrations to the above parameters by considering the transport processes described in section 1.1. For that reason, the mathematical models have been proposed, and techniques were developed to solve them. Among them, three models as pseudocontinuum , cell, and Discrete Packing

Model (DPM) have been schematically represented in Figure 1.3, and further explained below.

Among the available fixed bed reactor models, the pseudo-continuum models are the most frequently addressed ones. According to the Froment's (1974) classification, pseudo-continuum models can be grouped in two categories; the pseudohomogeneous and the heterogeneous models. The former consider the bed as a single phase, while the latter distinguish between temperatures and concentrations in the bulk gas phase and those inside or at the surface of the catalyst. In other words, in the pseudohomogeneous model, the intra-particle and inter-phase processes are not important, and the concentration and temperature in the internal field are the same as those in the external field by which the reaction rate is obtained. However, in the heterogeneous model, transport processes play a finite role and the equations for the internal field have to be solved in order to obtain the reaction rate (Doraiswamy and Sharma, 1984).

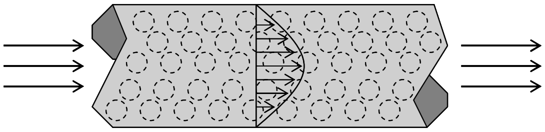

(a) pseudo-continuum

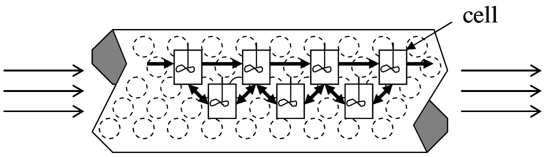

(b) cell model

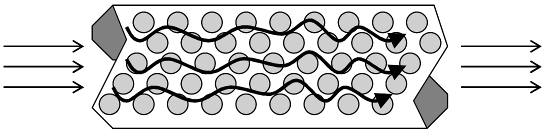

(c) DPM

Figure 1.9 Fixed bed reactor models; (a) pseudo-continuum model, (b) cell model, (c) DPM (re-produced from Dixon, 2006).

1.4.1 Pseudohomogeneous models

The basic model, used in most of the studies, is the pseudohomogeneous one-dimensional (1D) model, which only considers transport by plug flow in the axial direction. The conservation equations may be written for the steady state and single reaction carried out in a cylindrical tube as:

$$u_s \frac{\partial C}{\partial z} + \rho_S r_A = 0 \tag{1.44}$$

$$u_s \rho_B c_p \frac{\partial T}{\partial z} - \rho_S (-\Delta H) r_A + 4 \frac{U}{d_t} (T - T_r) = 0 \tag{1.45}$$

where u_s is superficial velocity, C is concentration, ρ_S is catalyst density, r_A is rate of disappearance of A, ρ_B is bulk density, c_p is heat capacity, T is temperature, $(-\Delta H)$ is heat of reaction, U is overall heat transfer coefficient, T_r temperature of surroundings, d_t is tube diameter, and z is the axial direction.

If radial gradients have to be accounted for, the model becomes two dimensional. For this case, the continuity and the energy equations can be written as follows, for a single reaction and steady state:

$$(D_{er})_s \left(\frac{\partial^2 C}{\partial r^2} + \frac{1}{r} \frac{\partial C}{\partial r} \right) - u_s \frac{\partial C}{\partial z} - \rho_S r_A = 0 \tag{1.46}$$

$$k_{er} \left(\frac{\partial^2 T}{\partial r^2} + \frac{1}{r} \frac{\partial T}{\partial r} \right) - u_s \rho_B c_p \frac{\partial T}{\partial z} + \rho_S (-\Delta H) r_A = 0 \tag{1.47}$$

The effective diffusion in radial direction (D_{er}), describes the contribution arising from the transport in the fluid and corresponds to the mixing. $(D_{er})_s$ represents this parameter based upon the superficial flow velocity. Similarly, k_{er} shows the radial thermal conductivity.

1.4.2 Heterogeneous models

The basic model of the heterogeneous category considers only transport by plug flow again, but distinguishes between conditions in the fluid and in the solid. A 1D heterogeneous model which accounts for the interfacial gradients may be represented as:

For fluid:

$$u_s \frac{\partial C}{\partial z} + k_g a_v (C - C_s^s) = 0 \tag{1.48}$$

$$u_s \rho_B c_p \frac{\partial T}{\partial z} - h_f a_v (T_s^s - T) + 4\frac{U}{d_t}(T - T_r) = 0 \tag{1.49}$$

For solid:

$$k_g a_v (C - C_s^s) = \rho_S r_A \tag{1.50}$$

$$h_f a_v (T_s^s - T) = \rho_S (-\Delta H) r_A \tag{1.51}$$

with boundary conditions of $C=C_0$ and $T = T_0$ at $z = 0$. Here, k_g is mass transfer coefficient, a_v is pellet surface area per reactor volume, h_f is the heat transfer particle for a film surrounding the particle, and T_s and T_s^s (C_s and C_s^s) are temperature (concentration) inside solid and at the solid surface respectively.

When the resistance to mass and heat transfer inside the pellet is important, the rate of reaction is not uniform throughout the particle. This time, the solid phase modeling equations, (1.50) and (1.51), may be replaced with the following equations (for a spherical pellet, as an example):

$$\frac{D_e}{\xi^2}\frac{d}{d\xi}\left(\xi^2 \frac{dC_s}{d\xi}\right) - \rho_S r_A (C_s, T_s) = 0 \tag{1.52}$$

$$\frac{k_e}{\xi^2}\frac{d}{d\xi}\left(\xi^2 \frac{dT_s}{d\xi}\right) + \rho_S (-\Delta H) r_A (C_s, T_s) = 0 \tag{1.53}$$

with the additional boundary conditions:

$$\frac{dC_s}{d\xi} = \frac{dT_s}{d\xi} = 0 \qquad \text{at } \xi = 0 \tag{1.54}$$

$$-D_e\left(\frac{dC_s}{d\xi}\right) = k_g(C_s^s - C) \qquad \text{at } \xi = d_p/2 \tag{1.55}$$

$$-k_e\left(\frac{dT_s}{d\xi}\right) = h_f(T_s^s - T) \qquad \text{at } \xi = d_p/2 \tag{1.56}$$

where ξ is the pellet radial distance. Here, a single particle is considered, not the solid as a whole when the intra-particle profiles are to be dealt with. These equations are in the second order, and highly nonlinear. That means, iterative solution procedure has to be necessary in each computational node. For the isothermal simple reactions, analytical solution is possible. However, in order to consider the intra-particle gradients, the effectiveness factor, η, was introduced. In the classical sense, η is a factor that multiplies the reaction rate at the particle surface conditions to yield the rate that is actually experienced when the conditions inside the particle are different, which can be represented as:

$$\eta = \frac{\textit{rate of reaction with diffusion resistance}}{\textit{rate of reaction with surface conditions}} \tag{1.57}$$

The use of η reduces the system equations into the following algebraic equations:

$$k_g a_v (C - C_s^s) = \eta \rho_S r_A(C_s^s, T_s^s) \tag{1.58}$$

$$h_f a_v (T_s^s - T) = \eta \rho_S (-\Delta H) r_A(C_s^s, T_s^s) \tag{1.59}$$

with $\eta = f(C_s^s, T_s^s)$. In practice, η may be calculated as:

$$\eta = \frac{\int_0^V r_A(C_s, T_s)\rho_S \frac{dv}{V}}{r_A(C_s^s, T_s^s)} \tag{1.60}$$

where V is the pellet volume.

The general two dimensional heterogeneous models may be represented by the following mathematical model:

$$\varepsilon D_{er}\left(\frac{\partial^2 C}{\partial r^2}+\frac{1}{r}\frac{\partial C}{\partial r}\right)-u_s\frac{\partial C}{\partial z}-k_g a_v (C-C_s^s)=0 \qquad (1.61)$$

$$k_{er,f}\left(\frac{\partial^2 T}{\partial r^2}+\frac{1}{r}\frac{\partial T}{\partial r}\right)-u_s \rho_B c_p\frac{\partial T}{\partial z}+h_f a_v (T_s^s-T)=0$$

(1.62)

$$k_g a_v (C-C_s^s)=\eta\rho_p r_A \qquad (1.63)$$

$$h_f a_v (T_s^s-T)=\eta\rho_B(-\Delta H)r_A + k_{er,s}\left(\frac{\partial^2 T_s}{\partial r^2}+\frac{1}{r}\frac{\partial T_s}{\partial r}\right) \qquad (1.64)$$

where ε is bed voidage, k_g is mass transfer coefficient, a_v is pellet surface area per reactor volume, and $k_{er,f}$ and $k_{er.f}$ are effective thermal conductivity for the fluid phase and respectively for the solid phase (Froment and Bishoff, 1990).

1.4.3 Cell models

The mixing cell model has been proposed as alternative to pseudo-continuum models. This model considers the bed to consist of two dimensional network of perfectly mixed cells with two outlets to the subsequent row of cells. Alternative rows are offset half a stage to allow for radial mixing. In the steady-state, a pair of algebraic equations must be solved for each cell. This model was proposed by Deans and Lapidus (1960) and applied by McGuire and Lapidus (1965) to non-steady-state cases. The equivalence between the predictions of pseudo-continuum and cell models has been extensively studied by many workers. Recently, Jiang et al, (2000) considered discrete cell approach to model low Re single phase flow, and comparison of the results with the Navier-Stokes based CFD predictions showed an agreement with 10% deviation. This approach has not been addressed frequently in the modeling studies especially for the high Re industrial flow conditions based on being far away from the true hydrodynamics.

1.4.4 DPM

DPM approach does not simplify the geometrical complexities of the packing, or replace them as the pseudo-continuum model. An alternative and complementary use of CFD in fixed bed simulation has been to solve the actual flow field between the particles which is the key point in DPM. The application of CFD to packed bed modeling is on the increase and has recently been reviewed (Dixon et al., 2006). In our work, we have used CFD as a modeling tool to create 3D DPMs. Details of our methodology is given in Chapters 3, 4, and 5.

1.5 Steam Reforming Reaction

One of the most common applications of the fixed bed reactor is the steam reformers where steam reforming reaction takes place. The steam reforming of hydrocarbons is the most important and economic industrial process for the production of hydrogen and synthesis gas which is becoming an important fuel for various purposes such as Fischer Tropsch chemistry. The generation of syn-gas dates from the first quarter of the last century with the development of the classical Haber Bosch process in 1917, based on the reaction of steam with coke. In 1931 Standard Oil built a plant to generate hydrogen from refinery off-gases at Baton Rouge; the reforming reaction took place over a catalyst in vertical tubes in parallel rows in a radiant, fired furnace. Work in ICI in the 1950s led to a more stable catalyst, operated at economic steam ratios without excessive carbon formation and resistant to poisons. In 1959 ICI started up the first large-scale pressure steam reformer using naphtha as a feed. This plant and technology became the forerunner to over 400 plants subsequently licensed around the world in areas where natural gas (methane) was not readily available. Since then, development of the catalyst has allowed plants to be run at higher pressure and temperature, using feedstocks with different hydrogen:carbon ratios.

In the last 25 years the increased availability of natural gas has resulted in its use as the main feedstock for steam reforming with development of the catalyst for longer life, higher activity, reduced carbon formation and with improved physical attributes.

The last 5 years have however seen a shift in emphasis. Two new applications of syn-gas are becoming of increasing importance: the manufacture of liquid fuels from remote, marginal or stranded natural gas, and generation of hydrogen from natural gas or liquid fuels to power mobile and stationary fuel cells (Stitt, 2005).

The highly endothermic reaction takes place in the steam reformers which generally have a tube and shell design. A large number of catalyst-filled tubes are used for this purpose. Due to the endothermic nature of the reaction, energy should be supplied to the tubes from the outside usually by a series of burners. That's why, the steam reformer operates at very high temperatures (approximately 1000 K).

The base reaction taking place in steam reforming is:

$$\text{(I) } CH_4 + H_2O \rightarrow CO + 3H_2 \qquad (1.65)$$

Simultaneously a water gas shift reaction is taking place:

$$\text{(II) } CO + H_2O \rightarrow CO_2 + H_2 \qquad (1.66)$$

These two reactions were considered by scientists coupling with the following reaction:

$$\text{(III) } CH_4 + 2H_2O \rightarrow 2CO_2 + 4H_2 \qquad (1.67)$$

Although, the water gas shift reaction is slightly exothermic, the overall process is highly endothermic.

The main process step involves the reaction of steam with a hydrocarbon over a catalyst to form hydrogen and carbon oxides, however, there are several other steps to remove impurities and maximize hydrogen production. The typical process can be schematically represented by Figure 1.4 which is taken from web site of Johnson Matthey Catalysts.

Due to the high temperature and high flow conditions, it is not easy to have measurements for flow or temperature patterns inside the reactors. Currently the only experimental data that can be obtained inside industrial tube and shell steam reformers are pyrometer measurements of the external tube temperature. Even though, this method only gives a superficial indication of the internal situation, it can also identify problem areas in heat absorption inside the reformer, due to non-uniform packing. Therefore, CFD can give a lot more information easily and without disturbance of the original temperature and flow field in the reformer tubes.

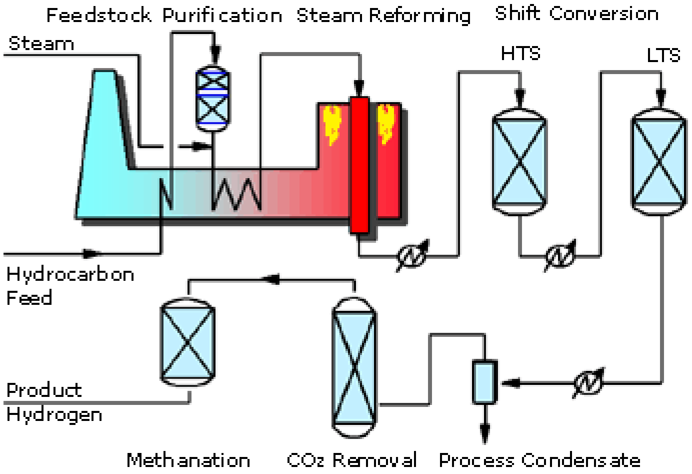

Figure 1.10 Generalized steam reforming plant

In our work we have used typical industrial steam reforming inlet conditions obtained from a Johnson Matthey detailed reformer model of a methanol plant steam reformer. Accordingly, we have selected the kinetic expressions, obtained with a Johnson Matthey catalyst, performed by Hou and Hughes (2001).

A set of experiments were carried out by the authors to study the intrinsic kinetics of methane steam reforming over a Ni/α-Al_2O catalyst, accompanied by the reverse water gas shift reaction over the mentioned commercial catalyst in an integral reactor under the conditions of no diffusion limitation. In addition, the main reactions involved in methane steam reforming were analyzed thermodynamically and the effect of pressure and steam:methane ratio was examined. A reaction mechanism was proposed by the authors, and the first three reactions given above were considered with the kinetic rate equations developed by Langmuir-Hinshelwood-Hougen-Watson (LHHW) approach and Freundlich's adsorption concept. The proposed kinetic mechanism was quite similar to the one proposed by Xu and Froment (1989a);

1) H_2O reacts with surface nickel atoms, yielding adsorbed oxygen and gaseous hydrogen.
2) Methane reacts with surface nickel atoms, yielding adsorbed CH_2 radicals and adsorbed H atoms.
3) The adsorbed radicals CH_2 and adsorbed oxygen react to yield adsorbed CHO and adsorbed hydrogen.
4) Adsorbed CHO dissociates to adsorbed CO and H, or reacts with adsorbed oxygen, yielding adsorbed CO_2 and H in parallel.
5) Adsorbed CO reacts with adsorbed oxygen to form CO_2, or desorbs into the gas phase.

The final kinetic model was found as;

$$r_1 = \frac{k_1}{p_{H2}^{1.25}}(p_{CH4} p_{H2O}^{0.5})(1 - \frac{p_{H2}^3 p_{CO}}{K_1 p_{CH4} p_{H2O}})/(DEN)^2 \qquad (1.68)$$

$$r_2 = \frac{k_2}{p_{H2}^{0.5}}(p_{CO} p_{H2O}^{0.5})(1 - \frac{p_{H2} p_{CO2}}{K_2 p_{CO} p_{H2O}})/(DEN)^2 \qquad (1.69)$$

$$r_3 = \frac{k_3}{p_{H2}^{1.75}}(p_{CH4} p_{H2O})(1 - \frac{p_{H2}^4 p_{CO2}}{K_3 p_{CH4} p_{H2O}^2})/(DEN)^2 \qquad (1.70)$$

$$DEN = 1 + K_{CO} p_{CO} + K_H p_H^{0.5} + K_{H2O} p_{H2O} / p_{H2} \qquad (1.71)$$

The reaction rate and equilibrium constants in the rate expressions were defined to be temperature-dependent through the Arrhenius and van't Hoff equations,

$$k_i = A_i \exp\left(-\frac{E_i}{RT}\right) \tag{1.72}$$

$$K_i = A(K_i)\exp\left(-\frac{\Delta H_{i,a}}{RT}\right) \tag{1.73}$$

The particular values of the activation energies, heats of adsorption and pre-exponential constants are available in Hou and Hughes (2001), and were used in our work without alteration.

1.6 Propane dehydrogenation

The direct dehydrogenation of alkanes to alkenes can be found in the literature in the literature since the early 1930s. Commercially, however, alkenes are mainly produced by fluid cracking or as a by-product from pyrolysis/cracking furnaces. These processes are capital-intensive and require product separation and purification. This has led to specific catalytic dehydrogenation processes.

Besides economic reasons, two main fundamental problems are responsible for the lack of the commercial application of direct dehydrogenation. First, the dehydrogenation reaction is endothermic. For the dehydrogenation of propane (C_3H_8), $\Delta H^\circ_{874\ K}$ is about 124 kJ/mol. This limits the equilibrium conversion to ~18% at 774 K, and ~50% at 874 K at atmospheric pressure. Because of the increase in the volume, the reaction is best done in low pressure.

The second reason is the fast deactivation of the commercial catalyst due to coke formation which is less than an hour at 874 K. Platinum/alumina (Pt/Al_2O_3) and chromia/alumina (Cr_2O_3/ Al_2O_3) are the two types of catalysts that are commonly used. In some cases, silica or zirconia is used as the support for the catalyst material. Many studies were done on both kinds of catalysts, such as the one of Hou and Hughes (2002) for Pt/Al_2O_3 catalyst, and the work of Stitt et al. (1999) for Cr_2O_3/ Al_2O_3 catalyst.

The rate expression of this reaction is as follows:

$$r = k(C_{C3H8} - \frac{C_{C3H6}C_{H2}}{K}) \tag{1.74}$$

where C is concentration, k is rate constant, and K is equilibrium constant.

Current processes employ mainly fixed bed operation, but because of necessarily high temperatures for the endothermic process catalyst deactivation occurs. To overcome this high temperature requirement, different alternative procedures have been suggested such as oxidative dehydrogenation and the use of membrane reactor. In recent years the membrane reactors are highly suggested in reaction engineering which allows a higher conversion or better selectivity.

The reasons of the selection of this reaction in our work were; having the strongly endothermic nature as the MSR, and having simpler rate expression and higher intra-particle activity as compared to the MSR. In other words, with MSR and PDH reactions, our diffusion/reaction application method will be considered for different reactions with lower and higher intra-particle activities, and therefore the applicability of the method will be understood better. We did not consider the coke formation, and as a result, catalyst deactivation in here.

2. Literature

A fixed bed model can be composed of the separate models for the fluid flow, heat transfer, and mass transfer or species transport. Usually empirical correlations are used for the description of these processes inside fixed beds. The small-scale structure of the packing in the large-scale tube (the bed container) allows for a great deal of stochastic averaging of the flow patterns, which are an essential part of the model, resulting in a successful use of empirical parameters. The empirically determined model parameters use averaged flow and temperature profiles over the diameter of the bed in modeling other functions such as reactions or control aspects of the industrial application. When, however, the tube-to-particle diameter ratio (N) decreases, the void space distribution in the bed can no longer be interpreted as continuous. The literature on determining flow patterns and heat transfer patterns for low N cases has been covered in detail by Nijemeisland (2002).

Regarding the main goal of this study, CFD applications to the fixed bed reactors, reactor modeling with MSR and PDH are summarized in the following sections of this chapter.

2.1 CFD applications to fixed bed reactors

Numerical modeling is applied to fixed beds in many different aspects. Although the approach to the dispersion of mass and heat through Fick’s and Fourier’s laws was challenged, and a wave model was first developed over 40 years ago (Stewart, 1965), one of the earliest fixed bed CFD simulations was applied by Dalman et al. (1986). They used two-dimensional models to investigate flow behavior in an axisymmetric radial plane. This limited the packing possibilities severely but gave a first insight of the flow patterns in the fixed beds. This study showed that eddies formed in between the spherical catalyst particles which led to a region of poor heat transfer. The effects of Re and Pr numbers on this process were also investigated, and showed an increasing problem with heat transfer as the Reynolds number increased.

Stewart et al. (1991) modeled packed tube reactors under mild restrictions. The fluid phase was modeled with equations of change, valid for laminar and turbulent flows. Under standard assumptions, the mass and energy conservation equations were linear and their solutions found to be superimposed to describe packed tube processes with any desired kinetics. The authors also tried to amplify their approach by special experiments.

The general numerical technique for modeling three-dimensional, single phase gas flow patterns in packed beds were given by Parsons and Porter (1992). Specifically they represented a method for implementing a vectorial form of the Ergun equation in a CFD package. The approach was validated by comparison with independent experimental results.

Lloyd and Boehm (1994) studied a two-dimensional case; they used the commercial FE package FIDAP and considered 8-spheres in line as catalyst particles. In this study the influence of the sphere spacing on the drag coefficients was investigated. It was also found that heat transfer from the spheres decreased with decreased sphere spacing.

As computer capabilities are increasing the extent to which CFD can be applied to complicated systems has increased considerably. Earlier studies using a 3-sphere model (Derkx and Dixon, 1996) were performed as one of the first models in 3D simulation of fixed beds. This study focused on using CFD to obtain traditional modeling parameters such as the Nu_w numbers. An 8-sphere model followed (Logtenberg and Dixon, 1998a; 1998b) the packing was modeled as two layers of four spheres, both layers perpendicular to the flow in the tube with a tube-to-particle diameter ratio, $N = 2.43$. Effective heat transfer parameters obtained from these CFD results matched theoretical model predictions (Dixon and Creswell, 1979) reasonably well. These studies were limited by the simplicity of the flow models used to obtain data, e.g. the absence of contact points between the spheres and the wall and amongst the spheres themselves. Another point for improvement in this model was the small number of spheres, which resulted in less than realistic flow patterns. More recently, a 10-sphere model, N = 2.86, incorporating contact points between the particles and between the particles and the wall (Logtenberg et al., 1999) was developed. The 10-sphere model, solved in ANSYS 5.3, showed flow behavior and heat transfer behavior in such detail that cannot be measured in standard experimental setups or described using conventional packed bed models. By using three-dimensional models for these simulations the packing need not be symmetrical (an implied feature in two-dimensional modeling), this way the true nature of the wall effects are shown, as they would be present in a low-N tube.

Gulijk (1998) studied to calculate transversal dispersion in a structured packed bed using CFD. The calculations were done using the parallel code CFX-4.1. To simplify the case, the Toblerone model was developed which models the flow intersecting triangular channels. This model determined well the design properties for a reactor operation. The liquid flow field was solved using Ergun equation to account for porous flow through the pellets. By the Toblerone model it has been found that the transversal dispersion coefficient is a factor 40 higher compared to single phase packed bed flow. This result reminded the authors that, liquid transversel dispersion in this kind of packing would not be a limiting problem when designing a reactor.

At the same time, Esterl et al. (1998) implemented a numerical method for the calculation of the fluid flow through packed beds. A computer code which solves the three dimensional incompressible Navier-Stokes equations with an implemented Chimera grid scheme was modified by the authors here. By this modification, they studied the laminar fluid flow through the narrow gaps of the packing in detail. Up to 500 particles were taken into consideration by the distributed memory of workstation clusters and massively parallel processors. They have seen a good agreement with empirical data given in literature such as pressure drop.

The influence of bed geometry on its frictional resistance under turbulent flow conditions was studied by Tobis (2000). Author presented both experimental and numerical investigations of air turbulent flow through six model packings composed of spheres in cubic arrangement. For different model packings, different turbulence promoters were inserted between the spheres. Theoretical study was done by FLUENT CFD code. The turbulence was modeled by the standard κ-ε model, Spalart and Allmaras, and the Reynolds Stress models to compare predictions of the frictional resistances. Although there is a large discrepancy of the values of Ergun constants, this comparison showed an acceptable agreement according to the author. It was noted that, the bed porosity and the bed hydraulic diameter were not sufficient to describe hydrodynamic properties of an arbitrary designed packing. Tobis also mentioned that, the CFD approach appeard to be more general than any Ergun-like semi-empirical correlation. However, it was also stated that, more detailed experimental and theoretical studies of fluid flow through complex bed structures are required.

With the increasing computational capacity and modeling experience, a 44-sphere model was created with $N = 2$ by Nijemeisland and Dixon (Nijemeisland and Dixon, 2001). This specific geometry was used to validate CFD results in fixed beds by comparing radial temperature profiles of the simulations with experimental data in an identical setup. This work showed that with the proper considerations of the limitations of the simulation and experimental setup taken into account, both qualitative and quantitative agreement was established between CFD simulation and experiments. It was also shown that, CFD produces the same data as is obtained experimentally, we can use the advantage of the CFD; where a lot more information is available than is used for the comparison of CFD data with experimental data, data that cannot be obtained through traditional experimental measurement.

Zeiser et al. (2001) studied the behavior of a reacting, viscous flow inside the complex geometry by means of a lattice Boltzmann method. Monte-Carlo (MC) simulation of the packing process was used for generation of three different geometries of spherical particles as $N = 10$, $N = 6$, and $N = 5$. MC simulated packed beds were found to be in reasonable agreement with correlations gained from experimental investigations in terms of the void fraction distribution. The domain for the 3-D simulation of the flow field was discretized by 102 x 102 x 250 cells. Periodic boundary conditions were used perpendicular to the main flow direction. The results for the local velocity distributions obtained with the lattice Boltzman method show the channeling effects close to the walls that were observed in experiments. In addition to that, chemical reacting flow around a single catalytic particle was studied by the effect of molecular diffusivity and dispersion.

CFD modeling of different types of packing and experimental validation study was carried out by Calis et al. (2001). CFX-5.3 commercial CFD code was used for different bed structures ($1 \leq N \leq 2$). In each case 8-16 particles were used. An unstructured grid was applied in the form of tetrahedral cells, but 5 layers of prismatic cells were taken into consideration close to particle and wall surfaces for laminar flow. There were no prismatic cells for turbulent flow, and Re number up to 10000 was studied. Consequently, the grids prepared for laminar and turbulent flows were different. For turbulent flow, k-ϵ model and Reynolds-Stress Models were considered. Standard wall functions were used in case of turbulent flow. Experimental data, on the other hand, were obtained by a setup of $1 \leq N \leq 2$. Polyethylene spheres were supported by a wire mesh screen. Experimental Re's were varied from about 100 to about 6000. Pressure drops were measured across a bed length of about 500mm. Local velocity profiles were measured with laser-Dopler anemometry (LDA). After a comparison of modeling and experimental results, it was concluded by the authors that, CFD code predicts the pressure drop characteristics of the studied systems within an average error of about 10%. For the turbulent cases, both turbulence models were found to be adequate. However, it was observed that, Ergun equation over predicts the experimental friction factors by an average of 80% in these cases.

Zeiser et al. (2002) analyzed the flow field and pressure drop in fixed bed reactors with lattice Boltzmann method as in the previous study of the same group. For the computations, a three dimensional 19-speed (D3Q19) lattice Boltzman automata with single time BGK-relaxation was used. A parabolic velocity profile at the inlet and a fixed static pressure at the outlet were chosen for simulations. It was observed that, the discretization of spherical objects introduces a significant error. To investigate this error, the lattice Boltzman implementation and a finite volume approach with collocated grids were compared in a convergence study. It was found that, the error in the dimensionless pressure drop decreases for both methods with approximately second order when refining the mesh and finally the same dimensionless pressure drop was reached. Authors remarked that, the lattice Boltzman simulations can produce the same accuracy as the finite volume approach using much coarser grids. The 3D representation of the geometric structure was carried out by MC simulation with the aspect ratio of 3 (N = 3). The simulations were mainly done on a NEC SX 5 vector-parallel computer at the High-Performance Computing-Center in Stuttgart, Germany, using the lattice Boltzmann code BEST. The considered Re number interval was in between about 0.1 and 10. Although author had some insight at the end, they also stated that, detailed simulations were necessary to examine all flow effects caused by the radial and circumferential inhomogeneties of the packing.

The pressure drop caused by a turbulent single fluid flow was modeled for a complex geometry by Tobis (2002). This model was compared and verified experimentally in the model systems of complex geometry. Experimental model packing consisted of 8000 spheres of 38mm diameter glued together in a cubic arrangement. Also, various complex structures were created by inserting different obstacles between the spheres. The pressure drop measurements were performed under the air flow rate of Re number = 1200. Numerical modeling was carried out as interstitial flow modeling, superficial flow modeling, and structural macro correlations (SMC). Interstitial flow modeling was made by commercial CFD code FLUENT with the κ-ε turbulence model. It was discussed that, superficial flow model that is based on the empirical correlation, cannot be used alone to design a novel packing geometry. But the author pointed out that, if it coupled with an appropriate CFD code, it should enable flow prediction within large complex structures. It was also shown that, SMCs may facilitate the pressure drop prediction within the structures composed of different packing geometries.

Another pressure drop study was done through structured packings with CFD modeling by Petre et al. (2003). They developed a combined mesoscale and microscale predictive approach to apprehend the aerodynamic macroscale phenomena in structured packings. The method consists in identifying patterns by the representative elementary units (REU). An element of a structured packing was made up of an ensemble of Toblerone-like triangular flow channels. Non-structured tetrahedral meshing was applied for each REU by Gambit 1.2. For different structural type of REU's, flow field simulations were made by FLUENT version 5.5. The RNG κ-ε turbulence model was used, and simulations were done over a wide Re number range spanning up to 40000. The modeling study was validated by an experimental dry pressure drop data for five different packing types based on a thorough survey of the available pressure drop data published over the last two decades.

Another attempt of implementing lattice Boltzmann method to solve flow field in the fixed bed reactor was made by Freund et al. (2003). They have also applied MC method to synthetically generate packings of spherical particles in an aspect ratio of 5 (N = 5). Studied Re number range was in between 0.1 and 100. As an experimental validation of the global flow behavior, the pressure drop of the packing was compared with measurements and well known correlations from literature. For that purpose, flow measurements for N = 4 and N = 6.15, and a pressure drop correlation available in literature were taken into consideration by the authors. Simulation results were found generally in good agreement with the pressure drop correlation and with the measurements. The 3D flow field for N = 5 was resolved on a computational grid of 150 x 150 x 750 voxels, The steady state flow results were obtained in about 40000 iteration steps which took about 2 h on six processors of an NEC SX-5e shared-memory vector-parallel computer.

Magnico (2003) simulated the packed bed to obtain the hydrodynamic and transport properties. To generate random packings with N = 5.96 and with N = 7.8, the Bennet method was chosen by which sequential addition of new spheres can be done on a basal horizontal plane. The number of spheres for N = 5.96 was 326 and for N = 7.8 was 620. In order to solve the Navier-Stokes equations, the finite volume method was set up with a collocated grid. At the ends of the reactor periodic conditions were specified. The numerical results were found to be in good agreement with Ergun correlation in terms of normalized pressure drops for Re number in between 0.1 and 200. Radial profile of the porosity and the normalized superficial axial velocity at N = 5.98 and for Re number of 7 were compared with the experimental data available literature. It was seen that they fit to each other well. The validation of the Lagrangian method, that is used generally to characterize the mass transfer properties in the zones close to the wall, was found reasonable by comparing the results with the experimental ones available in literature. The author also investigated the relation between probability distribution function and the mass transfer, and he did not observe any relation which is given in detail in the article.

CFD modeling technique was applied by Romkes et al. (2003) for different purposes at this time. Authors wanted to find mass and heat transfer characteristics of a composite structured catalytic reactor packing (CSP) and they wanted to see whether CFD can be used to develop simple engineering correlations for this type of packing. To do that CFX-5.3 software was used for aspect ratios in between N = 1 and N = 5. Laminar simulations were done for 1.27×10^{-4} < Re number < 127, and turbulent simulations for 127 < Re number < 1.27×10^{5}.Three different turbulent models; κ-ε, RNG κ-ε, and the Reynolds Stress were considered. The heat transfer rate was predicted within an error of maximum 10% depending on the correlation chosen for comparison. It was also found that RNG κ-ε model gave better heat transfer predictions with the available experimental data. For the mass transfer predictions, the model agreed well with the experimental values within an error of less than 15%.

CFD simulation of steam reforming reaction was carried out considering Hou and Hughes (2001) kinetics by Dixon et al. (2003). In this study, a 120-degree slice of the bed cross-sectional area which was called wall segment, WS, was considered as model geometry. This segment was based on a full bed structure with N = 4. Simulations were done by FLUENT regarding spherical and cylindrical catalyst particles. Steam reforming kinetics was modeled considering the thermal effects of the reactions, which were represented by the inclusion of temperature dependent heat sinks in solid particles. The egg-shell nature of the reaction and diffusion in the spherical catalyst particles were represented in different activity levels from completely active case to 5% active case defined according to the particle radius. It was seen that the latter one shows the eggshell nature well. Particle deactivation was also studied for spherical particles, with turning off the heat effects of the reactions for just one particle. Heat sinks approach was applied to cylindrical particle geometry by 5% activity. Finally, it was concluded that, the results seemed to be physically reasonable, indicating that this approach can provide useful information about flow and energy in a catalyst tube under reaction conditions.

A comparative study was made by Nijemeisland et al. (2004) to investigate the influence of internal voids in cylindrical particles on heat transfer performance in the near wall region of a steam reforming packed bed reactor tube. For the representative wall segment of full cylindrical particles, the thermal effects of the steam reforming reaction were represented with heat sinks approach.

The comparison of the heat transfer performance by just considering the heat flux given radially through the reactor wall, was given with and without applying the heat sinks approach. As a result, it was observed that, when heat sinks were included in the particles to represent the thermal effects of the reaction, the heat transfer performance of a packing of full cylinders was shown to change markedly, both qualitatively and quantitatively.

Utilizing the typical steam reforming inlet operating conditions, simultaneous wall heat transfer and fluid flow were simulated in the WS models with and without wall conduction (Dixon et al., 2005). The simulations were run with the packings of solid spheres, and cylinders with 1, 3, and 4 longitudinal holes. It was observed that, the wall conduction has very little effect on the average wall temperature, whereas it has a strong effect on the tube wall temperature distribution which might have implications for the tube life.

Guardo et al. (2005) investigated the influence of the turbulence model in CFD modeling of wall to fluid heat transfer in packed beds. For that purpose, the geometry of a fixed bed composed of 44 homogeneous stacked spheres in a cylindrical container was simulated by the commercial software FLUENT 6.0. The studied range of Re number was between 127 and 912. Although Re number values were not so high, the authors used all the turbulence methods available in the software; κ-ε (standard, realizable, RNG), Spalart-Allmaras, and κ-ω. The obtained results of pressure drop along the bed with CFD simulation were compared with the Ergun correlation. All models showed good agreement with the Ergun's prediction, but Spalart-Allmaras turbulence model showed slightly better agreement. Wall Nusselt number values were compared with the empirical model proposed by Dixon and Cresswell (1979). The CFD results showed reasonable fitting with the empirical models. The other observed facts were; the realizable κ-ε model over-estimates the turbulent kinetic energy dissipation (ε), additional diffusion terms in κ-ω model can affect the estimation of heat transfer parameters, the turbulent viscosity was under-estimated by RNG κ-ε model, and CFD total heat flow estimation was larger for the standard κ-ε model. To resolve the wall effects the parameter y^+ should be in the desired interval, which is $30 < y^+ < 60$ for κ-ε models. The authors claimed that, their y^+ values were out of this range, and they could not obtain the suitable ones either by a coarser mesh or by a finer mesh. The reasons of these facts were having highly skewed elements in the small gaps of the geometry, and requirement of high computational demand for developing and solving it respectively. The authors concluded that, the reason for having better results by Spalart-Allmaras method could be due to the fact that, this model uses a coupling between wall functions and damping functions for near wall treatment.

Instead of considering the entire packed bed or representative segment of the bed, some of the researchers consider only some part of the couple of particles, which is called unit cell approach. Gunjal et al. (2005) studied different packing arrangements of spheres with a unit cell approach. These representative unit cells were modeled by GAMBIT 2.0 geometry generation software, and solved by FLUENT 6.1.18 where periodic flow conditions were set up. The CFD predictions were compared with the experimental data available in literature for the Re number range in between 12.17 and 204.74. It was observed that, simulated results showed good agreement with the experimental data except the lowest value of Re number (12.17). By further investigation, authors decided that, this problem arose due to possible difficulties in maintaining a steady flow at a very low flow rate. Then, another comparison was made between CFD predictions and analytical solution. To do that, new simulations were carried out at Re number of 0.001 and compared with the analytical solution and lattice Boltzmann simulation results available in literature. It was seen that, CFD simulations were in substantial agreement with the both results. The CFD-predicted values of the average drag force acting on particles were compared with the results obtained by Lattice Boltzmann simulations available in literature for the moderate Re number values. It was also seen that, this comparison gave a good agreement. The authors made some more investigations for the influence of Re number considering values of 1000 and 2000, and of particle arrangement on velocity distribution. The comparative results were given in the paper in detail.

In order to check the mesh sensitivity, and compare the CFD predictions with the theoretical solutions, Guardo et al. (2006) considered a single suspended sphere in an infinite fluid as part of the heat transfer investigation of fixed bed reactor with spherical particles. The single particle case was studied with a Re range between 0.33 and 3300, and for different mesh densities Nusselt numbers were calculated and compared to the predictions of Ranz and Marshall correlation. Although good agreement was not seen with the correlation, the optimum mesh structure was selected and utilized in the fixed bed model where 44 spheres was used with N=3.923. To include the contact points between the particles, the spheres were overlapped by 0.5% of their diameters. Simulations were carried out by FLUENT 6.2 for very low Re values ($9 < Re < 100$) to investigate the mixed (free + forced) convection heat transfer at high pressure. As a result of this study, modified correlations were obtained for Nu_{Free} and Nu_{Forced}. Recently, they have tested their correlations for a supercritical fluid in laminar regime (Guardo et al., 2007) including mass transport. The authors found good agreement between numerical, experimental, and the predictions of their modified correlation for the heat transfer coefficient. They have also seen a good agreement between the correlation for mass transfer coefficient from the literature and the numerical and experimental results within the same flow regime.

Laguerre et al. (2007) compared experimental results to two different modeling approaches for transient heat transfer by free convection in a packed bed. The first modeling approach was CFD application by FLUENT, and the second one was a conventional pseudo continuum packed bed modeling approach. In both experimental and CFD modeling studies a cubic arrangement of spheres was utilized. 1% of particle overlapping based on the diameter was applied in CFD modeling. In the packed bed modeling, the Darcy-Forchheimer equation was used to predict the superficial velocity. Conductive and radiative heat transfer was considered between the particles, and free convection was applied between the particle surfaces and the fluid in the same model. The experimental results were compared to the models by local temperatures values, temperature profiles and contours, and velocity fields. The results of both models were in good agreement with the experimental findings. Authors compared both methods, and less computation time was observed for packed bed model, whereas the details of the fluid flow the temperature fields were obtained by the CFD model. They have also stated the limitations of packed bed approach as the need of suitable correlations to describe the transport processes for a given geometry.

Recently, by our group (Dixon et al., 2007) intra-particle reaction and gradients were resolved for steam reforming regarding our WS model with porous spherical packing. The intra-particle effects such as conduction, species diffusion and reaction were coupled to realistic 3D external flow and temperature fields. It was noticed that, the usual assumption of symmetric species and temperature fields inside the pellets holds for particles away from the tube wall, but particles placed in the strong temperature gradient near the tube wall show significant deviations.

In summary, with increasing computational resources, CFD applications have moved towards the 3D realistic geometries on fixed bed modeling. Up to the present day, for low-N tubes, influence of bed geometry on fluid flow and heat transfer has been extensively studied with models having different numbers of catalyst pellets. Besides simple reaction inclusion to the simulations with LBM to obtain species and conversion profiles in the bed, prior to our reaction heat effects approximation method, there were no significant reaction consideration inside of the catalyst particles. Therefore, coupling 3D realistic flow field to the diffusion/reaction, which especially takes place close to the particle surface, with CFD was the necessary “next step” in order to investigate the intra-particle gradients, and ultimately create realistic packed bed models to predict the design considerations well.

2.2 Packed bed reactor modeling with reaction

In this part, the pseudo-continuum type of modeling has been reviewed. One of the important pseudohomogeneous modeling applications on the methane steam reforming reactions, as of our interest, was carried out by Xu and Froment (1989b) by investigating the diffusional limitations of the intrinsic rate expressions previously obtained by them (1989a) and making a reactor simulation. First, authors measured the pore size distribution of the steam reforming catalyst by mercury penetration and nitrogen desorption. By this data they calculated the effective diffusivity. Considering the continuity equations with a spherical catalyst particle and experimental data, the authors found the tortuosity factor. A modified collocation method was used to obtain parallel pressure profiles of the reacting components in the catalyst pellet. The authors also discussed in detail the results of the simulation on an industrial steam reformer and they observed that, the partial pressures of the catalyst surface components were very close to the equilibrium values at the axial locations exceeding the half of the reactor length.

A heterogeneous model including coupled chemical reactions and diffusional limitations in catalyst pellet was derived by Salmi and Warna (1991) for the fixed bed reactors. An algorithm which combines orthogonal collocation for the pellet equations and a backward difference method for the bulk phase equations was derived to obtain a numerical solution of the reactor model. By this algorithm the pellet and the bulk phase equations were solved in a sequential manner. Authors considered different diffusion settings such as effective diffusion coefficient approach and Stefan-Maxwell equations, for two different reactions: the water-gas shift reaction and the methanol synthesis. They have observed that, the two different diffusion settings did not make a major difference for the whole reactor. However, the Stefan-Maxwell equations required much more computational effort.

Papageorgiou and Froment (1995) took into consideration pseudohomogeneous and the heterogeneous models accounting for radial voidage profiles. This was done by coupling the available correlation for void fraction and the momentum equations, which were written as the contribution of each phase expressed in terms of the voidage of the element. This concept was applied by utilizing local superficial velocities and an introduction of a friction factor that could be obtained by Ergun equation which accounts for both viscous and kinetic energy loses with the effect of voidage. Authors presented psuodohomogeneous and heterogeneous models with the incorporation of radial structural nonuniformities (radial voidage profie). The radial voidage profile was kept constant along the height of the reactor. For each reactor model, the set of governing equations forms a system of coupled partial differential equations which were discretized by finite differences (of second order accuracy) and solved by an iterative procedure. After certain comparisons of these two models with previously generated approaches, it was found that, heterogeneous model provides better insight in terms of reactor behavior and it explicitly accounts for the nonuniformity of fixed beds with respect to both structure and transport processes involved. Authors claimed that, with the potential of the computer technology (available at that time), heat transfer models for fixed beds should use the velocity profiles in order to provide a more accurate description of the distribution of the resistance to heat transfer as caused by the nonuniformity of the flow.

A two-dimensional (2D) peusohomogeneous dispersion model was used to simulate a steam reformer by Kvamsdal et al. (1999) considering the kinetic model given by Xu and Froment (1989) with additionally a coke formation. The heat transferred to the reactor tube was calculated by axially varying overall heat transfer coefficient multiplied with a temperature change. For wall heat transfer coefficient and effective thermal conductivity, literature correlations were used. Authors claimed that, the outer reactor tube wall temperature was very sensitive to the correlations, but none of them predicted the realistic values. However, methane conversion was sensitive to the correlations. They have also observed that, using the axially varying physical properties and gas velocities has a minor effect on temperature distribution. For that reason they have considered the inlet conditions to determine the effective thermal conductivity.

Balakotaiah and Dometi (1999) have used the Center Manifold Theorem to derive a pseudohomogeneous type model for packed-bed catalytic reactors. For the combined heat and mass transfer problem the effective equation that authors derived was different from the standard pseudohomogeneous models used in literature. For example in addition to usual dispersion terms, the effective model includes corrections to the convection and source terms as well as additional cross-coupling convection terms between the species and energy balances. By this model, they have focused on determining the conditions under which the solution exists. It was shown that, when a reaction occurs in the pellet, the effective model may reach to a solution only if the interphase transfer time is smaller than both residence and characteristic reaction time.

Froment (2000) generated a model for the conceptual design of new reactor configurations, and given its fundamental kinetics basis, for the development of more performing catalysts considering the steam and CO_2 reforming of natural gas. For this case feed was not only methane, but also composed of propane and ethane too. Eighteen possible elementary reaction steps were taken into consideration for steam and CO_2 reforming of natural gas, and the intrinsic rate equations were obtained. The detailed reaction scheme is given by the author. The diffusional limitations were introduced through the modeling using appropriate characterization of the structure of the catalyst particle and accurate equations for the molecular and Knudsen-diffusivities. The continuity equations for CH_4 and CO_2 were written and related algebraic equations were obtained. The effective diffusivities appeared in the continuity equations were given by

$$D_A^e(r_i) = \frac{\varepsilon_s}{\Gamma}\left(\frac{1}{D_{mA}} + \frac{1}{D_{K,A(r_i)}}\right)^{-1} \tag{2.1}$$

Where, D_m and D_K are the molecular and Knudsen diffusivity of component I respectively. The symbol ε represents the porosity of the particle and Γ the tortousity factor, expressing the topology of the pore network. The pose size distribution was measured using a commercial equipment and the tortousity factor was obtained from the fitting data on the reverse of the water gas shift reaction; carried out in a representative tubular reactor.

Coke formation was also considered by the author because of leading to deactivation and even disintegration of the catalyst. To simulate an industrial steam reformer, the one dimensional heterogeneous reactor model was introduced (Froment and Bischoff, 1990). The model simulation results were investigated in detail and the final conclusion was given by the author as, the approach was found to be powerful tool for the analysis, simulation and design of this process.

A one-dimensional (1D) heterogeneous reactor model was used for catalytic oxidation and methane steam reforming by Avci et al. (2001). To reduce the execution time, the heterogeneity was tested by Mears' criterion for interfacial transfer, and Weisz-Prater criterion for intra-particle diffusion, and the related terms were not incorporated into the model. Two different bed arrangements were studied with different types of catalyst materials: the dual bed structure where Pt/δ-Al_2O_3 and Ni/MgO-Al_2O_3 were consecutively arranged, and the mixed structure where two catalysts were physically mixed. The model predicted comparable methane conversion to experimental one in dual bed operation, but not in mixed bed scheme. In both cases model did not predict the hydrogen composition well as compared to experimental data.

In the paper of Pedernera et al. (2003), the steady state operation of large scale primary reformers was analyzed by means of a two dimensional heterogeneous model. The model accounts for the strong diffusion limitations in the catalyst particle at each axial and radial reactor position. The kinetic model reported by Xu and Froment (1989a) was adapted, and therefore to evaluate diffusional resistances the particle mass balances were numerically solved. The reforming unit which had cylindrical catalyst particles with cylindrical holes, was studied by such a simplification that, the complex geometry of the catalyst particles were represented by an equivalent annular model. As being a heterogeneous model, the governing equations for the bulk and the catalyst particle were generated for this system. For the catalyst particle, the effective diffusivities were calculated using expressions given by Xu and Froment (1989a).

Obtained temperature profiles were analyzed radially considering different positions for firing which is considered to give necessary heat for the reactions. The methane reaction rate ($r_{CH4} = r_1 + r_3$) was observed that, the reaction occurs in a narrow zone close to the catalyst surface (only at the outer 2.5% of the equivalent particle radius). It was also seen that, for the different types of firing positions, the radial methane reaction rates were strongly decreased from the tube wall to the center of the reactor.

The pseudohomogeneous approach was applied to a simulation study of the steam reforming of methane by Gallucci et al. (2004) in both a tubular fixed bed reactor and a tubular membrane reactor. The advance of the membrane reactor was defined by the authors that, CO free hydrogen can be produced at the end of the process, which is a direct fuel for fuel cells. For this purpose, the kinetics reported by Xu and Froment

(1989a) was implemented into this study. Validation of the model was carried out by comparing the simulation results with the theoretical predictions available in literature in terms of methane conversion which is defined as;

$$X_{CH_4} = \frac{CH_{4_{in}} - CH_{4_{out}}}{CH_{4_{in}}} 100 \tag{2.2}$$

The methane conversion results were also compared for both types of reactors with the experimental results available in literature. All the comparisons made for the validation of the model gave a good agreement with the compared cases.

Koning et al. (2006) studied an improved version of 1D model of a tubular packed bed reactor for different types of generic reactions. In 1D models, which are used if the computational effort should be small, the reaction rates are calculated using the average temperature over the cross-section of the reactor. In the improved model that authors suggested, and involves the implicit equations, the radial temperature profile was analytically approximated to improve the prediction of the average reaction rate. Authors compared their results with a conventional 1D model, and found similar or better results with less computational effort.

A 2D heterogeneous model, which accounts for transport in solid and fluid phases with axial and radial dispersions, was considered by Machac et al. (2006) for studying heat and mass transport in a catalytic bed reactor where exothermic carbon monoxide (CO) oxidation reaction takes place. In the model for mass and energy balances, partial differential equations were considered in the fluid phase, and ordinary differential equations were used in the solid phase. Authors used COMSOL Multiphysics in their work, and they observed hot spots near the inlet of the reactor under the operating conditions of the study. They indicated that, the reduction in CO concentration can drastically decrease the value of the hot spot.

2.3 Modeling Propane Dehydrogenation Reactor

PDH modeling studies are usually related with the coke formation process. There can be found many works in literature about PDH reactor modeling. We will only focus on some of the recent applications here with different types of reactors, although our interest will be on the fixed bed reactors.

The derivation of kinetic and deactivation model, including by-product and coking reactions over the Cr_2O_3/Al_2O_3 catalyst has been described for conventional fixed bed reactor by Stitt et al. (1999) for an isothermal case. Due to the necessary regeneration/deactivation cycle, dynamic modeling was necessary to compare with experimental data. Comparison of predicted and measured accumulated carbon deposits showed an agreement. The fitted rate expression was obtained based on the fitted carbon deposition rate.

A modeling study in a rotating monolith reactor was carried out by the same authors (Stitt et al., 2001). Rotating monoliths have been proposed as reactors for concentrating low level components in gas streams such as H_2S, and for the separation of bulk chemicals such as normal alkanes. Based on the overall heat balance calculations, side reactions and coke formation were eliminated from the model as not having the significant contribution. The model included the following features; dehydrogenation reactions, catalyst oxidation and reduction reactions, heat transfer, heat balance, and rotational pumping. This model has been used for the process feasibility of a rotating monolith reactor with the rapid catalyst cycling.

Hou and Hughes (2002), made a comparative simulation analysis in composite and microporous membrane reactors. In the mathematical model the following assumptions were made: steady state and isothermal operations, plug flow reactor with a large reactor length/pellet diameter ratio, and no pressure drop. The Pt/Al_2O_3 catalyst was used. The reaction kinetcs were obtained from the experimental data produced in an integral fixed bed reactor with the same catalyst. As a result of the simulations, authors mentioned the increase in propane conversion for the composite membrane reactor with an increase in sweep gas flowrate. In the porous membrane reactor, on the other hand, they have noticed a little effect on conversion. They have also compared the cocurrent and countercurrent flow patterns for the reactors, and an increased conversion was observed for the composite membrane with countercurrent flow.

A novel reverse flow reactor was considered by van Sint Annaland et al. (2002). The sequential reactor configuration for the PDH/fuel combustion reaction system on a Pt/Al_2O_3 monolithic catalyst was modeled to include thermodynamic equilibrium effects. Using a detailed simulation model, authors showed that for the reaction system in the mentioned catalyst, most of the propane conversion is lost at the end of the reactor due to low exit temperatures resulting from the reverse flow concept. They have also noticed that, adding methane to the propane/air feed during the exothermic reaction cycle (shift of the reaction to produce propane) allows direct control of the temperature and thus the propane conversion during the endothermic cycle.

3. Segment vs. Full Bed Model: Validation Study

Industrial application of low tube-to-particle diameter ratio beds are in the range of N=3 to 8. After the validation study of N=2 bed with experimental data for heat transfer (Nijemeisland and Dixon, 2001), N=4 models started to be considered in our group as more practical tube-to-particle diameter ratio beds.

To focus on the near-wall region, a wall-segment (WS) geometry was created previously (Nijemeisland, 2002) regarding the computational constraints. WS model consists of one third of the tube circumference (120 degree segment) and three axial layers of particles as shown in Figure 3.1 for full cylinders packing. There are 12 particles in the model, and number 10 and 12 are hidden behind the particles shown.

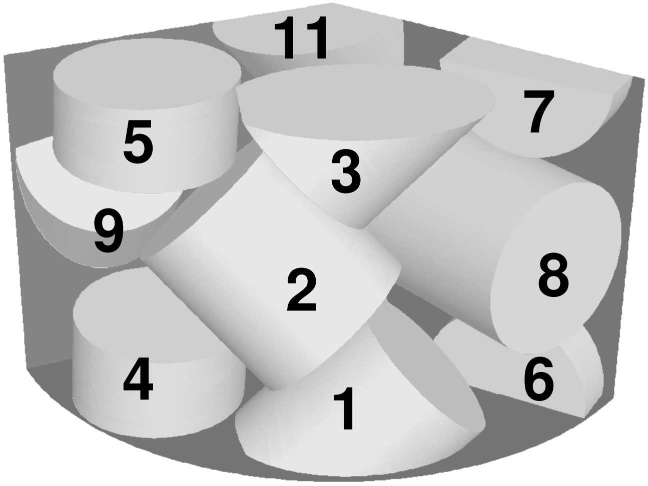

Figure 3.1 3D view of WS model and corresponding particle numbers

The geometry shown in Figure 3.1 was designed to create a packed bed environment for a single central particle in the geometry. The particle, number 2, in the middle row of the three axial rows of particles, and located tangentially near the center of the segment model, was the main particle. The most of the other particles are not entirely in the WS geometry. The particles in the top and bottom layer make up the periodic boundaries, and have identical locations to satisfy translational boundary conditions.

To decide on the orientation of the particles, an experimental orientation study was performed on packing cylinder particles with 1:1 ratio in a N=4 bed. From large selection of packing structures, the most common situation was used as a base geometry in which the main particle axis makes a 45 degree angle with the column axis (Nijemeisland, 2002).

The first attempt of WS model was with a spherical packing, and regarding the geometric feature of spherical particles, side walls were set as symmetric in the model. In cylindrical packing same setting has been applied. A preliminary study (Leising, 2004), suggested that, this symmetric side constraints could influence the flow and heat transfer phenomena. Therefore, the aim here was to compare the segment of cylinders with a full bed of cylinders by means of flow and heat transfer features to understand the restrictions of the segment model, and validate accordingly for the further use of it.

3.1 WS model development

The WS model geometry was created by 3D geometry generation software, GAMBIT 2.2.30. Positioning of the particles was performed by a sequence of transformation which is shown in Figure 3.2 for particle number 1, the lower front particle in the model. The base position is (1) where particle is at the origin of the model, as default. Then, it is rotated by 45 degree according to positive x direction, which is (2). Afterwards, it is translated by 1.45 unit length in negative x direction, (3). Finally, the particle is placed to its position in the segment model by rotating 40 degrees in positive z direction, (4). Note that wire frames of the previous positions are retained in each sketch for comparison. Similar sequences are available for each of the particles, and are given in Appendix 1.

The particles are equilateral with a size of 0.0254 m, whereas the model height is 0.0508 m. The overall bed voidage was adjusted to be 0.50. The main model frame has shifted by 0.001016 m downwards compared to Nijemeisland's original model, as might be noticed in the Figure 3.1, to obtain non-skewed cell elements due to the sharp cut-off locations. This movement did not affect the periodicity, and periodic condition was established in another repetitive pattern.

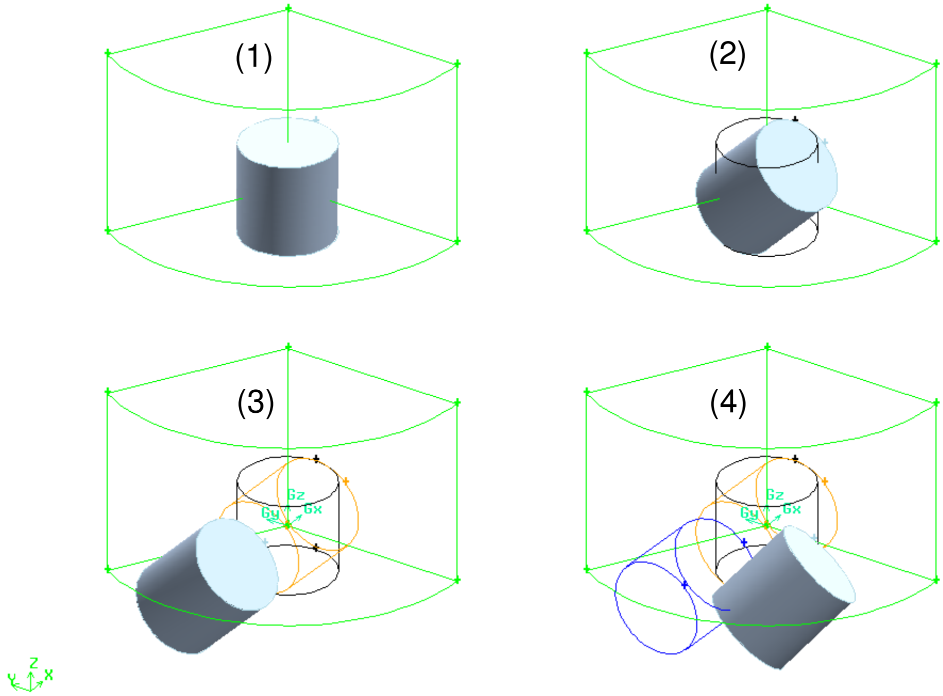

Figure 3.3 Sequence of transformations from (1) to (4) to place bottom front particle

The particle placement steps are given in Appendix 1. The computational grid was generated with unstructured tetrahedral volume and triangular surface elements of size 0.000762 m, which resulted in 1.7 million cells.

3.2 Full bed model development

The complete wall (CW) full bed model was generated while keeping the 12 WS particles at their original positions and introducing 12 new particle elements into the model, as shown by Figure 3.4. The cylindrical particles did not touch each other or the tube wall, as for the WS model. In order to obtain the same overall bed voidage as the WS model, one particle (number 12) had to be moved by 0.004826 m in the positive y direction in the CW model. The translational periodicity was conserved in the CW model, and all the dimensions were kept constant to maintain tube to particle diameter ratio N=4 in both models.

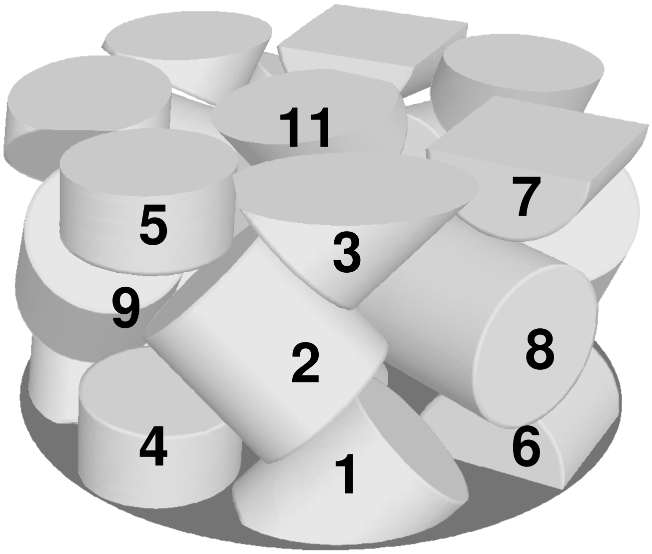

Figure 3.4 3D view of CW model and corresponding particle numbers

As in the WS model, the computational grid was generated with tetrahedral volumes and triangular surface elements of size 0.000762 m, which resulted in 5.1 million cells. The particle placement steps for the CW model are given in Appendix 2.

3.3 Simulations

The simulations were performed at typical steam reforming inlet conditions which were obtained from a Johnson Matthey detailed reformer model of a methanol plant steam reformer. The specified conditions and the applied boundary conditions for the simulations are shown in Table 3.1 and correspond to a particle Reynolds number based on superficial velocity of 9850 (based on diameter of sphere of equivalent volume). Since the CW model size is three times bigger than the WS model, the mass flowrate of the CW model was adjusted according to that proportion to maintain the superficial velocity the same.

Table 3.1 Reactor conditions and fluid properties at the inlet of a typical steam reformer tube

T_{in} [K]	q_{wall} [kW/m^2]	P [kPa]	ρ [kg/m^3]	c_p [J/kg.K]	k_f [W/m.K]	μ [Pa.s]
824.15	113.3	2,159	6.1616	2395.38	0.0876	3.10^{-5}

The constant heat flux boundary condition at the tube wall was selected for the runs as being more realistic because the energy supply from the burner to the tube wall is mainly radiative, and the temperatures on the external tube walls of industrial reformers are not constant. The pressure of the system at the inlet was set to be approximately 20 atmospheres, as steam reforming is carried out at high pressures. The same inlet temperature was set for both fluid phase and for the bottom particle surfaces. The other variables noted in Table 3.1, the fluid properties, ρ, c_p, k_f, and μ, were calculated for a user-defined fluid with the properties of the inlet reaction mixture. The solid thermal properties were those of alumina (ρ_s=1947 kg/m^3, c_{ps}=1000 j/kg-K, and k_s=1.0 w/m.K).

The simulations were run to first determine the isothermal flow solution in the periodic segment, and subsequently to determine the energy solution. The solution of flow and energy was decoupled, as the temperature-dependence of the gas properties was not expected to influence flow at the extremely high industrial flow rate simulated here. This assumption allowed the flow to be treated as periodic, independently of the temperature field. The gas heated up slightly as it passed through the segment, so the temperature field could not be treated as periodic. A uniform inlet temperature had to be specified, and to overcome the thermal entry effects, the models were virtually “stacked” by setting the outlet conditions of one stage as inlet conditions for the next stage (Nijemeisland and Dixon, 2004). This technique provided a developed temperature field for the models although axial conduction between segments could not be included. All the heat transfer results presented here are for the third segment in the stack.

The WS model simulations were done on a 32 bit workstation PC with 3.20 GHz CPU, whereas the CW model was simulated on a 64 bit multiprocessor workstation.

The SIMPLE pressure-velocity coupling algorithm was selected with the first order upwind scheme for the momentum, turbulence, and energy solutions. Convergence of the iterations was verified by monitoring the residuals, pressure drop, and mass and energy balances. For flow, the under-relaxation factors (URF's) were set to values 0.2 lower than the defaults recommended by Fluent. The solution was iterated until the residuals and pressure drop values became stabilized, and the residuals were reduced to values between 1×10^{-3} and 1×10^{-4}. The periodic flow boundary conditions assured a good mass balance. Therefore, it was not necessary to demand a higher accuracy in residuals. A different strategy was applied for the energy calculations. First, fast initial convergence was obtained using a URF of 1, and then the URF was switched to 0.9 to stabilize the iterations and approach a constant residual of magnitude below 3×10^{-8}. The energy balance error was always below 0.05% of the wall heat supply value.

3.4 Mesh independence

The mesh dependence for the WS model was investigated in earlier work (Nijemeisland and Dixon, 2004). For CW model, relatively finer and coarser two mesh sizes were considered with unstructured tetrahedral/triangular elements of sizes 0.000762 m and 0.001016 m. The computational resources, and software features did not allow us to consider lower sizes.

The flow simulations were compared in terms of pressure drop values and axial velocity contours obtained by vertical and horizontal visual planes. The planes are shown in Figure 3.5, and the contours are in Figures 3.6 and 3.7. The pressure drop comparison and model sizes are given in Table 3.2.

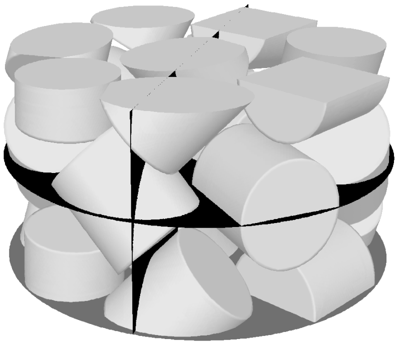

Figure 3.5 Vertical and horizontal visual planes (in black color)

Table 3.2 Model sizes and pressure drop comparison

Definition	Cell Size (m)	Model size (# of cells)	Pressure Drop (Pa/m)
Finer mesh	0.000762	5.17 million	2330
Coarser mesh	0.001016	2.42 million	2300

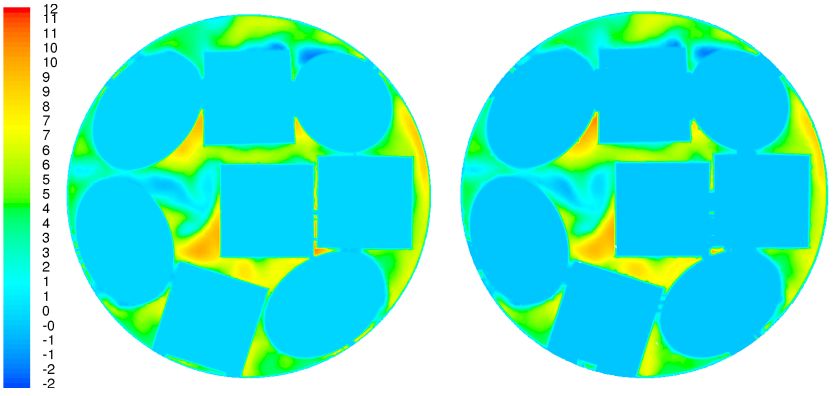

(a) (b)

Figure 3.6 Horizontal visual plane axial velocity contours in m/s (a) for finer mesh, and (b) for coarser mesh.

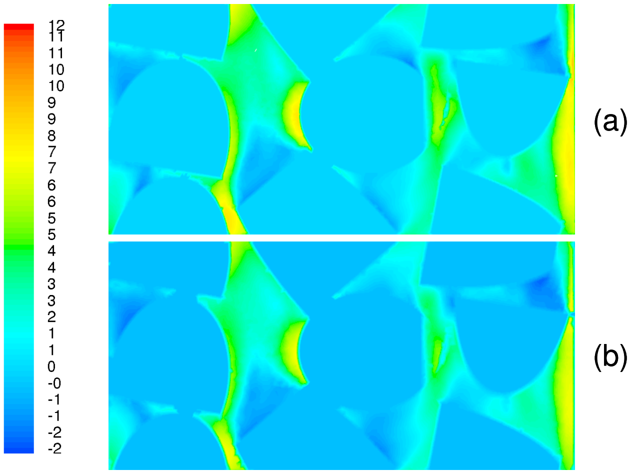

Figure 3.7 Vertical visual plane axial velocity contours in m/s (a) for finer mesh, and (b) for coarser mesh.

The qualitative and quantitative comparison showed that, 75% reduction in cell size, which helps to reduce the model size by half, did not have a significant effect on flow features. Although, this was observed, we kept the cell sizes same, as 0.000762 m in both WS and CW models for further comparisons of them.

3.5 WS and CW Comparison results

WS and CW model comparison was made by flow and temperature contours, profiles, and heat uptake of the pellets regarding the endothermic effects of reactions, and these were separately discussed in the next sections.

3.5.1 Flow field comparison

The qualitative flow field comparisons may be obtained by investigating the pathlines and velocity fields represented by visual vertical and horizontal planes as shown in Figure 3.5 for CW model and Figure 3.8(a) for WS model. The chosen planes cut the models into two equal pieces vertically and horizontally. The vertical plane position was selected in the center of the WS model to compare flow features at a location expected to be least influenced by the side symmetry conditions of the WS model. The same visual vertical plane was placed into the CW model. On the other hand, the horizontal plane was selected to show flow features both close to and far from the symmetry walls of the WS model. For further analysis the models were virtually divided into the three sections of 30º, 60º, and 30º given in Figure 3.8(b). The 30º side sections were expected to be influenced by symmetry planes (Leising, 2005). Therefore, the middle 60º section was tested individually in the analyses, with the comparison of full 120º segments of both models also given in the following sections.

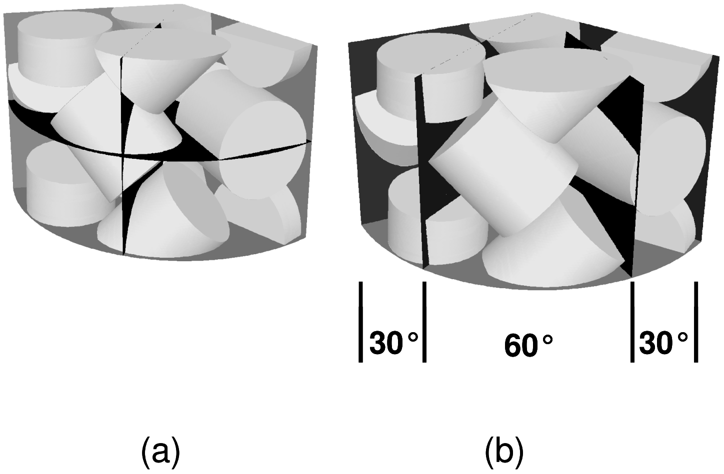

Figure 3.8 (a) Vertical and horizontal visual planes in WS model, (b) the 30°, 60°, and 30° sections shown on the WS model.

The pathline plots as shown in Figure 3.9 were obtained by tracking virtual particles released from the dimensionless radial position r/r_t = 0.98 in the 120º sections. Both models captured similar pathlines, including the vortex type flow feature on the upper side of particle 2, the accumulated flow on the bottom of particle 5, and the flow covering the top of particle 8. However, there were some differences observed including the vortex type of back flow on top of particle 4 in the WS model, more accumulated flow on the bottom of particle 5 in the CW model, and an inclined flow over the circular face of particle 8 in the WS model. All these different flow features occur in the 30º side sections. These observations imply the influence of the symmetry side restrictions on the flow field in the WS cylinder model.

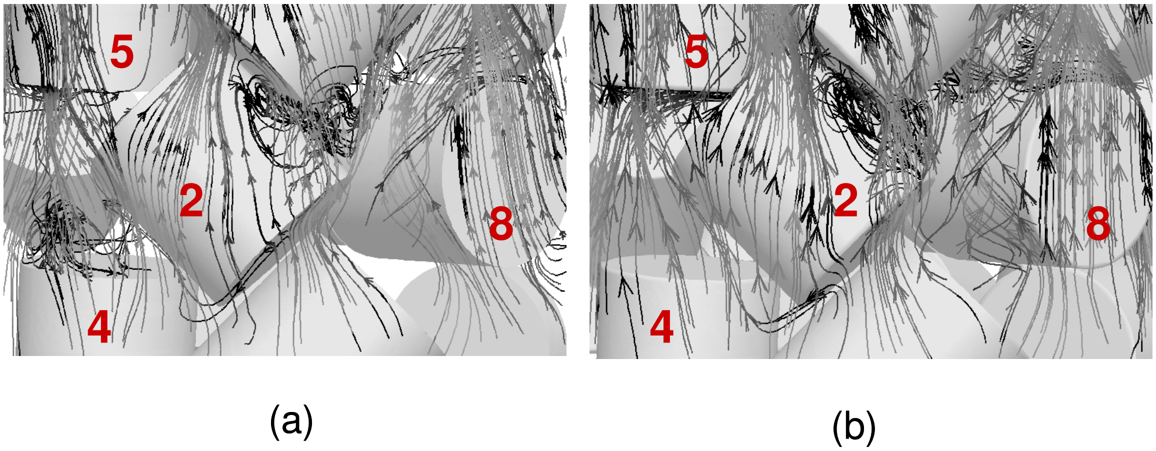

Figure 3.9 Comparison of pathlines of (a) the WS model, (b) the CW model.

Figures 3.10 and 3.11 represent the axial velocity magnitude contours of both models according to the visual horizontal and vertical planes. The horizontal plane flow contours are shown in Figure 3.10(a) for the WS model and in Figure 3.10(b) for the CW model. The corresponding WS portion of the CW model was emphasized by lines superimposed on the CW model contour. The basic flow feature which occurred between particles 8 and 12 was captured in both models with a 5% quantitative difference in terms of the maximum axial velocity seen close to particle 12. There was also quantitative and qualitative agreement for the flow in between particles 9 and 2 in both models. The vertical plane axial velocity contours given in Figures 3.11(a) and 3.11(b) for the WS and the CW models show similar agreement between the models. The corresponding WS portion of the CW model was again emphasized, by the square box shown in both parts of Figure 3.11. The flow feature in between the particles was qualitatively captured well in both models with the same quantitative difference in the maximum axial velocities as was observed in the horizontal plane contours. The overall axial velocity difference between the models reflects the difference in overall pressure drop; the WS model pressure drop is higher than the CW model one by 30%. Although the pressure drop difference is not emphasized in detail in this study, and will be addressed in a separate publication, it may be suggested that the symmetry walls create a squeezing constraint on the flow so that such a quantitative difference in the pressure drop could be observed with only a slight discrepancy in the maximum axial velocity magnitude.

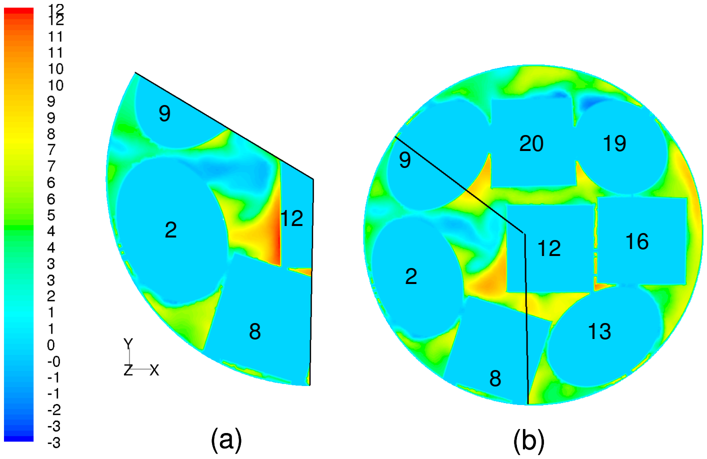

(a) (b)

Figure 3.10 Axial velocity (m/s) comparison according to the horizontal planes of (a) the WS model, (b) the CW model.

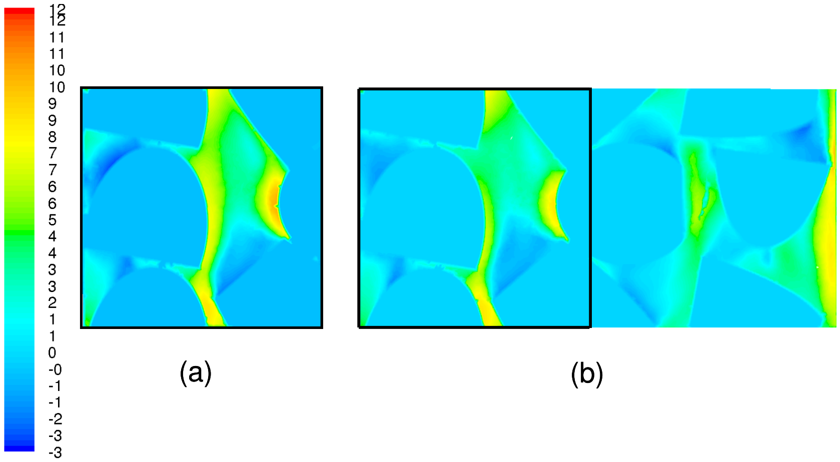

(a) (b)

Figure 3.11 Axial velocity (m/s) comparison according to the vertical planes of (a) the WS model, (b) the CW model.

3.5.2 Temperature field comparison

Due to the endothermic nature of the overall steam reforming reactions, heat must be supplied from the outside of the reactor tubes and is absorbed by the catalyst particles. Heat sinks in the particles were used to mimic the heat effects of the endothermic steam reforming which will be described in detail in Chapter 4. The qualitative heat transfer comparison is shown by the overall bed temperature fields given in Figure 3.12. The corresponding 120° portion of the CW model is emphasized by the drawn side wall lines shown in Figure 3.12(b). When this portion of the CW model was compared to the WS model shown in Figure 3.12(a), overall similarity was observed with some deviations such as relatively hotter sections on particles 2, 3, 4, and 5 in the CW model.

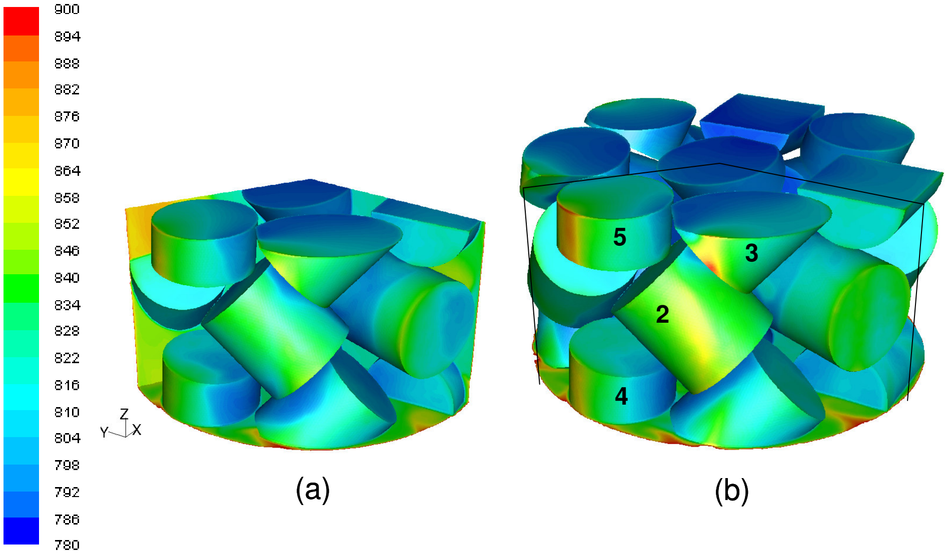

(a) (b)

Figure 3.12 Overall bed temperature (K) field comparison of (a) the WS model, (b) the CW model.

The maximum and average particle surface temperatures for the WS and CW models are compared in Table 3.3. Agreement between the two models is very good for average surface temperatures, while differences in maximum temperatures are somewhat larger. It is known that the effects of excessive temperatures in and on the steam reformer tubes are quite dramatic as described in the Chapter 1. Therefore, although the deviations given in Table 3.3 are not too large, the reasons for any discrepancy should be understood well.

Table 3.3 Comparison of maximum and average surface temperatures for selected particles.

Particle	WS model		CW model	
No.	T_{max} [K]	T_{ave} [K]	T_{max} [K]	T_{ave} [K]
2	853.3	812.0	867.7	812.7
3	859.7	814.0	900.4	816.1
4	851.2	814.7	869.9	818.2
5	870.9	824.2	880.7	831.4

For this purpose, temperature and axial velocity contour maps were generated for the radial position r/r_t=0.98 and for the 120º segments, as given in Figures 3.13 and 3.14. The contour map coordinates are axial segment height, Z, and segment arc length S. All maps were created using the same temperature and velocity scales, for easier comparisons. Figure 3.13 shows hotter zones in the CW model, compared to the WS model, at r/r_t=0.98, at the same positions as was noticed in Figure 3.12. Section A represents the related portion of the contour map where particles 4 and 5 are positioned, and Section B shows the related portion for particles 2 and 3.

The hotter spots in Sections A and B for the CW model can be related to the lower velocity field on the same sections shown in Figure 8. Comparison of the axial velocity maps in sections A and B in Figure 8 shows that the WS model has overall higher velocity and the regions of highest velocity are slightly greater in magnitude than for the CW model. This observation could be explained by considering that when the velocity of fluid which flows around the particles is low, especially at the near wall region, the heat supplied from the tube side will reach the particles more easily, instead of being removed by the flowing fluid parallel to the wall. As a result, the particles and the fluid flowing around them will become hotter. The higher velocity in the near wall region of the WS model might be a consequence of the symmetric side restrictions. When there are no restrictions, as in the CW model, the velocity at the region of interest becomes lower and the fluid may find more free space to flow, depending on the local voidage in the complementary 240° section of the CW model.

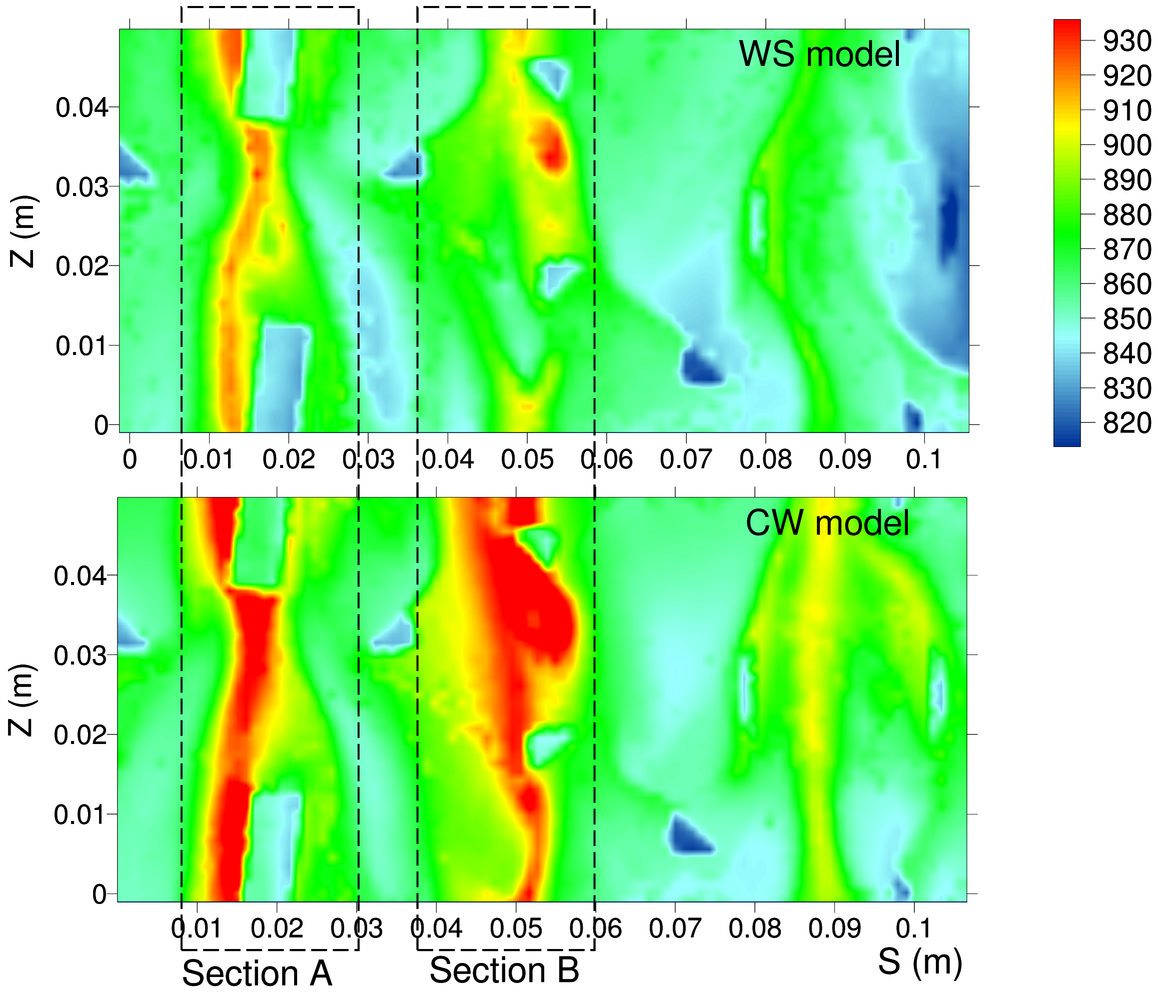

Figure 3.13 Temperature contour (K) map comparison of 120° segments of the WS and the CW models drawn at r/r_t=0.98.

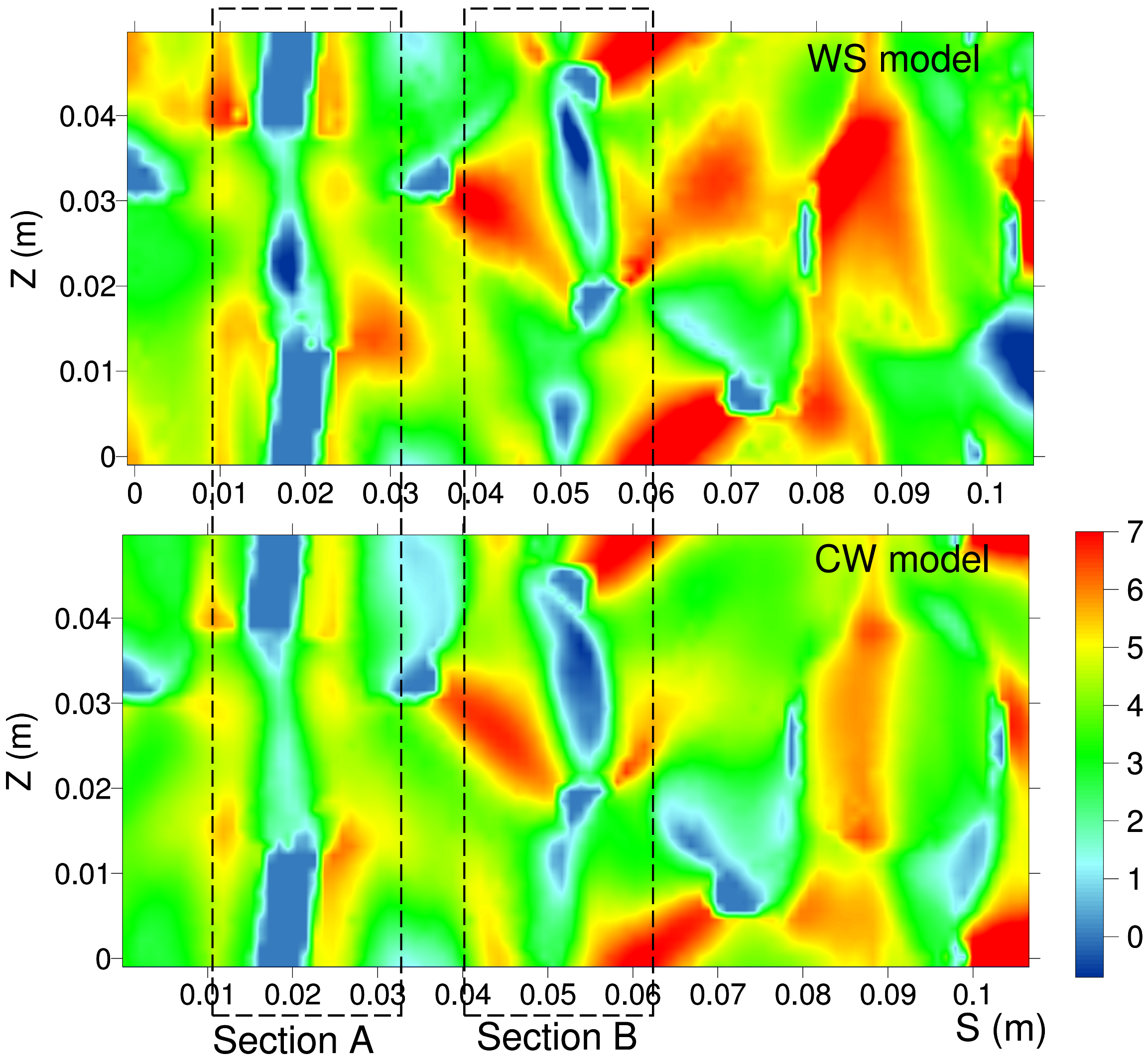

Figure 3.14 Axial velocity contour (m/s) map comparison of 120° segments of the WS and the CW models drawn at r/r_t=0.98.

As opposed to the local differences discussed above, the overall quantitative differences noticed on the temperature and velocity contour maps between the two models shown in Figures 3.13 and 3.14, can be explained by considering the particle positions of the CW model. Figure 3.10(b) shows the local voids near to the particles 16 and 20 within the horizontal plane view. Fluid might have a tendency to escape to these voids of the CW model and therefore, relatively lower overall velocity on the contour map shown in Figure 3.14 for the CW model could be seen.

3.5.3 Radial temperature and velocity profiles

Radial profiles were obtained by averaging the value of interest at various constant values of r, over (Z, Θ) surfaces. Each surface was defined at a different radial position from the center of the tube to the tube wall, having the same height as the model in the axial direction. It was previously observed (Leising, 2005) on laboratory scale flow and heat transfer simulations of the WS model with cylindrical packing that, in the radial temperature profiles, up to 5-6 ºC deviation occurred between the cases where averaging over the entire 120º segment and averaging over only the middle 60º part of the segment were compared. Regarding the industrial conditions, an even larger deviation may be expected due to the side wall effects. Therefore, radial profiles of axial velocity and temperature were obtained by averaging separately over 120º and 60º sections of the radial planes, and are shown in Figures 3.15 and 3.16.

Although there are some discrepancies observed, average axial velocity profiles of both models, given in Figure 3.15, are comparable and in good agreement with each other. The higher axial temperatures observed in the WS model around the radial positions of 0.20, 0.30 and at the wall confirms the explanation of the previous section for the influence of the side restrictions on the overall flow field.

The temperature profiles given in Figure 3.16 show that, at the center of the tube, the results of both models are exactly the same. At radial positions closer to the tube wall they start to deviate. The averaged temperatures in the CW model are usually higher than the WS model, and the difference reaches its maximum at the wall. The lower averaged axial velocity closer to the wall in the CW model shown in the Figure 3.15 can be directly related to the higher averaged temperatures as seen in the Figure 3.16. A similar relationship between the velocity and temperature fields was also addressed in the temperature field comparison section.

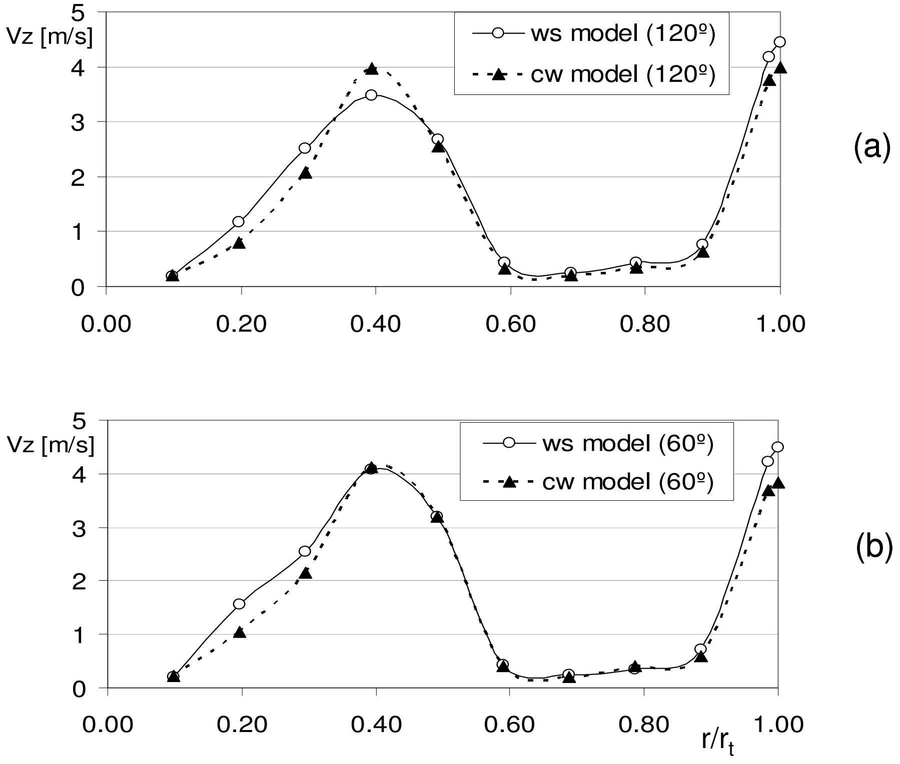

Figure 3.15 (a) CW and WS models radial profiles of axial velocity averaged over all sections (120°). (b) CW and WS models radial profiles of axial velocity averaged over central sections (60°).

The WS and the CW models are in better agreement over the central 60º portion, than over the entire 120º section of the models, although they are in quite good agreement for both cases. The comparison of Figures 3.15(a) and 3.15(b) showed a difference between the models in the axial velocity profiles at the radial position r/r_t=0.40. In the WS model, some portion of particle 12 intersected the axial plane created at that radial position. In the CW model, however, there was no intersection, due to the movement of this particle when generating the CW model to obtain the same overall bed voidage as the WS model. Therefore, the presence of particle 12 in the axial plane of the WS model at that radial position caused a lower averaged axial velocity over the 120º section shown in Figure

3.15(a). On the other hand, the axial planes created for the 60º portion did not cover the location of particle 12. As a result, there was no difference between the two models in averaged axial velocities at r/r_t=0.40, as shown in Figure 3.15(b). The difference in the averaged axial velocities at that radial position, shown in Figure 3.15(a), was reflected by the temperature profiles of the two models discussed above, in such a way that they started to differ after r/r_t=0.40 shown in Figure 3.16(a), which presents the profiles over the 120º section of the models. For the temperature profiles averaged over the 60º portions of the models shown in Figure 3.16(b) however, the results were found to be the same for both models up to the mid-tube and departure started only after the radial position of 0.60.

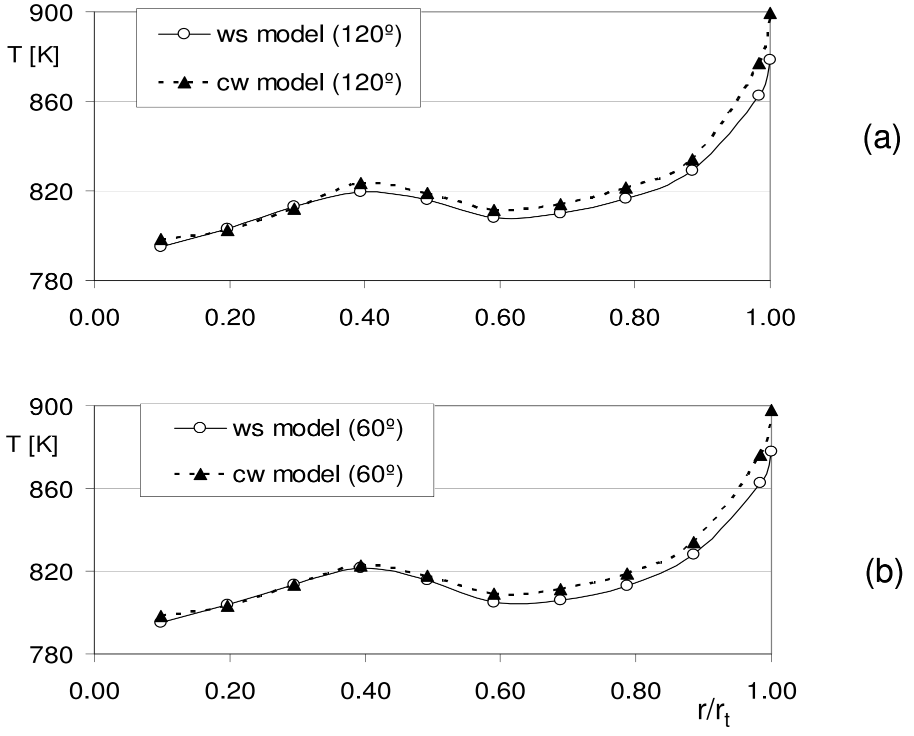

Figure 3.16 (a) CW and WS models radial temperature profiles averaged over all sections (120°). (b) CW and WS models radial temperature averaged over central sections (60°).

When the averaged radial velocity and temperature graphs of the 120º and 60º portions of the models are compared to each other, the only significant difference can be observed around r/r_t= 0.40 and 0.50. Furthermore, the maximum temperature difference between the 120º and 60º portions was found as 2-3 ºC in the CW model, and 3-4 ºC in the WS model. This was not expected to be so low for the industrial operating conditions, considering the local differences in flow and temperature. Thus, it can be said that averaging the values over the entire radial surfaces mitigates the local differences due to the side wall effects.

3.5.4 Heat uptake comparison

Another quantitative comparison between the WS and the CW models can be made by considering the overall heat uptake by the catalyst particles. Table 3.4 shows the ratio of heat uptakes of the WS and the CW models for five particles (1, 2, 3, 4 and 5). These five particles are the only ones that are the same size in both models, as they lie entirely within the 120° segment. The heat uptakes according to these particles for both models are quite comparable to each other with a maximum deviation of 6%.

Table 3.4 Heat uptake comparison between the CW and WS models, for the five particles common to both.

Particle No.	Heat uptake WS/Heat uptake CW (W/W)
1	1.003
2	1.005
3	1.019
4	0.989
5	0.942

For particles 4 and 5, the CW model heat uptakes are slightly higher than for the WS model. This observation can be coupled to the related argument drawn in the temperature field comparison section. The hotter surfaces of these particles in the CW model could have this kind of effect on the total heat uptake. For the other particles, on the other hand, the WS model has a higher heat uptake. This might appear contradictory if the hotter spots on the surfaces of particles 2 and 3 of the CW model are considered, which were shown in Figure 6. However, it can be seen from Figure 7 that the particles 4 and 5 are positioned closer to the tube wall than the others. A lower axial velocity in the near wall region was observed in the CW model (Figures 8, 9 and 10). Combination of these observations suggests that, due to lower velocity in the near wall region of the CW model, the particles closer to the wall get more heat than the others. Table 3.3 shows a different situation for particles 1, 2, and 3 which are not as close to the wall. Thus, the low velocity field in the near wall region could not create an environment in which these particles get more heat in the CW model than in the WS model.

Finally, considering particle 2, as being the only complete particle in the WS model and in the 120º section of the CW model, a very good agreement in the heat uptake of this particle was found between the two models.

3.5.5 Conclusions

The comparison of the WS model and the CW model was carried out by just considering the related portion of the CW model. The flow and heat transfer characteristics were examined in terms of flow pathlines, axial velocity contours, temperature fields and contours, and heat uptake. As a result of this examination, generally a good agreement was observed between the two models.

The main difference in geometries of these models was the symmetry side wall boundary conditions of the WS model. This was not a realistic condition for the cylindrical packings, but it was the only suitable approach to generate a lower-cost segment model.

The effects of the symmetry side wall conditions on the overall parameters were studied. Although the overall axial velocities and temperatures were only slightly different, the overall pressure drops were not comparable to each other. The discrepancy on the pressure drop could be explained due to the squeezing constraint of the symmetry walls on the flow.

The radial temperature profiles of the two models averaged over Z and Θ were found quite comparable for the full wall segment (120º section) which validates the earlier work (Nijemeisland et al., 2004). The agreement between the two models in the averaged profiles might not have been expected à priori, especially when the local differences were considered. This conclusion may emphasize that averaging the parameters might have cancelled the local differences especially at the axial planes examined in this study at the different radial positions. The different behavior observed in the WS model at the local regions closer to the side walls can be attributed to side wall restrictions regarding the discrepancies seen in the flow pathlines, temperature fields of the models, and temperature and velocity contours shown by the selected visual planes. On the other hand, in the center of the models, general flow features were well-reproduced by the two models. Therefore, the side wall effects on the WS model could be reduced while focusing on the central near wall region. To support this idea, a comparison was made of profiles averaged over the 120º and central 60º sections of the models. A slightly better agreement was observed in the averaged profiles between the two models when averaging was restricted to the corresponding central 60º sections of the models. Furthermore, the local flow and heat transfer properties of the two models were also found to be more comparable when the analysis was confined to these sections.

As a result of all of the above observations, in the cases where the computational constraints dominate so that a reduced size model is required, and the area of interest is on the local properties instead of the overall averaged ones as in the case of the near wall region of the low N systems, as in this work, the WS model becomes a reasonable choice to investigate the transport properties, if the analysis is focused on particle 2 which is positioned in the central near wall region.

4. Approximation of Reaction Heat Effects

In addition to using CFD to obtain understanding and information about the transport processes in a packed tube of inert particles (Nijemeisland and Dixon, 2004), it is also desirable to simulate tube behavior with active catalyst particles

Modern catalyst pellet design has developed from cylinders and Raschig rings to pellets with internal holes and/or external lobes and grooves (Sie and Krishna, 1998). These complex shapes provide larger external surface areas which leads to higher catalyst activity, as reactants have easier access into the pellets, at the cost of lower particle structural integrity. In addition, lower pressure drop results from the increased bed voidage, and the increased activity and heat sinks can also lead to lower tube wall temperature and longer tube life (Stitt, 2005; Bruno et al. 1988). The role of the various features of the complex pellets in affecting tube wall heat transfer, and their consequences for tube temperature profiles and wall temperatures is not well integrated into the design process. One reason for this is the loss of catalyst particle detail by the use of approximations such as the equivalent-volume sphere and similar one-dimensional shapes (Penernera et al., 2003; Mariani et al., 2003). There was a need for detailed study to capture the effects of changes in particle design at a constant pressure drop condition.

The choice of constant pressure drop as a basis for comparison was motivated by considering that catalyst improvements are used to increase volumetric average activity and to reduce overall plant capital cost (or facilitate uprate of an existing reformer). Pressure drop is an economically important parameter in steam reforming. In a methanol or ammonia plant, for example, any pressure drop in the upstream part of the plant must be recovered in the syngas compression stages prior to the respective synthesis loops. Increases in volumetric activity tend, therefore, to be balanced in design by increases in flow rate per tube at constant pressure drop. Some of the trade-offs in going from a traditional Raschig ring pellet to a modern 4-hole geometry are illustrated in Table 4.1, reproduced here from the original source (Stitt, 2005).

Table 4.1 Benefits of modern catalyst pellet design on reformer performance

	17 mm Raschig Rings	17 mm Raschig Rings	L x D: 19x14 mm 4-hole
Plant rate (relative)	100	112	112
Max. TWT (°C)	921	940	921
CH_4 slip (mol% dry)	4.4	4.8	4.3
Approach to equil. (°C)	3	6	2
Pressure drop (kg/cm^2)	2.3	3.1	2.8

The simulation results in Table 4.1 show that the effect of increasing plant rate with Raschig rings is to increase tube wall temperature (TWT), methane slip, pressure drop and to give a worse approach to equilibrium. Switching to 4-hole catalyst geometry allows the same plant rate increase with no increase in tube wall temperature or methane slip, an improved approach to equilibrium, and a more moderate increase in pressure drop. These results suggested that evaluation of various catalyst geometries at constant pressure drop would be a rational approach.

Heat transport processes in non-reacting packed tubes have been investigated by CFD simulation of packings of inert particles (Nijemeisland and Dixon, 2004). The inclusion of the heat effects of reaction in catalyst particles would allow a more realistic evaluation of different particle shapes and structures for the reactor performance. The diffusion, conduction and reaction inside the catalyst pellets could, in principle, be solved by 3D CFD simulations. However, diffusion limitations in the particles are quite strong for steam reforming reactions, as shown by the computed low effectiveness factors (Pedernera et al., 2003). Simulation of species transport by diffusion in the porous particles would yield highly stiff diffusion-reaction equations, and such models would be extremely expensive to compute.

In view of these considerations, we have developed an approximate approach that captures the main heat effects of the reactions by including heat sinks and sources inside the solid regions.

4.1 Model development

The geometries with the cylindrical particles packings of different numbers and sizes of internal voids are shown in Figure 4.1. In all of the WS models used in this study, the twelve equilateral cylinder catalyst particles of size 0.0254 m were placed at the same positions with a same transformation procedure described in Chapter 3. The main aspects of the geometries were the different sizes, numbers and locations of the longitudinal internal voids of the catalyst particles. Therefore, in 1-hole, 3-holes, and 4-holes geometries, the particles have the same internal void size with a standard diameter of 0.0073 m. In the 1-big-hole geometry, the void diameter was doubled which results in the same overall bed voidage as the 4-holes geometry. On the other hand, the internal void diameters were reduced by a factor of √2 of the standard diameter for the 4-small-holes geometry. For each particle configuration, a more detailed characterization is given in Table 4.2, normalized to the values for full cylinders for each quantity.

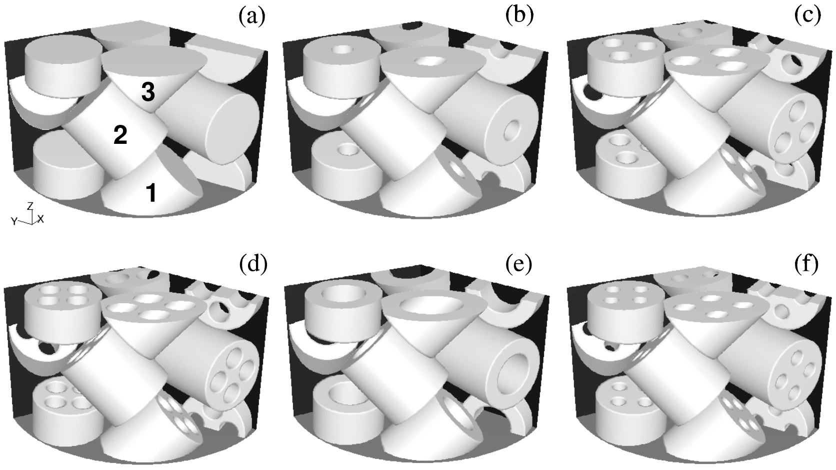

Figure 4.1 The WS cylinder model geometries: (a) full, (b) 1-hole, (c) 3-hole, (d) 4-hole, (e) 1-big-hole, and (f) 4-small-hole models.

Table 4.2 Properties of the catalyst pellets

Model	Overall Bed voidage (normalized)	GSA (normalized)
Full	1.000	1.00
1-hole	1.082	1.16
4-small-holes	1.164	1.49
3-holes	1.246	1.49
1-big-hole	1.329	1.27
4-holes	1.329	1.66

4.1.1 Mesh refinement

In order to achieve an accurate representation of the flow in the near-wall region, which determines the successful predictions of wall–bounded turbulent flows, a fine enough grid structure has to be created in the wall-fluid contact regions. This may be achieved by the prism layer implementation on the walls and setting the unstructured tetrahedral/triangular elements for the sections outside of the prism region. To decide on the suitable prism layer and unstructured element sizes, a validation study was carried out in two different ways. The heat transfer properties were investigated by considering a single cylinder particle in a box assembly as shown in Figure 4.2. Since the overall voidage in this model was very high ($\varepsilon=0.93$), the influence of prism layer implementation on the pressure drop was not considered. However, the pressure drop sensitivity was tested with our full cylinders WS model where we have a lower bed voidage ($\varepsilon=0.50$), which creates a significant pressure drop value.

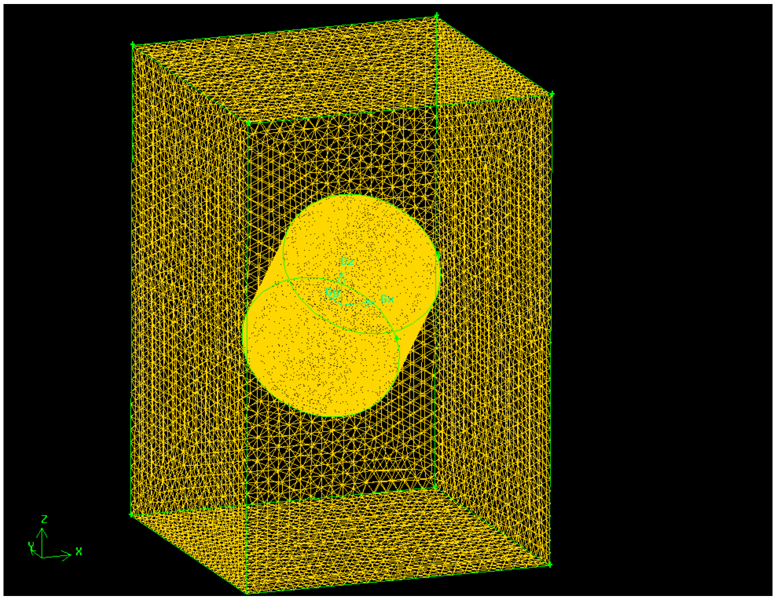

Figure 4.2 Single cylinder in a box assembly

4.1.1.1 *Cylinder in a box model*

In the model, a single equilateral cylinder with the same size as the cylinders used in the WS models was considered in a 45 degree rotated form in positive x direction. A rectangular box was created with a size of 2 x 2 x 3 units considering the cylinder dimension as 1 unit. The side walls were symmetric, and top and bottom surfaces were periodic where fluid enters from bottom as in the WS models. The fluid and solid material properties and operating conditions were also the same as WS model settings. To model turbulence, the κ-ε RNG turbulence scheme with EWT was selected.

Four layers of prisms were introduced on the interior particle surface to cover almost 3% of the particle radius. The rest of the particle volume was meshed by unstructured (UNS) tetrahedral cell elements.

In order to save the computational size, on the faces of the rectangular box, triangular face elements were selected with a size of 0.002032 m, whereas inside of the box volume which is essentially the fluid section, the finer mesh structures were set as described below.

To investigate the effect of the first prism layer height on the simulation results, different first layer heights from 2.54×10^{-5} m to 1.78×10^{-4} m were considered on the exterior surface of the particle with totally 10 layers of prisms. The outside of the prism layers, through the fluid volume, was meshed with the same size used in the solid particle volume. So in short, this case, "Case-1", was described as: varying the first prism layer height, and keeping the UNS mesh size outside the prism region constant.

In the "Case-2", the first prism layer height was kept as 5.05×10^{-5} m as used in one of the models of the Case-1. Again 10 layers of prisms were implemented. In the outside of the prism region 0.000508 m, 0.000762 m, and 0.001016 m sized tetrahedral elements were used, separately. In short this case was described as: keeping the prism structure constant, varying the UNS mesh size outside the prism region.

As a "Case-3", there were no prism layers, and the entire fluid domain was meshed with tetrahedral elements in 0.000508 m, 0.000762 m, and 0.001016 m sizes separately.

As an example of the grid structure, the horizontal plane cross section view is shown in Figure 4.3 for the model with the first prism layer height of 5.05×10^{-5} m, and UNS grid size of 0.000508 m. In the figure an arbitrary section was enlarged to show the prism layer structure in detail both in solid and fluid sides. The blue line was drawn to distinguish the fluid and solid regions in the enlarged view.

As a first step, the isothermal flow solution was obtained with periodic top and bottom settings, as shown by the flow pathlines released from the bottom surface in Figure 4.4. Then, in the non-periodic domain, the energy equation was solved using the periodic flow solution as a flow field and considering the endothermic effects of the MSR which is the main interest of this chapter, and the application details are given in the following sections.

The comparison of different cases was made by the particle heat uptake, and particle surface temperature contours.

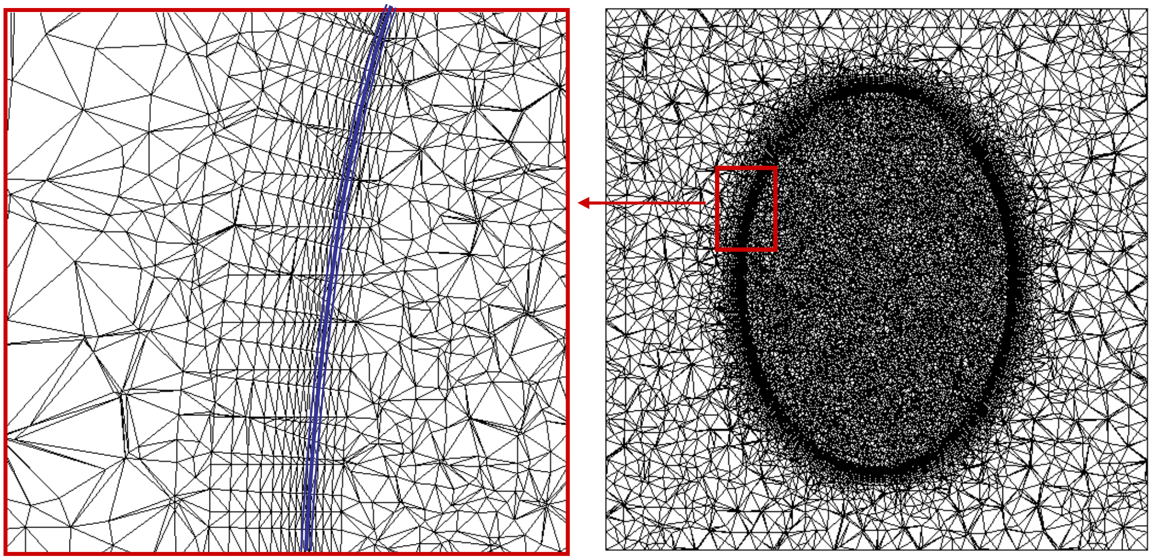

Figure 4.3 The sample grid structure view.

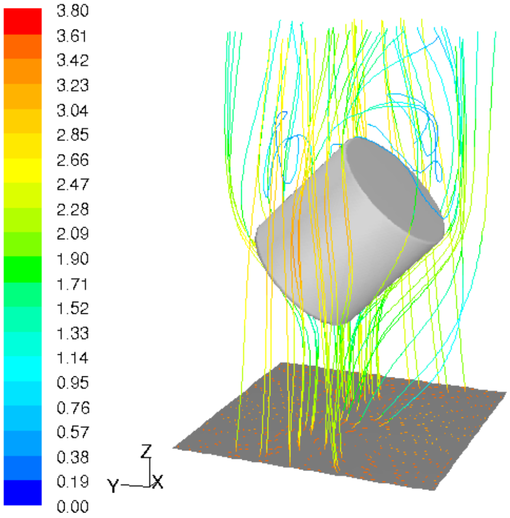

Figure 4.4 The flow pathlines colored by velocity magnitude (m/s).

Case1: The model details and normalized heat uptake values are given in Table 4.3. The heat uptake values were normalized based on the value obtained by the model-(b) which has a recommended y^+ value ($y^+=1.0$). The y^+ changes from 0.5 to 3.6, and varies in proportion with the first prism layer height as expected regarding the y^+ definition given in equation (1.30). As can be seen from Table 4.3, the heat uptake values decreased to an asymptotic value with a decrease in first prism layer height. Totally 4% change was observed in the heat uptakes.

Table.4.3 Case-1 model details and normalized heat uptakes

Description	First prism height (m)	UNS size (m)	y^+	Normalized heat uptake
model-(a)	2.54×10^{-5}	0.000508	0.50	0.998
model-(b)	5.08×10^{-5}	0.000508	1.00	1.000
model-(c)	7.62×10^{-5}	0.000508	1.50	1.004
model-(d)	1.27×10^{-4}	0.000508	2.50	1.018
model-(e)	1.78×10^{-4}	0.000508	3.60	1.036

The particle surface temperature contours are shown in Figure 4.5. The slight increase in the temperatures can be noticed with the increase of first prism layer heights. This increase is more pronounced at the lower corner of the particle where wall shear stress is higher, as expected due to the flow direction. The influence of flow around the particle can additionally be observed with the temperature variation on the particle surface for all of the models. The flow pathlines shown in Figure 4.4 can be coupled to these observations. The temperatures were lower on the upper side walls, and on the most part of the top surface as a result of the wiggly back flow which occurred near to those places.

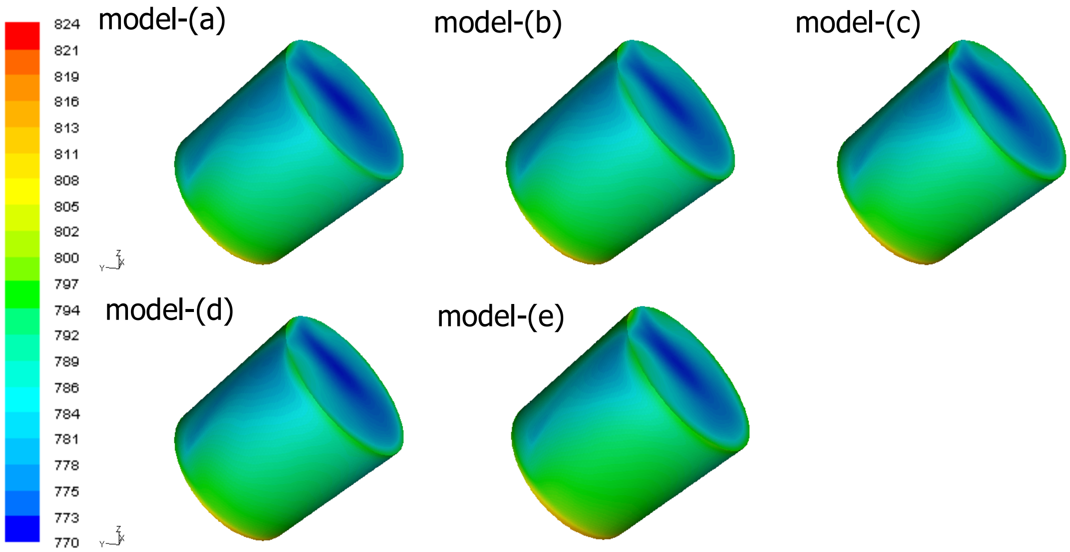

Figure 4.5 The particle surface temperature contours (K) of the Case-1 models.

Case-2: The first prism layer height of 5.08x10^{-5} m was selected as constant in this case because the recommended y^+ value was obtained with that structure. The heat uptake values are represented in Table 4.4 in the normalized form based on the same model emphasized in Case-1.

Maximum 4% decrease in the particle heat uptake was observed within the increase in the UNS size while keeping the prism structure unchanged. By these three models, no particular relation was observed between the UNS size variation and the heat uptake change. In essence, a relation could probably be observed if the structured mesh would be applied instead of UNS.

Table.4.4 Case-2 models UNS sizes, and normalized heat uptakes

Description	First prism height (m)	UNS size (m)	Normalized heat uptake
model-(b)	5.08x10^{-5}	0.000508	1.000
model-(f)	5.08x10^{-5}	0.000762	0.961
model-(g)	5.08x10^{-5}	0.001016	0.972

The particle surface temperatures of these three models are shown in Figure 4.6. The model (b) contour was repeated in this figure to make the comparison easier. As can be seen in the figure, the temperature change was not as pronounced as in the Case-1. So, we may conclude that, varying the UNS grid while keeping the prism structure unchanged, did not affect temperature field significantly.

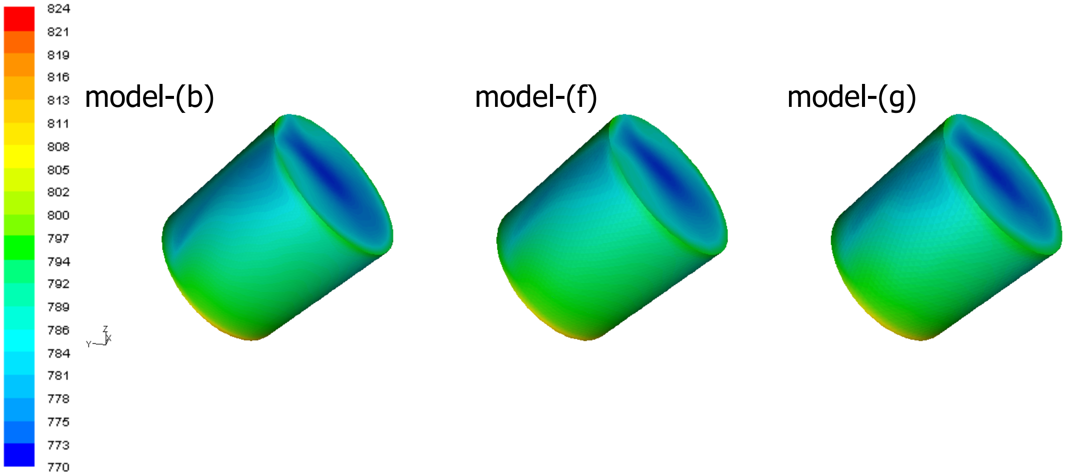

Figure 4.6 The particle surface temperature contours (K) of the Case-2 models.

Case-3: In this case there were no prism layers, and entire domains were meshed by the UNS grid. The particle heat uptake values are normalized based on again the model-(b) results, and shown in Table 4.5. The influence of prism layer implementation can be understood well by these normalized heat uptake values given in Tables 4.3-4.5. For all of the models, the higher particle heat uptakes were obtained than the base model, model-(b). Among them, the lower UNS size model, model-(h) has the higher particle heat uptake. Also, it was observed that an increase in UNS size shows a decrease in heat uptake. According to this trend, we could reach to the same heat uptake value if we would increase the UNS size more. However, as being an averaged parameter, particle heat uptake may not be enough alone to reach a final conclusion. For that reason, we consider the surface temperature contours additionally.

Table.4.5 Case-3 models UNS sizes, and normalized heat uptakes

Description	UNS size (m)	y^+	Normalized heat uptake
model-(h)	0.000508	5.70	1.164
model-(i)	0.000762	7.80	1.083
model-(j)	0.001016	9.60	1.070

When UNS gets bigger, the y^+ also gets bigger. So, we would reach to the preferred y^+ value for the standard wall functions ($y^+ \approx 30$) with an increased UNS size keeping the flow conditions same. However, this is impractical for our WS models where the gap between the particles is not enough to implement a grid with that size.

The important deviation in particle surface temperatures for these models as compared to the models with prism layers can be seen in Figure 4.7. The surface temperatures were much more uniform in this case, and they were not as affected from the flow patterns as the prism implemented models were.

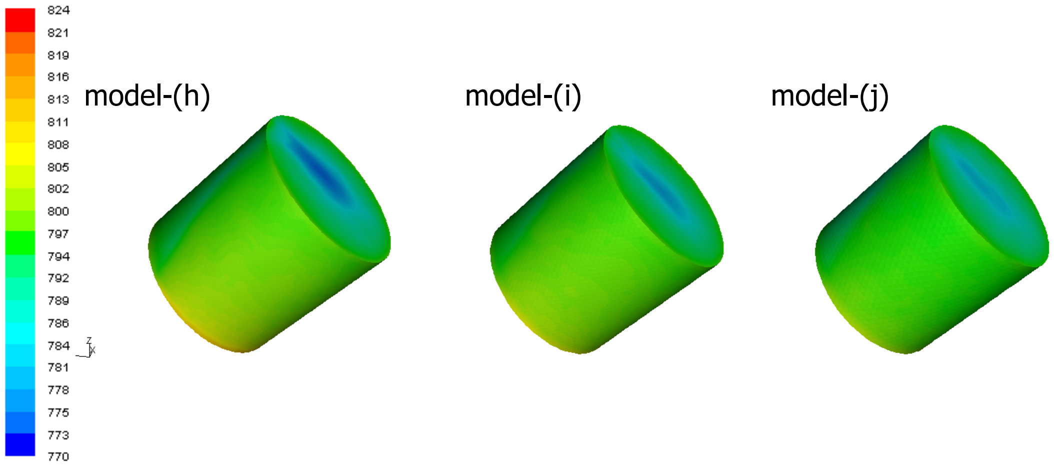

Figure 4.7 The particle surface temperature contours (K) of the Case-3 models.

In summary, a significant impact of prism layer implementation was observed on the particle surface temperature distributions and heat uptakes. Therefore, these observations suggested the importance of implementing prism layers especially when dealing with the heat transfer problems.

4.1.1.2 Full cylinders WS model

The WS model, as shown in Figure 3.1, was used in this study with three different cases where different meshing options were considered as in the single cylinder in a box study. Since the main focus was the fluid side here, the solid particles were meshed with UNS grid structure, and were not changed for different cases. Even for some cases, the solid particles were removed from the model to reduce the computational expense.

For all of the cases, periodic flow simulations were carried out at the inlet conditions of steam reforming. Convergence was controlled by monitoring the momentum and turbulence residuals, and pressure drop and y^+ magnitudes. The RNG κ-ε turbulence model was selected with standard wall functions for “Case-a”, and EWT for “Case-b” and “Case-c”.

Case-a: Only UNS grid was used for the entire fluid domain with six different sizes from 0.00033 m to 0.00127 m. The pressure drop change as a result of the different UNS mesh applications is shown with a suitable trend-line in Figure 4.8(a).

Increase in the UNS mesh size reduced the pressure drop prediction. But this change was not proportional. On the other hand, the cylinder wall y^+ value, shown in Figure 4.8(b), was almost proportionally affected by the UNS size change. Actually, a proportional relationship could be expected regarding the definition of y^+, but there were small discrepancies for some data points regarding the linear trend-line. These small perturbations may be due to the unstructured nature of the grid, and accordingly, having different cell centroids for the cells nearest to the wall.

Additionally, the exponential effect of the mesh size on the model sizes was shown in Figure 4.8(c) with a suitable trend-line for the data set. In total, four times reduction in the

UNS mesh size causes 70 times increase in the fluid volume. This huge impact, which brings a computational burden, only results in a 16% change in pressure drop based on the lower pressure drop value. Note that, the y^+ values were not in the recommended range for any wall treatment with any of the mesh sizes here, and it was not possible to create a model having a suitable y^+ value due to the computational constraints, as can be understood from the trend of the total number of cells shown in Figure 4.8(c).

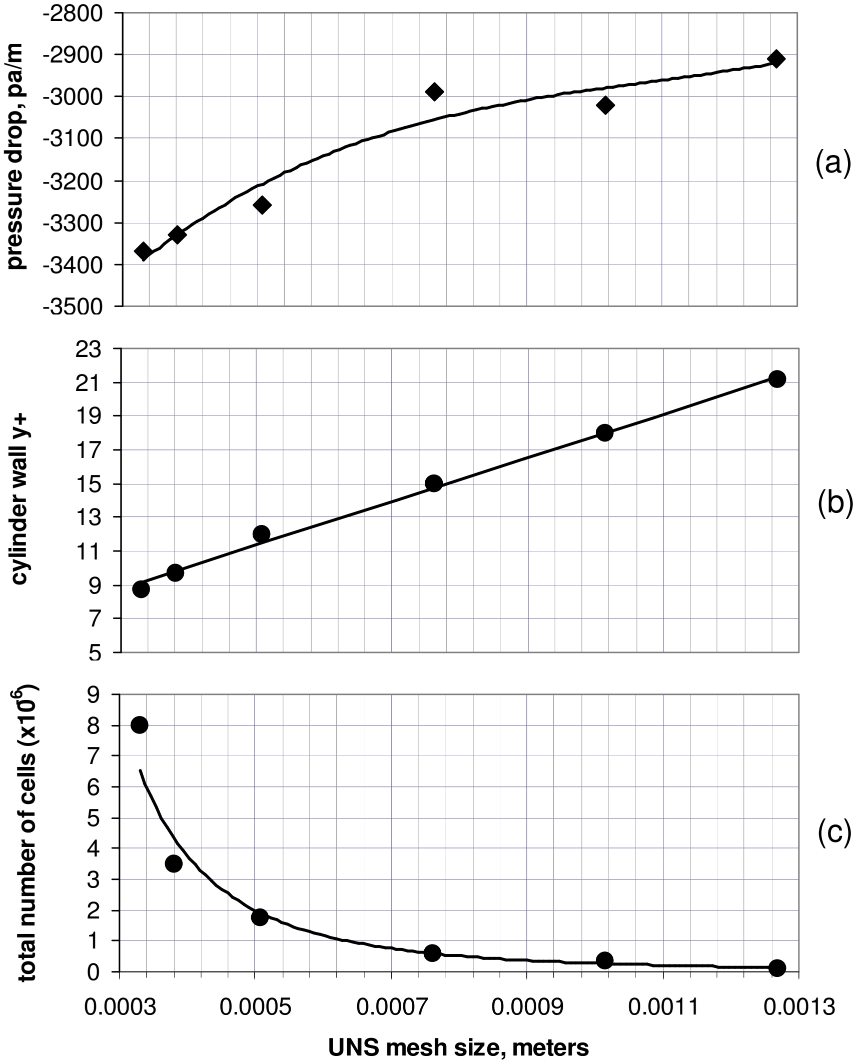

Figure 4.8 For Case-a, the changes in (a) pressure drop, (b) y^+, and (c) number of cells in the fluid region.

Case-b: In this case, the prism layers were implemented on the exterior surfaces of the particles and on the tube wall. The first prism layer height was varied from 10^{-6} m to 10^{-4} m. The UNS grid was applied for the rest of the fluid volume with a size of 0.000762 m. The details of the prism layers are given in Table 4.6. As can be seen in the table, for some models, different numbers of same sized prism layers were implemented, to understand the related effects on the pressure drops. Especially for the models with $0.0025\text{x}10^{-3}$ m and $0.0051\text{x}10^{-3}$ m heights of first prism layer, three different cases of total numbers of layers were studied. Obviously we have space limitations in WS models to apply the same number of layers for different first heights. Regarding all the cases, maximum total prism height change was 30% based on the highest one, and mostly the total height was kept around $0.07874\text{x}10^{-3}$ m ± 6% (in 17 cases out of 22).

The pressure drop and y^+ variation was shown in Figure 4.9(a) and 4.9(b) respectively with the suitable trend-lines.

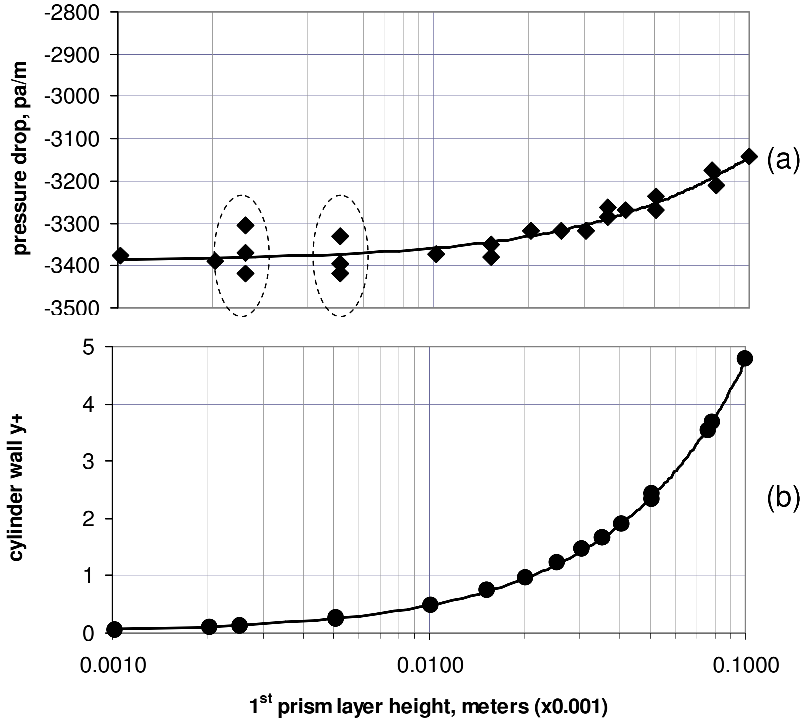

Figure 4.9 For Case-b, the changes in (a) pressure drop, and (b) y^+.

Table.4.6 Case-b models prism layer details

1st Prism layer height $x10^3$ (m)	Total prism height $x10^3$ (m)	Number of layers
0.0010	0.07874	12
0.0020	0.07874	12
0.0025	0.07366	8
0.0025	0.07874	12
0.0025	0.07874	5
0.0051	0.10414	8
0.0051	0.07874	12
0.0051	0.07874	5
0.0102	0.07366	5
0.0152	0.08128	4
0.0152	0.07874	5
0.0203	0.07366	3
0.0254	0.07874	3
0.0305	0.09144	2
0.0356	0.07112	2
0.0356	0.07874	2
0.0406	0.08128	2
0.0508	0.10160	2
0.0762	0.07620	1
0.0787	0.07864	1
0.1000	0.10000	1

The pressure drop scale was kept same as the one in Figure 4.8(a) to make the comparison easier. Within this study, although the first layer height was changed by a factor of 100, the pressure drop variation was around 7% based on the lower pressure drop regarding the data points laying on the trend-line, which is much less as compared to the variation in Case-a

The pressure drop difference of the models with different numbers of layers, notified with dashed lines on Figure 4.9(a), was maximum 3%. Note that, the y^+ values for those models were very much lower than the recommended value 1.0.

Since the prism layer structures were regular as compared to UNS grids, the exact proportional trend was observed in the change of y^+ values with the first prism height as shown in Figure 4.9(b).

Case-c: Regarding the recommended y^+ value, the prism structure with 0.254×10^{-4} m first prism layer height and 0.7874×10^{-4} m total height, was chosen as the base, and different UNS mesh sizes were implemented for the rest of the fluid domain from 0.00046 m. to 0.00127m. The pressure drop and y^+ variations were shown in Figure 4.10(a) and 4.10(b) respectively.

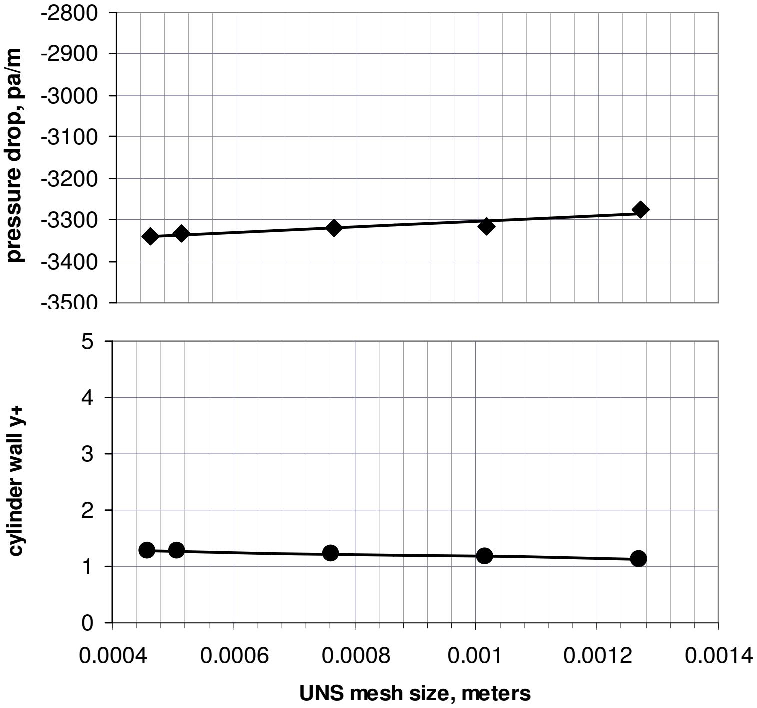

Figure 4.10 For Case-c, the changes in (a) pressure drop, and (b) y^+.

In this case, less than 2% pressure drop variation was observed, with the 1% change in y^+ values. So, it may be concluded that, the pressure drop value was not significantly affected, with the change in UNS mesh size by a factor of three, for the prism structure that kept the y^+ value on the recommended level.

As a result of the findings of this study, to continue the approximation of the reaction heat effects, we have selected the prism structure of the Case-c and the UNS mesh size of 0.000762 m. to define the fluid region in our models. Regarding the computational constraints, the prism layers were only implemented on the tube wall and on the external surfaces of the particles 1, 2, and 3 as considering the particle 2 as the test particle, and the particles 1 and 3 as the particles standing below and above the test particle to create a fine grid structure for the main focus area.

4.1.2 Meshing the pellet

Based on the industrial observations (Stitt, 2005), and the one-dimensional particle simulations (Pedernera et al., 2003), steam reforming reactions take place within the 2-5% of the particle radius from the surface. Setting the UNS grid with the same size of the fluid would not be enough to define that region. Lowering the mesh size of the particle volume would increase the model size. Moreover, one of the aims of the approximation of the reaction heat effects was to investigate different activity levels from 2% to 5%. Therefore, considering all of these restrictions, we have implemented six equal-height prism layers to the internal wall of the test particle number 2 to cover the 6% of its radius for all of the models shown in Figure 4.1. The outer region of the prism layers in the test particle volume was meshed with 0.000508 m. UNS grid, which was low enough to not to create skewed cells especially for the models with internal holes. The other 11 particles were meshed by UNS grid with the same size as the fluid region. The selection of the active 2-5% of the test particle is given in the next section, by which the grid structure of the pellet can be understood better.

4.2 Verification of the selection of the active region

The position and orientation of the cylindrical particles had to be obtained for this verification. Further, the positions of the internal voids in the cylinder had also to be known. To get these, we made use of the procedure that was followed when the wall segment models were constructed. A sequence of operations, rotations and transformations, which was exemplified for particle number 1 in Figure 3.3, was then used to find the coordinates of cylinder center points, and top surfaces. Each operation was represented by either 3 x 3 matrix for a rotation, or a 3-vector for a translation. Similarly, the top and center points for each internal hole in the particle were calculated.

The selection of the active region could then be tested for each particle with those coordinates. FLUENT defines an identification (ID) number for each surface and volume element in the geometry. Therefore each solid particle has a different ID number. As a first step, the user-defined code prepared for this purpose recognizes the particle with a specified number. Each solid catalyst particle is composed of many computational volumetric cells. The code stores the centroid coordinates of each cell. As an example, consider an arbitrary numerical cell which is illustrated by a blue dot as “Point (x_p, y_p, z_p)” in Figure 4.11. This schematic represents a sample solid cylindrical particle with the corresponding points necessary for the user-defined code. Additionally, the geometrical center coordinates of the solid particle, and the top-center coordinates of the top surface of the same solid particle are available from the procedure described above, and are given as input to the code. These points are shown by red dots as “Center (x_c, y_c, z_c)” and “Top (x_t, y_t, z_t)” respectively in Figure 4.11, along with the distances calculated from their coordinates.

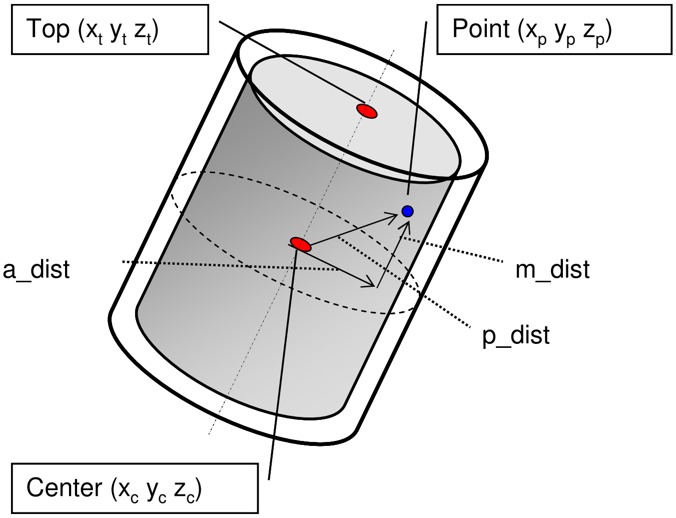

Figure 4.11 Sample solid particle and corresponding points for the verification of the selection of active region

The main idea of this verification study was to decide by a user-defined code whether a cell of interest will be located in the defined 2%, 3%, and 5% active regions or not. The active region is schematically shown by the non shaded area in Figure 4.11, and the corresponding algorithm for this code is given in Figure 4.12. To understand the relative location of each and every computational cell within the solid particle volume, three different distances were calculated. The distance between the "Center" and the "Point", denoted "p_dist", was calculated by equation (4.1). The projection of this point onto the visual central plane of the particle perpendicular to its axis was used for the "m_dist" and "a_dist" calculations. The "m_dist", calculated according to equation (4.2), is the distance between the "Point" and its corresponding projected point. The "a_dist" is calculated by the Pythagorean Theorem which gives the distance between the "Center" and the previous projected point, as given in equation (4.3).

$$p\_dist = \sqrt{(x_p - x_c)^2 + (y_p - y_c)^2 + (z_p - z_c)^2} \qquad (4.1)$$

$$m\_dist = \left| \frac{(x_t - x_c)(x_p - x_c) + (y_t - y_c)(y_p - y_c) + (z_t - z_c)(z_p - z_c)}{\sqrt{(x_t - x_c)^2 + (y_t - y_c)^2 + (z_t - z_c)^2}} \right| \qquad (4.2)$$

$$a\_dist = \sqrt{(p\_dist)^2 - (m\_dist)^2} \qquad (4.3)$$

The “m_dist” and “a_dist” were used for understanding the relative position of the cell of interest. These two distances were compared with a cut-off parameter “r_c” which is defined as 98% of the cylindrical particle radius for 2% activity, 97% of the cylindrical particle radius for 3% activity, and 95% of the cylindrical particle radius for 5% activity. Any point located inside the hypothetical cylinder volume with a radius of “r_c” corresponds to the inactive region of the catalyst particle. The comparison had to be done considering the radial and axial dimensions of the catalyst particle. So, when “a_dist” is compared with “r_c”, the corresponding radial decision could be made. Similarly, the comparison of “m_dist” and “r_c” could lead to the axial decision. As given in the algorithm shown in Figure 4.12, both conditions had to be satisfied to decide on the inactive region.

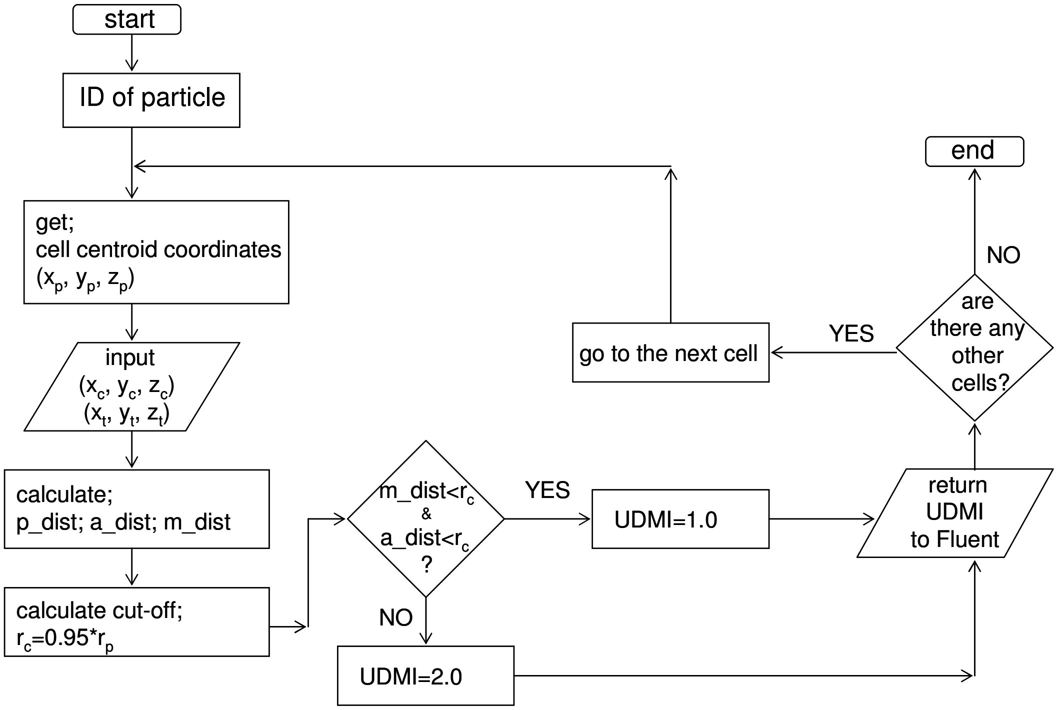

Figure 4.12 The algorithm for the verification of selection of active region for a full cylinder.

The extension to consider internal voids followed the same principles. Additional "Center" and "Top" points were available which now lay on the axis of each circular void, and the distance of an arbitrary cell centroid from the axis, and thus from the surface of the void, could be calculated. Assuming that diffusion limitations would act in the same manner for all surfaces, whether on the particle external surface or on the internal void surface, the same cut-off value was used for all surfaces.

The active and inactive regions were distinguished from each other by setting different user-defined-memory-indexes (UDMI) for the cells in these regions. These indexes were selected arbitrarily as 1.0 for the inactive region and as 2.0 for the active region, and were shown with different colors by FLUENT which made those regions visually distinguishable. The same procedure was applied for each cell of the solid particle by getting the corresponding cell centroid coordinates. After all the cells of one solid particle were covered, the same code was applied to the other solid particles.

The selection of the active regions of the solid particles with the described code is given in Figure 4.13 for the one hole cylinders model as an example with the vertical cross-sectional view of particle 2. An arbitrary section was enlarged to emphasize the active region selection better, considering the grid structures of the model. The active region was colored red, whereas the inactive region was colored green. The blue color represents the fluid section and the UDMI of 0.0 was set as default by FLUENT. It should be noted that, the use of prism layers facilitated the successful working of algorithm. Although the related figures were not shown here, the algorithm was also successful for the other models. The sample user-defined code is given in Appendix 3(a).

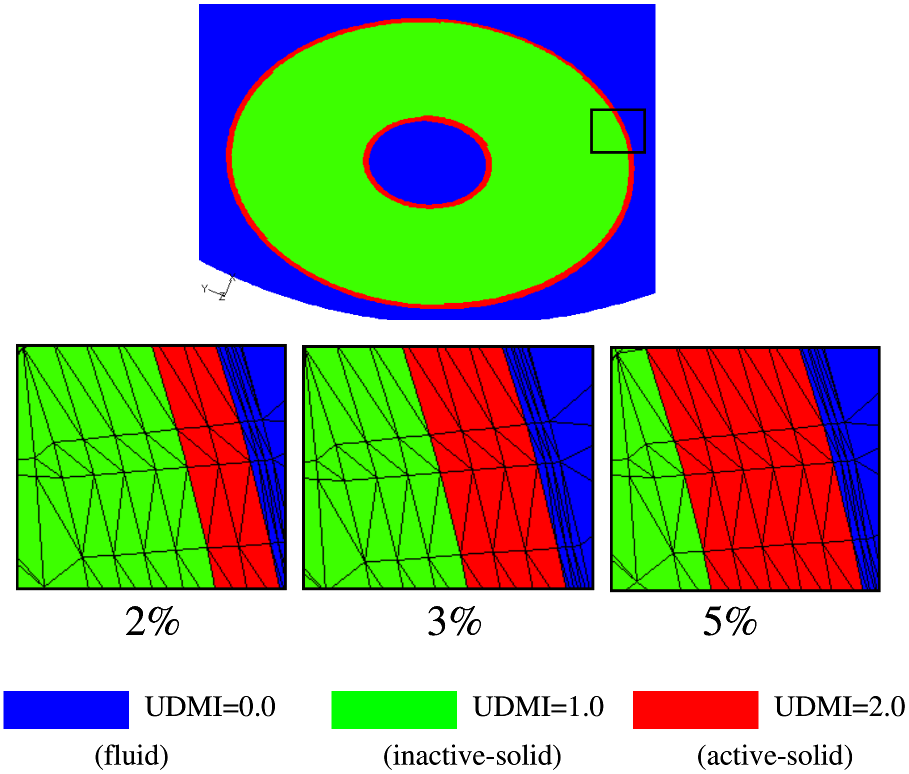

Figure 4.13 Active region selections for 2%, 3%, and 5% activity levels.

4.3 Introducing the steam reforming heat effects

The heat effects of the steam reforming reactions, equations (1.65)-(1.67), were introduced by a second user-defined code. The main structure of this code is similar to the one considered for the verification of the active region selection. The algorithm for this related code is given in Figure 4.14.

As a first step, the reaction rate and equilibrium constants, partial pressures and heats of reaction were input to the code. The code has 12 sub-codes corresponding to each of the 12 solid particles, and the above constants were just entered once in the beginning of the code before the sub-codes. FLUENT can provide a loop over the cells in a particular volume region. For a particular computational cell of a solid particle, the code recalls the cell temperature and centroid coordinates from FLUENT. Analogously to the verification part, the code calculates the relative position of the cell within the solid particle by equations (4.1), (4.2), and (4.3). In order to make comparative analysis, the 2%, 3%, and 5% activity levels were individually considered. In steam reforming reactions, temperatures are usually high and around 1000 K. Since the reaction rate expressions were not developed for low temperatures, it was decided to use a low-temperature cut-off of 500 K to prevent any possibility of anomalous results. If the cell temperature was less than the cut-off temperature, reaction was suppressed so that there would not be any heat effect. If the temperature was high enough, the algorithm would decide on the location of the cell by radial and axial comparison (for full cylinders) in the same way as expressed in the verification part. Additional tests were performed for particles with internal voids, again as described in the previous section. As a result of that decision, either the cell would be in the inactive region so that there would not be any heat effect, or the code calculated the temperature-dependent reaction rate constants and equilibrium constants, and reaction rates by equations (1.68) through (1.73). The heat generated by the reactions was calculated by multiplying the reaction rates with the corresponding heat of reaction terms for all three reactions and summing them up. The units on all source terms must be in the form of heat generation-rate per volume (Fluent, 2005). Therefore, the heat generation term was multiplied by the solid density in order to obtain the source term "Q" according to equation (4.4).

$$Q = \rho_s \sum_i r_i (-\Delta H_i) \tag{4.4}$$

The UDF code must return back to the main code the derivative of the source term with respect to the dependent variable of the transport equation, which is the temperature in this case. This term is used in the Finite Volume method to linearize the source term. Therefore, derivatives of all the temperature-dependent parameters of the source term were calculated in order to get the derivative of the source term. Once this term was returned back to the main code, the same procedure was applied for each cell of the solid particle. After all the cells of one solid particle were covered, the same procedure was applied to the other solid particles with different sub-codes.

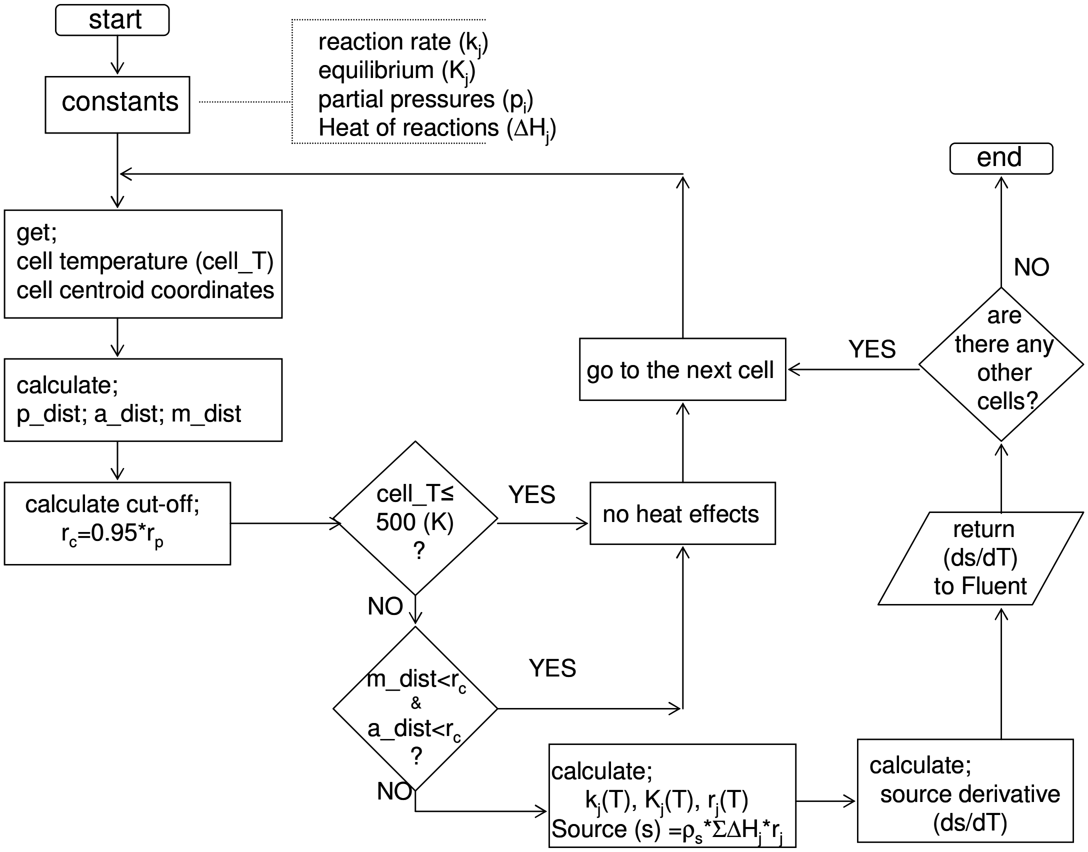

Figure 4.14 The algorithm for the application of reaction heat effects

The sample application code is given in Appendix 3(b). The necessary information about the user-defined functions can be found in Fluent (2005).

4.4 Procedure

For each model, isothermal flow simulations with axially-periodic inlet and outlet conditions were first carried out at the constant specified pressure drop to obtain an initial flow field. The mass flow rate corresponded to a particle Reynolds number of approximately 9,500 based on superficial velocity and the particle diameter of a sphere of equivalent volume to the cylindrical particle, ignoring voids. The flow was fully turbulent under these conditions, and the RNG κ-ε turbulence model was selected with the

Enhanced Wall Treatment (EWT) approach in order to accommodate values of y^+ close to unity on the surfaces with prism layers. The velocity components and κ, ε values obtained from the top/bottom surfaces of the periodic flow solution were set as the inlet boundary conditions for the subsequent non-periodic flow and energy simulations. The computation of the periodic flow solution as an initial step allowed us to obtain non-uniform flow inlet conditions, thus avoiding artificial entrance effects in the non-periodic simulations.

In order to get rid of the thermal entry effects due to the uniform inlet temperature setting, and to achieve a well-distributed temperature field, the non-periodic temperature, velocity and pressure fields were computed in three stages. A uniform heat flux was set on the tube wall (curved surface of wall segment) for all three stages. In the first stage, a uniform inlet temperature was specified, and a flow and energy solution calculated. Then the outlet temperature field from the first stage was set as the inlet temperature condition of a second stage, and the solution was re-computed. Finally, the outlet temperature field from the second stage was set as the inlet temperature condition of a third stage, and the source/sink terms for reaction heat effects were activated. In that way, the models were virtually "stacked" up to the third stage. The first two stages in this procedure may be regarded as "pre-heating" to eliminate thermal entry effects, in which the same amount of energy was supplied to the fluid for each model. As the flow field was also re-calculated, the resulting (nominally constant) pressure drop values changed slightly, and are given, normalized based on the full cylinders model, in Table 4.7. The final pressure drop values were within a maximum ±2% variation for all the models.

Table 4.7 Pressure drop and TWT values (3% activity)

Model	Pressure drop (normalized)	TWT (normalized)
Full	1.000	1.000
1-hole	1.015	1.000
4-small-holes	1.003	0.995
3-holes	0.981	0.992
1-big-hole	0.989	0.991
4-holes	0.984	0.991

4.5 Results and discussion

Intra-particle temperature fields: The temperature field inside test particle 2 is shown in Figure 4.15 for the full particle case. Three planes have been defined: the "horizontal" plane bisects the particle axis at the midplane, and the two "vertical" planes are parallel to the particle axis and perpendicular to each other. Vertical plane-1 is roughly perpendicular to the tube wall and vertical plane-2 is roughly parallel to the tube wall. The temperature contours show that the particle is nonisothermal for all three activity levels, and emphasize the non-symmetric nature of the temperature field inside the particle, similarly to previous results obtained for spherical particles (Dixon et al., 2003). The particle is subjected to a strong heat flux from the tube wall, convective heat transfer from the surrounding fluid, and heat sinks due to reaction. The balance between these yields a fairly strong temperature gradient across the particle from tube wall towards the bed center (horizontal plane and vertical plane-2). Average temperature differences of 47.5 °C for 2% activity, up to 53.9 °C for 5% activity, were calculated. As activity increases the particle becomes cooler on average, suggesting that heat transfer from the tube wall becomes more limiting as the particle becomes more active. Temperature gradients are milder in the plane parallel to the tube wall (vertical plane 2).

We may compare the simulation results more quantitatively by the bed radial profiles of velocity and temperature. The radial profiles shown here were obtained considering the middle 60º part of the segment model in order to get rid of the possible effects of imposing the symmetry plane side conditions as described in Chapter 3.

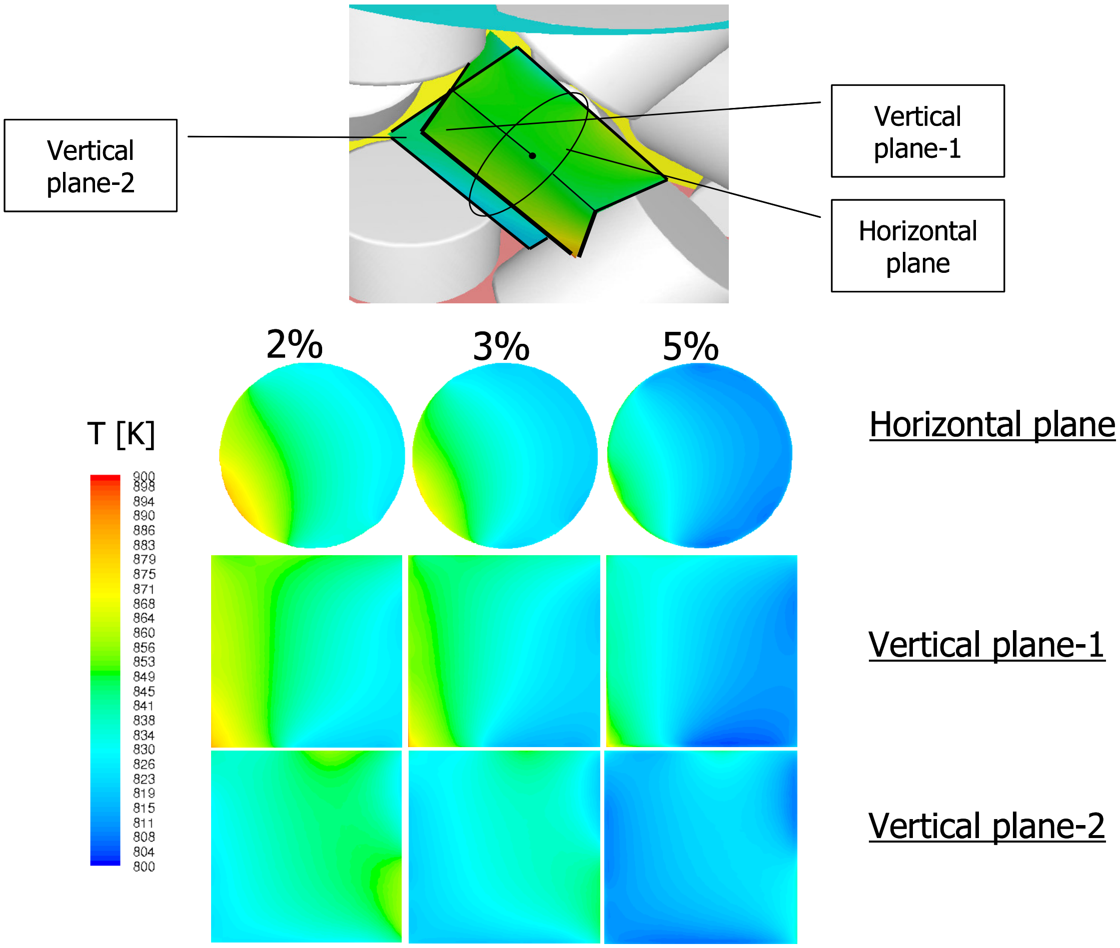

Figure 4.15 Temperature contours on vertical and horizontal planes through test particle 2.

Flow and temperature fields for 3% activity were compared for all geometries. The effects of different catalyst activity levels on models with and without internal holes were investigated for the full, 1-hole, and 4-hole geometries only.

Velocity profiles: Radial profiles of superficial axial velocities are shown for all the geometries in Figure 4.16(a). There is a strong S-shaped variation in superficial axial velocity across the tube radius, for all the models. Peaks in velocity occur at the dimensionless positions $r/r_t = 0.40$ and 1.00, and regions of low velocity appear for $r/r_t \leq 0.3$ and $0.55 \leq r/r_t \leq 0.9$. The magnitudes of the axial velocities are quite similar for all the particle geometries in the bed center and near the wall. There is a substantial difference in axial velocities for all the models at the dimensionless radial positions between 0.55 and 0.9. Figure 4.15(a) also shows that we capture the no-slip decrease of v_z to zero at the wall very well with the boundary-layer mesh there.

The explanation for these observations can be related to the corresponding bed voidage profiles, shown in Figure 4.16(b). The full cylinder results show that more solid is present for $r/r_t = 0.30$ and $0.55 \leq r/r_t \leq 0.9$, corresponding to the lower superficial velocities. The voidage curves at these positions are distinct and increase following the order of increasing particle voidage (and thus increasing bed voidage) given in Table 4.2. Note that the voidage for the 1-big-hole particles (and for the 1-hole particles, to a lesser extent) is distributed spatially quite differently to the voidage for the multi-hole particles, for $0.55 \leq r/r_t \leq 0.9$. For $0.3 \leq r/r_t \leq 0.55$ and $r/r_t \geq 0.9$ there is less solid and the velocity profiles coincide, as they are only weakly affected by the particle features, and the highest axial velocities occur where the voidage exceeds 90%.

The local bed viodage variations at the dimensionless radial position $0.55 \leq r/r_t \leq 0.9$ can be coupled to the similar local axial velocity variations at the same position. However, the axial velocities near the center of the bed ($r/r_t < 0.3$) did not reflect the bed voidage differences there as clearly because of the smaller areas available for sampling of the velocities and the area weighted averaging of the axial velocities.

Overall, the magnitudes of the axial superficial velocities are higher for particles with higher voidage, such as the 4-hole and 1-bighole particles. This is a consequence of the standardization to constant pressure drop as a basis for comparison in these runs. Higher voidage allows higher mass flow rate for the same pressure drop, resulting in higher superficial velocity. This is seen especially in the range $0.55 \leq r/r_t \leq 0.9$, where velocity for the full cylinders is lowest, and for the 4-hole and 1-big-hole cylinders velocity is highest.

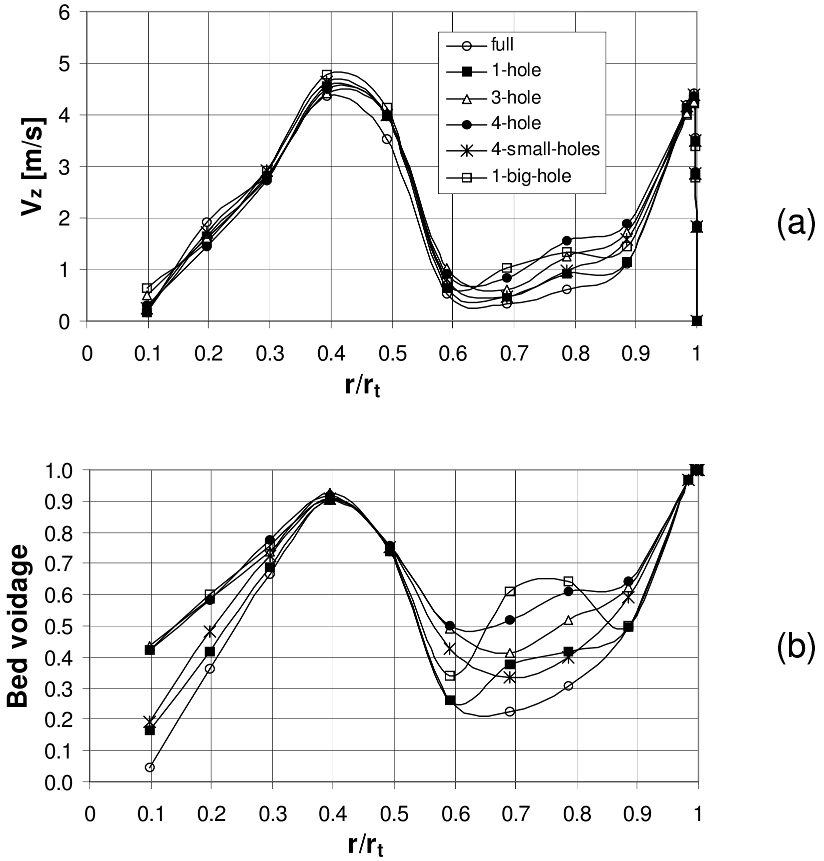

Figure 4.16 Radial profiles of (a) axial velocity, and (b) bed voidage for all the models.

Effects of particle features: The fluid and solid temperature radial profiles are given in Figures 4.17(a) and 4.17(b), respectively for a baseline particle activity value of 3%. It was noticed that, the solid phase temperatures lie some 10-20 °C lower than the fluid phase ones, due to the heat sinks caused by endothermic reaction in the solid particles.

This was an important observation in terms of the modeling approach in reaction engineering. As described in Chapter 1, one of the common packed tube models is known as the “pseudohomogeneous” model, which considers the same fluid and solid temperatures in the bed, as leading to a single phase bed. Obviously, the temperature difference in solid and fluid phases showed that, for the reactions with strong heat effects, this model should not be selected.

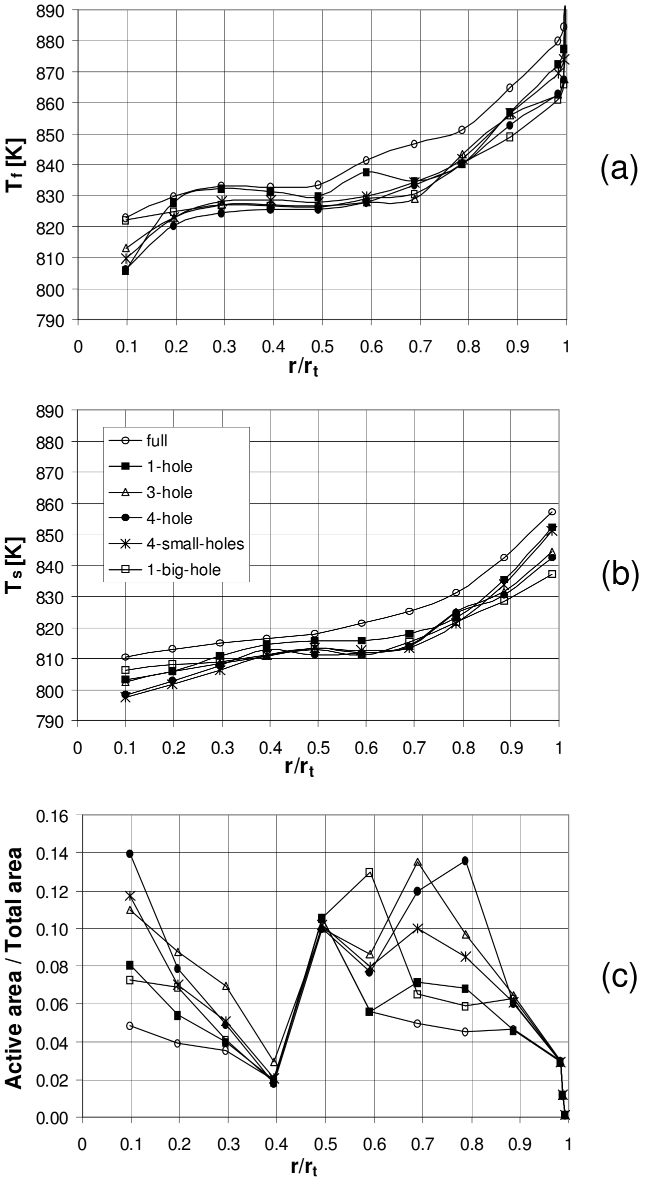

Figure 4.17 Radial profiles of (a) fluid temperature, (b) solid temperature, and (c) distribution of active cells for 3% activity level.

It should be noted that here, and in Figure 4.17, the tube wall temperatures are not included, as they were so much higher than the temperatures in the rest of the bed that their inclusion would overly compress the scale of the graph. The tube wall temperatures for 3% activity are presented in Table 4.7 above.

An example of a profile of pseudohomogeneous temperature, along with the solid and fluid area vertex averaged temperature profiles is shown in Figure 4.18 for full cylinders model and 3% particle activity value. The pseudohomogeneous temperature profile exhibit a strong S-shape, and this curve was exactly reproduced as weighting the fluid and solid temperatures by the void fraction applicable at each radial position, according to the formula:

$$T(r) = \varepsilon(r)T_f(r) + [1 - \varepsilon(r)]T_s(r) \tag{4.5}$$

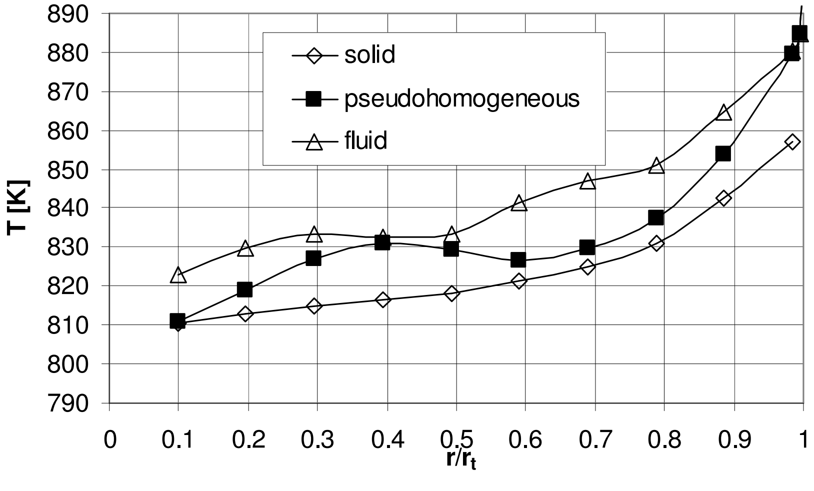

Figure 4.18 Temperature profiles of full cylinders model for 3% particle activity.

Mears (1971) derived a well-known criterion for the neglect of the temperature difference between the particle and the fluid, based on a Taylor series expansion of the reaction rate about the bulk fluid temperature:

$$\frac{E}{RT_0}\left|\frac{(-\Delta H)r(c_0,T_0)dp}{hT_0}\right| < 0.30 \qquad (4.6)$$

where E is activation energy for reaction, R is gas constant, T_0 is bulk fluid temperature, -ΔH, is heat of reaction, $r(c_0,T_0)$ is reaction rate at fluid conditions, dp is particle diameter, and h is gas-solid heat transfer coefficient.

The criterion, given in equation (4.6) for the rate not to deviate by more than 5% from the value calculated at the bulk fluid temperature was not satisfied for the dominant MSR reaction, reaction-III given in equation (1.67). The left hand side of the equation (4.6) was found as 21.0, which is lower from the criterion value 0.30, by a considerable margin, and also confirms the conclusions drawn above from Figures 4.17 and 4.18. More recent criteria for the use of the pseudohomogeneous model (Dometti et al., 1999) are based on comparisons of qualitative features of the bifurcation diagrams of one-phase and two-phase models for exothermic reactions, and are thus not applicable to the endothermic reactions of the present study.

For both fluid and solid temperatures, the full cylinder temperature profiles are some 5-10 °C above the other models. The 1-hole cylinder temperatures lie below those of the full cylinders and just slightly above the others, while there is no discernable difference between the multi-hole and 1-big-hole particle temperature profiles, for both fluid and solid. The lower temperatures for the multi-hole cylinders can be related to the effects of including different numbers and sizes of internal holes and thus increasing the active surface for reaction. The 1-big-hole fluid and solid temperatures are lower than would be expected for $r/r_t \geq 0.9$, and the reason for this is not apparent.

The tube wall temperatures, given in Table 4.7, show similar trends. The full and 1-hole cylinders are highest, while the 4-hole and 1-big-hole cylinders are lowest. Since the interstitial velocity close to the wall is the same for all models (see Figure 4.16(a), and note that superficial and interstitial velocities are essentially the same there), the near-wall heat transfer resistance will also be the same. The flux is constant, so the temperature difference driving force between the wall and the bed will also be constant, and the wall temperature will fall to follow the bed temperature.

Since the active cells result in heat sinks for the steam reforming reactions near the tube inlet, it is reasonable to expect that the temperature profiles would be affected by the amount and location of active mesh cells, especially the solid phase temperature. Figure 4.17(c) shows the distribution of active cells along the radial coordinate. A strong variation with tube radius is observed, with a large spread between the different particle geometries. The effects of the locations and sizes of the holes in the particles can be seen in the locations of the maxima in active cells for the 1-big-hole, 3-hole and 4-hole particles between $r/r_t = 0.6$ and $r/r_t = 0.8$. In particular, the 1-big-hole and 4-hole particles have their active cells in very different locations, despite having the same overall bed voidage. There is some general correspondence between activity and temperature; for example, the full cylinders have the lowest overall activity and the highest temperature, and temperatures are lower for all models in regions where activity is higher, such as $r/r_t \leq 0.3$ and $0.55 \leq r/r_t \leq 0.9$. The local variation in active cell profiles is not, however, reflected in the local solid or fluid temperature profiles. The “bump” in the 1-hole fluid profile may correspond to the minimum in activity at $r/r_t = 0.6$, but there are very few similar points of correspondence. An explanation for this lack of strong temperature variation is that as the active cells locate the heat sinks at the edges of the particles they act as “guard” coolers and force the entire particle to a lower temperature. The temperature profiles would then be expected to follow the distribution of total solid volume rather than the distribution of active solid volume. Comparison with Figure 4b does not appear to support any strong trends, however, which suggests that the high flow rate causes convective heat transfer to dominate and the effects of conduction and heat sinks to be secondary. This would explain the overall similarity of the temperature profiles, with differences only in small features of the profiles.

Effects of particle activity level: As previously mentioned, 2%, 3%, and 5% particle activities were considered for comparative analysis. Full, 1-hole, and 4-hole models were used for this comparison. Figure 4.19 shows the radial fluid and solid temperature profiles for these models and given activity levels. For each activity level, the temperatures decrease on going from full to 1-hole to 4-hole particles, due to increased active surface area.

The fluid temperature profiles are quite similar to each other for different activities. Changes in active cells by 250% (from 2% to 5%) change T_f by only a few degrees, most probably because the added active cells inside the particles increase the heat sink strength by only a small amount compared to the enthalpy needed to change the temperature of the strong fluid flow.

As would be expected, increasing the activity creates lower solid temperature profiles for all of the models especially at the local positions where the bed voidage is low, such as $r/r_t < 0.2$ and $0.6 < r/r_t < 0.8$. These profiles were obtained by averaging the local temperatures over only the solid surface areas in each radial plane. A more substantial difference is seen in this case when activity is increased from 2% to 5%, and a decrease of approximately 20 °C in solid temperature occurs for each of the three particle types.

The effects of particle activity level on the tube wall temperatures are given in Table 4.8. This shows the area-weighted averages of the tube wall temperatures on the packing side, and the temperature drop across the wall, ΔT_w, due to the wall conduction.

Table 4.8 Activity effects on tube wall temperatures

	2%		3%		5%	
	TWT	ΔT_w	TWT	ΔT_w	TWT	ΔT_w
Full	1047.4	23.0	1046.8	23.0	1046.2	23.0
1-hole	1047.2	23.5	1046.6	23.5	1045.9	23.5
4-hole	1038.1	23.4	1037.5	23.4	1036.8	23.4

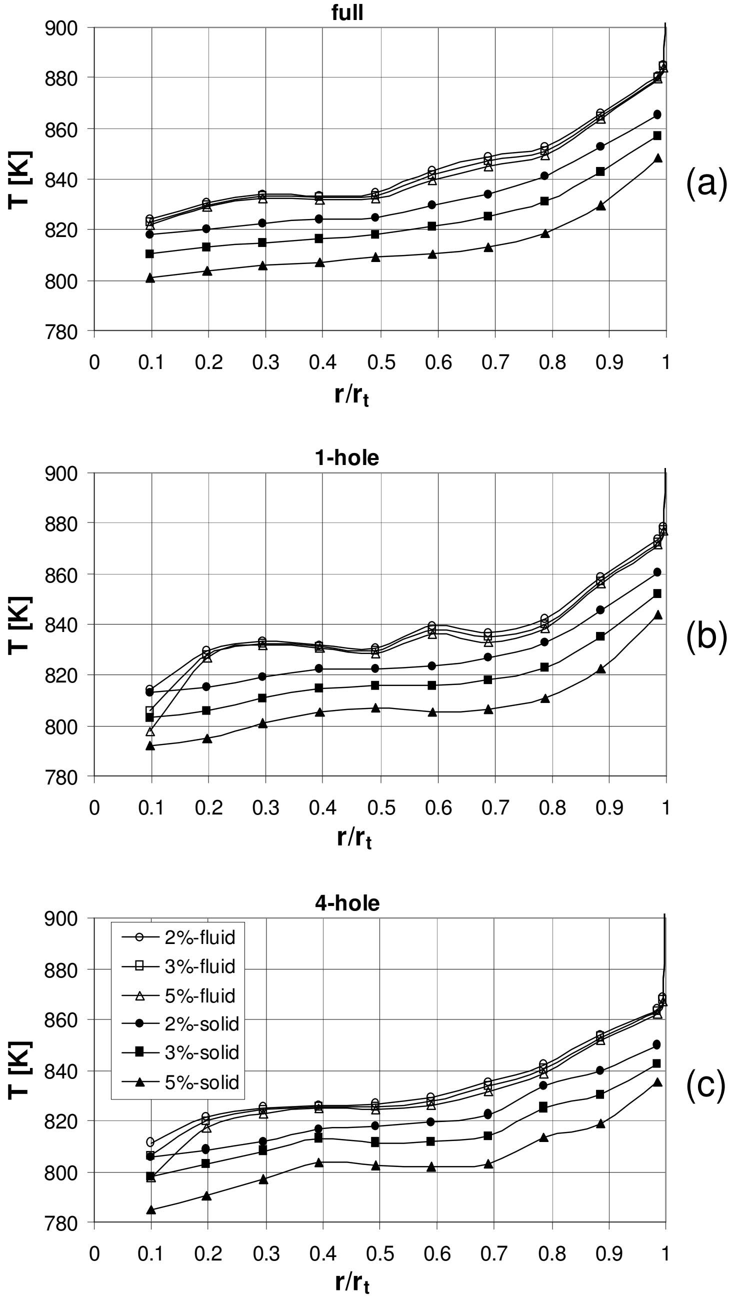

Figure 4.19 Fluid and solid radial temperature profiles for three activity levels for (a) full, (b) 1-hole, and (c) 4-hole cylinder packings.

The wall temperature differences between the outside of the tube and inside of the tube were quite comparable to each other for every model and activity level, which should be expected considering the same heat flux and wall properties were applied for all the models. The differences can be seen in individual wall temperatures for the models. Lower wall temperatures were obtained for the 4-hole cylinders model than the others as an effect of introducing multiple inner holes into the particles to increase the GSA. However, wall temperatures for a particular catalyst design were not affected by different activity levels, an unexpected result. The reason for this observation is suggested to be the gap between particles and the tube wall, which was intentionally kept so as not to have convergence problems due to contact points.

Heat uptake comparison: The fine near-surface mesh obtained by placing prism layers inside particle 2, allows us to compare the heat uptake values of that particle for different geometries and different activity levels. Table 4.9 shows the heat uptakes and GSA values for particle 2, normalized with respect to the full cylinders model and 3% activity as the base case.

Comparing from row to row in Table 4.9 shows that the increase in GSA assured by an increasing number of equal-size internal holes corresponds to an increased heat uptake for all the activity levels. The heat uptake increase does not appear to be directly proportional to GSA; the increment from full to 1-hole is considerably lower than the 16% increase in GSA, and the increase from 1-hole to 4-hole is also lower than the corresponding increase in GSA. Similarly, comparing column by column in Table 4.9 shows that increased activity level corresponds to increased heat uptake. The increase in heat uptake, as before, does not appear to be directly proportional to the increase in activity level.

The lowest heat uptake was achieved by 2% activity of full and 1-hole cylinders models, whereas the highest heat uptake was obtained by 5% activity of the 4-hole cylinder model. Almost equal heat uptakes were obtained for 3% activity of full cylinders model and 2% activity of 4-hole cylinders model. Similarly, the heat uptakes at 5% activity of the full cylinders model and at 3% activity of the 4-hole cylinders model were almost the same.

Table 4.9 Particle heat uptakes normalized to 3% activity, full cylinders model

	Activity level			GSA
	2%	3%	5%	
Full	0.746	1.000	1.372	1.00
1-hole	0.744	1.011	1.411	1.16
4-hole	0.998	1.369	1.939	1.66

The heat transfer uptake was compared for all particle types, again considering only particle 2, at 3% activity level. Referring to Table 4.2, the 1-big-hole and 4-hole particles have the same bed voidage, but they had very different heat uptakes, so this did not suggest that heat uptake would correlate with bed voidage. On the other hand, again from Table 4.2, the 4-small-holes and 3-hole particles have the same GSA, and since their heat uptakes were observed to be close, it was decided to correlate heat uptake with GSA. The normalized heat uptake based on the full cylinders model at 3% activity and the GSA values based on the full cylinders model were therefore plotted in Figure 4.20.

Two groups of data points were observed in Figure 4.20. For the first group, which is composed of the full, 1-hole, and 1-big-hole cylinders geometries, the heat uptake values are almost not affected by the GSA variation. The second group, which is the 3-hole, 4-hole, and 4-small-holes cylinders models, showed a stronger dependence on GSA. For the models having the same GSA values (4-small-holes and 3-hole), the heat uptake values were also the same. This result shows the effect of introducing more internal holes on the heat uptake performances, and gives partial support to the idea that heat uptake should increase with GSA, but it is not directly proportional to it. The finding that an increase in GSA gives rise to a lower increase in heat uptake is again due to the fact that the overall process is heat transfer limited.

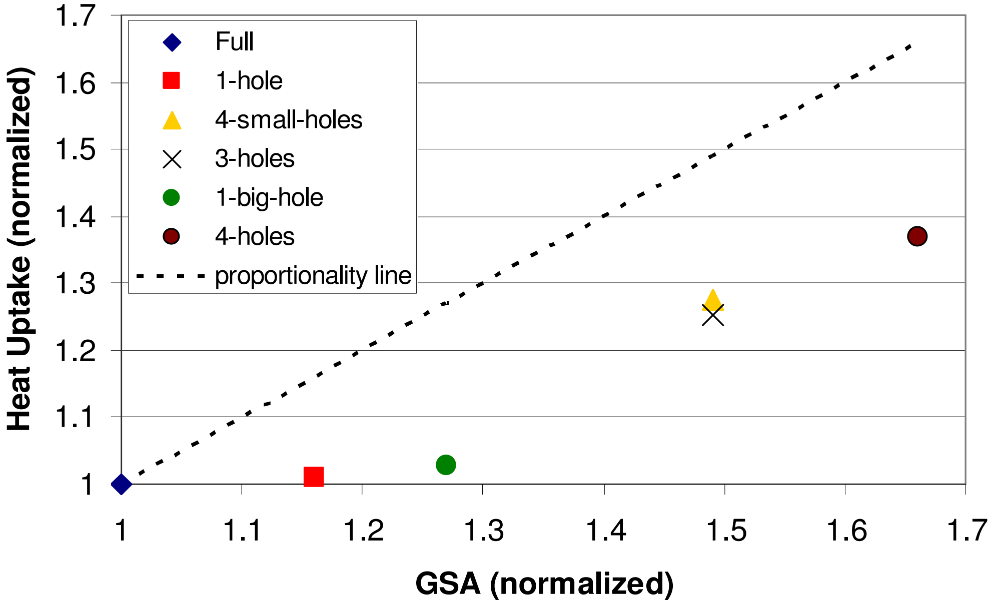

Figure 4.20 Heat uptake for test particle 2 versus geometric surface area (GSA).

Effects of particle thermal conductivity on the particle temperatures: In Figure 4.21 we show the variation of solid temperature through test particle 2 for three different values of the particle thermal conductivity: k_s = 1.0 W/m-K, corresponding to the alumina support, k_s = 21.0 W/m-K, corresponding to the alumina support impregnated uniformly with 22 wt% Ni catalyst, and k_s = 0.0001 W/m-K, approximating a "worst-case" scenario of zero thermal conductivity. The profiles in Figure 4.21 show that the difference between the catalyst particle solid temperature with and without metal impregnation is very small, suggesting that adequate conduction inside the particles is provided by the alumina support. The temperature of the higher-conductivity Ni-alumina particle is slightly higher overall, and more uniform, although still far from isothermal. The increase in thermal conductivity resulted in an increase in heat uptake for this particle of approximately 9%. The drastically lower temperatures of the "worst-case" scenario are caused by the inability of the heat to transfer from the particle surface to the inside of the particle, to balance the heat consumption by reaction. The temperature therefore falls until the reaction is essentially quenched. Heat uptake in this case fell to about 5% of the original value.

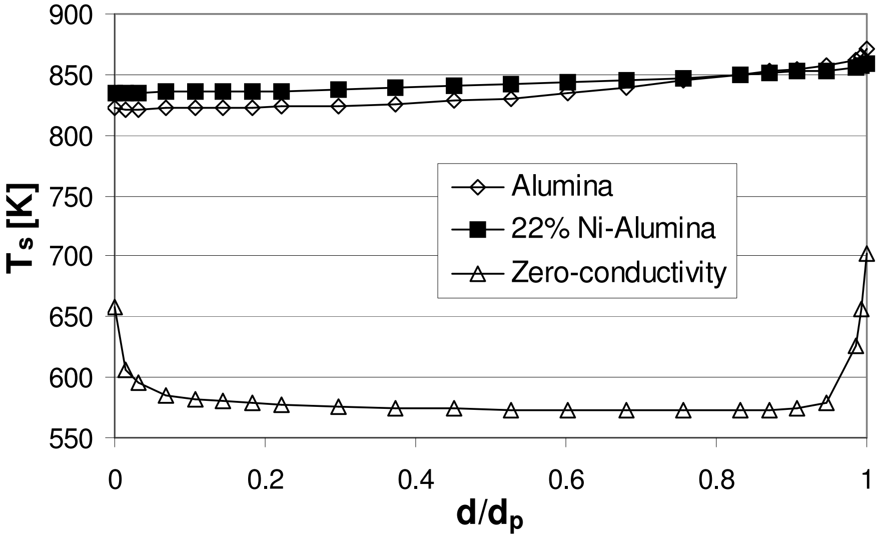

Figure 4.21 Solid temperature profiles through test particle 2 for three different values of particle thermal conductivity at 3% activity level.

4.6 Conclusions

The simulation of the six different particle types having different numbers and sizes of internal holes showed that cylindrical particles placed at the tube wall have non-symmetric temperature fields and a substantial temperature difference across them, which is only slightly mitigated by the incorporation of metal catalyst. Reaction and deactivation rates will also change markedly in the wall particles, and will be difficult to compute accurately using simplified pellet models.

The location of the heat sinks in the tube can be changed by particle design, but for steam reforming this has little effect on the fluid and solid radial temperature profiles. This is probably due to the domination of convective heat transfer at high Re. The effect of cooling the entire particle by the heat sinks caused by reaction at the particle surface may also have de-emphasized the importance of heat sink location.

Three different activity levels were compared for the full, 1-hole, and 4-hole cylinders models. The fluid temperatures were relatively insensitive to activity level, but solid temperatures showed significant changes. No effect was seen on tube wall temperature but this may have been caused by the omission of wall-particle contact points in the simulations. The test particle heat uptake increased monotonically with GSA as expected, but the increase was not proportional, which was attributed to heat transfer limitations. Particle thermal conductivity varied over a realistic range did not have a strong effect on the temperature profiles.

5. Diffusion/Reaction Application

Diffusion of the reactants from the surface of the catalyst to the interior of its pores constitutes one of the resistances in a reaction system catalyzed by the solid surface. In reactor modeling for the reactions with strong diffusion limitations, simplified approaches are selected as described in the Problem Statement. The most frequently used simplifications may be illustrated as the Figure 5.1 for the endothermic reactions.

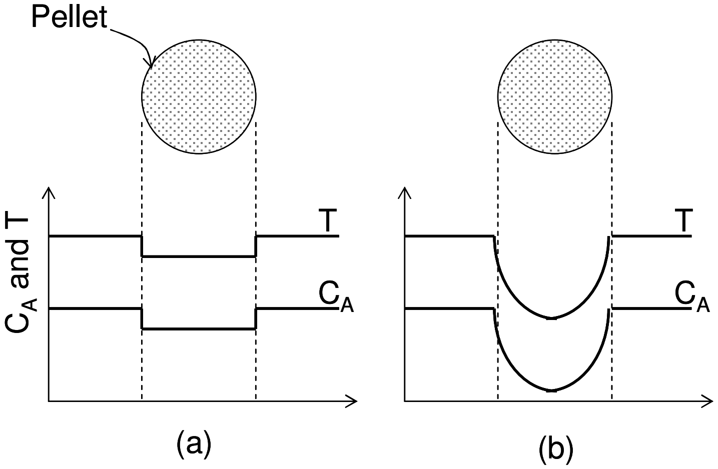

Figure 5.1 Illustration of reactor modeling simplifications for endothermic reactions as: (a) isothermal particle, and (b) uniform and symmetric distributions (re-produced from Levenspiel, 1972).

Isothermal particle, where temperature is constant throughout the particle, can be illustrated as Figure 5.1(a). The uniform and symmetric temperature and composition distributions can be sketched as Figure 5.1(b). These simplifications with the main assumptions such as the usage of lumped transport parameters would be preferable for the high N tubes. However, for the low N tubes where the presence of tube wall has an effect on the large proportion of the entire particles, these simplifications and assumptions would be misleading regarding the strong temperature gradient due to the wall heat flux. Therefore, the objective of this part was to improve the understanding of intra-particle transport phenomena by explicitly including conduction, species diffusion and reaction with realistic 3D external flow and temperature fields. Regarding the different particle activity levels, as described in Chapter 1, two different endothermic reactions were considered: MSR and PDH.

5.1 Model development

Two types of WS models were selected for this study: a full cylinders packing was used as the generic model, and a 4-hole cylinders packing to represent the commercial interest. The models were re-meshed to implement prism layers on the external and internal surfaces of the particles, including the tube wall. The fluid side prism structure was the one used in Case-c, described in section 4.1.1.2, and the solid side prism layers covered at least 3% of the particle radius from the surface. The mesh specifications for full cylinders and 4-hole cylinders packing were given in Appendix 4.

The total model sizes were found to be 2.03 x10^6 cells for the full cylinders model, and 3.46 x10^6 cells for the 4-hole cylinders. The grid structures of full cylinders and 4-hole cylinders models are shown in Figures 5.2 and 5.3 respectively.

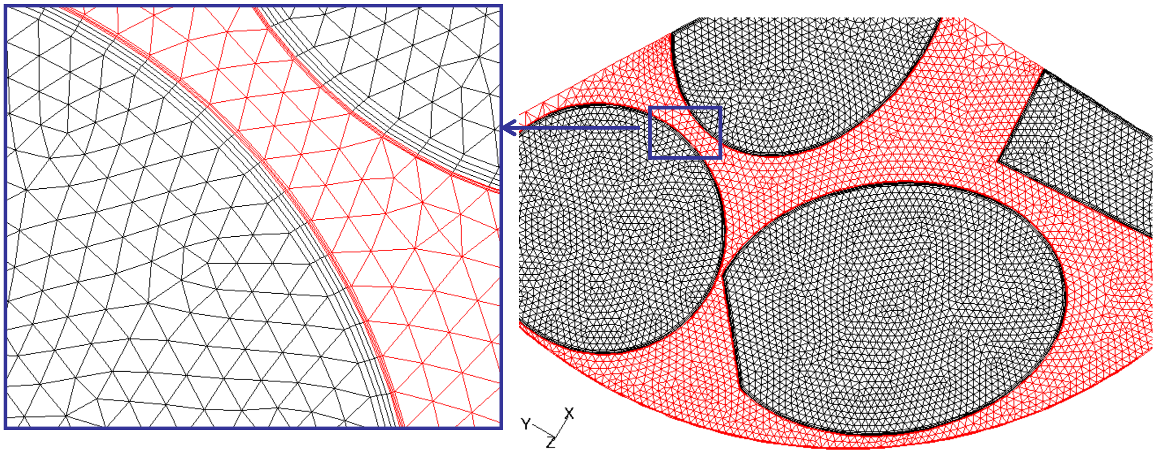

Figure 5.2 Grid structure of full cylinders model, and enlarged view of an arbitrary section.

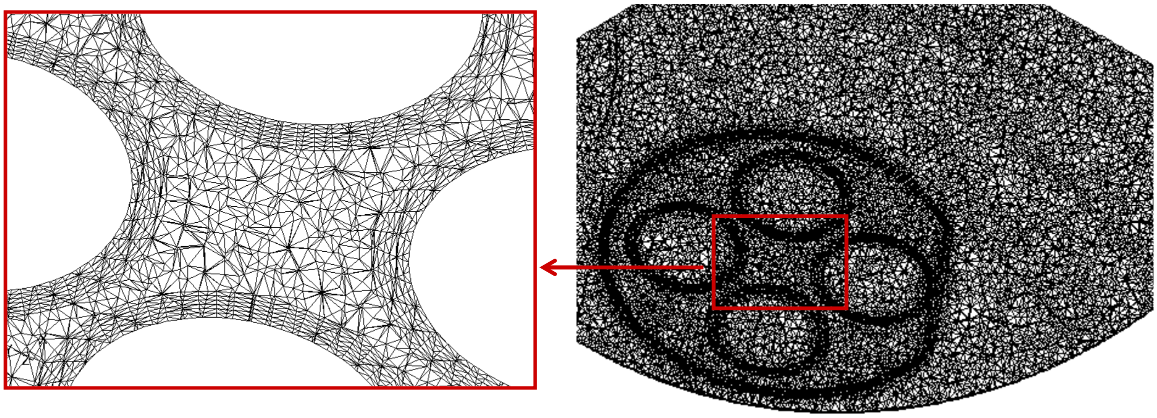

Figure 5.3 Grid structure of 4-hole cylinders model, and enlarged view of an arbitrary section.

In Figure 5.2, the top plane view mesh structure is shown where the fluid cells were colored by red and solid cells colored by black. An arbitrary section was enlarged to represent the prism structure in fluid and solid in detail. In Figure 5.3, the middle plane view mesh structure is shown. In the enlarged view, the fluid cells were removed to make the view clear.

In order to enable the intra-particle transport processes, the catalyst particles were converted into the *porous* structure from *solid*, which was the default setting and used for the particles in the previous part of this work. FLUENT defines additional *surface walls* which covers the *solid* volumes. So, once the solid volumes were converted into *porous*, those *surface walls* had to be converted into *interior* surfaces. This was a necessity, because the solid walls are impermeable, so they would prevent the species transport takes place between the pellet and the bulk fluid. Note that, in heterogeneous reactions, the three main mechanisms may be described as the adsorption of the reactants from the bulk fluid on the pellet, reaction, and desorption of the products to the bulk fluid.

FLUENT essentially considers the porous structure as a fluid zone. Porous media are modeled by the addition of a momentum source term to the standard fluid flow equations. The porous model allows setting additional inputs to model porous region including the porosity value and velocity field information in the region. The porosity value was set to 0.44 as Hou and Hughes (2001) used for the steam reforming catalyst. Additionally, the velocity components were fixed and set to zero in the porous media to create a comparable pellet structure with the solid particles.

The simulations were first run to determine an initial isothermal constant-composition flow solution in the segment with periodic top and bottom conditions. This flow field was used subsequently to perform the energy and species solution in the non-periodic domain. It was observed that the changes in the flow field had minor effects on the reaction rates when the momentum and turbulence iterations were included to the energy and species iterations (Dixon et al., 2007).

The RNG κ-ε turbulence scheme was selected with EWT, and the SIMPLE pressure-velocity coupling algorithm with the first order upwind scheme was utilized. The convergence was monitored by the pressure drop value for the flow runs, and checking the energy balance and the reaction rates in the test particle for energy and species simulations in addition to the residuals. The computations were carried out on a Sun Microsystems SunFire V440 with 4 x 1.06 GHz processors.

5.1.1 MSR operating conditions

The same reactor conditions and fluid properties were used here as given in Table 3.1. Since the particles were converted into porous, the thermal conductivity of the pellets was set as 1.717 w/m-K to obtain the effective thermal conductivity as 1.0 w/m-K (as given in Chapter 3 for alumina) accounting for the pellet porosity. The other pellet properties were the same as given in Chapter 3.

Species transport in the porous pellets was modeled by effective binary diffusivities calculated from straight-pore Knudsen and molecular diffusion coefficients, and corrected using pellet porosity and tortuosity. The details of these hand calculations are given in Appendix 5(a). The dilute approximation method based on the Fick's law was selected, and diffusive flux values were calculated according to equation (1.25) by FLUENT. The hand-calculated effective diffusivity values for each species, given in the Appendix 5(a), are defined as $D_{i,m}$ values. Actually, the multi-component method was additionally tested by defining the binary diffusivities, D_{ij}, and no significant difference was observed in the results. Therefore, the results shown in the next sections for MSR reaction were obtained by the dilute approximation method.

5.1.2 PDH operating conditions

The reactor conditions and the fluid properties are given in Table 5.1. The inlet mass fractions were 0.90 for C_3H_8, 0.05 for C_3H_6, and 0.05 for H_2.

The pellet properties were same as for the MSR particles. The diffusivities were calculated with the same procedure as the MSR calculations, and the values are given in the Appendix 5(b). For this reaction there were differences in the results for dilute approximation and multi-component methods, and therefore both results were represented in the relevant section.

Table 5.1: Reactor conditions and fluid properties for PDH reaction

T_{in} [K]	q_{wall} [kW/m^2]	P [kPa]	ρ [kg/m^3]	c_p [J/kg.K]	k_f [W/m.K]	μ [Pa.s]
874.15	2.0	0.101	1.8081	2180.25	0.0251	$8.01.10^{-6}$

5.2 Introducing MSR diffusion/reaction

A used-defined code was created to describe the sinks/source terms in the catalyst particles. In the user-defined code, the species source/sinks terms were defined as the following:

$$S_{Species,i} \equiv \rho_S (\alpha_{i,1} r_1 + \alpha_{i,2} r_2 + \alpha_{i,3} r_3) M_i \qquad (5.1)$$

where $\alpha_{i,j}$ represents the stoichiometric coefficient of component i in the reaction j. For example, for the reactions I, II, and III as given in equations (1.72), (1.73), and (1.74), the stoichiometric coefficients for CH_4 are:

$\alpha_{CH4,I} = -1.0 \quad \alpha_{CH4,II} = 0.0 \quad \alpha_{CH4,III} = -1.0$

Whereas the stoichiometric coefficients for H_2 are:

$\alpha_{H2,I} = 3.0 \quad \alpha_{CH4,II} = 1.0 \quad \alpha_{CH4,III} = 4.0$

The heat generation by the reactions was calculated by the same method as described in equation (4.4). As in the previous user-defined code, the code must return back to the main code the derivatives of the source terms with respect to the dependent variables of the transport equation, which are the mass fractions of the species, and temperature in this case. The algorithm of the species source/sinks calculations is shown in Figure 5.4.

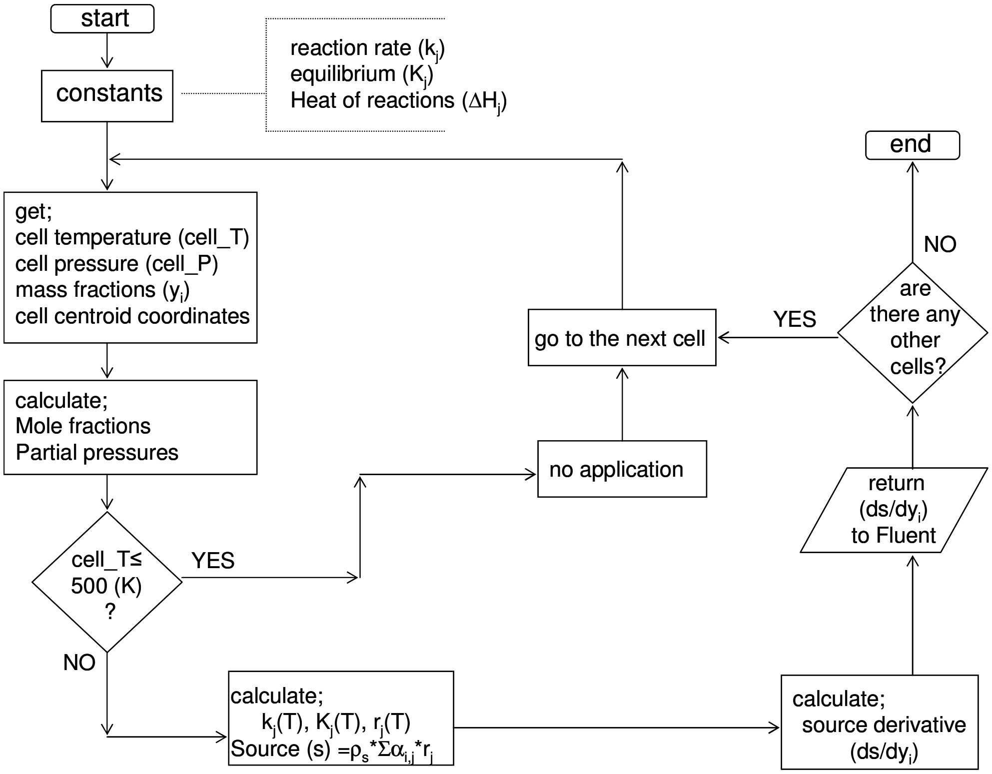

Figure 5.4 The algorithm for the species sinks/source calculations for diffusion /reaction application

The steps of the algorithm shown in Figure 5.4 were similar to the ones shown in Figure 4.13. One of the major differences was the mole fractions were not constant here, and they were calculated with the mass fractions that were obtained from the main computational domain by the code. The code has 5 sub-codes corresponding to energy term, and the terms for each species except the one with the largest mass fraction. Since the mass fraction of species must sum to unity, the Nth mass fraction was determined by N-1 solved mass fractions. When the species transport is turned on in the main computational domain of FLUENT, a list of the constituent species can be entered as fluid mixture. One has to keep in mind that the order of the species in that list is important. FLUENT considers the last species in the list to be the bulk species. Therefore, the most abundant species, that is the one with the largest mass fraction, must be set as the last one in the list (Fluent, 2005). In the MSR case this is water (H_2O).

The heat generation algorithm was similar to the species sinks/source one. The differences were; the source calculation where equation (5.1) was used instead of equation (4.4), and the derivative terms which were based on the temperature, not species mass fractions. The code is given in Appendix 3(c).

5.3 MSR diffusion/reaction application results

The full cylinders and 4-hole cylinders WS models were used for the MSR reaction implementation.

5.3.1 Full cylinders model

First, the flow results were obtained and compared to those from the solid particle model. Then, the reaction/diffusion application was done.

5.3.1.1 Flow simulation

To solve the momentum and turbulence equatios, the URF's at 0.05 less than the default values were used. The flow pathlines, released form the bottom surface for the porous particle model is shown in Figure 5.5(a). The pathlines are used to illustrate the flow for tube inlet conditions, and show the deflection of the flow around the porous regions. Flow features, such as regions of backflow and jet flow correspond to those in solid particle model shown in Figure 5.5(b).

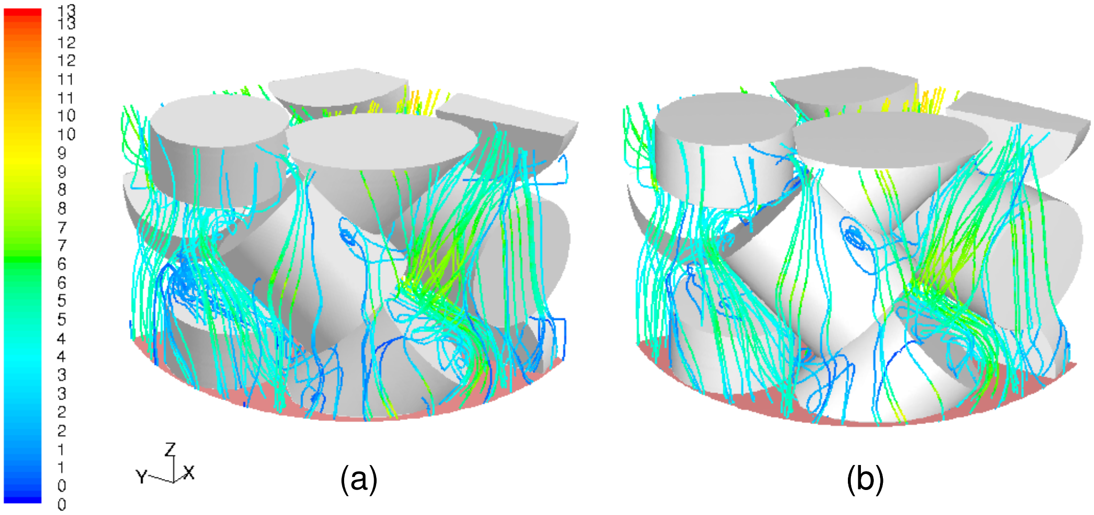

(a) (b)

Figure 5.5 The flow pathlines released from bottom, and colored by velocity magnitude (m/s) for (a) porous particle model, (b) solid particle model.

Additionally, middle plane velocity magnitude contours are shown in Figure 5.6(a) and 5.6(b) for porous particle and solid particle models respectively. The porous particle settings created very similar results to the solid particle simulations.

A quantitative comparison may be carried out by considering the radial profiles of axial velocities for both porous and solid particle models, which is shown in Figure 5.7. Note that, the velocity profiles for both cases were almost same. These results confirmed that the change in treatment of the particles did not induce any significant changes in the simulations.

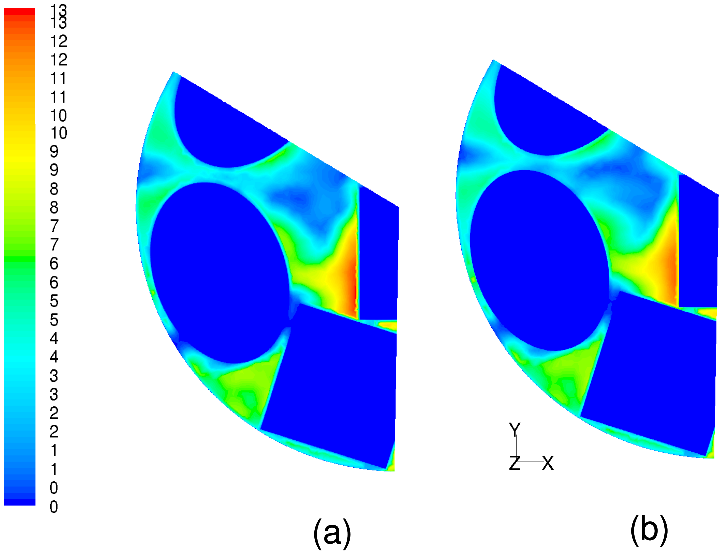

(a) (b)

Figure 5.6 The middle-plane view velocity magnitude contours (m/s) for (a) porous particle model, (b) solid particle model.

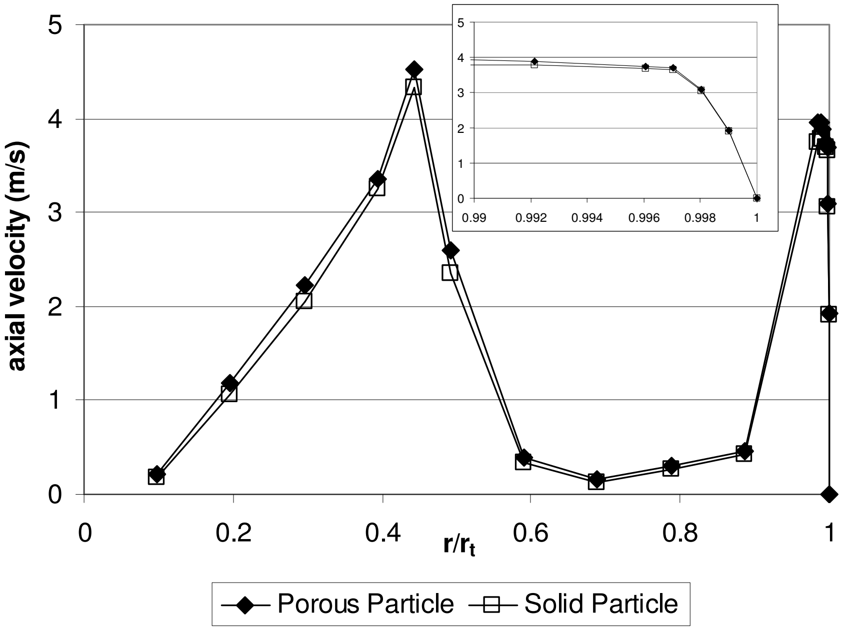

Figure 5.7 Radial profiles of axial velocities for porous and solid particle models.

5.3.1.2 Energy and species simulation

The energy and species balance equations were solved with URF's of 0.05 less than default values. For the converged solution, the residuals plot, the methane consumption rate for particle 2, and the heat balance plots are given in Appendix 6(a).

The diffusion/reaction implementation may be investigated by the variations of the temperature and species on the test particle surface and inside of the particle, by the radial profiles obtained for the entire model, and by the reaction engineering parameter effectiveness factor.

Particle surface variations: As a test particle, the particle number 2 surface temperature contours with the real position of the particle in the bed, and the open form of the surface are shown in Figures 5.8(a) and 5.8(b) respectively. The hotter spot on the front section of the particle 2 can be noticed as a result of the wall heat transfer. The open form of the particle 2 surface shows the significance of the wall heat transfer in a better way. The back surface of the particle 2 was 50 degrees colder than the front surface. As a result of the endothermic effects of the reactions, the lower surface temperatures have to be expected than the bulk fluid value (824.15 K). However, the tube wall heat transfer over-compensated for the endothermic effects of the reactions on the surfaces closest to the tube wall, which resulted in the hotter sections.

The cooler sections of the back surface may also be related to the relatively increased velocity field as shown in Figure 5.7 at $r/r_t \approx 0.40$. This particular radial position corresponds to the back of particle 2, and the heat transfer rate between the bulk phase and the particles in that region may be interrupted by the high velocity flow convection.

The local deviations on the particle 2 side surface are further shown for CH_4 and H_2 mass fractions in Figure 5.9. As can be noticed, the depletion in CH_4 results in the production in H_2. The local circular region which showed methane mass fraction minima, and corresponding hydrogen mass fraction maxima, at the S=0.03 m must be related to the vertex type of flow feature which occurred on that part of the surface.

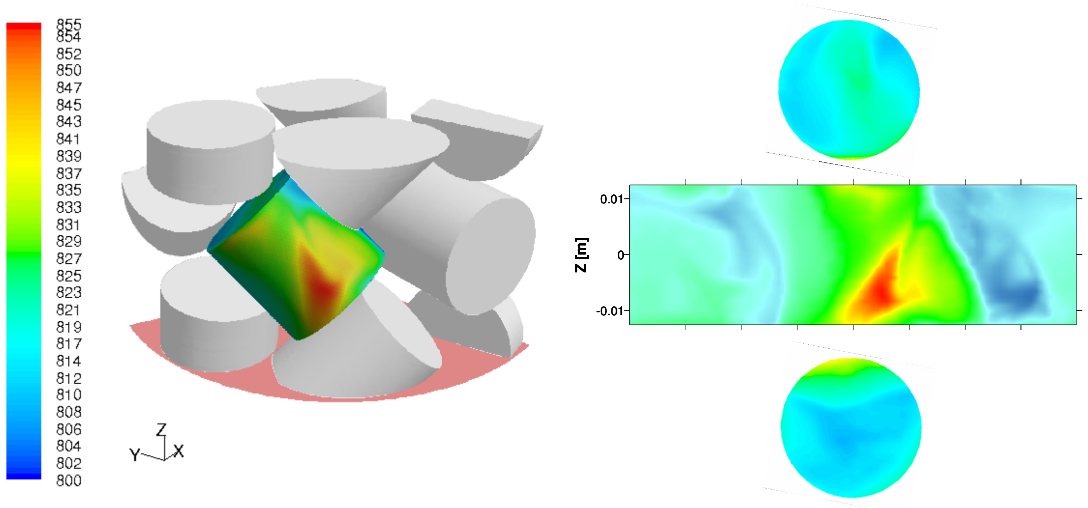

(a) (b)

Figure 5.8 The full cylinders particle 2 surface temperature contours (K) for (a) the position of the particle in the bed, (b) the open form of the surface.

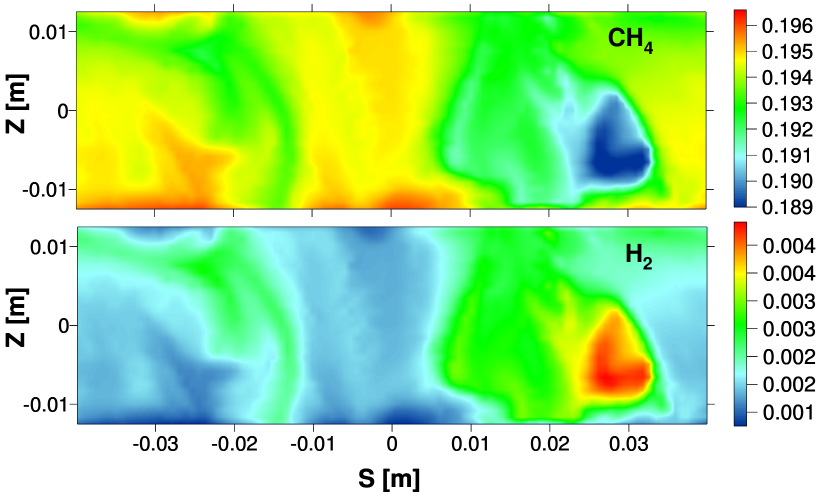

Figure 5.9 The full cylinder particle 2 side surface mass fraction contours for CH_4 and H_2.

The intra-particle variations: To investigate the intra-particle variations, the same vertical planes as used in Chapter 4 were utilized here, and shown in Figure 5.10(a).

In the figure, the radial center of the planes were scaled as the origin, and the two ends as r/r_p=-1.0 and r/r_p=+1.0, where r is the radial position in the particle, and r_p is the particle radius. In the axial direction, the origin was set to the lower corners, and the particle relative height was scaled as L/L_p=1.0 where L is the axial position in the particle, and L_p is the particle length.

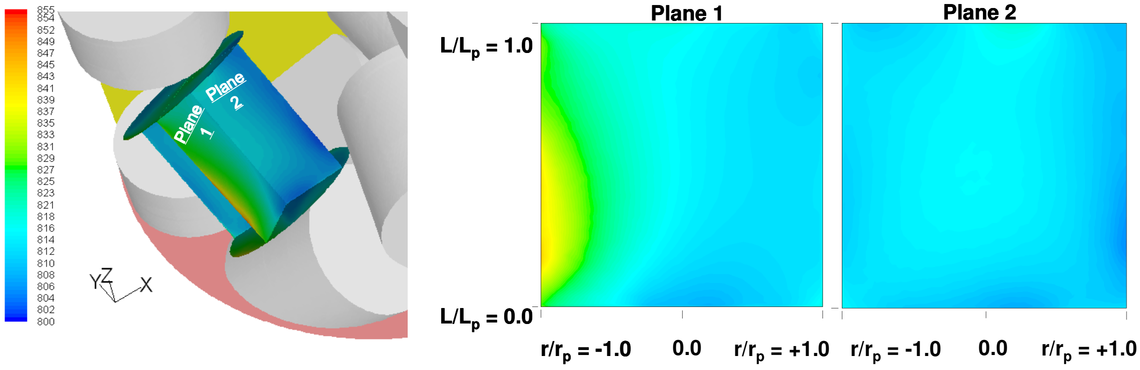

(a) (b)

Figure 5.10 (a) Visual planes to investigate the intra-particle variations, and (b) the temperature contours on those planes for full cylinders model.

At the r/r_p=-1.0 of the plane 1, which is the closest section of the particle to the tube wall, the temperature was very high. Note that, this high temperature region was not on the axial center, L/L_p=0.50, of the particle. This is because of the rotated position of the particle, and as a result of this rotation, the lower end of the particle was closest to the tube wall. For the other positions on the plane 1, the temperature did not vary so much. For the entire plane 2, approximately 10 degrees of temperature variation was observed.

Although we have shown the intra-particle temperature variation with the reaction heat effects approximation method (Figure 4.15), different intra-particle temperature fields were observed in Figure 5.10(b). If we compare the plane 1 contours, the hotter spots can be seen in both figures with qualitative and quantitative differences. Although in Figure 4.15 the contours were given for different activity levels, which affected the magnitude of the temperature, the hotter spot was located on the lower corner for every activity level. However, it was located at slightly higher position along the particle length for the contours obtained by the diffusion/reaction application approach. Additionally, on the hotter spots relatively lower temperature value was observed by the diffusion/reaction application method. These observations can be related to the methodologies behind the two approaches. The approximation method considers the uniform activity closer to the surface of the particle, and intra-particle temperature field is calculated with the constant bulk fluid species concentration values. On the other hand, the activity in diffusion/reaction application is defined by the physics, and temperature and species concentrations are calculated based on that. Obviously, considering the bulk species concentrations in the pellet, and setting the constant activity in the approximation method, creates a higher intra-particle temperature field for the reaction to proceed. However, if the concentrations are calculated according to the temperature filed, reaction again proceeds to reduce the reactants, and therefore reduce the intra-particle temperatures. In the diffusion/reaction application method the hotter spot was seen only at the closer point of the particle to the tube wall. However, in the approximation method the hotter spot on the lower corner of the particle was due to the combined effect of activity set on the side and on the bottom surfaces. The same effect was not seen on the top corner as standing relatively far from the tube wall.

As the benefit of diffusion/reaction application, the intra-particle species variations could also be investigated. Regarding the same visual planes, the CH_4 and H_2 mass fraction contours are shown in Figure 5.11.

As a result of the high temperature and corresponding reaction rate, a strong depletion of methane near the tube wall was observed in plane 1 contours of Figure 5.11. Accordingly, the increased hydrogen production was noticed on the same region. More uniform species distributions were observed in plane 2 contours as a consequence of very reduced near wall effects.

A more quantitative comparison can be obtained from the plots of CH_4 consumption rate, r_{CH4}, which is the sum of rates of reactions I and III, given in equations (1.72) and (1.74), as shown in Figure 5.12.

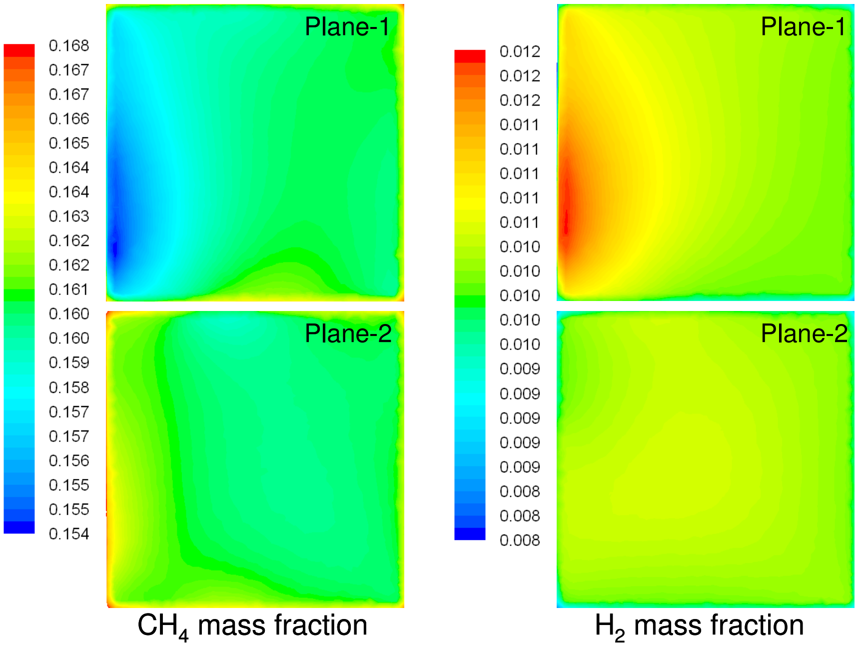

Figure 5.11 CH_4 and H_2 mass fraction contours on Plane-1 and Plane-2 for full cylinders model.

The plots show the change of CH_4 consumption rate along the length of the pellet for different radial positions. As can be seen from plane 1 plot, at the near wall region, the reaction rate was very high as a result of high temperature. For the radial positions away from the near wall region, the rates were reduced down. After the second half of the pellet, from r/r_p =0.0 to r/r_p =+1.0, the rates were almost the same.

Plane 2 reaction rates were almost the same for all radial positions with the same magnitude as the results obtained in the second half of plane 1. The main difference was seen at r/r_p=+0.97, where the CH_4 consumption rate was lower than the other radial position results. The lower temperature at that position, which is shown in Figure 5.9(b), created the lower reaction rates.

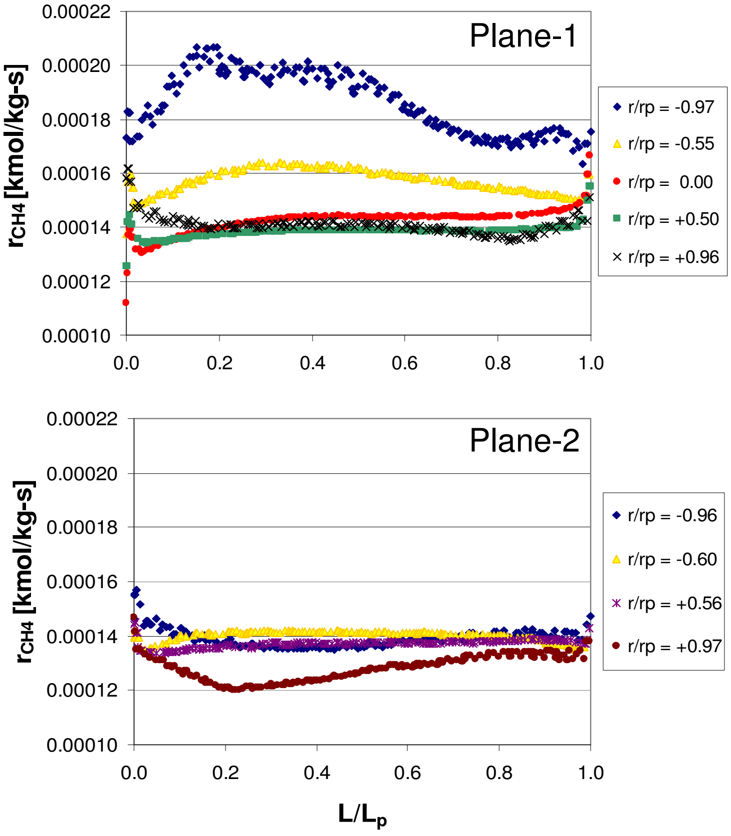

Figure 5.12 The CH_4 consumption rate plots for planes 1 and 2.

All the observations on plane 1 and plane 2 discussed here showed the strong temperature dependence of the MSR reactions.

The radial profiles: The radial temperature profiles, obtained similarly as described in Chapter 3, are shown in Figure 5.13. Additionally, temperature profiles for individual phases are shown in the same figure. The S-shape overall profile exhibits the combined effects of these phases along with the void fraction profile which is shown in Figure 4.18 previously for the full cylinders model.

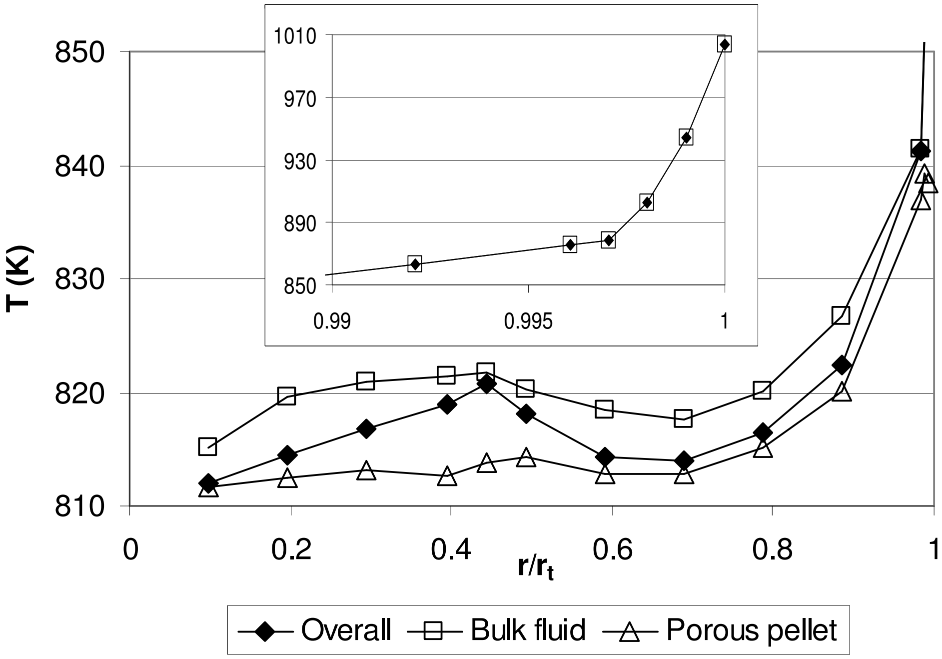

Figure 5.13 Radial temperature profiles, MSR full cylinders model.

The CH_4 and H_2 mass fraction profiles were also obtained for the same radial positions for which the temperature profile was obtained, and are shown in Figure 5.14. The strong S-shape overall CH_4 profile was observed which was again strongly influenced by the void profile. The bulk fluid values did not change much from the initial values. However, the overall mass fractions inside the pellet were influenced by the void fractions, especially for the radial positions of $r/r_t \approx 0.40$ and $r/r_t \approx 1.00$ where the maximum local voidage values were observed. The mirror effect can be noticed between the CH_4 and H_2 profiles as a result of the nature of the reactions: CH_4 is consumed and H_2 is produced.

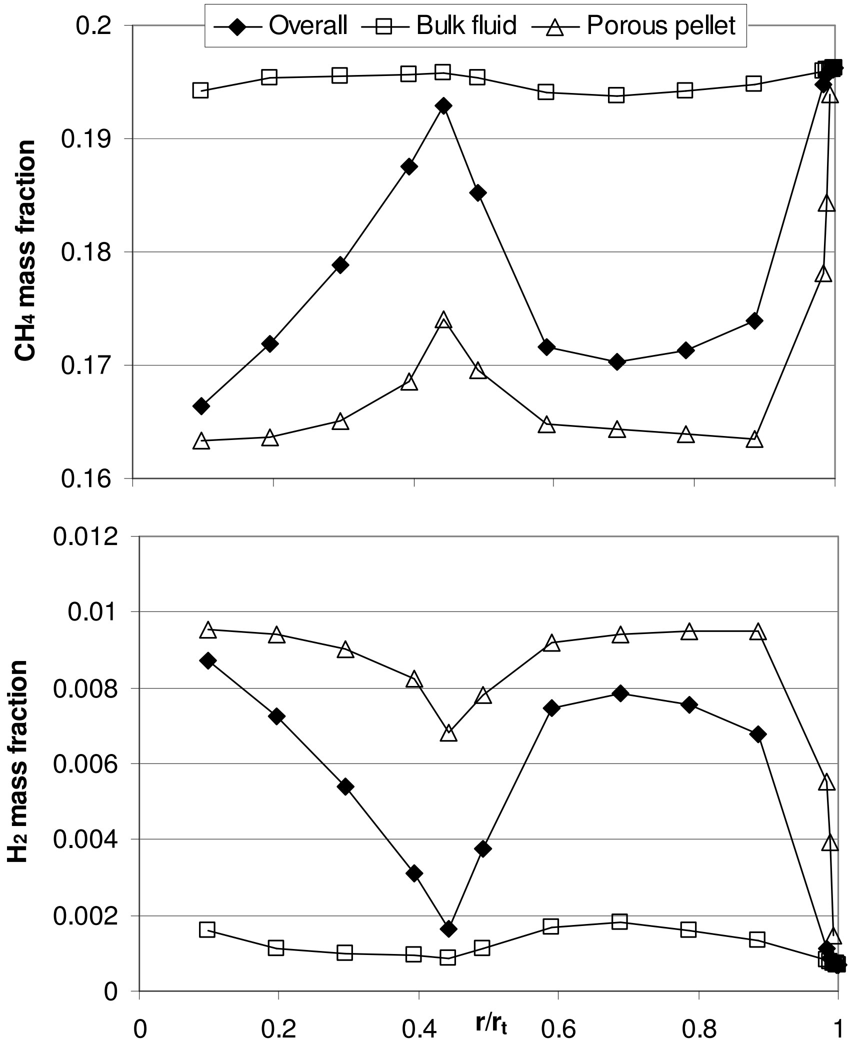

Figure 5.14 Radial CH_4 and H_2 profiles for full cylinders model.

The effectiveness factor: As described in Chapter 1 and defined in equation (1.54), the diffusion resistance on the reaction rate can be expressed with the effectiveness factor, η. It has been known that there are strong diffusion limitations on the MSR reaction, and most of the kinetic studies neglect them (Xu and Froment, 1989a). In the context of the requirements of quick analysis and process improvement implementations for todays design engineering environment, the concept of intra-particle gradients and effectiveness factor is quite valuable in reasoning and decision making (Rase, 1990).

To calculate the effectiveness factor, based on the definition, we needed the averaged reaction rate in the catalyst particle, and the reaction rate on the particle surface. For the reaction rate inside of the particle, the rates were calculated for each computational cell, and the volume averages were taken. This was done by a user-defined code, and it is given in Appendix 3(d) for the particle 2. The reaction rates were then returned to FLUENT and obtained from its user interface.

For the surface reaction rate calculation, the surface temperatures, and species mole fractions were exported in an ASCII file for each surface cell. Using this ASCII file, a spreadsheet was prepared to calculate the reaction rates for each cell, and then the area averaged values were obtained.

These calculations were carried out for the three reactions of interest, and the effectiveness factors for particle 2 were obtained by the equation (1.54) as:

$$\eta_{reaction-III} = \frac{1.01952\times10^{-5}}{1.21931\times10^{-4}} = 0.0836 \qquad \eta_{reaction-I} = \frac{8.43953\times10^{-7}}{5.20169\times10^{-6}} = 0.1622$$

$$\eta_{reaction-II} = \left|\frac{-1.47770\times10^{-7}}{2.43370\times10^{-7}}\right| = 0.6072$$

As can be noticed, the surface reaction rates were higher than the particle reaction rates, which results in the effectiveness factors of less than unity. It can also be noted that, the reaction-III is the dominant reaction as compared to the others, by an order of magnitude of the reaction rates. So, the low effectiveness factor for the dominant reaction is in agreement with the industrial observations (Stitt, 2005), and with the pseudocontinuum modeling results (Pedernera et al., 2003).

The reaction-II, which is known as the water-gas-shift reaction (WGSR), is strongly equilibrium limited due to the thermodynamic constraints at high temperatures. Therefore, there is a strong tendency to proceed in the reverse direction. The negative reaction rate obtained for WGSR in the particle was due to this phenomenon. However, the surface reaction rate was in the forward direction, which implied that the CO_2 and H_2 diffused to the bulk fluid more easily, and since the equilibrium level was not reached, the reaction proceeded in the forward direction which resulted in a positive reaction rate value.

In order to calculate the effectiveness factors for a pellet that is not affected by the tube wall, particle number 12 was additionally considered, although it was not entirely in the model. This particle is standing at the back of particle 2 at the same axial position as shown in Figure 5.15.

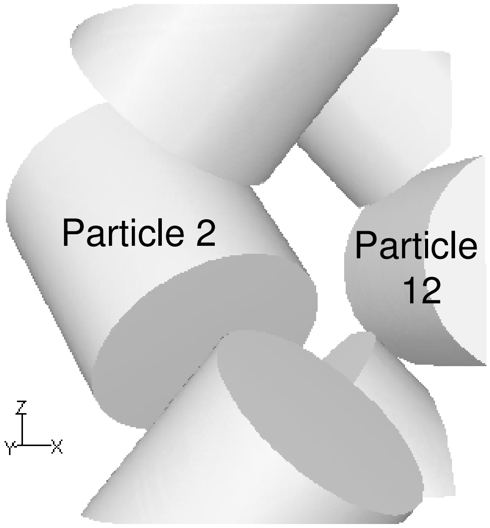

Figure 5.15 Particle 2 and 12 relative positions in WS model.

The reaction rates for particle 12 were calculated as described above and the effectiveness factors were found to be:

$$\eta_{reaction-III} = \frac{1.11173\times10^{-5}}{1.23545\times10^{-4}} = 0.1106 \qquad \eta_{reaction-I} = \frac{9.26538\times10^{-7}}{3.86538\times10^{-6}} = 0.2399$$

$$\eta_{reaction-II} = \left|\frac{-1.78318\times10^{-7}}{2.27753\times10^{-7}}\right| = 0.7829$$

When the effectiveness factors of particle 2 and particle 12 are compared, the higher values for the particle away from the wall can be noticed, although this difference was not too much.

The wall effect on the effectiveness factor, as an averaged reaction engineering parameter, may be utilized to obtain the radial effectiveness factor profiles for the entire model. Again, regarding the definition of the η, we needed the surface reaction rates for each radial position. For this reason, particle surface planes were created in addition to the available visual radial planes. In Figure 5.16(a) the previously generated radial plane is shown at $r/r_t = 0.89$ as an example case where the particles were colored by red, and the fluid was colored by yellow. The particle surfaces plane, which is shown in Figure 5.16(b) for the same radial position, was created considering only the outer shell intersections of the particles at the same radial position.

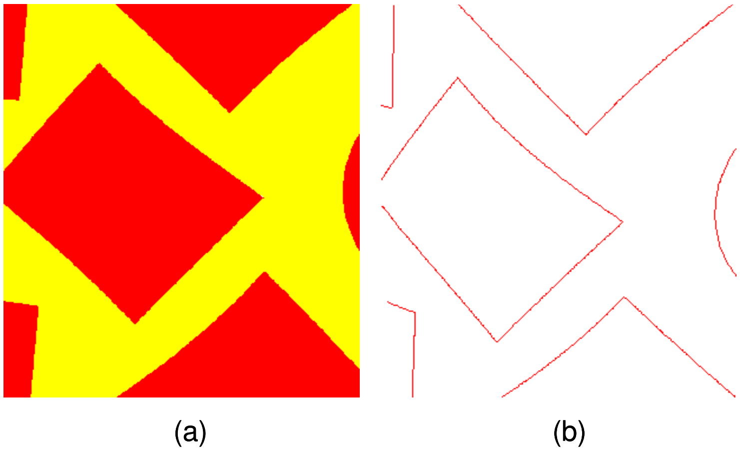

Figure 5.16 (a) the particle and fluid regions, and (b) the particle surfaces for the radial position of $r/r_t = 0.89$.

The temperatures and the species mole fractions were obtained from these surface planes for each radial position, and reaction rates were calculated on a spreadsheet. The obtained surface reaction rate radial profiles are shown in Figure 5.17 for reactions I and III. The increasing trend of the surface reaction rates can be noticed for both of the reactions towards the tube wall where the maximum values were reached. Figure 5.17 also represents the near wall effects on the particle surfaces which directly reflected to the surface reaction rates. Fluctuations were observed around the $r/r_t = 0.40$ position for both of the reactions. The reason for these changes can also be related to the local bed voidages. The reaction rates had to be calculated utilizing the temperature and species information for the less solid surface area in the related radial positions. Therefore, the area averaged values were more sensitive to the maximum or minimum values as a result of their contribution to the final averaged value.

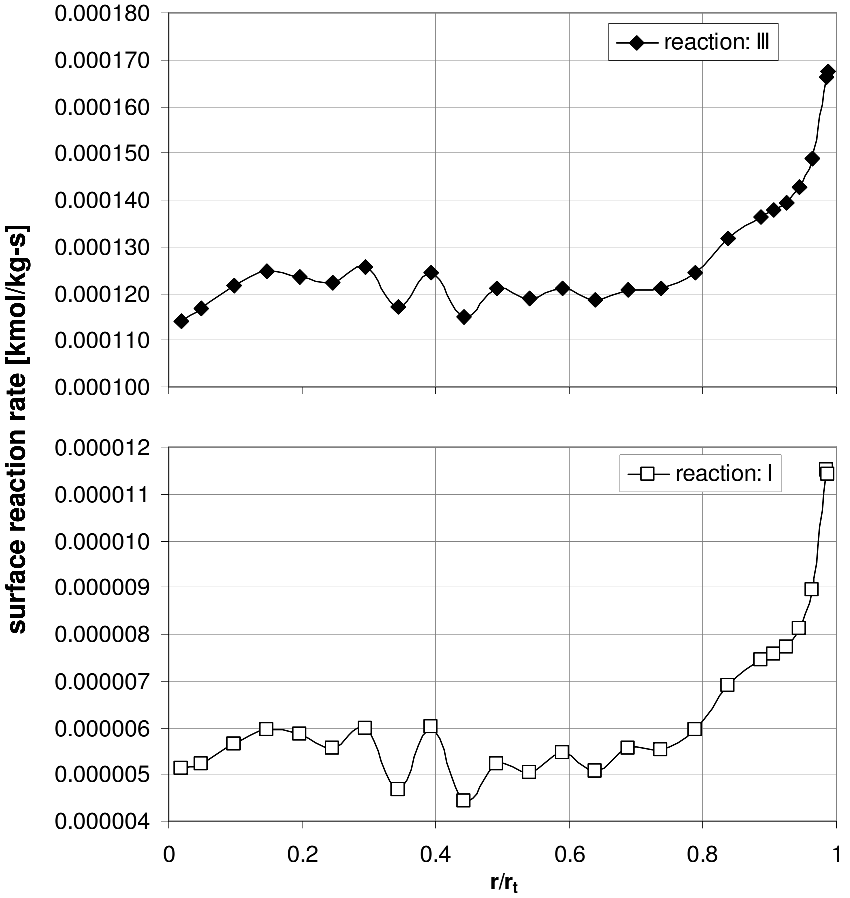

Figure 5.17 The surface reaction rate profiles for reactions I and III.

To obtain the radial effectiveness factor profiles, a representation of the reaction rate profile inside the pellets was necessary. The available pellet reaction rates for particles 2 and 12 were utilized for this purpose. If the particle 2 reaction rate is considered as the pellet reaction rate closest to the wall, and the particle 12 reaction rate is considered as the pellet reaction rate at the center of the tube, the reaction rate profile may be obtained by the following expression:

$$r_{pellet}(r) = r_{particle\_2} \times \frac{r}{r_t} + r_{particle\_12} \times (1 - \frac{r}{r_t}) \qquad (5.2)$$

where r is the radial position in the reactor tube, r_t is the tube radius. According to this expression the pellet reaction rate profiles were obtained as linear curves.

Utilizing the pellet and surface reaction rate profiles, the effectiveness factor profiles were obtained as shown in Figure 5.18.

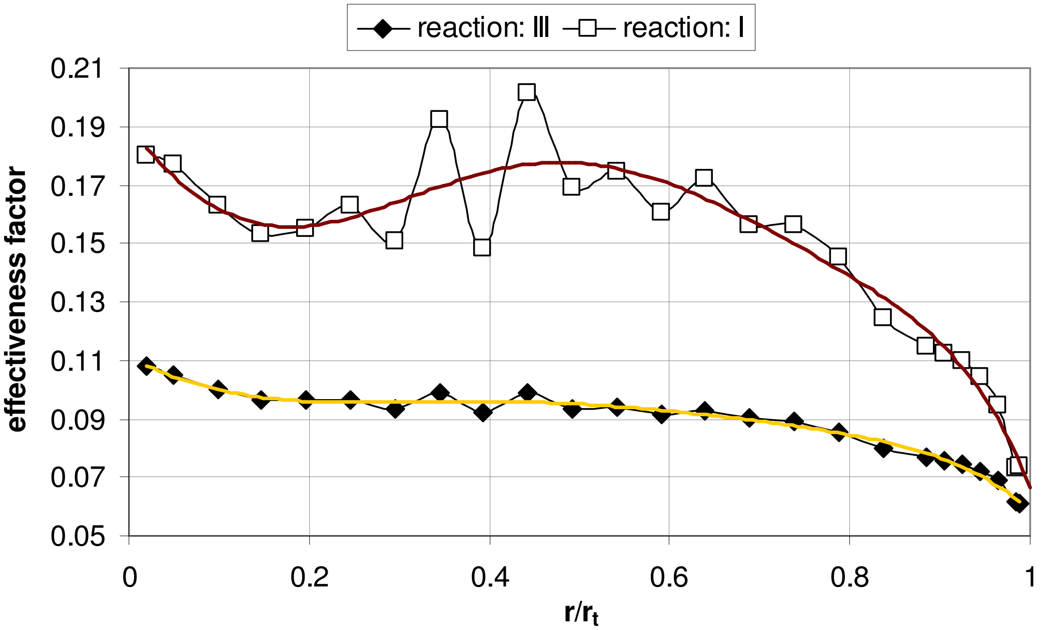

Figure 5.18 The effectiveness factor profiles for reactions I and III.

The polynomial trend-lines were added to the above figure with a yellow color for reaction III, and a red color for reaction I. Towards the near wall region, the effectiveness factors decreased for both reactions as a combined effect of surface reaction rate shown in Figure 5.17, and pellet reaction rates calculated by equation (5.2). Higher effectiveness factors of reaction I than reaction III were observed, although they came closer in the near wall region.

The other method of obtaining the pellet reaction rate profile may be to consider the step change in pellet reaction rates instead of setting a linear change as described above. This can be done by considering particle 12 reaction rate from $0.0 \leq r/r_t < 0.5$, and particle 2 reaction rate for $0.5 \leq r/r_t \leq 1.0$ as the pellet reaction rate profile. Then, the effectiveness factor profiles can be obtained with the same surface reaction rate values used above. The comparison of the effectiveness factor profiles obtained by a linear and by a step change in the pellet reaction rates is shown in Figure 5.19 for only the dominant reaction.

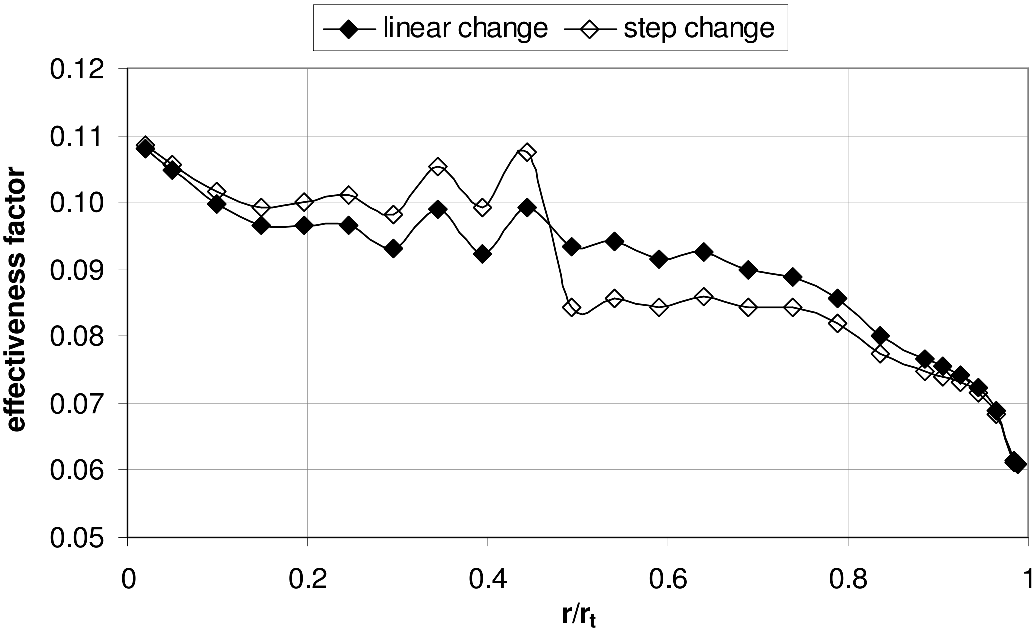

Figure 5.19 The effectiveness factor profiles for reaction III with linear and step change in pellet reaction rates.

As can be seen in Figure 5.19, the step change effect is noticeable in the center of the model, and there was not a smooth transition as in the linearly varied one. However, in total, the trends were quite similar in both cases.

There is an order of magnitude difference observed in effectiveness factors obtained by us and Pedernera et al. (2003) where they have focused on the axial middle location of the reactor. The methodological difference was that, we have utilized the realistic 3D flow field around the explicitly positioned realistic catalyst particles, and considered the interactions between the bulk fluid and the pellets in our modeling. However, Pedernera et al. considered the pseudocontinuum approach to make one-dimensional particle simulations, as summarized in Chapter 2.

We will make use of our effectiveness factor profile in Chapter 6 where we will compare the results obtained in this chapter with the explicitly created pseudocontinuum model.

5.3.2 4-hole cylinder model

As in the full cylinders model simulations, first the flow solution was obtained, and then the reaction/diffusion was applied.

5.3.2.1 Flow simulation

The flow simulation was carried out by solving the momentum and turbulence equations as before. The URF's were selected as 0.05 less than the default values. The flow pathlines, released from the bottom surface are shown in Figure 5.20.

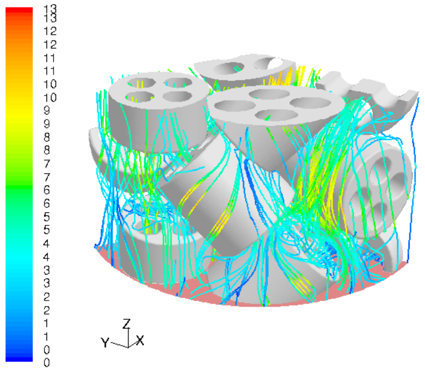

Figure 5.20 The flow pathlines released from bottom, and colored by velocity magnitude (m/s) for 4-hole model.

5.3.2.2 Energy and species simulation

To reach the converged energy and species simulation, iterations were started with the URF values of 0.05 for 3000 iterations. After the residuals were flattened out, the factors were increased to 0.20 for 500 iterations. Then, they were raised to 0.50 for 500 iterations more. Finally the simulations were completed with the URF's of 0.80, totally in 21000 iterations. The residuals plot, the methane consumption rate for particle 2, and heat balance change during the iterations are given in Appendix 6(b).

Particle surface variations: The surface temperature contour of particle 2 is shown in Figure 5.21(a) for the exact location of the particle in the bed, and in Figure 5.21(b) for the open form of it.

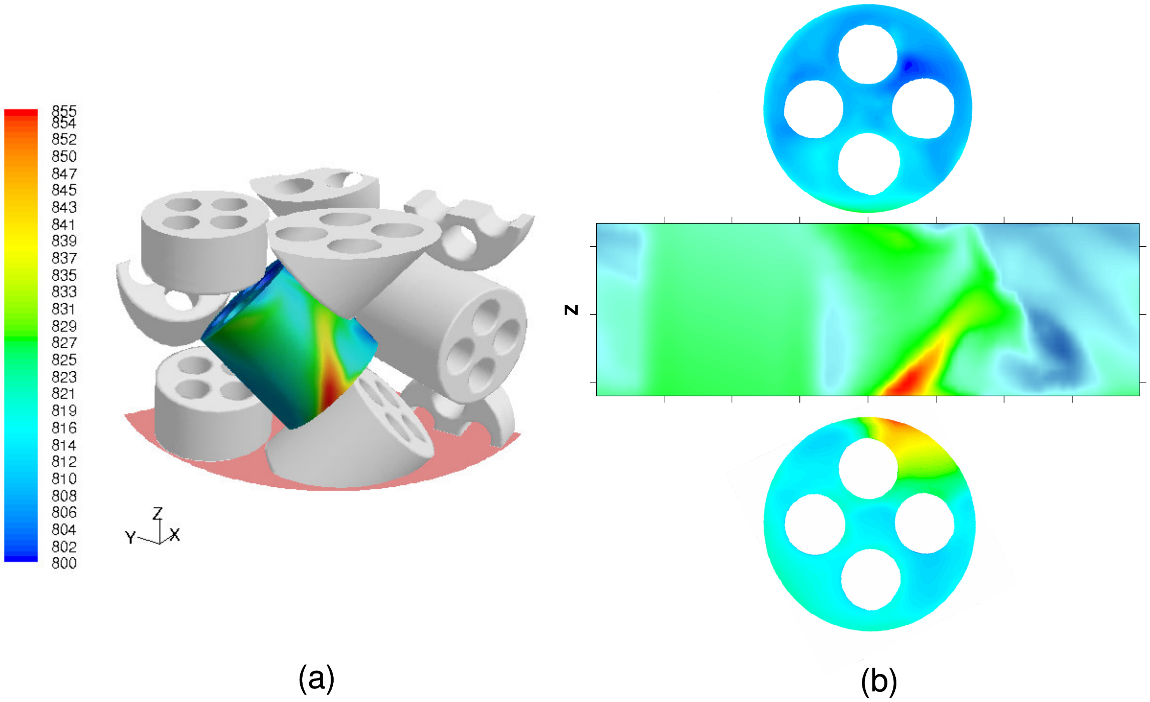

Figure 5.21 The 4-holes particle-2 surface temperature contours (K) for (a) the position of the particle in the bed, (b) the open form of the surface.

The hotter section on the particle surface for the closest point to the tube wall can be noticed for this model in a slightly less pronounced way as compared to the full cylinders model shown in Figure 5.8. The hotter section originated from the lower corner of the particle, and propagated upwards with the flow convection. The related hotter region of the particle bottom surface can be seen in the open form of the surface, and mostly the closest internal hole to that section was influenced by the wall effect. This situation may be clearly seen in Figure 5.22. The internal hole that was affected by the tube wall is shown with a dashed line bordered rectangle.

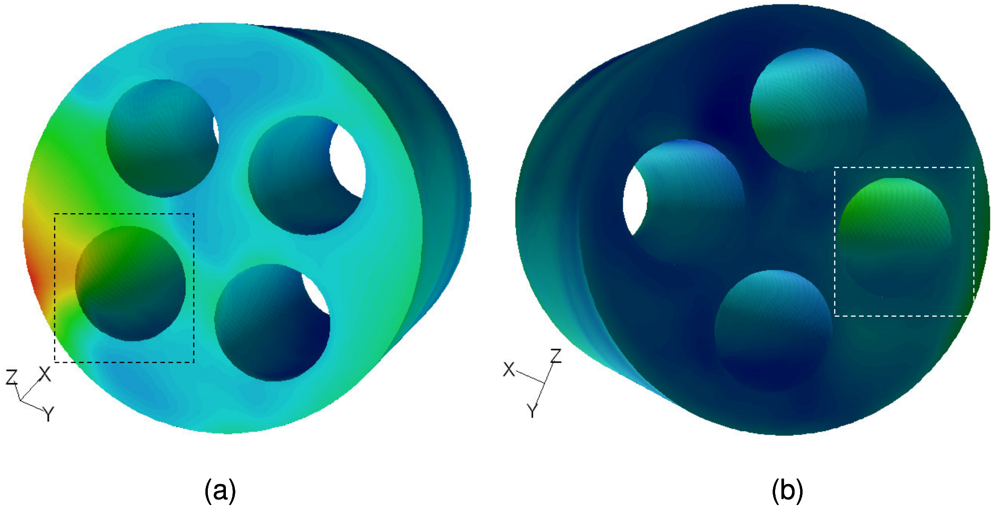

(a) (b)

Figure 5.22 The 4-hole cylinders model particle 2 detailed view (a) bottom, (b) top.

Previously, the flow field comparison of the models with different sizes and numbers of internal holes was investigated (Nijemeisland, 2002), and it is not the scope of our work. On the other hand, to emphasize the benefit of multi-hole catalyst particles regarding the diffusion/reaction taking place in them, the above observation may be coupled to the Figure 5.23 where the pathlines passing through the holes of the particle 2 are shown. In Figure 5.23(a), the pathlines are colored by the velocity magnitude which represents the different velocity fields inside the holes, whereas in Figure 5.23(b), they were colored by the static temperature which shows the temperature difference of the fluid passing through the holes. The hole with the hotter surface, shown in Figure 5.22, is represented by the dashed lines in Figure 5.23. Although the velocity passing through that hole was higher than the other holes, the fluid heated up while passing through that hole. This was achieved by conduction from the inside wall of that hole to the fluid, and by convection in the fluid. Ultimately, these phenomena are triggered by the tube wall heat transfer. Increasing the particle fluid contact area, or GSA, with introducing multiple holes, and effects of transport phenomena may be further investigated by intra-particle temperature and species variations.

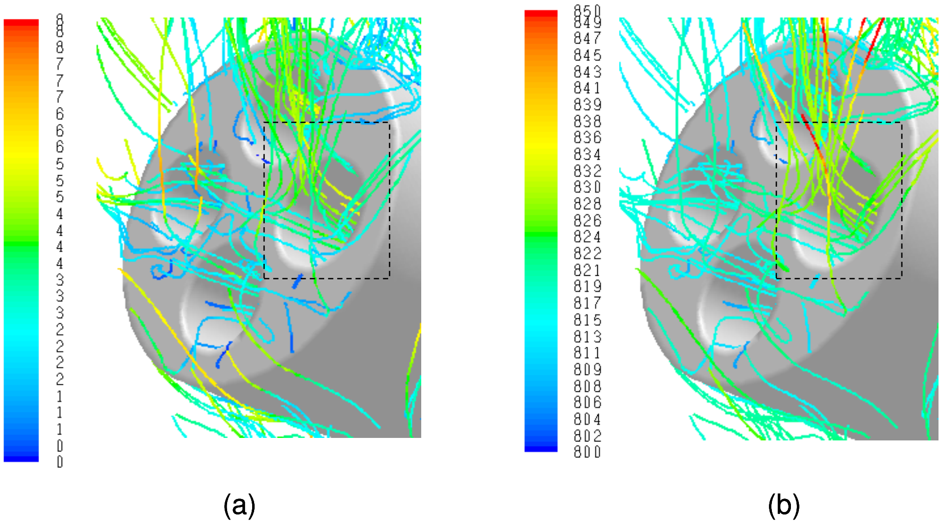

Figure 5.23 The pathlines of flow passing through the holes of particle 2, colored by (a) the velocity magnitude (m/s), and (b) the static temperature (K).

The intra-particle variations: To investigate the intra-particle temperature and species variations, the 45 degree rotated versions of plane 1 and plane 2 along the particle axis were generated as plane 3 and plane 4 which intersect the internal holes in the model. The plane 1 and plane 2 temperature contours are shown with their original positions in Figure 5.24(a), and with the transformed versions in Figure 5.24(b).

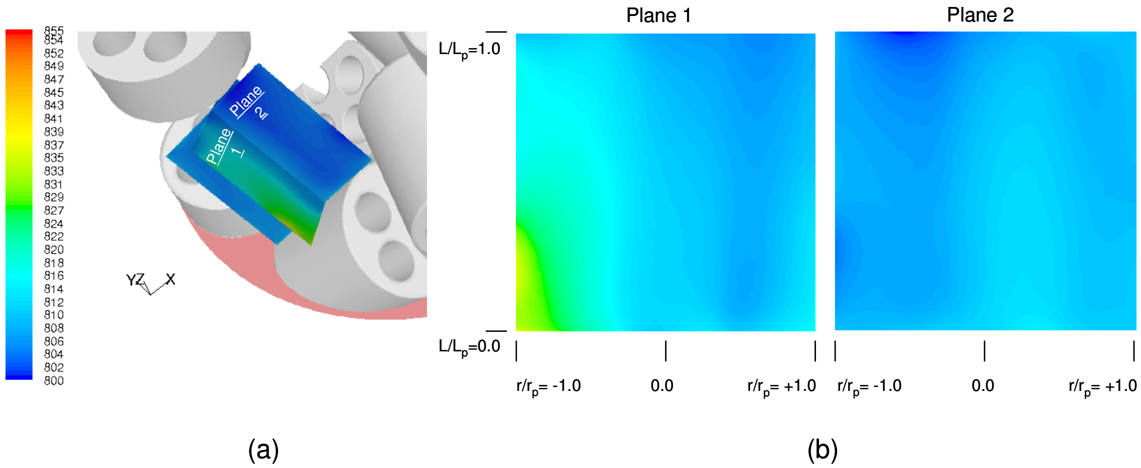

Figure 5.24 (a) Visual planes 1 and 2 to investigate the intra-particle variations, and (b) the temperature contours on those planes for 4-hole cylinders model.

The maximum temperature was reached on the lower left corner of plane 1, and the particle gradually cooled down towards the inside of it due to the reaction heat effects. The relatively cooler and hotter longitudinal patterns were seen on the planes in Figure 5.24(b) as a result of the contribution of the surfaces of the inner holes located close by. Additionally, the CH_4 and H_2 mass fraction contours on the same planes are shown in Figure 5.25. The strong methane depletion and hydrogen production can be noticed on the lower left corner of the plane 1 where the higher temperature region was seen in Figure 5.24(b). Right after that, at the position $r/r_p \approx -0.5$, the sudden increase in CH_4, and a decrease in H_2 mass fractions were observed with a small spot on the bottom of plane 1. This position was very close to the nearest hole, and plane 1 was almost intersected by that hole. Therefore, the species mass fractions were influenced by the bulk fluid values in that point. Since the intra-particle temperature value at that position was similar to the fluid temperature, we have not seen a difference in the temperature contour.

The plane 2 CH_4 and H_2 contours can be directly supported by the temperature contours. At the position of $-1.0 < r/r_p < 0.0$, as a result of the lower temperatures, the higher methane and lower hydrogen mass fractions were seen. However, the effects of increase in temperature at $0.0 < r/r_p < 0.5$ on the methane and hydrogen quantities were noticeable.

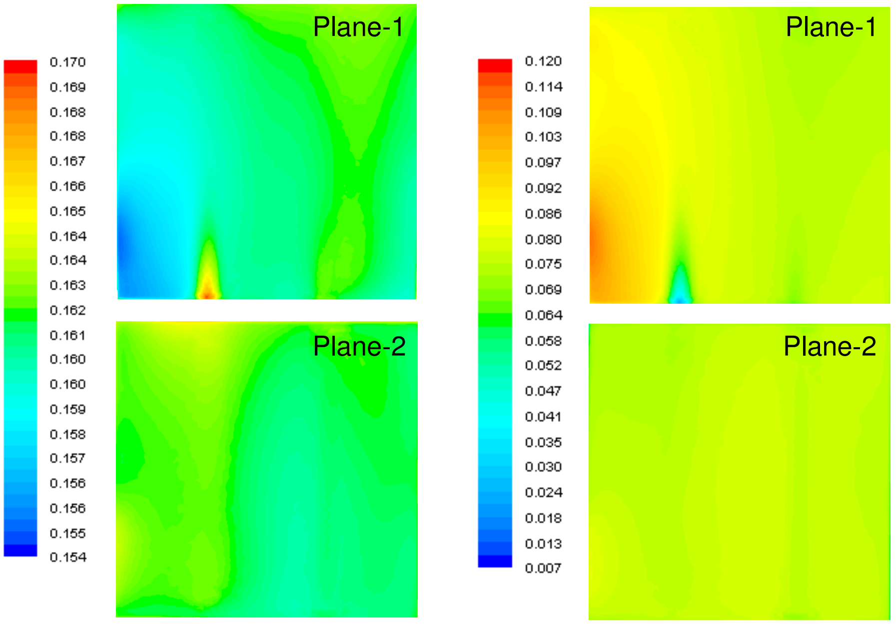

CH_4 mass fraction

H_2 mass fraction

Figure 5.25 CH_4 and H_2 mass fraction contours on Plane-1 and Plane-2 for 4-hole cylinders model.

The plane 3 and plane 4 temperature contours are shown in Figure 5.26. These planes were created at the positions where the holes are intersected almost at their centers. The temperature difference of different holes can be seen well here as a supporting argument to the above. Fluid passing through the closest hole to the tube wall has the higher temperature. The temperature of the catalyst region closest to the tube wall was also higher.

The species distributions on planes 3 and 4 are presented in Figure 5.27. Note that the scales are different in plane 3 and 4 than plane 1 and 2 in order to capture the fluid values. It was observed that, the fluid region mass fractions mostly stayed at the inlet conditions. From the fluid to the pellet regions, a sharp transition was noticed due to the strong diffusion limilations.

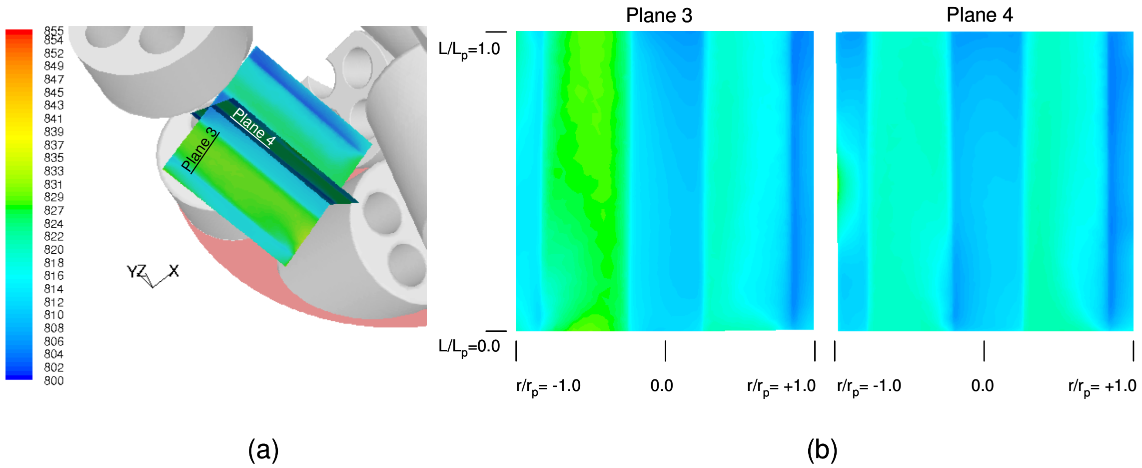

Figure 5.26 (a) Visual planes 3 and 4 to investigate the intra-particle variations, and (b) the temperature contours on those planes for 4-hole cylinders model.

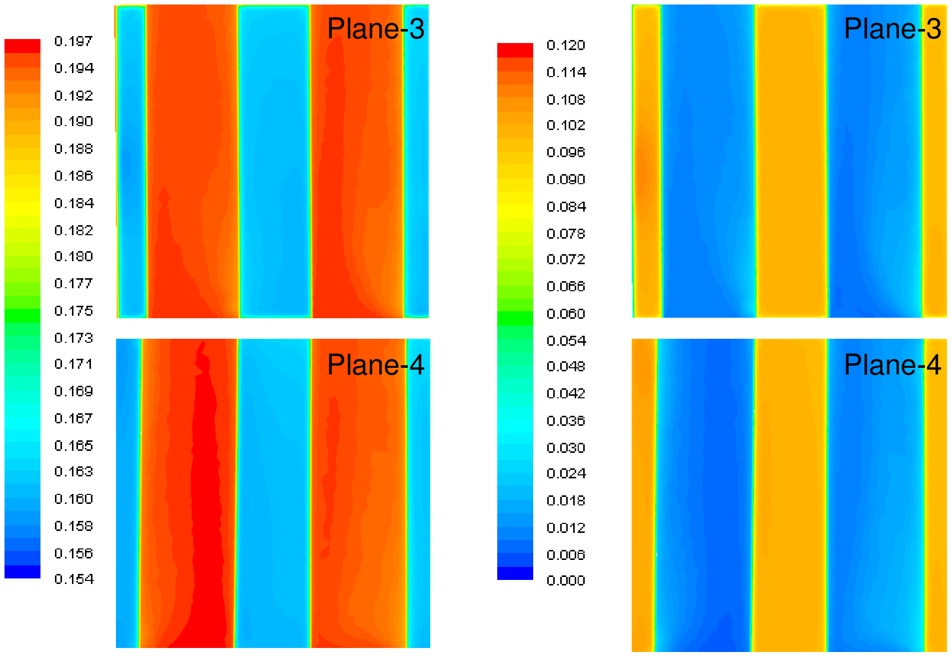

CH_4 mass fraction

H_2 mass fraction

Figure 5.27 CH_4 and H_2 mass fraction contours on Plane-3 and Plane-4 for 4-hole cylinders model.

The radial profiles: As in the full cylinders case, similar radial profiles were obtained. In Figure 5.28 the overall (pseudohomogeneous), and fluid and solid region temperature profiles were shown. Again, a similar combined effect of the fluid and solid regions was observed on the overall profile with the local porosity influence. Additionally, the overall temperature profile was lower than in the full cylinders model, as in the case of the reaction approximation discussed in Chapter 4.

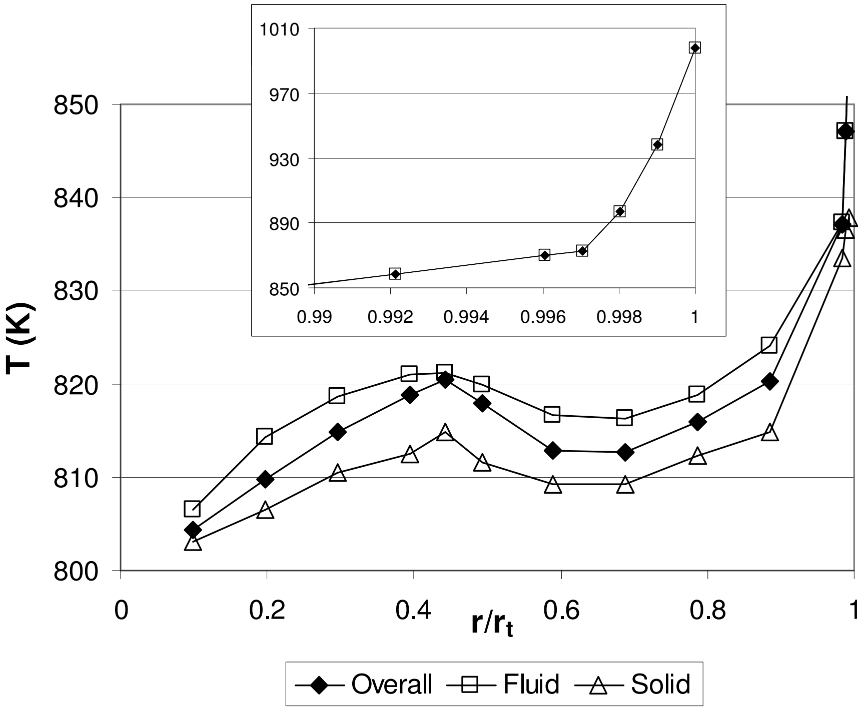

Figure 5.28 Radial temperature profiles, MSR 4-hole cylinders model.

The CH_4 and H_2 mass fraction profiles are presented in Figure 5.29. Similar features are observed in the species profiles with the full cylinders, except the noticeable difference in the overall profiles in the region $0.6 < r/r_t < 0.9$. The bed porosity profiles of full and 4-hole cylinders were shown in Figure 4.16, and there was a significant difference in that region: the 4-hole cylinders model had a higher voidage than the full cylinders. As a result of that, the fluid region compositions influenced the overall species profiles to create higher CH_4 and lower H_2 contents in $0.6 < r/r_t < 0.9$.

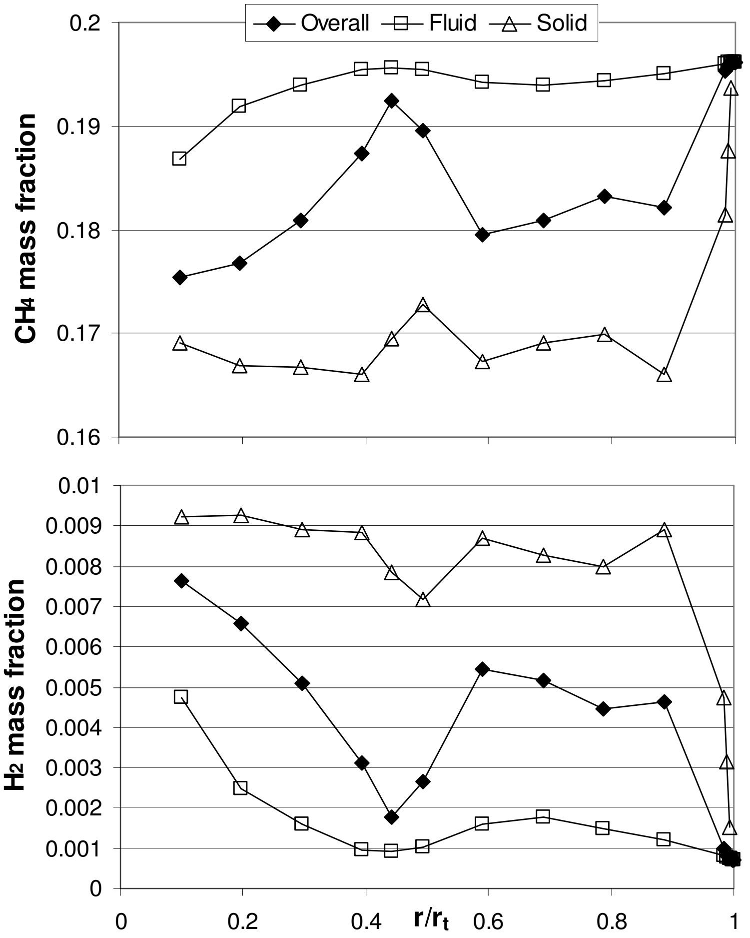

Figure 5.29 Radial CH_4 and H_2 profiles for 4-hole cylinders model.

The effectiveness factor: For the 4-hole cylinders model particles 2 and 12, the effectiveness factors were obtained with the same procedure described for the full cylinders model. For reactions I and III, the values are found to be:

Particle 2

$$\eta_{reaction-III} = \frac{2.51065\times10^{-5}}{1.14770\times10^{-4}} = 0.21875 \qquad \eta_{reaction-I} = \frac{1.85686\times10^{-6}}{4.50823\times10^{-6}} = 0.41250$$

Particle 12

$$\eta_{reaction-III} = \frac{2.13930\times10^{-5}}{1.12563\times10^{-4}} = 0.19005 \qquad \eta_{reaction-I} = \frac{1.60310\times10^{-6}}{4.94254\times10^{-6}} = 0.32430$$

At a first glance, we have obtained higher effectiveness factors for the front particle than for the back particle, contrary to the findings of the full cylinders model. Probably for 4-hole cylinders model, particle 12 is not the best choice to consider as a representative back particle. Since particle 12 was not entirely in the model, the section where inner holes were located stayed outside of the model, and we did not see the effect of the inner holes on the surface reaction rates, and ultimately on the effectiveness factors.

When we compare the effectiveness factors of reaction III for 4-holes and full cylinders models, we see a 260% increase due to the 66% GSA improvement with inner holes inclusion.

5.4 Introducing PDH diffusion/reaction application and results

The PDH diffusion/reaction implementation was applied only to the full cylinders model by the same procedure utilized in the MSR reaction application. The user-defined code created for this purpose is given in Appendix 3(e).

The flow solution was obtained for 4000 s^{-1} Gas Hourly Space Velocity (GHSV) (Jackson and Stitt, 2004) at steady-state condition which corresponds to the Reynolds number of 350 based on superficial velocity and the particle diameter of a sphere of equivalent volume to the cylindrical particle. Although, in general, this value is quite low to be considered as in the turbulent region, the complex flow field in fixed bed reactors has been modeled with different turbulent schemes by many researchers for even lesser Reynolds number values (Romkes et al., 2003; Guardo et al, 2004). We have selected the RNG κ-ε turbulence scheme with EWT approach for this study.

The flow solution was obtained by URF's of 0.05 less than default values and the flow pathlines are shown in Figure 5.30. Relatively smooth flow features were observed as a result of the lower superficial velocity setting.

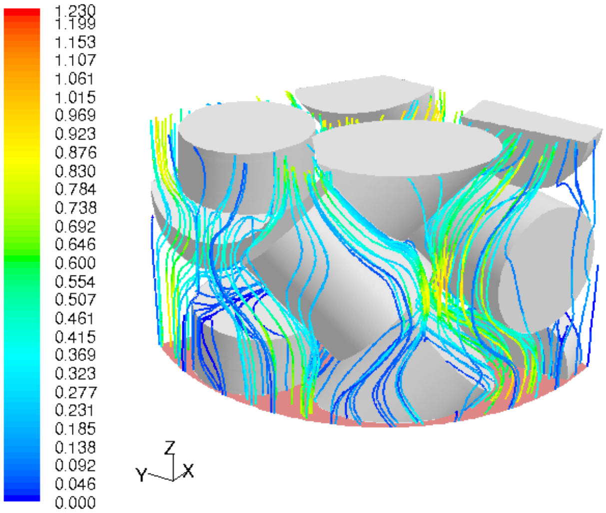

Figure 5.30 Flow pathlines released from bottom, and colored by velocity magnitude (m/s) for PDH reaction.

The PDH diffusion/reaction implementation was carried out with two different diffusion coefficient settings as described before. For the dilute approximation method, the pre-calculated $D_{i.m}$ values were defined, whereas for the M-C method, the binary diffusivities, D_{ij}, were set into the materials menu of FLUENT, and $D_{i.m}$ values were calculated by FLUENT with equation (1.26). The main difference in these two methods was that the pre-calculated $D_{i.m}$ values were obtained by us from molecular and Knudsen diffusivities for dilute approximation method, whereas, the $D_{i.m}$ values were calculated by FLUENT from the mass fractions and binary diffusivities only for M-C method. As mentioned before, these values are given in Appendix 5(b).

The diffusion/reaction application results are compared for particle surface variations, intra-particle variations, and effectiveness factors

Particle surface variations: The test particle surface temperature contours are shown in Figure 5.31. Thirty to forty degrees higher surface temperatures were obtained by the dilute approximation method. Significantly hotter sections along the particle axis were noticed on the front of the test particle as opposed to the hotter spots seen at the lower corner of the test particle in the MSR reaction applications.

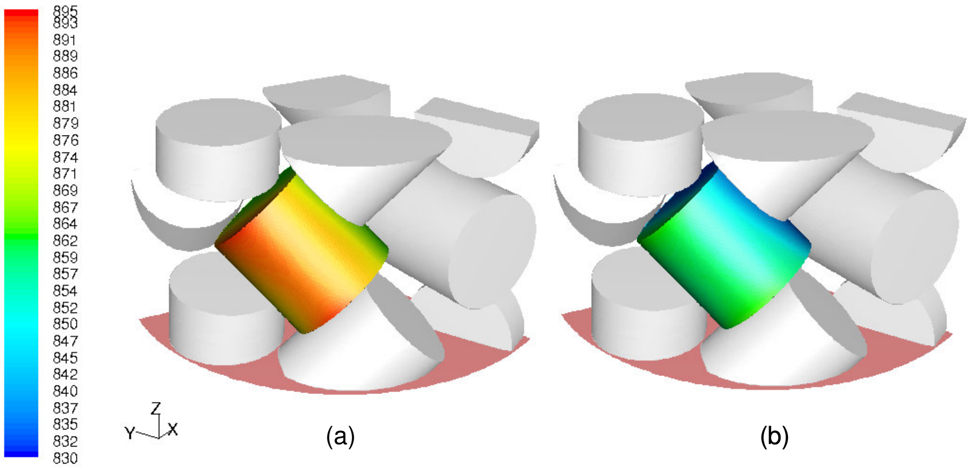

Figure 5.31 Surface temperature contours (K) obtained with the simulations by (a) dilute approximation method, and (b) M-C method.

The intra-particle variations: Figure 5.32 shows the intra-particle temperature variation on planes 1 and 2 for both cases.

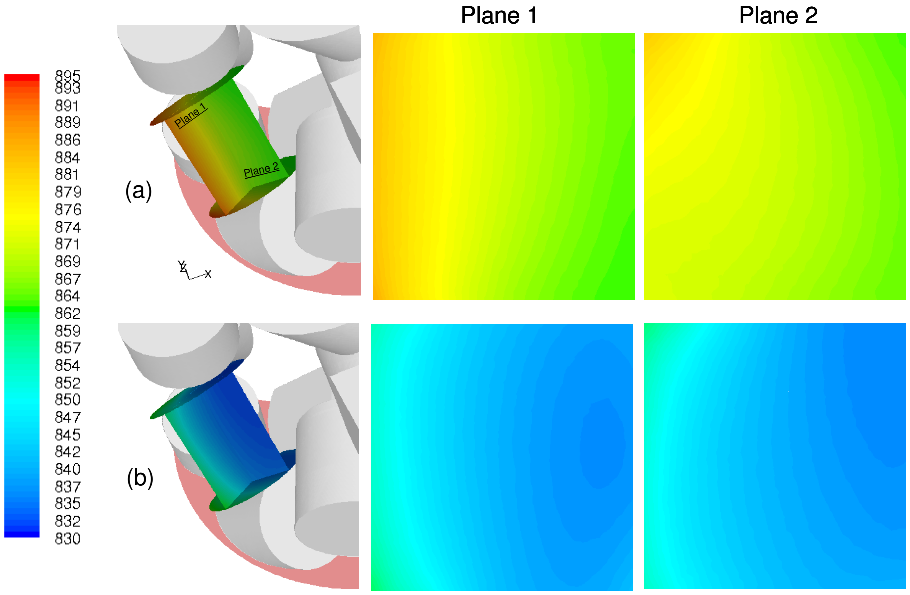

Figure 5.32 Intra-particle temperature contours (K) on the planes 1 and 2 for the simulations of (a) dilute approximation method, and (b) M-C method.

Plane 1 temperature contours of the dilute approximation, as shown in Figure 5.32(a), presented a uniform axial transition throughout the particle. On the other hand, the intra-particle temperature transition was different in the M-C method; the corners stayed at higher temperature, but the central location in the axial direction was cooled down more. The plane 2 contours were similar, and the left section of the particle was hotter than the right section in that plane for both cases. The tube wall heat transfer effect was not expected there; however, due to the lower velocity observed in the fluid near to that part of the surface which did not create a strong resistance between fluid and solid, the temperature stayed relatively closer to the bulk value.

The surface and intra-particle temperatures were lower for the results obtained by the M-S method where 80% more heat uptake was observed.

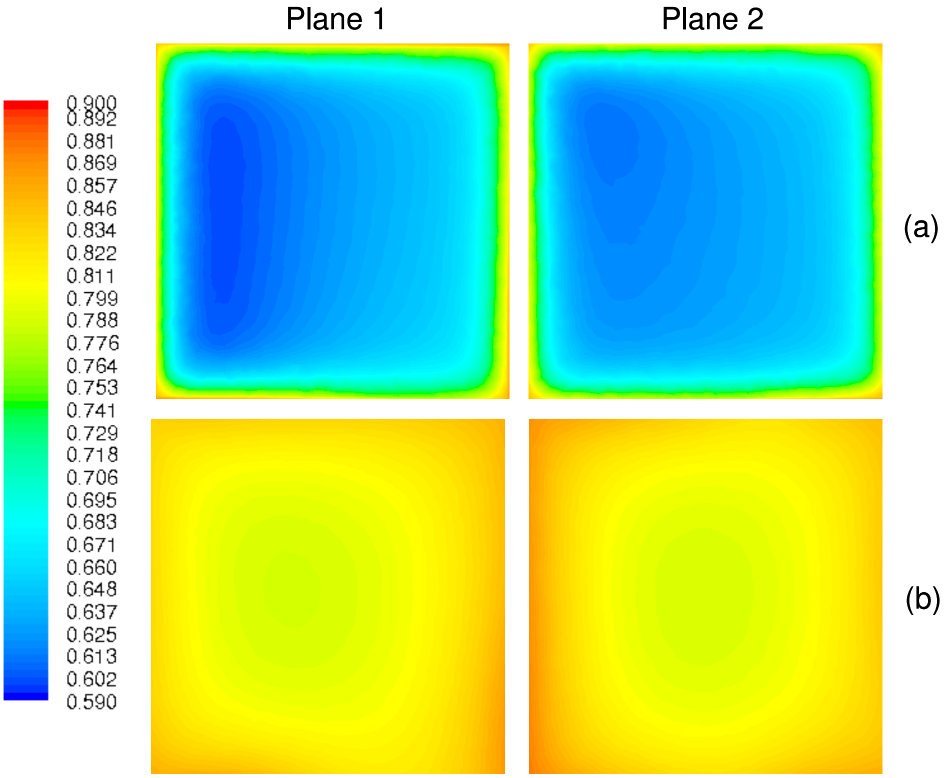

Figure 5.33 Intra-particle C_3H_8 mass fraction contours on the planes 1 and 2 for the simulations of (a) dilute approximation method, and (b) M-C method.

The propane (C_3H_8) mass fraction contours are shown in Figure 5.33 for planes 1 and 2 for both cases. As in the temperature contours, there were significant differences for C_3H_8 mass fraction qualities and quantities for both cases. As a result of high intra-particle temperatures observed for dilute approximation simulations, the C_3H_8 consumption rate was high, and lower mass fractions were observed in most of the particle. The reaction mostly took place in the outer region of the particle; therefore a sudden change was seen in that region. The near wall effect was noticed in the particle close to the tube wall along the particle axis in plane 1. The M-C method simulation results, on the other hand, were quite different, and lower C_3H_8 consumption rate was observed which resulted in higher C_3H_8 mass fraction contours on both planes. The reaction took place inside of the particle not in the outer shell, which presented the higher activity level of the particle with M-C method. Additionally, a more uniform C_3H_8 distribution was seen with the simulations carried out with M-C diffusion method.

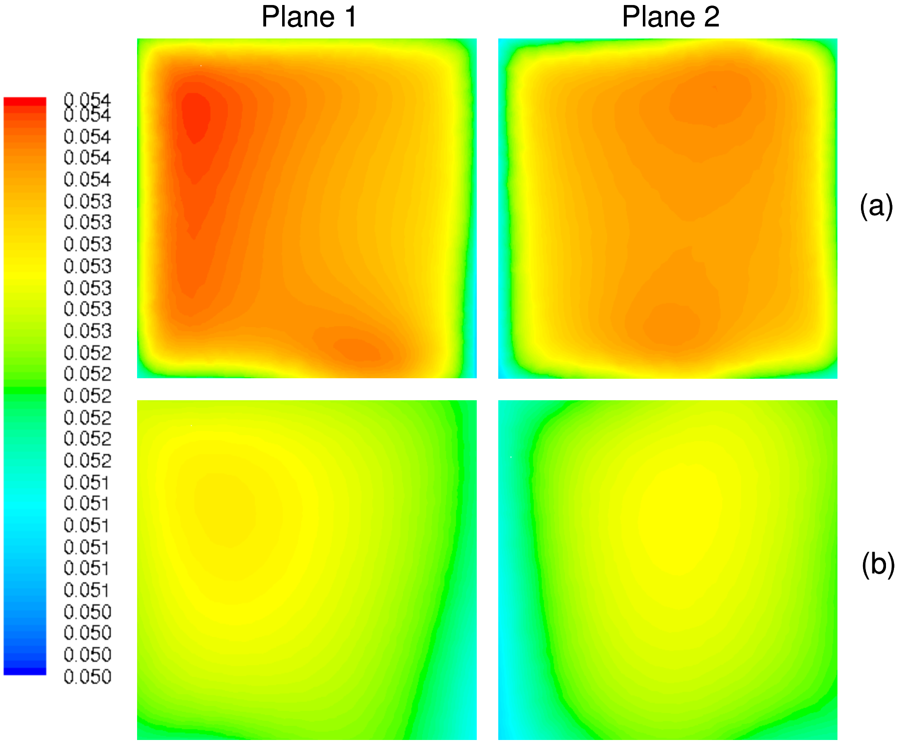

Figure 5.34 Intra-particle H_2 mass fraction contours on the planes 1 and 2 for the simulations of (a) dilute approximation method, and (b) M-C method.

The hydrogen production rate may be compared with the H_2 contours on the same planes for both cases. As expected, more hydrogen production was observed mostly in the outer shell with the dilute approximation method. Whereas the hydrogen mass fractions were low, and the particle was mostly active through its center with the M-C method. However, the H_2 distribution was not as uniform as the C_3H_8 distribution.

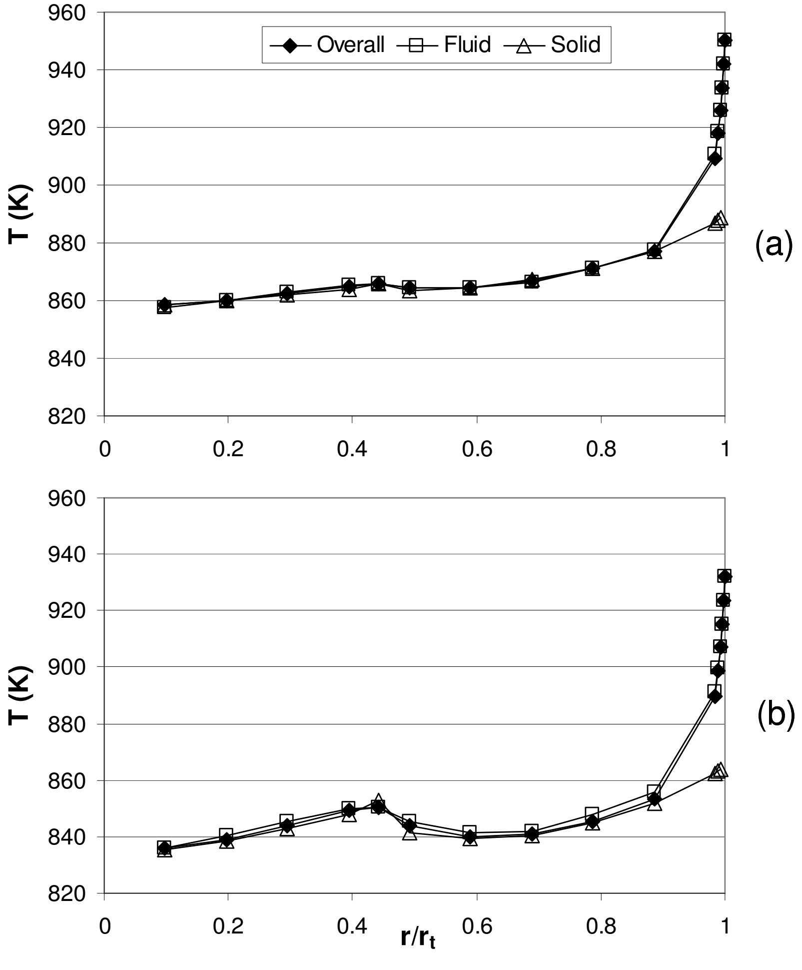

Figure 5.35 Radial temperature profiles for PDH with (a) the dilute approximation, and (b) M-C method simulations.

The radial profiles: As shown in Figure 5.35(a) and (b), the dilute approximation method temperature profiles were higher than the M-C method results as a supporting observations of temperature contours. For the dimensionless radial position 0.0< r/r_t <0.9, there were no differences in solid and fluid phase profiles, and in overall profile as a consequence, with the dilute approximation method. There was some difference seen in M-C method results. However, the main discrepancy was noticed in the near wall region between the solid phase and the fluid and overall phase results for both methods. The heat is transferred from the tube wall, and is not carried up as efficiently with the flow convection due to the low velocity flow field. Therefore fluid temperatures stayed high, and as a result of the heat sinks in the solid region due to the endothermic nature of the reaction, solid temperatures kept low in the near wall region. The overall temperatures were almost the same as the fluid phase values in that region, because of having very high local bed voidages explicitly in that area.

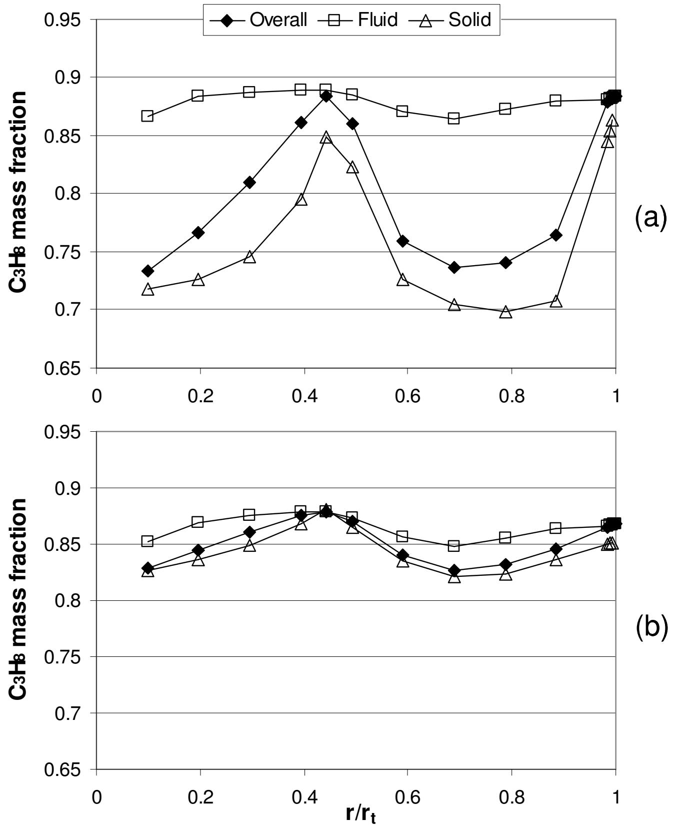

Figure 5.36 Radial C_3H_8 mass fraction profiles for PDH with (a) the dilute approximation, and (b) M-C method simulations.

The propane mass fraction radial profiles are shown in Figure 5.36. At a first glance, strong “S” shape overall and solid region profiles were seen for the dilute approximation results as well as a strong difference between the fluid and solid profiles. Local high voidages at r/r_t =0.44 and r/r_t =0.98 affected the solid phase and overall profiles to create local maxima. The solid and fluid phase profiles were close to each other in M-C method application. These profiles can be coupled to the contour graphs shown in Figure 5.33. The sudden change in the C_3H_8 mass fractions contour graph was noticeable in the radial profiles presented in the Figure 5.36(a) for the dilute approximation method, and the moderate change in the M-C method contour graph was predictable from the radial profiles shown in Figure 5.36(b).

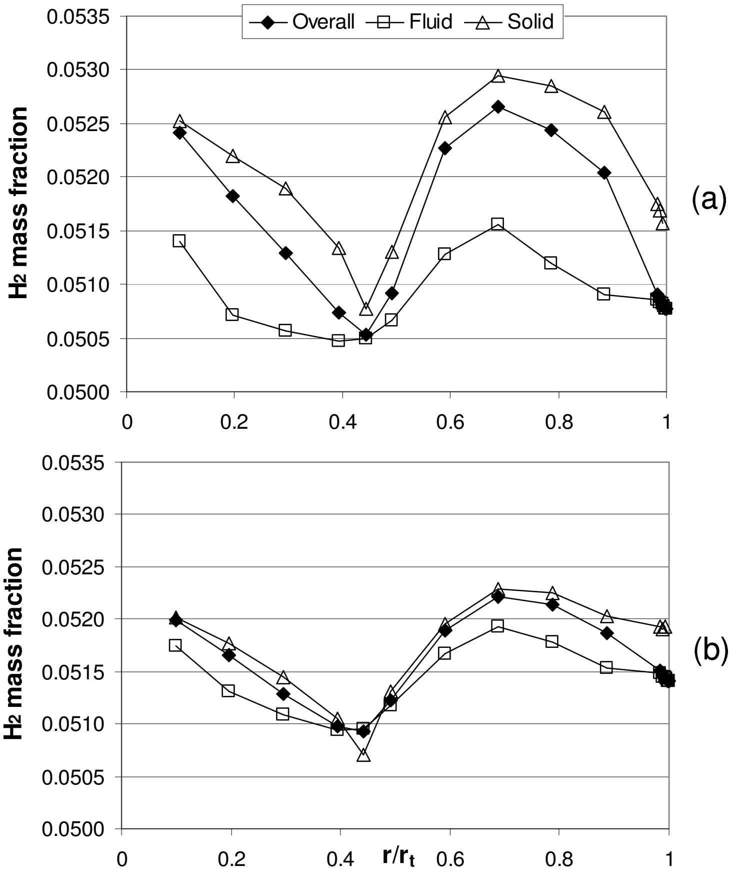

Figure 5.37 Radial H_2 mass fraction profiles for PDH with (a) the dilute approximation, and (b) M-C method simulations.

The hydrogen mass fraction profiles are presented in Figure 5.37. Similar observations were made as for the propane mass fraction profiles, and closer fluid and solid region profiles were seen in the M-C method results. As expected, there was a relation between the hydrogen contour graph and mass fraction profiles shown in Figures 5.34 and 5.37(b).

The effectiveness factor: For dilute approximation method and M-C method results, the effectiveness factors were calculated for front (particle 2) and back (particle 12) particles.

The dilute approximation

$$\eta_{particle-2} = \frac{1.17374\times10^{-3}}{4.86436\times10^{-3}} = 0.2410 \qquad \eta_{rparticle-12} = \frac{1.22889\times10^{-3}}{4.23179\times10^{-3}} = 0.2900$$

M-C method

$$\eta_{particle-2} = \frac{1.89617\times10^{-3}}{2.74443\times10^{-3}} = 0.6910 \qquad \eta_{rparticle-12} = \frac{2.10446\times10^{-3}}{2.66879\times10^{-3}} = 0.7885$$

The higher effectiveness factors were obtained with the M-C method results than the dilute approximation method by almost a factor of 2.8. The effectiveness factor values can be coupled to the intra-particle contours and radial profile observations.

To understand the reason of having different effectiveness factors with dilute approximation and M-C method, the relative sizes of the molecules must be considered. The C_3H_8 and C_3H_6 molecules are alike each other, and much bigger than the H_2 molecule (almost 9 times in molecular volumes). Therefore, the C_3H_8/H_2 and C_3H_6/H_2 binary diffusivity values are much bigger than the C_3H_8/C_3H_6 one. Note that, for the dilute approximation, the effective diffusivities are calculated by considering the molecular and Knudsen diffusivities. So, in dilute approximation case, Knudsen diffusion dominates the effective diffusivity calculations. However, for the M-C method, the effective diffusivities are calculated utilizing the binary diffusivities where molecular difference plays an important role. Therefore, the calculated effective diffusivities for dilute approximation method are order of magnitude smaller than the ones calculated by

FLUENT with only binary diffusivities as given in Table 5.2. As a result of this difference, higher particle effectiveness for M-C method was obtained.

Table 5.2 Effective diffusivities used in different cases (m^2/s)

	Dilute approximation	M-C
$D_{C_3H_8,m}$	4.2×10^{-6}	8.2×10^{-5}
$D_{C_3H_6,m}$	3.7×10^{-6}	5.0×10^{-5}
$D_{H_2,m}$	1.9×10^{-5}	2.9×10^{-4}

Since the species molecular sizes are comparable to each other for MSR reaction compounds, there were no differences observed between the results of different diffusivity settings, and therefore only dilute approximation results were shown in the previous section.

As expressed in the PDH reaction introduction given in Chapter 1, and in the literature overview in Chapter 2, this reaction has been mostly investigated with the coke formation in modeling studies regarding different reactor types than the one used here to increase the yield and conversion. On the other hand, this reaction has been known with the high effectiveness factor, or with the high particle activity (Jackson and Stitt, 2004), and this was the main reason that we have considered this reaction in our study to implement our diffusion/reaction application to a different activity level reaction than the MSR. Although we have not considered different features of this reaction as described above, based on our observations the M-C method may be considered as more suitable selection for diffusive flux modeling in the PDH reaction.

5.5 Conclusions

The diffusion/reaction implementation method has been applied to two different reactions, MSR and PDH, and two different geometrical models with full and 4-hole cylinders packings.

The MSR reaction application results showed strong temperature gradients and induced species fields within the wall particles. Strong diffusion limitations affected the temperature and species parameters to create non-symmetric and non-uniform fields. All these observations were contrary to the conventional assumptions used in reactor modeling. Based on our observations the usage of conventional modeling methods may result in mis-evaluations of reaction rates, and ultimately the design considerations may be affected such as the mis-prediction of the tube lives.

The PDH reaction was considered to study the reaction with lower diffusion limitations. Based on the different diffusion coefficient settings, different particle activity levels, or effectiveness factors were obtained. Regarding the larger molecular sizes of propane and propene as compared to hydrogen, the realistic diffusion modeling would be achieved by the multi-component method where the effective diffusivities calculated by the binary diffusion coefficients.

6. Pseudo-continuum Modeling

The representative reactor models with valid parameters can be invaluable tools for the decision making processes during the design and operation. In real world problems, on the other hand, the time constraints and economic facts force some compromise with ideal models to establish the suitable procedures in design and operation. Therefore up to the present, several types of models have been developed to satisfy the operating conditions as summarized in Chapter 1.

In reality the fixed bed reactor character is heterogeneous, regarding the fluid flow between the catalysts, the transport processes between the fluid and catalyst, and reaction taking place on the catalyst pores. The major flow is in the axial direction, and energy flow can be in both axial and radial directions with the influence of wall heat transfer (Rase, 1990). However, due to the mentioned constraints, to minimize these complexities, simplified models such as pseudo-continuum (P-C) models have been used. Basic reactor simplifications, besides the presented pellet behavior in Figure 5.1, may be additionally illustrated in Figure 6.1 for endothermic conditions.

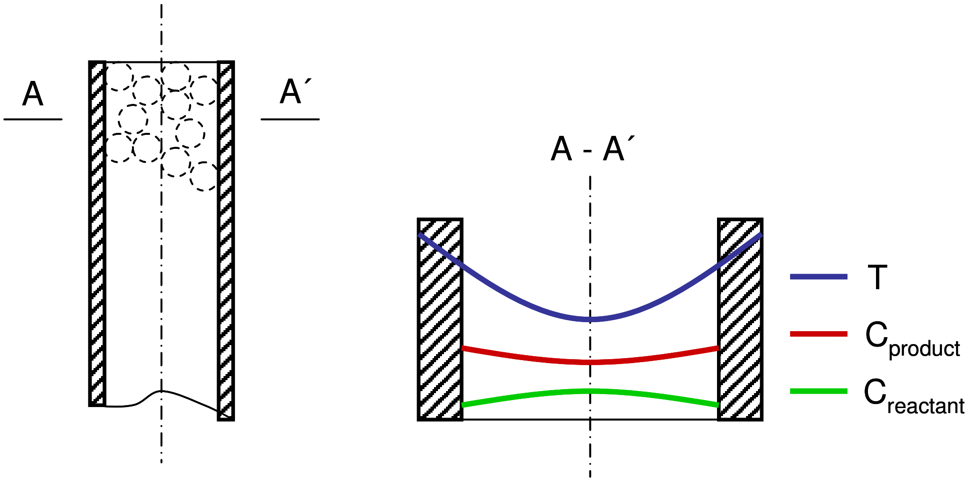

Figure 6.1 Basic reactor simplifications for the endothermic conditions (Re-produced from Rase, 1990).

As presented in the sketch, endothermic reaction heat is removed at the center of the tube, which means that the radial gradient of temperature mostly exists on the tube wall. Because of this gradient, concentration gradients will also occur.

The fluid behavior is usually considered with a constant superficial velocity, or with some general smooth shape radial velocity profiles through the packed bed. For large N (tube-to-particle diameter ratio) tubes, the deviation from a constant velocity is confined to only a small fraction of the cross-section adjacent to the tube wall. Whereas, for the low N tubes, a substantial portion of the cross-section is affected by the wall. A representative plot is shown in Figure 6.2 regarding the flat, correlation based, and DPM results based radial profiles of axial velocities.

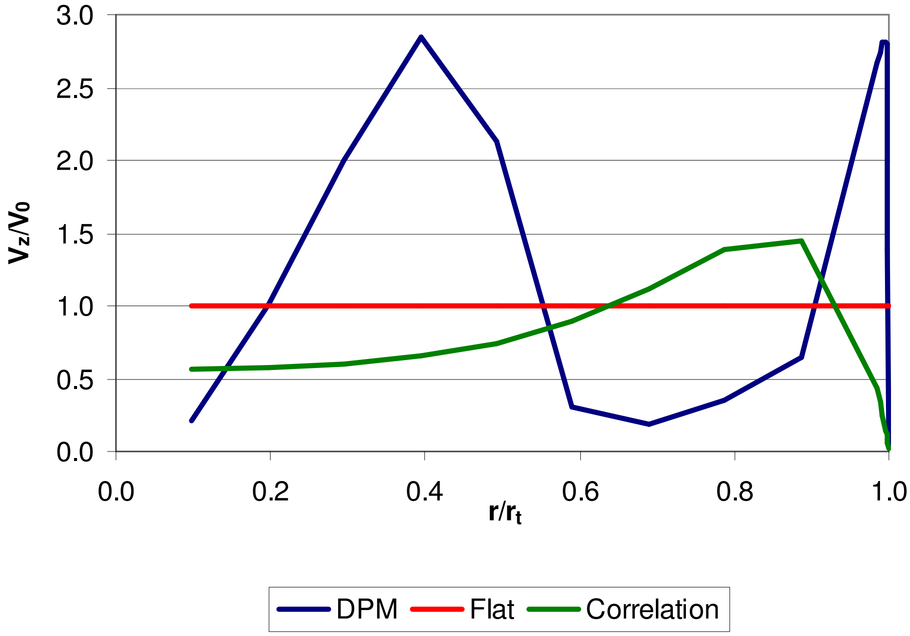

Figure 6.2 Radial profiles of dimensionless axial velocities for flat, correlation based, and DPM results based settings.

The correlation-based smooth curve was obtained from Tsotsas and Schlunder (1988) for which the details are given in Appendix 7(a), and DPM results were from our CFD simulation of full cylinders packing WS model. Although the flat and the smooth curve velocity profiles cannot exist with the presence of realistic packing, especially for the low N tubes, the influence of the wall region is thought to be lumped into the parameters applicable for heat and mass transfer as a conventional approach. Therefore with these lumped parameters, the near-wall effects are aimed to not to be ignored by the selection of either flat or smooth curve profiles.

Our aim here was to create a best P-C model with the appropriate parameters or correlations to obtain the profiles of the parameters, and compare the energy and species simulation results with previously obtained 3D DPM results by CFD as given in Chapter 5.

6.1 Model development

The P-C models are basically represented by 2D partial differential equations as summarized in Chapter 1, and numerical methods are used to reach the solution. Therefore, researchers mostly create codes in different programming languages to solve these 2D equations.

Since our aim was to establish a comparative study with 3D DPM simulation results, we did not want to introduce scaling problems with the utilization of 2D P-C model. Therefore we have generated a 3D model by GAMBIT as shown in Figure 6.3(a) as a P-C model with just fluid phase as in the conventional approach. The 10 layers of prism structure were implemented on the tube wall with the same features as applied in WS models. The outside of the prism region was meshed with tetrahedral UNS grid elements of 0.000762 m size. Total model size was 350,000 cells. The mesh structure is shown with an enlarged view of an arbitrary section in Figure 6.3(b) for the top surface.

The “velocity inlet” boundary condition was selected for the bottom surface, and “outflow” condition was applied for the top to ensure mass conservation without any additional operating condition setting (i.e. temperature and composition) for the outlet. As in the WS models, the side walls were set as symmetric.

The energy and species simulations were performed by FLUENT 6.2.16 with the pre-defined velocity profile. For a flat profile, as in Figure 6.2, the constant superficial velocity was defined for all the computational cells. For the radial position dependent curves, shown in Figure 6.2 as smooth curve and DPM, a user-defined code was prepared to express the correlation or radial-position-dependent velocity function, and defined within each computational cell by just one momentum iteration. The reason for that iteration was not to solve the flow, but to propagate the radial position dependence of the local superficial velocities on each cell.

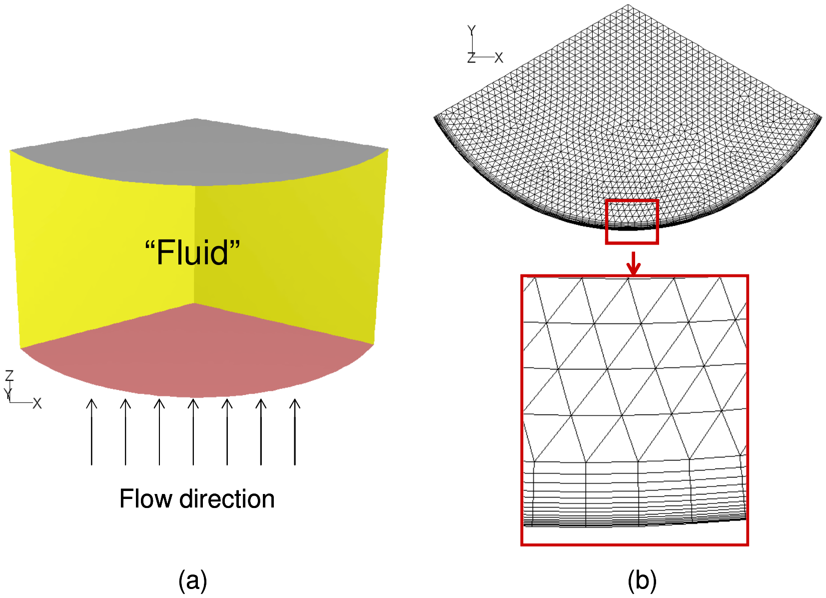

(a) (b)

Figure 6.3 3D P-C model (a) general view, and (b) mesh structure.

Except for the thermal conductivity, the same fluid properties and reactor operating conditions were used as given in Table 3.1. For the thermal conductivity we have either used a constant effective value (k_{er}), or a radial k_{er} profile.

6.2 Thermal conductivity determination

In order to obtain the most appropriate P-C model, different correlations were selected from literature to calculate and define different operating conditions and effective transport parameters. For the k_{er} determination, a separate study was carried out where only wall heat transfer was considered, and the obtained radial temperature profiles with different velocity settings were compared to the DPM results

Case-1: The first case was to consider the constant k_{er} value for entire domain. To calculate alternative k_{er} values, the prediction methods defined by Dixon (Dixon and Cresswell, 1979; Dixon, 1988), and Bauer and Schlunder (1978a, 1978b) were utilized. The details of correlations are given in Appendix 7(b). Similar values were calculated with the both methods as 87.4 w/m-K from Dixon, and 84.0 w/m-K from Bauer and Schlunder.

The temperature profile was obtained utilizing the flat velocity profile as shown in Figure 6.2, and Dixon's correlation result for the k_{er}. Figure 6.4 represents the comparison of this temperature profile with the DPM result. As can be seen, the Case-1 temperatures in the core of the bed were in quite good agreement, whereas at the near wall region, the DPM predictions were not captured by the constant k_{er} setting. Obviously, the near wall heat transfer phenomenon was not defined in the P-C model with the constant velocity and thermal conductivity settings.

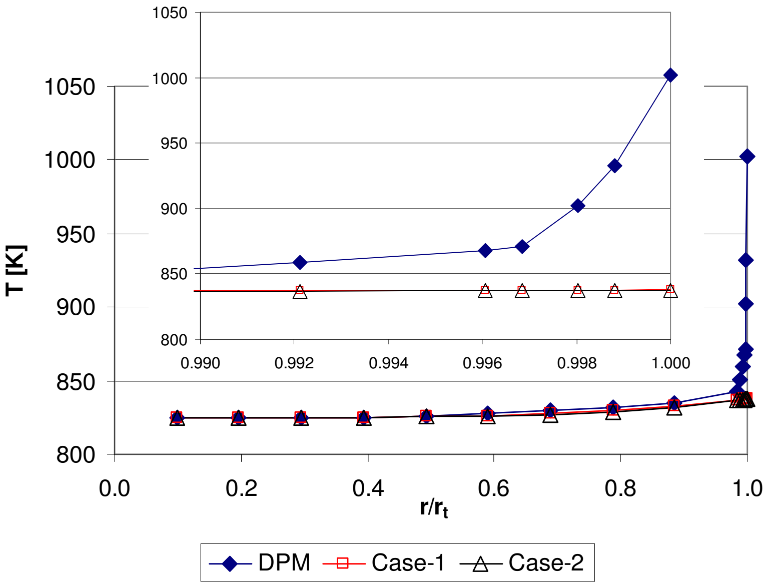

Figure 6.4 Radial temperature profiles based on DPM, Case-1, and Case-2 results.

Case-2: To be able to capture the near wall heat transfer phenomenon, a smooth curve velocity profile, shown in Figure 6.2, was utilized instead of using flat velocity profile. This application was carried out by a user-defined code, as given in Appendix 7(a). The resulting temperature profile was also shown in Figure 6.4, and apparently no significant improvement was observed. From Case-1 and Case-2 results, although the smooth curve velocity profile provided a viscous damping near the wall, the limiting factor seemed to be the k_{er} setting.

Case-3: Instead of using the constant k_{er} value, the Winterberg and Tsotsas (2000) correlation was utilized to obtain the effective thermal conductivity curve. The details of the correlation and the prepared user-defined code to define the correlation into FLUENT are given in Appendix 7(b). Authors considered two parameters, the slope parameter K_1 and the damping parameter K_2, in their expressions which are not à priori fixed, but subject to determination by comparison of the results obtained by this correlation and available experimental data. It was additionally noted that, different pairs of K_1 and K_2 may be almost equally successful in describing the same experimental data. Therefore we have considered three different pairs of K_1 and K_2, and the results are shown in Figure 6.5 along with the DPM results. The results obtained with the pair (b) captured the fluid temperature adjacent to the tube wall, however it was not successful at the dimensionless radial position of $0.900 < r/r_t < 0.998$. The pair (c) and DPM results were mostly in agreement, however, near wall effects could not be predicted in spite of the slight improvement as compared to Case-1 and Case-2 near wall region results. The results obtained by pair (a) were in between the other pairs.

Generally, the benefit of the effective thermal conductivity correlation was seen with this application. We have better results than the constant k_{er} setting, at the near wall region, and the core of the tube modeled well, as expected and observed in the other cases.

The sudden temperature increase in the near wall region of DPM must be related to the boundary layer resolution, which must be coupled to the sudden damping in the DPM velocity profile at that region as shown in Figure 6.2. Therefore, the next step would be the consideration of DPM velocity profile.

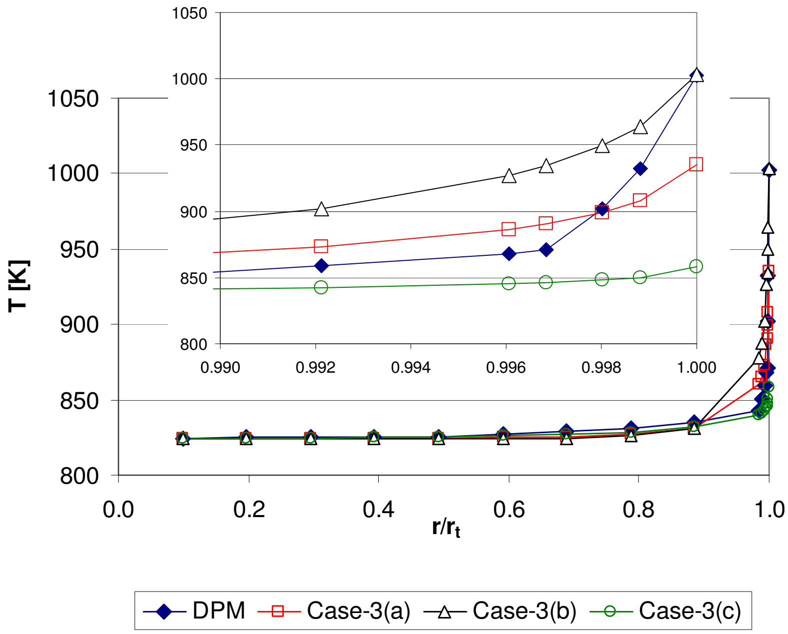

Figure 6.5 Radial temperature profiles based on DPM, and Case-3 results.

Case-4: The DPM velocity profile was exactly reproduced by polynomial functions, and set into FLUENT by a user-defined code which is given in Appendix 7(a). Similarly, three different pairs of K_1 and K_2 were considered, and the obtained temperature profiles are shown in Figure 6.6.

The results obtained by the pair (b) captured the fluid temperature adjacent to the tube wall, and better temperature values were seen in $0.900 < r/r_t < 0.998$, as compared to the Case-3. The maximum deviation was less than 40 degrees at $r/r_t = 0.997$. On the other hand, pair (c) captured the near wall temperatures very well up to $r/r_t = 0.997$. However, at $r/r_t = 0.999$, 80 degrees difference was observed with the DPM results. Pair (a) can be considered as one of the optimum profiles to compensate for the deviations mentioned for pairs (b) and (c).

Additionally, at $r/r_t = 0.9$, a slight disagreement was noticed between the DPM and all the pair results. In spite of that, the most representative temperature profiles were obtained utilizing the DPM-fitted velocity profile, and the k_{er} profile.

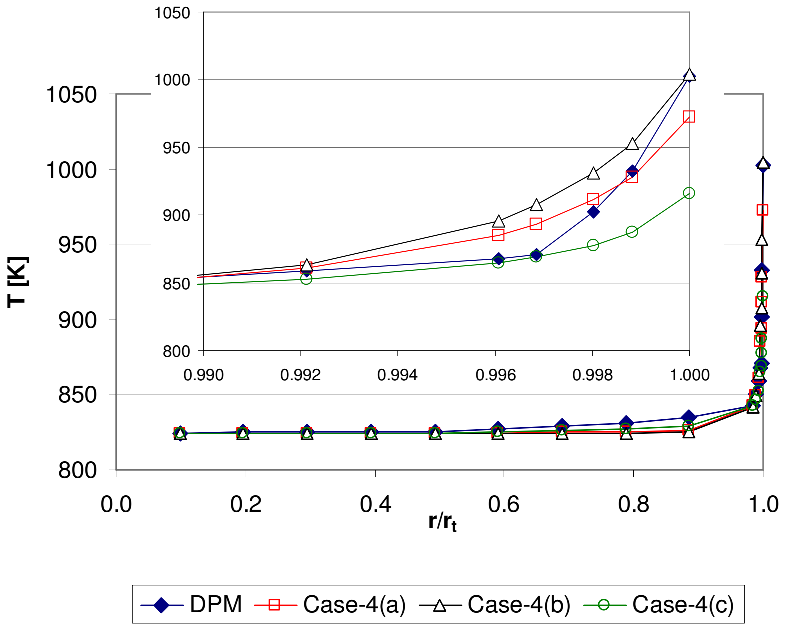

Figure 6.6 Radial temperature profiles based on DPM, and Case-4 results.

6.3 P-C modeling for MSR reaction

The MSR reaction was introduced in P-C modeling with a similar user-defined code as was utilized in DPM simulations with source/sinks terms to express the effects of reaction on temperature and species quantities. The important difference in P-C modeling was that these source/sinks terms were considered for the entire fluid domain and the calculations incorporated the pseudo-solid phase by the bed voidage term, $[1-\varepsilon(r)]$, in the source/sinks terms as expressed below for the energy and species balance equations:

$$u_s \rho c_p \frac{\partial T}{\partial z} - k_{er}\left(\frac{\partial^2 T}{\partial r^2} + \frac{1}{r}\frac{\partial T}{\partial r}\right) = \rho_B(-\Delta H) r_A \eta [1-\varepsilon(r)] \quad (6.1)$$

$$u_s \frac{\partial C}{\partial z} - D_{er}\left(\frac{\partial^2 C}{\partial r^2} + \frac{1}{r}\frac{\partial C}{\partial r}\right) = \rho_B r_A \eta [1-\varepsilon(r)] \quad (6.2)$$

The right hand side of the equations (6.1) and (6.2) is the source/sinks term which was defined by a user-defined code. Additionally we have introduced another term, effectiveness factor, η, in our P-C model to express the diffusion limitations. As a reminder, from DPM simulations we have obtained different effectiveness factor values for front (number 2) and back (number 12) particles, as well as the effectiveness factor profile as shown in Figure 5.18. We have used all three of them separately in this part of the work to make a comparison.

The effective diffusivity (D_{er}) values were calculated form correlations provided by Specchia et al. (1980), Bauer and Schlunder (1978a; 1978b), and Rase (1990), and found to be 0.002150, 0.005659, and 0.007485 m^2/s respectively. Details of these correlations are provided in Appendix 7(c). The results were not significantly affected when these different values were used as effective diffusivities in P-C modeling.

In general, the main modeling parameters can be considered as velocity, effective thermal conductivity, effective diffusivity, bed voidage, and effectiveness factor. Either constant values or spatial functional terms are utilized for these parameters. Since we have previously investigated the velocity and k_{er} parameters, a further consideration was carried out for the effectiveness factor and bed voidage in this section. The energy and species solutions were reached with the residuals in the order of 10^{-8} within a few iterations (~20).

The effectiveness factor investigation: Although the most suitable velocity and k_{er} settings were already seen in the previous section, as the basic application in the P-C modeling, a flat velocity profile, constant effective parameters and bed voidage were utilized in this investigation. For k_{er}, the value obtained from Dixon correlation, for the bed voidage the value of WS model with full cylinders packing, and for the D_{er} the one obtained by Bauer and Schlunder correlation were utilized. As a result of the energy and species simulations, the obtained overall heat uptake values (Q), tube wall temperatures (TWT) and methane conversions (X_{CH4}) are given in Table 6.1 with the DPM results to make a comparison. Equation (2.2) was used for the X_{CH4} calculations. The temperature and, methane and hydrogen mass fraction profiles are presented in Figure 6.7.

Table 6.1 P-C modeling results for different effectiveness factors, and DPM results.

	η-front particle	η-back particle	η-profile	DPM
Q [w]	214.5	288.5	215.0	253.2
TWT [K]	836.2	835.6	836.4	1004.8
X_{CH4} [%]	0.356	0.488	0.354	0.530

The DPM TWT value was not reached by any P-C model as a consequence of flat effective thermal conductivity and axial velocity profiles. Although the overall heat uptake value of DPM was not reproduced, comparable values of Q were obtained with different effectiveness factor settings. If we compare the front and back particle results, we see a reduced heat uptake as a result of lower η-front particle. This can be explained with the influence of the reduced effectiveness factor on the RHS of the equation (6.1). The higher diffusion barrier due to the lower η reduces the reaction heat effect, and therefore less heat is transferred into the pseudo-positioned particles to establish the energy balance. The η-profile heat uptake value was quite similar to the η-front particle value, although the profile was obtained considering both the front and back particle reaction rates. Figure 5.18 shows the possible reason for this observation. At the dimensionless radial position of $0.85 \leq r/r_t \leq 1.00$, the local effectiveness factors were lower than the front particle values, as noted in section 5.3.1.2. Because of this, the reaction heat effects were reduced as compared to the ones obtained by the constant front and back particle effectiveness factor settings in that particular position. Therefore, as a result of the contribution of the reduced heat effects in that region to the total heat uptake, the higher heat effects due to the η-back particle were lost with the utilization of the η-profile, which resulted in very similar heat uptake values with the η-front particle simulation.

The DPM heat uptake value, which was found to be in-between the front and back particle results, could not be obtained by the η-profile setting, although the near wall particle effectiveness was defined by that profile. This situation might be understood well when the tube wall temperatures were compared. Obviously, the near wall temperature field of DPM was not reproduced by any effectiveness factor setting as a result of not using the suitable effective thermal conductivity. The temperature profiles shown in Figure 6.7(a) represent this situation. Actually, with the parameters used in this investigation, the entire DPM radial temperature profile was not obtained. We have selected the basic, and frequently addressed P-C modeling parameters, and it was clear that, the DPM and P-C predictions were not in agreement.

Although the reactor models that we have been considering in our studies are too short in length to obtain a comparable conversion value with any experimental or industrial data, we have utilized the methane conversion as another control parameter for P-C model testing. It was observed that the conversion obtained with the η-back particle simulation was the closest one to the DPM results with 8% deviation.

Figures 6.7(b) and (c) represent the P-C modeling results of CH_4 and H_2 mass fractions respectively. The DPM profiles shown in the figure were only the bulk fluid mass fractions, as previously shown in Figure 5.14 with overall and porous pellet profiles. Since the P-C model essentially considers only the fluid region, the overall or porous pellet profiles were not the appropriate parameters to make a suitable comparison. The mass fraction profiles obtained from the P-C models with different effectiveness factors were not in agreement with the DPM profiles, and they were almost constant. The lower CH_4 and higher H_2 mass fractions were noticed for the η-back particle simulations as compared to the η-front particle and η-profile results, as a consequence of higher effectiveness value.

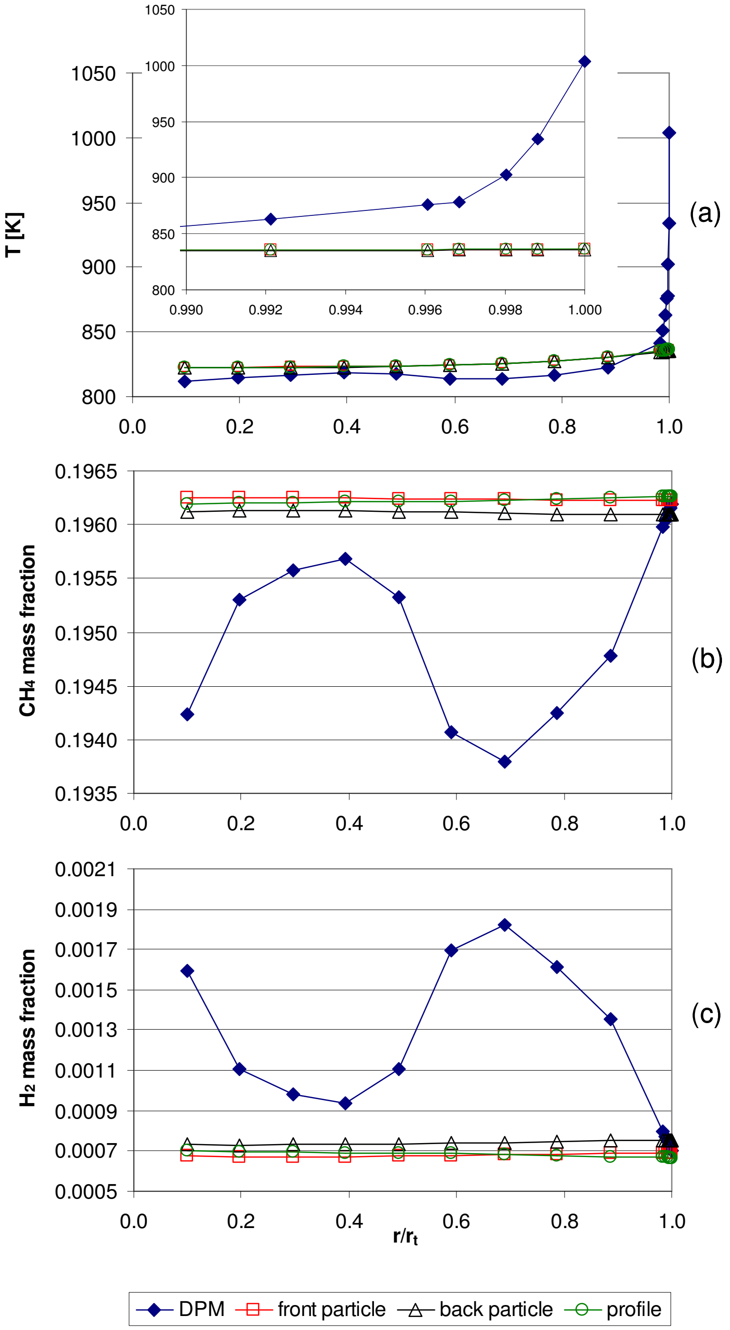

Figure 6.7 The radial profiles of (a) static temperature, (b) CH_4 mass fraction, and (c) H_2 mass fraction obtained by the P-C model with different effectiveness factor settings.

By this investigation, different effectiveness factors were compared to each other and to DPM results while considering constant effective parameters. As a next step, the bed voidage correlations were considered to create radial profiles instead of using constant values.

The bed voidage parameter investigation: The same velocity, thermal conductivity and effective diffusivity values were utilized as before. The η-profile was applied to define the diffusion limitations. The bed voidage correlations provided by Winterberg and Tsotsas (2000) and Bey and Eigenberger (2001) were considered. In addition to these correlations, the DPM bed voidage profile was re-produced by fitted polynomial functions and applied by a user-define code into the P-C model. The details of the correlations and the code are given in Appendix 7(d). The obtained voidage profiles are shown in Figure 6.8. The DPM profile presented in the figure is the one obtained from WS model, and the reproduced one by the polynomial functions was exactly the same.

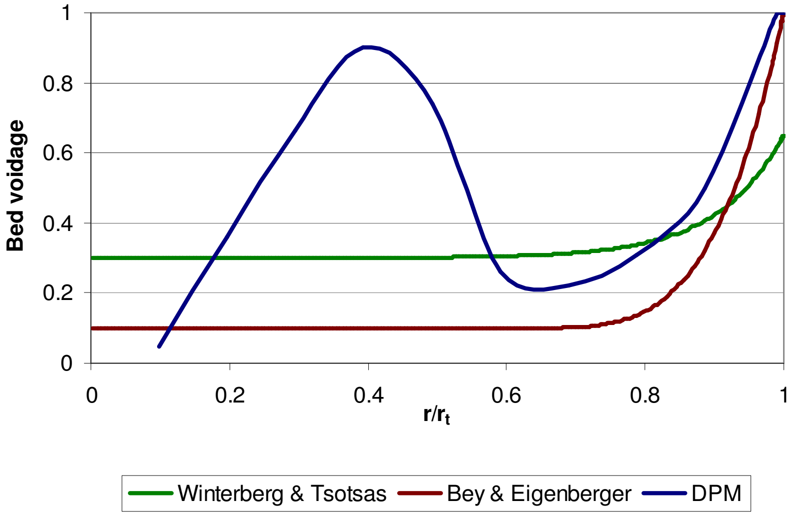

Figure 6.8 Radial bed voidage profiles obtained by the correlations, and from DPM.

As can be seen from the above figure, none of the correlations created a representative bed voidage profile. Both of them created flat profiles at the core and, an increasing trend at the wall region. The Winterberg and Tsotsas (W-T) correlation estimated very low maxima near the wall as compared to the DPM bed voidage. The Bey and Eigenberger (B-E) correlation captured the full void region near the wall, but a steep decrease was observed for the latter part. Actually, the B-E correlation consists of two different expressions for the wall and the core regions. The bed voidage value at the center of the model can be set to a higher value than the minimum, which occurs radially almost at the half of the bed. By doing that, a sinusoidal curve would be obtained in the core of the bed, However, as can be seen in Figure 6.8, the minimum occurs at the core of the bed, not at $r/r_t \approx 0.65$ in DPM. Therefore, the core and the half of the bed voidage values were kept the same, which created a flat profile in the core.

The P-C model results with these three different bed voidage settings were compared to the DPM results in Table 6.2 for Q, TWT, and X_{CH4} values, and in Figure 6.9 for radial temperature and species profiles.

Table 6.2 P-C modeling results for different bed voidages, and DPM results.

	Winterberg & Tsotsas	Bey & Eigenberger	DPM-fitted	DPM
Q [w]	274.0	329.7	221.9	253.2
TWT [K]	835.9	835.8	836.4	1004.8
X_{CH4} [%]	0.450	0.523	0.360	0.530

The heat uptake result obtained by the P-C model with W-T correlation was lower than the one obtained by B-E correlation. The higher voidage profile obtained by W-T correlation in the core of the bed had an inductive effect on the right hand side of the equation (6.1), which reduced the magnitude of the source term. As a result of that, the reaction heat effects were reduced, and lower Q value was reached by W-T correlation.

W-T and B-E correlation models predicted 8% and 30% more heat uptake values than the DPM result respectively, whereas the value obtained by the DPM-fitted voidage profile was lower than the DPM value by 12%. On the other hand, B-E correlation predicted the closest methane conversion value to the DPM result.

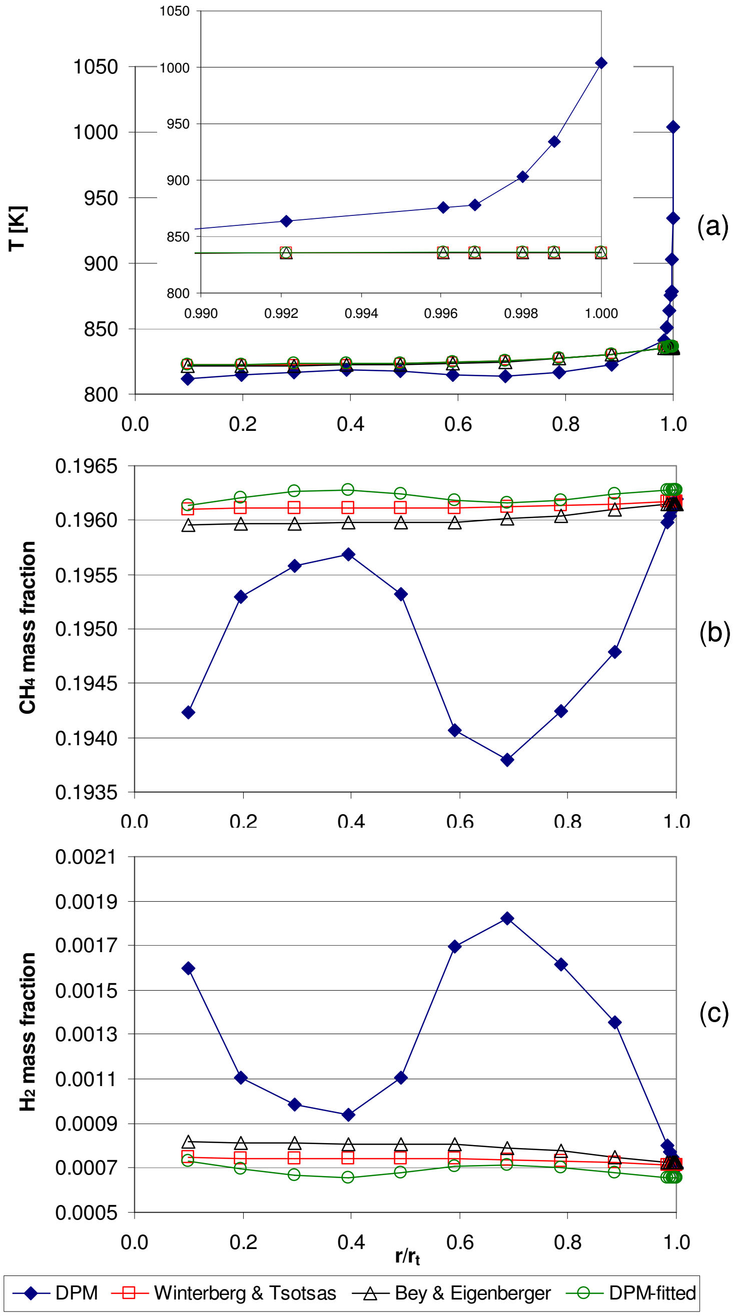

Figure 6.9 The radial profiles of (a) static temperature, (b) CH_4 mass fraction, and (c) H_2 mass fraction obtained by the P-C model with different bed voidage settings.

The TWT values and temperature profiles were different from the DPM results, as observed before.

There were slight effects of the B-E correlation on the methane and hydrogen mass fraction profiles as shown in Figure 6.9 (b) and (c) especially at the near wall region as a result of the sharp damping created there. Since the near wall bed voidage was not pronounced that much with W-T correlation, no significant variation was observed on the related profiles. Although the strong S-shape profiles were not captured, the more variation in the mass fraction profiles was seen for the DPM-fitted model predictions.

At the end of the bed voidage parameter investigation, the DPM-fitted profile was selected for the next stage where the most representative P-C model was aimed to be produced by considering the appropriate effective thermal conductivity and the DPM-fitted parameters.

The P-C model with DPM-fitted parameters: To reproduce the averaged results of the DPM, the DPM-fitted profiles were utilized for the parameters. Axial velocity and bed voidage radial profiles were already obtained above from the DPM-fitted polynomial functions. Additionally, the effective diffusivity profile was created from the DPM as shown in Figure 6.10 by taking the mass fraction weighted average of each species. The blue line presented in Figure 6.10 was reproduced by polynomial functions, and set to the P-C model with a user-defined code, which is given in Appendix 7(c).

Previously obtained effectiveness factor profile, η-profile, and the thermal conductivity profile (Winterberg and Tsotsas, 2000) were utilized. Based on the three different K_1 and K_2 pairs, the obtained Q, TWT and X_{CH4} values are given in Table 6.3 and, the temperature and methane and hydrogen profiles are shown in Figure 6.11 with the DPM results for comparison.

The heat uptake values of the P-C models were close to the DPM value with 7.5% maximum deviation. The averaged TWT was exactly re-produced by P-C (1) model where the Q value was 5.3% lower than the DPM result. In order to obtain a close Q value to the DPM result, the P-C (2) model was created with different K_1 and K_2 pairs, which increased the TWT by 100 degrees. One can conclude that, when the DPM Q value was asymptotically reached in the P-C model with different K_1 and K_2 values, the TWT would exceed the DPM predictions by hundreds of degrees. Another parameter pair was utilized to create the P-C (3) model, which predicts the lower TWT. Although the TWT predictions were strongly affected by different K_1 and K_2 pairs, the least influence was seen on the methane conversion predictions, and the maximum deviation form DPM prediction was found as 0.082%.

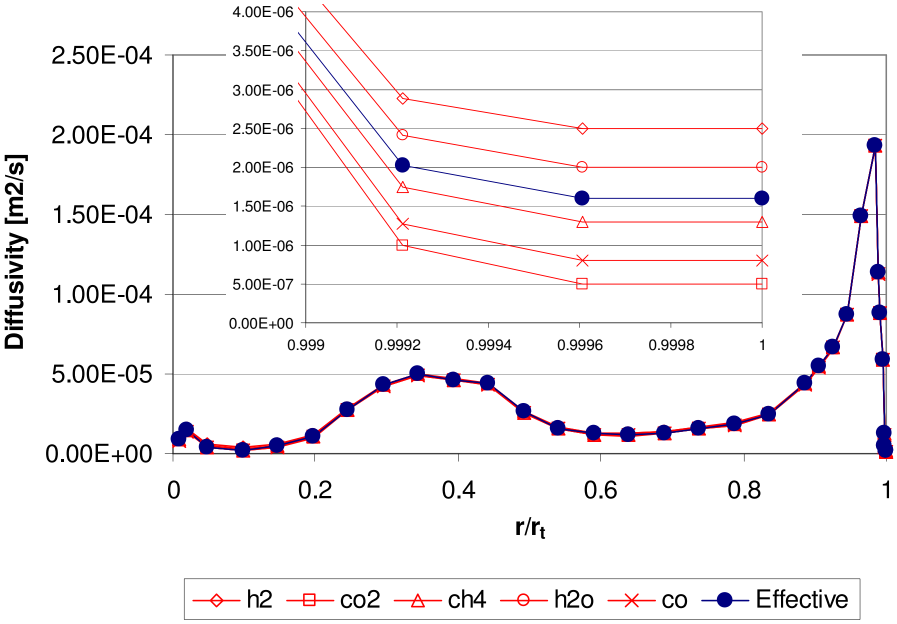

Figure 6.10 The species and effective diffusivity profiles obtained from the DPM.

Table 6.3 P-C modeling results with DPM-fitted parameters, and DPM results.

	P-C (1)	P-C (2)	P-C (3)	DPM
Q [w]	239.8	245.0	234.1	253.2
TWT [K]	1004.3	1104.1	876.4	1004.8
X_{CH4} [%]	0.600	0.596	0.612	0.530

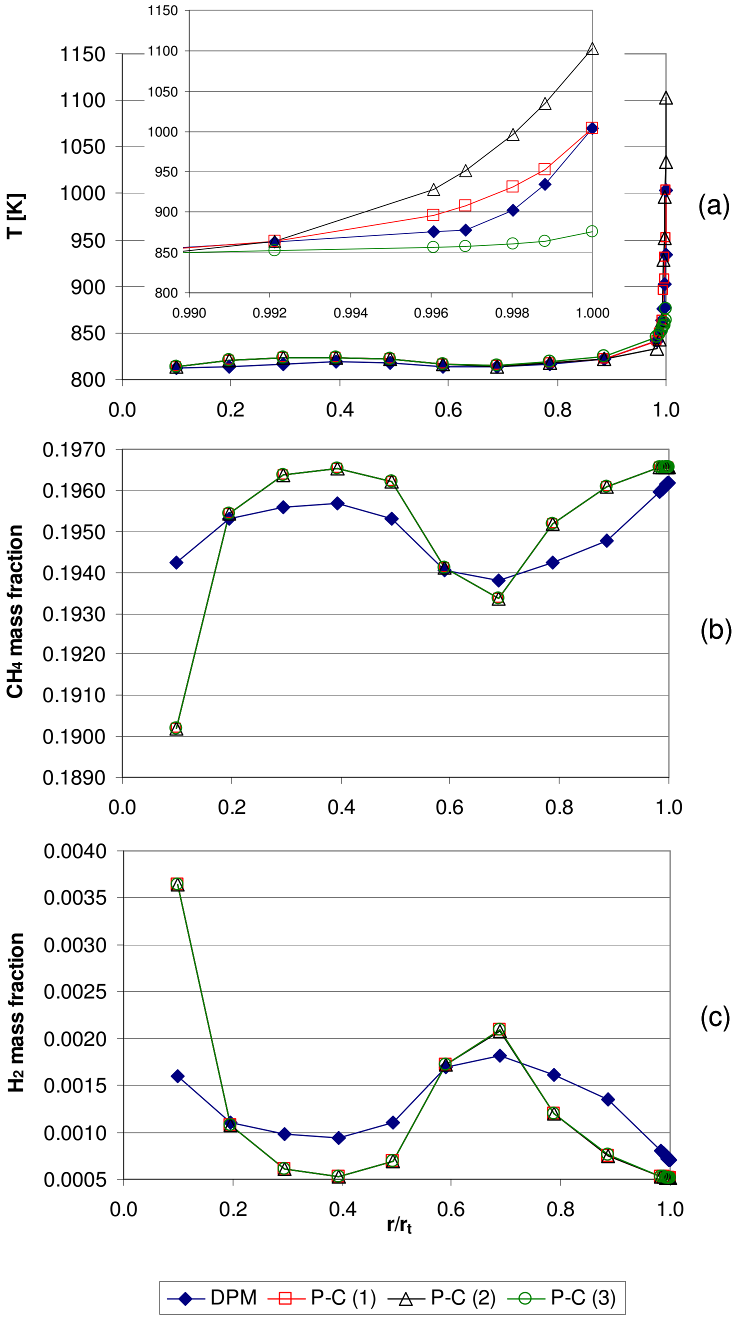

Figure 6.11 The radial profiles obtained by the DPM-fitted P-C models.

The temperature profiles, shown in Figure 6.11(a), were almost the same for all P-C models, and were in good agreement with the DPM profile. The near-wall deviation was enlarged, and the well-established TWT result was additionally seen for P-C (1) in the figure. The local deviation between the P-C (1) model prediction and the DPM profile at $0.996 \le r/r_t \le 0.999$, was around 20 to 30 degrees, and this was the best agreement for near-wall performance among the all P-C models considered so far. The over prediction of the P-C (2) model, and the under prediction of the P-C (3) model was observed at the near wall region which can be incorporated to the TWT values.

Although the increase in TWT is related to the total heat uptake, as creating a driving force between the bulk fluid and the wall temperatures to increase the heat transfer rate which ultimately increases the heat uptake as result of the endothermicity, the higher TWT values were not reflected by the heat uptakes in the same order of magnitude. This is because the local temperature deviation between the P-C models appears only at $0.996 \le r/r_t \le 1.000$, and the same temperature field is present for the rest.

The P-C model methane and hydrogen mass fraction profiles were no different than each other, and in good agreement with the DPM profiles as shown in Figure 6.11(b) and (c). When the profiles obtained here were compared to the other profiles presented in Figures 6.7 and 6.9, a drastic difference can be noticed. The reason for capturing the DPM prediction was because of considering the DPM-fitted effective diffusivity profile instead of the flat profiles. The strong S-shape P-C model mass fraction profiles were departing from the DPM results at the core of the bed. After careful investigation, this situation was understood as an artifact created by the lower velocity field at the center of the tube regarding the applied DPM-fitted axial velocity profile. In the DPM model, the velocity profile was obtained considering the entire radial surface with both fluid and solid regions, and lower bed voidage values were obtained in the core of the bed as presented in Figure 4.16(b) for the full cylinders WS model. Therefore, the contribution of zero velocities from the solid region reduced the averaged velocity value. In P-C modeling when the DPM-fitted axial profile was applied, the reduced velocity value at that radial position was literally considered as a velocity field. So this results in the reduced effect of the first term given in the left hand side of the equation (6.2), on the species balance. Thus, the diffusive flux was the only effective term to balance the source term. The lower bed voidage and higher effectiveness factors at the core of the bed created a higher source term, and as a result, a higher composition difference. For this reason, the higher methane consumption, and higher hydrogen production were seen at that radial position. Although the effective diffusivity value at the core was an order of magnitude higher than the one of the near wall region, it was not enough to compensate for the increase in the source term to keep the compositions unaffected.

6.4 Conclusions

The comparative study was carried out regarding the pseudo-continuum (P-C) and discrete packing models (DPM). Different correlations were utilized in order to express the velocity, thermal conductivity, bed voidage, and diffusion coefficients in the P-C models either in the form of flat profiles (constant values) or in the form of expressions to define the radial position dependence.

It was observed that the flat or correlation-based effective parameter profiles were not enough to express the features of the DPM in terms of heat uptakes, tube wall temperatures, species conversions, and radial temperature and species profiles.

To create the most representative P-C model, the DPM-fitted parameters were utilized, and comparable results were obtained to the DPM predictions. It was seen that the temperature profiles were very much affected by the velocity and thermal conductivity definitions. On the other hand, species profiles were significantly influenced by properly defined effective diffusivity profiles.

The final conclusion would be that the pseudo-continuum models cannot fully reproduce the DPM results due to the complex model structure which cannot be represented by the correlations or DPM-fitted expressions in a simplified model.

7. Conclusions and Recommendations

7.1 Conclusions

At the end of this written document, we can evaluate our observations based on the different phases of the research regarding the main goal that we had in our minds at the beginning. Therefore, the interim conclusions reached at the end of the chapters will not be repeated here, and the observations will be expressed with a global point of view of the research.

Our objective was to investigate the interaction between the chemistry taking place in the particle, and the transport processes surrounding it for the low-N fixed bed tubes utilizing the CFD. Regarding the consequences of wall heat transfer in low-N tubes that have been expressed in the problem statement, generating the proper 3D geometry was the first cornerstone of our work. For this reason we have validated our smaller size geometry, which was selected due to the computational constraints.

The pseudo-continuum type of packed bed models do not account for the actual environment for the reacting particles, and therefore, almost always symmetric and sometimes uniform temperature and species distribution is assumed inside of the pellets. In our work, utilizing the benefits of the CFD, the diffusion/reaction has been introduced into the pellets within the realistic 3D reactor conditions, and contrary to the conventional approach, the non-symmetric and non-uniform intra-particle temperature and species variations have been obtained for the near wall particles, and extensively investigated in detail for the first time.

Furthermore, it has been shown that, the strong near wall gradients as observed by discrete packing models, either approximating the reaction heat effects or implementing the diffusion/reaction into the catalyst particles, cannot be captured by the simplified pseudo-continuum models.

The significance of our observations is that utilization of the conventional simplified methodology will definitely lead to an incorrect evaluation of the reaction rates, and consequently the design considerations such as tube wall temperature and pellet and reactor dimensions.

The strong impact of our findings must be expected on fundamental reaction engineering by moving away from empiricism towards a more rigorous treatment of the pellet, and on the industry by preventing the tube failure and obtaining improved reaction conversion, thus having positive consequences for the plant safety and efficiency, and for pollution prevention and sustainable engineering regarding the particular importance of methane steam reforming on the hydrogen economy.

7.2 Recommendations

In this section, we will describe some of the research areas either we have touched but not completed, and thus have not discussed in the main body of the text, or came to our attention but they were either not part of the main focus of this work or time/computational resources were not available to spend more effort on them.

7.2.1 Particle orientation

Diffusion/reaction implementation was done on the specific WS model where the test particle was located in 45 degree rotated form close to the tube wall. To answer the question if the orientation of the test particle would be important for the near wall transport processes, we re-considered the previously created WS models with different test particle orientations (Nijemeisland, 2002) with improved mesh structure on the wall-fluid contact areas by prism layers. Additionally, another WS model was generated to consider, in general all the possible basic particle placements as presented in Figure 7.1. The model numeration was started from two, regarding the model with 45 degree rotated test particle as WS-1.

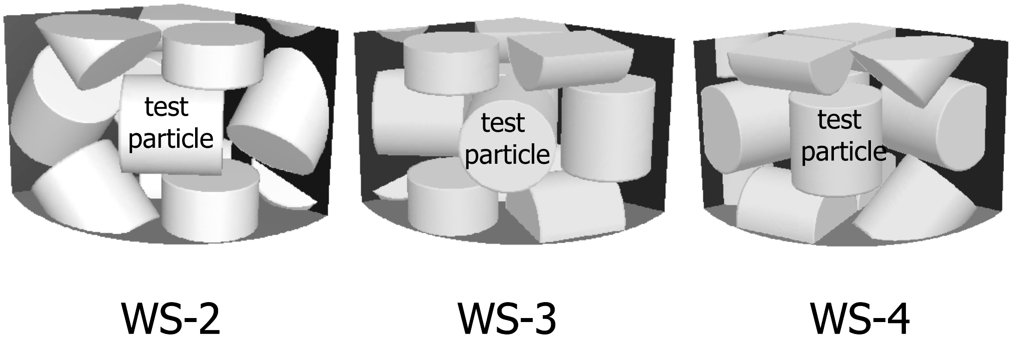

Figure 7.1 Different WS models

We have obtained the preliminary results for WS-4 model, and surface and intra-particle temperature variation is shown in Figure 7.2.

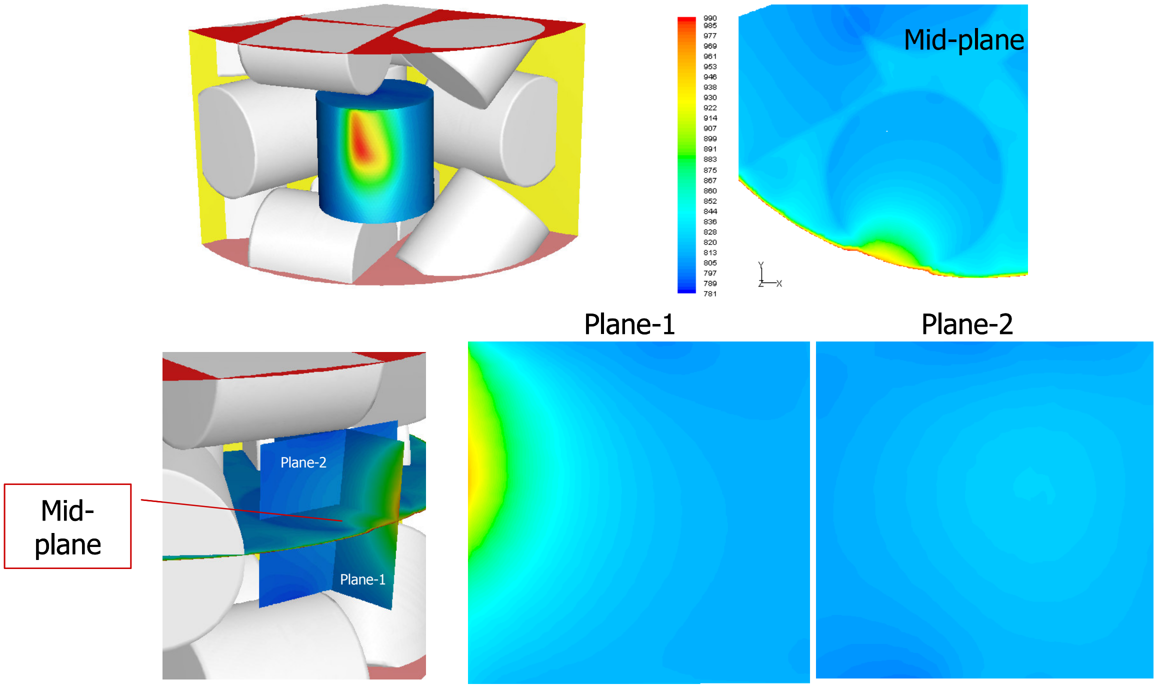

Figure 7.2 The preliminary temperature contours of test particle, model WS-4.

We have observed similar hotter sections as seen on WS-1 model test particle surface at the closest section to the tube wall. Obviously, the flow convection, which takes place between the pellet surface and the tube wall, affected the particle surface temperature, and this hotter section has occurred on the upper part of the pellet.

The effectiveness factors were calculated for front and back particles, and less effective particles were found than the WS-1 model:

$$\eta_{front\ particle} = 0.06746 \qquad \eta_{back\ particle} = 0.07560$$

Keep in mind that the back particle orientations of WS-1 and WS-4 models were also different. So, these preliminary results showed that, the particle orientation is important for both front and back particles. Therefore, it is worth to continue with WS-2 and WS-3 models to investigate up to what extent the modeling parameters such as the tube wall temperature and the particle effectiveness can be affected.

7.2.2 Wall to wall contact points

As stated in the main body of this document before, we have intentionally kept a gap between the particle to particle, and the particle to tube wall contacts, so as not to face convergence problems due to skewed elements that occur with grid generation on these contacts.

Previously, N = 2.43 tube with 10 spherical particles was modeled with contact points (Logtenberg et al., 1999), and agreement between the empirical correlations was observed in thermal conductivity predictions for high Re flows. In the later work (Nijemeisland and Dixon, 2001), for N = 2 tube with 44 spheres, the spherical particle contact points were modeled with a "near-miss" approach where as a first step, touching particles were placed and then the model was finalized by reducing their diameters 99-99.5% while keeping the same particle central coordinates to allow a gap between them. Based on the experiences of that work, the spherical packing WS model was created with 99.5% reduction.

Recently, the 0.5% overlapping spherical particle geometry was introduced (Guardo et al., 2006) without any meshing detail to prevent the convergence problems.

As a preliminary study, 99.8% reduced and 0.5% overlapping particles were created for spherical packing WS model with GAMBIT 2.2.30, and many skewed cells obtained especially for the overlapping case with UNS tetrahedral elements. Figure 7.3 presents the mid point-view of the models where particles are not colored. The 99.5% reduced particle case is also shown for comparison.

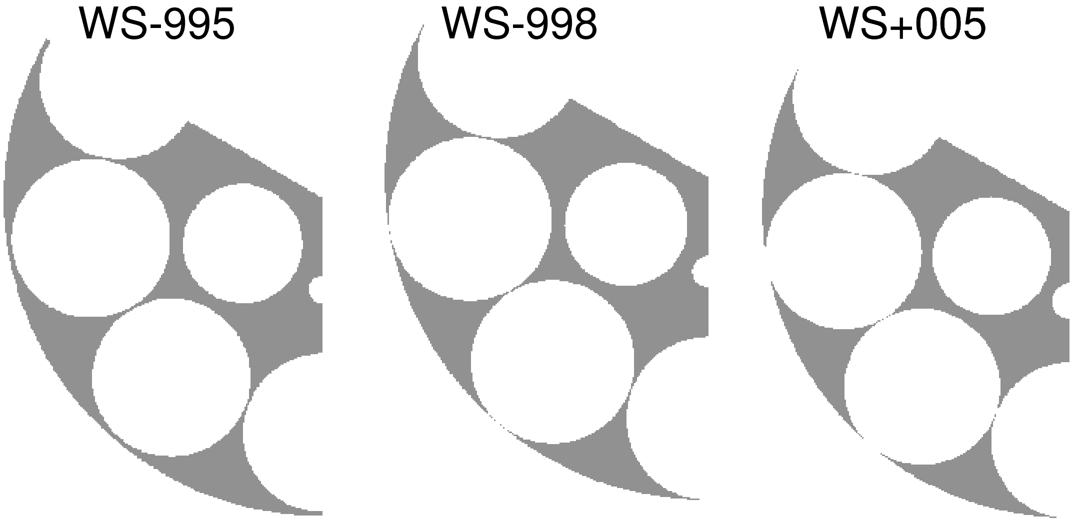

Figure 7.3 The mid-plane views of spherical packing WS models with 99.5% and 99.8% reduced, and 0.05% increased size.

The overall bed voidages of these models are 0.4147 for WS-995, 0.4062 for WS-998, and 0.3915 for WS+005. Based on our previous experiences, the momentum convergence can be achieved with very low URF's for the models with highly skewed cells. Thus, we have obtained the pressure drop values of WS-998 and WS+005 models with the same operating conditions as stated before, and normalized based on WS-995 model value:

$$\Delta P / L_{WS-998} = 1.160 \quad (Pa/m)/(Pa/m) \qquad \Delta P / L_{WS+005} = 1.740 \quad (Pa/m)/(Pa/m)$$

As can be noticed there was a dramatic difference for the overlapping model pressure drop value. Therefore, further investigation would have been performed to include the heat and mass transfer. However, the unreasonable temperature or species values that were calculated and stored for the skewed cells, due to their skewness of course, created a disastrous convergence problem.

We have not gone through these problems in the main body of the text, because our main interest was on the cylindrical packings, and there was not a convergence problem since cylindrical particles were not touching each other or the tube wall.

To solve the touching particle problem a better mesh is necessary, with suitable cell structure, and significant time has to be spent to create the model. Recently FLUENT announced that the version 6.3 has an additional feature that polyhedral cell elements can be used, which may reduce the skewness problem that occurs by tetrahedral cells. The utilization of version 6.3 would be a reasonable starting point to approach the problem, and the latest version of FLUENT became available in our institution couple of months ago.

Once the touching/overlapping particle models are created with spherical and cylindrical packings, the diffusion/reaction modeling can be performed to investigate the near wall gradients for the situation where there will be no gap between the tube wall and the particles.

7.2.3 Catalyst deactivation modeling

One of the important phenomena in catalytic reactions is the catalyst deactivation which occurs on all catalysts either gradually or fast. Among the deactivation processes, carbon formation, or fouling, is the frequently faced problem in many reactions including methane steam reforming and propane dehydrogenation. Fouling is the physically covering of active sites and/or the entire surface of the support, by carbonaceous or inorganic deposits. Severe fouling can lead to pore plugging which cuts off access to active regions and causes loss in activity. Moderate fouling causes a steady but slower decline in activity that can reach a rather steady and acceptable level for long-term operation (Rase, 1990).

For propane dehydrogenation, carbon formation occurs very fast, and therefore it has been considered with the main reaction all the time. Technically, a carbon formation is another reaction or reactions which can be expressed with separate reaction rates. The following reaction is known as the main carbon formation reaction in the propane dehydrogenation:

$$C_3H_8 \rightarrow 3C + 4H_2 \qquad (7.1)$$

The rate equation for the carbon formation may be expressed as:

$$\frac{dC_C}{dt} = r_C^0 \Phi_C \qquad (7.2)$$

where r_C^0 is the initial coking rate (fresh catalyst), and Φ_C is an activity factor as most frequently expressed:

$$\Phi_C = \exp(-\alpha \cdot C_C) \qquad (7.3)$$

where α is the deactivation parameter which was found to be a function of temperature (Jackson and Stitt, 2004).

To model the deactivation, the catalyst activity must be related to the coke accumulation which may be obtained by integrating the equation (7.2) with a suitable initial coking rate expression. The deactivation model can be coupled to the main reaction model and implemented into the pellet by a user-defined code. By this way, the overall reaction conversion and selectivity, and temperature dependence of the carbon deposition could be investigated in detail regarding the benefits of CFD.

Nomenclature

a_v	pellet surface area per reactor volume	$[m^2/m^3]$
C	concentration	$[kmol/m^3]$
c_p	fluid heat capacity	[J/kg-K]
d_p	pellet diameter	[m]
d_{pv}	particle diameter equivalent to sphere volume	[m]
d_t	tube diameter	[m]
$D_{A,m}$	effective diffusivity of species A in mixture	$[m^2/s]$
D_{er}	effective diffusivity	$[m^2/s]$
D_{md}	molecular diffusivity	$[m^2/s]$
D_K	Knudsen diffusivity	$[m^2/s]$
E	energy	[J]
g	gravitational acceleration	$[m/s^2]$
G	mass flow rate of the fluid	$[kg/m^2\text{-}s]$
h	heat transfer coefficient	[W/m-K]
k_g	mass transfer coefficient	[m/s]
k_i	reaction rate constant of reaction i	$[kmol/kg\ cat\text{-}s \cdot kPa^n]$
K_A	adsorption coefficient of species A	$[kPa^{-1}]$
K_j	equilibrium constant of component j	$[kPa^n]$
L_p	particle length	[m]
M_A	molecular weight of A	[kg/kmol]
N	tube to particle diameter ratio	[-]
P	static pressure	[kPa]
P_j	partial pressure of component j	[kPa]
q_{wall}	wall heat flux	$[W/m^2]$
Q	heat	[W]

r_c	cut-off ratio	[-]
r_p	particle radius	[m]
r_i	reaction rate (i=1,2,…), MSR	[kmol/kg cat-s]
r_i	reaction rate (i=1,2,…), PDH	[kmol/m^3 -s]
r_t	tube radius	[m]
R	gas constant	8.314 [J/mol-K]
S	arc length	[m]
Sm	source term	[…/m^3]
T	temperature	[K]
u,v,w	velocity components	[m/s]
U	overall heat transfer coefficient	[W/m-K]
U^+	dimensionless velocity, wall function unit	[-]
V_z	axial velocity	[m/s]
V_0	superficial velocity	[m/s]
x, y, z	cartesian coordinates	[-]
X_A	conversion of component A	[-]
y^+	dimensionless distance, wall function unit	[-]
Y_i	mass fraction of i	[-]
Z	height	[m]

Greek symbols

α	under relaxation factor	[-]
α_{ij}	stoichiometric coefficient	[-]
ϵ	bed voidage	[-]
ε	turbulence dissipation	[J/s]
ε_s	porosity of the particle	[-]

κ	turbulent kinetic energy	[J]
η	effectiveness factor	[-]
μ	viscosity	[Pa·s]
μ^t	turbulent viscosity	[Pa·s]
ρ	density	[kg/m^3]
Γ	tortuosity factor	[-]
τ	viscous stress tensor	[N/m^2]
α	under relaxation factor	[-]
ξ	radial coordinate in the catalyst (r/rp)	[-]
ΔH	enthalpy of the reaction	[kJ/mol]
$\Delta P/L$	pressure gradient	[Pa/m]
ΔT_w	temperature drop across the wall	[K]

Dimensionless numbers

Nusselt Number $Nu = \frac{hd_p}{k_f}$

Peclet Number $Pe = \frac{Gc_p d_p}{k_f}$

Prandtl Number $\Pr = \frac{c_p \mu}{k_f}$

Reynolds Number $\mathrm{Re} = \frac{\rho v d_p}{\mu}$

Abbreviations

B-E	Bey and Eigenberger
CFD	Computational Fluid Dynamics
CW	Complete Wall
DPM	Discrete Packing Model
EWT	Enhanced Wall Treatment
FD	Finite Difference
FE	Finite Element
FV	Finite Volume
GHSV	Gas Hourly Space Velocity
GSA	Geometric Surface Area
M-C	Multicomponent
MRI	Magnetic Resonance Imaging
MSR	Methane Steam Reforming
P-C	Pseudo-continuum
PDH	Propane Dehydrogenation
RNG	Renormalization Group
UDMI	User-defined Memory Index
UNS	Unstructured
URF	Under Relaxation Factor
TWT	Tube Wall Temperature
WGSR	Water Gas Shift Reaction
W-T	Winterberg and Tsotsas

References

Avci, A., K., Trimm, D., L., and Ilsen Onsan, Z. (2001), Heterogeneous reactor modeling for simulation of catalytic oxidation and steam reforming of methane. *Chemical Engineering Science*, **56**, 641-649.

Aparicio, L., M., (1997), Transient isotopic studies and microkinetic modeling of methane reforming over nickel catalysts. *Journal of Catalysis*, **165**, 262-274.

Balakotaiah, V., and Dommeti, S. M. S. (1999), Effective models for packed-bed catalytic reactors. *Chemical Engineering Science*, **54**, 1621-1638.

Bauer, R., and Schlunder, E. U. (1978a), Effective radial thermal conductivity of packing in gas flow. Part I. Convective transport coefficient. *International Chemical Engineering*, **18**, 181-188.

Bauer, R., and Schlunder, E. U. (1978b), Effective radial thermal conductivity of packing in gas flow. Part I. Thermal conductivity of packing fraction without gas flow. *International Chemical Engineering*, **18**, 189-204.

Bey, O., and Eigenberger, G. (2001), Gas flow and heat transfer through catalyst filled tubes. *International Journal of Thermal Science*, **40**, 152-164.

Buruno, S. P., Barreto, G. F., and Gonzalez, M. G. (1988), Effect of geometric characteristics of commercial catalysts for steam reforming. *Chemical Engineering Journal*, **39**, 147-156.

Calis, H., P., A., Nijerhuis, J., Paikert, B., C., Dautzenberg, F., M., and van den Bleek, C., M. (2001), CFD modeling and experimental validation of pessure drop and flow profile in a novel structured catalytic reactor packing. *Chemical Engineering Science*, **56**, 1713-1720.

Dalman, M., T., Merkin, J., H., and McGreavy, C. (1986), Fluid flow and heat transfer past two spheres in a cylindrical tube. *Computers & Fluids* **14**, 267-281.

Deans, H., A., and Lapidus, L. (1960), A computational model for predicting and correlating the behavior of fixed-bed reactors: I. Derivation of model for nonreactive systems. *American Institute of Chemical Engineers Journal*, **6**, 656-663.

Derkx, O., R., and Dixon, A., G. (1996), Determination of the fixed bed wall heat transfer coefficient using computational fluid dynamics. *Numerical Heat Transfer Part A*, **29**, 777-794.

Dixon, A., G., and Cresswell, D., L. (1979), Theoretical prediction of effective heat transfer parameters in packed beds. *American Institute of Chemical Engineers Journal*, **25**, 663-676

Dixon, A., G. (1988), Wall and particle shape effects on heat transfer in packed beds. *Chemical Engineering Communications* **71**, 217-237.

Dixon, A., G., and Nijemeisland, M. (2001), CFD as a design tool for fixed-bed reactors. *Ind. Eng. Chem. Res.*, **40**, 5246-5254.

Dixon, A., G., Nijemeisland, M., and Stitt, E., H. (2003), CFD simulation of reaction and heat transfer near the wall of a fixed bed. *International Journal of Chemical Reactor Engineering*, **1**, A22.

Dixon, A., G., Nijemeisland, M., and Stitt, E., H. (2005), CFD study of heat transfer near and at the wall of a fixed bed reactor tube: effect of wall conduction. *Ind. Eng. Chem. Res.*, **44**, 6342-6353.

Dixon, A., G., Nijemeisland, M., and Stitt, E., H. (2006), Packed tubular reactor modeling and catalyst design using computational fluid dynamics. *Advances in Chemical Engineering*, **31**, 307-389.

Dixon, A., G., Taskin, M., E., Stitt, E., H., and Nijemeisland, M. (2007), 3D CFD simulations of steam reforming with resolved intraparticle reaction and gradients. *Chemical Engineering Science, in press*.

Dometti, S., M.S., Balakotaiah, V., and West, D., H. (1999), Analytical criteria for validity od pseudohomogeheous models for paked-bed catalytic reactors. *Industrial & Engineering Chemistry Research*, **38**, 767-777.

Doraiswamy, L., K., and Sharma, M., M. (1984), *Heterogeneous reactions: analysis, examples and reactor design. Volume 1: Gas-solid and solid-solid reactions*, John Wiley & Sons, New York.

Ergun, S. (1952), Fluid flow through packed columns. *Chemical Engineering Progress*, **48**, 89-94.

Esterl, S., Debus, K., Nirschl, H., Delgado, A. (1998), Three dimensional calculations of the flow through packed beds. *Fluid Dynamics and Process Automation. Eur. Comput. Fluid Dyn. Conf.*, 4th, 692-696.

Fluent (2005), User's Guide version 6.2, Fluent Inc., Lebanon, NH.

Freund, H., Zeiser, T., Huber, F., Klemm, E., Brenner, G., Durst, F., and Emig, G. (2003), Numerical simulations of single phase reacting flows in randomly packed fixed-bed reactors and experimental validation. *Chemical Engineering Science*, **58**, 903-910.

Froment, G., F. (1974) Fixed Bed Catalytic Reactors, Technological and Fundamental Aspects. *Chemie Ingenieur Technik,* **26**, 374.

Froment, G., F. (2000), Production of synthesis gas by steam- and CO_2- reforming of natural gas. *Journal of Molecular Catalysis*, **163**, 147-156.

Froment, G., F., and Bischoff, K., B. (1990), *Chemical Reactor Analysis and Design*, 2nd Edition, Wiley, New York..

Fuller, E., N., Schettler, P., D., and Giddings, J., C. (1966) A new method for prediction of binary pas-phase diffusion coefficients. *Industrial & Engineering Chemistry,* **58**, 19-27.

Gallucci, F., Paturzo, L., and Basile, A. (2004), A simulation study of the steam reforming of methane in a dense tubular membrane reactor. *International Journal of Hydrogen Energy*, **29**, 611-617.

Guardo, A., Coussirat, M., Larrayoz, M., A., Recasens, F., and Egusquiza, E. (2005), Influence of the turbulence model in CFD modeling of wall-to-fluid heat transfer in packed beds. *Chemical Engineering Science*, **60**, 1733-1742.

Guardo, A., Coussirat, M., Recasens, F., Larrayoz, M. A., and Escaler, X. (2006), CFD study on particle-to-fluid heat transfer in fixed bed reactors: Convective heat transfer at low and high pressure. *Chemical Engineering Science*, **61**, 4341-4353.

Guardo, A., Coussirat, M., Recasens, F., Larrayoz, M., A., and Escaler, X. (2007), CFD studies on particle-to-fluid mass and heat transfer in packed bed reactors: Free convection effects in supercritical fluids. *Chemical Engineering Science, in press*.

Gulijk, C., V. (1998), Using computational fluid dynamics to calculate transversal dispersion in a structured packed bed. *Computers & Chemical Engineering*, **22**, 767-770.

Gunjal, P., R., Ranade, V., V., and Chaudhari, R., V. (2005), Computational study of a single-phase flow in packed beds of spheres. *American Institute of Chemical Engineers Journal*, **51**, 365-378.

Hicks, R., E. (1970), Pressure drop in packed beds of spheres. *Ind. Eng. Chem. Fundam.*, **9**, 500-502.

Hoffmann, K., A., and Chiang, S., T. (1993), *Computational Fluid Dynamics for Engineers, Volume II*, 1st Edition, Engineering Education System, Kansas.

Hou, K., Hughes, R. (2001), The kinetics of methane steam reforming over a Ni/α-Al_2O catalyst. *Chemical Engineering Journal*, **82**, 311-328.

Hou, K., Hughes, R. (2002), A comparative simulation analysis of propane dehydrogenation in composite and microporous membrane reactors. *Journal of Chemical Technology and Biotechnology*, **78**, 35-41.

Jackson, S., D. and Stitt, E., H. (2004), Propane dehydrogenation over chromia catalysts: microcatalysis, deactivation, macrokinetics, and reactor modeling. *ChemInform*, **35**, issue 23.

Jarosch, K., El Solh, T., and de Lasa, H., I. (2002), Modeling the catalytic steam reforming of methane: discrimination between kinetic expressions using sequentially designed experiments. *Chemical Engineering Science*, **57**, 3439-3451.

Koning, G., W., Kronberg, A., E., and van Swaajj, W., P., M. (2006), Improved one-dimensional model for a tubular packed bed reactor. *Chemical Engineering Science*, **61**, 3167-3175.

Kuijpers, J., A., M. and van Swaaij, W., P., M. (1998), Computational fluid dynamics applied to chemical reaction engineering. *Advances in Chemical Engineering,* **24**, 227-328

Kvamsal, H., M., Svendsen, H., F., Hertzberg, T., and Olsvik, O. (1999), Dynamic simulation and optimization of a catalytic steam reformer. *Chemical Engineering Science*, **54**, 2697-2706.

Launder, B., E. and Spalding, D., B.(1972), *Lectures in Mathematical Models in Turbulence*. Academic Press, London.

Launder, B., E. and Spalding, D., B. (1974), The numerical computation of turbulent flows. *Computer Methods in Applied Mechanics and Engineering*, **3**, 269-289.

Laguerre, O., Ben Amera, S., Alvarez, G., and Flick, D. (2007) Transient heat transfer by free convection in a packed bed of spheres: Comparison between two modeling approaches and experimental results. *Applied Thermal Engineering*, in press.

Leising, G. (2005), *M. S. Thesis*. Worcester Polytechnic Institute, Worcester, MA.

Lloyd, B. and Boehm, R. (1994), Flow and heat transfer around a linear array of spheres. *Numerical Heat Transfer, Part A*, **26**, 237-252

Levenspiel, O. (1972), *Chemical reaction engineering*. John Wiley & Sons, 2nd ed, New York.

Logtenberg, S., A., and Dixon, A., G. (1998a), Computational fluid dynamics studies of fixed bed heat transfer. *Chemical Engineering and Processing* **37**, 7-21

Logtenberg, S., A. and Dixon, A., G. (1998b), Computational fluid dynamics studies of the effects of temperature-dependent physical properties on fixed-bed heat transfer. *Industrial and Engineering Chemistry Research* **37**, 739-747

Logtenberg, S., A., Nijemeisland, M., and Dixon, A., G. (1999), Computational fluid dynamics simulations of fluid flow and heat transfer at the wall-particle contact points in a fixed bed reactor. *Chemical Engineering Science* **54**, 2433-2439

Machac, A., Henda, R., and Nilsson, B. (2006), Modeling of heat and mass transport in a nonlinear catalytic bed reactor. *Proceedings of the 2006 Nordic COMSOL Conference.*

Magnico, P. (2003), Hydrodynamic and transport properties of packed beds in small tube-to-sphere diameter ratio: Pore scale simulation using an Eulerian and a Langrangian approach. *Chemical Engineering Science*, **58**, 5005-5024.

Mariani, N., J., Keegan, S, D., Martinez, O., M., and Barreto, G., F. (2003), A one-dimensional equivalent model to evaluate overall reaction rates in catalytic pellets. *Trans. Inst. Chem. Eng. Part A*, **81**, 1033.

McGuire, M., and Lapidus, L. (1965), On the stability of a detailed packed bed reactor. *American Institute of Chemical Engineers Journal*, **11**, 85-95.

Mears, D., E. (1971), Diagnostic criteria for hest transport limitations in fixed bed reactors. *Journal of Catalysis*, **20**, 127-131.

Molerus, O. (1977), Druckverlustg leichung für die durch-strömung von kugelschüttungen im laminaren und im übergangs bereich. *Chem. Ing. Techn.*, **49**, 675.

Navier, M. (1827), Mémorie sur les Lois du Mouvement des Fluides. *Mem. De l'Acad. De Sci.* **6**, 389.

Nijemeisland, M., and Dixon, A., G. (2001), Comparison of CFD simulations to experiment for convective heat transfer in a gas-solid fixed bed. *Chemical Engineering Journal,* **82, 1-3**, 231-246

Nijemeisland, M. (2002), *Ph. D. Thesis*. Worcester Polytechnic Institute, Worcester, MA.

Nijemeisland, M., Dixon, A., G., and Stitt, E., H. (2004), Catalyst design by CFD for heat transfer and reaction in steam reforming. *Engineering Science*, **59**, 5185-5191.

Nijemeisland, M., and Dixon, A., G.(2004), CFD study of fluid flow and wall heat transfer in a fixed bed of spheres. *American Institute of Chemical Engineers Journal*, **50**, 906-921.

Ohta, M., Yamamoto, M., and Suzuki, M. (1995), Numerical analysis of a single drop formation process under pressure pulse condition. *Chemical Engineering Science,* **50**, 2923.

Owoyemi, O., Mazzei, L., and Lettieri, P. (2007), CFD modeling of binary-fluidized suspensions and investigation of role of particle-particle drag on mixing and segregation. *American Institute of Chemical Engineers Journal*, **53**, 1924-1940.

Patankar, S., V. (1980), *Numerical Heat Transfer and Fluid Flow*, Hemisphere, Washington, D.C.

Papageorgiou, J., N., and Froment, G., F. (1995), Simulation models accounting for radial voidage profiles in fixed-bed reactors. *Chemical Engineering Science*, **50**, 3043-3056.

Pedernera, M., N., Pina, J., Borio, D., O., and Bucala, V. (2003), Use of a heterogeneous two-dimensional model to improve the primary steam reformer performance. *Chemical Engineering Journal*, **94**, 29-40.

Petre, C., F., Larachi, F., Iliuta, I., and Grandjean, B., P., A. (2003), Pressure drop through structured packings: Breakdown into the contributing mechanisms by CFD modeling. *Chemical Engineering Science*, **58**, 163-177.

Persons, I., M., and Porter K., E. (1992), Gas flow patterns in packed beds: A computational fluid dynamics model for wholly packed domains. *Gas Separation & Purification*, **6**, 221-227.

Ranade, V. (2002), *Computational Flow Modeling for Chemical Reactor Engineering*, Academic Press, New York.

Rase, H., F. (1990), *Fixed-bed reactor design and diagnostics*. Butterworths Publishers, Stoneham, MA.

Reichelt, W. (1972), Zur berechnung des druckverlustes einphasig durchströmter kugel- und zylinderschüttungen. *Chem. Ing. Techn.*, **44**, 1068-1071.

Romkes, S., J., P., Dautzenberg, F., M., van den Bleek, C., M., and Calis, H., P., A. (2003), CFD Modeling and experimental validation of particle-to-fluid mass and heat transfer in a packed bed at very low channel to particle diameter ratio. *Chemical Engineering Journal*, **96**, 3-13.

Salmi, T., and Warna, J. (1991), Modeling of catalytic packed-bed reactors-comparison of different diffusion models. *Computers & Chemical Engineering*, **15**, 715-727.

Sie, S. T., Krishna, R. (1998), Process development and scale-up:II. Catalyst design strategy. *Reviews in Chemical Engineering*, **14**, 159.

Specchia, V., Balgi, G., and Sicardi, S. (1980), Heat transfer in packed bed reactors with one phase flow. *Chemical Engineering Communications*, **4**, 361-380.

Stewart, W., E. (1965), Transport phenomena in fixed-bed reactors. *Chemical Engineering Progress Symposium Series*, **61**, 61.

Stewart, W., E., Marr, D., F., Nam, T., T., and Gola-Galimidi, A., M. (1991), Transport modeling of packed-tube reactors-1. Framework for a data-based approach. *Chemical Engineering Science*, **46**, 2905-2911.

Stitt, E., H., Jackson, S., D., and King, F. (1999), Kinetic based deactivation modeling of an isothermal propane dehydrogenation reactor. *Studies in Surface Science and Catalysis*, **122**, 291-298.

Stitt, E., H., Jackson, S., D., Shipley, D., G. and King, F. (2001), Modeling propane dehydrogenation in a rotating monolith reactor. *Catalysis Today*, **69**, 217-226.

Stitt, E., H. (2005), *Reactor technology for syngas and hydrogen*. In Sustainable strategies for the upgrading of natural gas: fundamentals, challenges and opportunities, Derouane, E., Parmon, V., Lemos, F. and Ramoa-Ribiero, F. (eds.), NATO Science Series, Kluwer Press, **191**, 185.

Stokes, G., G. (1845), On the theories of internal friction of fluids in motion. *Transactions of the Cambridge Philosophical Society*. **8**, 287.

Tobis, J. (2000), Influence of bed geometry on its frictional resistance under turbulent flow conditions. *Chemical Engineering Science*, **55**, 5359-5366.

Tobis, J. (2002), Modeling of the pressure drop in the packing of complex geometry. *Industrial & Engineering Chemistry Research*, **41**, 2552-2559.

Tsotsas, E., and Schlunder, E., U. (1988), Some remarks on channeling and radial dispersion in packed beds, *Chemical Engineering Science*, **43**, 1200-1203.

Winterberg, M., and Tsotsas, E. (2000), Correlations for effective heat transport coefficients in beds packed with cylindrical particles. *Chemical Engineering Science*, **55**, 5937-5943.

van Sint Annaland, M., Scholts, H., A., R., Kuipers, J. A., M., and van Swaaij, W., P., M. (2002), A novel reverse flow reactor coupling endothermic and exothermic reactions. Part-II:Sequential reactor configuration for reversible endothermic reactions. *Chemical Engineering Science*, **57**, 855-872.

Vortmeyer, D., and Schuster, J. (1983), Evaluation of steady flow profiles in rectangular and circular packed beds by a variational method. *Chemical Engineering Science*, **38**, 1691-1699.

Xu, J., and Froment, G., F. (1989a), Methane steam reforming, methanation and water-gas shift: I. Intrinsic kinetics. *American Institute of Chemical Engineers Journal*, **35**, 88-96.

Xu, J., and Froment, G., F. (1989b), Methane steam reforming, II. Diffusional limitations and reactor simulation. *American Institute of Chemical Engineers Journal*, **35**, 97-103.

Yakhot, V., and Orszag, S.A.(1986), Renormalizarion group analysis. I. Basic theory. *Journal of Scientific Computing*, **1**, 3-51.

Zeiser, T., Lammers, P., Klemm, E., Li, Y., W., Bernsdorf, J., and Brenner, G. (2001), CFD-Calculation of flow, dispersion and reaction in a catalyst filled tube by the Lattice Boltzmann method. *Chemical Engineering Science*, **56**, 1697-1704.

Zeiser, T., Steven, M., Freund, H., Lammers, P., Brenner, G., Durst, F., and Bernsdorf, J. (2002), Analysis of the flow field and pressure drop in fixed-bed reactors with the help of Lattice Boltzmann Simulation. *Phil. Trans. R. Soc. Lond. A*, **360**, 507-520.

Appendices

Appendix 1: Particle placements of WS model

Table A.1 Placement of the particles in WS models

Particle	Placement steps		
1	R	+45	+x
	T	-1.45	+x
	R	+40	+z
2	R	-45	+x
	T	-1.45	+x
	T	+1	+z
	R	+20	+z
3	**C 1**		
	T	+2	+z
4	R	+5	+x
	T	-1.48	+x
	R	-9	+z
5	**C 4**		
	T	+2	+z
6	R	+90	+y
	T	-1.42	+y
	R	+5	+z
7	**C 6**		
	T	+2	+z
8	R	+90	+x
	T	-1.42	+y
	T	+1	+z
	R	-17.5	+z
9	R	+45	+x
	T	-1.45	+x
	T	-1	+z
	R	-40	+z
10	R	-45	+y
	T	-0.25	+x
11	**C 10**		
	T	+2	+z
12	R	+90	+x
	T	+1	+z
	T	-0.35	+y
	T	+0.2	+x

R=rotate, T=translate, C=copy

Rotations are in degrees, translations in inches, based on a 1 inch diameter, 1 inch height particle.

Appendix 2: Particle placements of CW model

Table A.2 Placement of the particles in the CW model in addition to 11 WS particles.

Particle	Placement steps		
12'	**C 12**		
	T	+0.19	+y
13	**C 2**		
	R	+105	+z
	T	-0.005	+z
14	R	+29.8	+x
	T	+1.45	+x
	R	-31	+z
15	**C 14**		
	T	+2	+z
16	**C 8**		
	R	+106.8	+z
	R	+10	+y
	T	-0.3	+x
	T	+0.26	+z
	T	-0.05	+y
17	**C 16**		
	R	+10	+z
	T	-0.09	+x
	T	+0.21	+y
	T	-1.01	+z
18	**C 17**		
	T	+2	+z
19	R	+30	+x
	T	+1.45	+x
	R	+44.7	+z
	T	+1.02	+z
20	**C 8**		
	R	+199	+z
	T	+0.03	+x
	T	-0.25	+y
	T	+0.05	+z
	R	+5	+x
21	R	-44.999	+x
	T	-1.45	+x
	R	-58	+z
22	**C 21**		
	T	+2	+z
23	R	+99.6	+z
	T	+0.055	+z
	R	+2	+x
24	**C 23**		
	T	+2	+z

Appendix 3: User-defined codes

(a) for the verification of the active region selection

Particle 2 of 4-hole cylinders model with 3% activity, as an example:

```
#include "udf.h"


DEFINE_ON_DEMAND(verif_2)
{
 Domain *d;
 int ID = 10;
 real cyl_rad, midpellet_dist, p_dist, axis_dist;
 real rc, xc, yc, zc, de, a, b, cc, den, xt, yt, zt, x[ND_ND], delta, rh, rhc;
 real xc_h1, yc_h1, zc_h1, xc_h2, yc_h2, zc_h2, xc_h3, yc_h3, zc_h3;
 real xt_h1, yt_h1, zt_h1, xt_h2, yt_h2, zt_h2, xt_h3, yt_h3, zt_h3;
 real a_h1, b_h1, c_h1, a_h2, b_h2, c_h2, a_h3, b_h3, c_h3;
 real p_dist_h1, p_dist_h2, p_dist_h3, axis_dist_h1, axis_dist_h2, axis_dist_h3;
 real xt_h4, yt_h4, zt_h4, xc_h4, yc_h4, zc_h4, a_h4, b_h4, c_h4, p_dist_h4, axis_dist_h4;

 Thread *t;
 cell_t c;

 d = Get_Domain(1);
 t = Lookup_Thread(d, ID);

 begin_c_loop(c,t)

   {
    C_CENTROID(x,c,t);

   xc = -1.36*0.0254;
   yc = -0.496*0.0254;
   zc = 1.04*0.0254;

   xt = -1.484*0.0254;
   yt = -0.163*0.0254;
   zt = 1.394*0.0254;

    a = xt-xc;
    b = yt-yc;
    cc = zt-zc;

    xc_h1 = -1.118*0.0254;
    yc_h1 = -0.407*0.0254;
    zc_h1 = 1.04*0.0254;

    xt_h1 = -1.239*0.0254;
```

```
yt_h1 = -0.075*0.0254;
zt_h1 = 1.394*0.0254;

a_h1 = xt_h1-xc_h1;
b_h1 = yt_h1-yc_h1;
c_h1 = zt_h1-zc_h1;

xc_h2 = -1.425*0.0254;
yc_h2 = -0.323*0.0254;
zc_h2 = 0.856*0.0254;

xt_h2 = -1.546*0.0254;
yt_h2 = 0.009*0.0254;
zt_h2 = 1.21*0.0254;

a_h2 = xt_h2-xc_h2;
b_h2 = yt_h2-yc_h2;
c_h2 = zt_h2-zc_h2;

xc_h3 = -1.607*0.0254;
yc_h3 = -0.585*0.0254;
zc_h3 = 1.04*0.0254;

xt_h3 = -1.728*0.0254;
yt_h3 = -0.253*0.0254;
zt_h3 = 1.394*0.0254;

a_h3 = xt_h3-xc_h3;
b_h3 = yt_h3-yc_h3;
c_h3 = zt_h3-zc_h3;

xc_h4 = -1.3*0.0254;
yc_h4 = -0.669*0.0254;
zc_h4 = 1.224*0.0254;

xt_h4 = -1.421*0.0254;
yt_h4 = -0.336*0.0254;
zt_h4 = -1.497*0.0254;

a_h4 = xt_h4-xc_h4;
b_h4 = yt_h4-yc_h4;
c_h4 = zt_h4-zc_h4;

cyl_rad = 0.5*0.0254;
rc = cut*cyl_rad;
rh = 0.1434*0.0254;

delta = (1-cut)*cyl_rad;
rhc = rh+delta;

den = a*a+b*b+cc*cc;
```

```
        de = -a*xc-b*yc-cc*zc;
        midpellet_dist = fabs((a*x[0]+b*x[1]+cc*x[2]+de)/sqrt(den));

        p_dist = sqrt((x[0]-xc)*(x[0]-xc)+(x[1]-yc)*(x[1]-yc)+(x[2]-zc)*(x[2]-zc));
        axis_dist = sqrt((p_dist*p_dist)-(midpellet_dist*midpellet_dist));

        p_dist_h1 = sqrt((x[0]-xc_h1)*(x[0]-xc_h1)+(x[1]-yc_h1)*(x[1]-yc_h1)+(x[2]-zc_h1)*(x[2]-
zc_h1));
        axis_dist_h1 = sqrt((p_dist_h1*p_dist_h1)-(midpellet_dist*midpellet_dist));

        p_dist_h2 = sqrt((x[0]-xc_h2)*(x[0]-xc_h2)+(x[1]-yc_h2)*(x[1]-yc_h2)+(x[2]-zc_h2)*(x[2]-
zc_h2));
        axis_dist_h2 = sqrt((p_dist_h2*p_dist_h2)-(midpellet_dist*midpellet_dist));

        p_dist_h3 = sqrt((x[0]-xc_h3)*(x[0]-xc_h3)+(x[1]-yc_h3)*(x[1]-yc_h3)+(x[2]-zc_h3)*(x[2]-
zc_h3));
        axis_dist_h3 = sqrt((p_dist_h3*p_dist_h3)-(midpellet_dist*midpellet_dist));

        p_dist_h4 = sqrt((x[0]-xc_h4)*(x[0]-xc_h4)+(x[1]-yc_h4)*(x[1]-yc_h4)+(x[2]-zc_h4)*(x[2]-
zc_h4));
        axis_dist_h4 = sqrt((p_dist_h4*p_dist_h4)-(midpellet_dist*midpellet_dist));

        if (midpellet_dist < rc && axis_dist < rc && axis_dist_h1 > rhc && axis_dist_h2 > rhc &&
axis_dist_h3 > rhc && axis_dist_h4 > rhc)
           C_UDMI(c,t,0)=0.0;
        else
           C_UDMI(c,t,0)=1.0;
       }
     end_c_loop(c,t)

    }
```

(b) for the application of reaction heat effects approximation

Particle 2 of 4-hole cylinders model, as an example:

```
#include "udf.h"

#define rgas 0.0083144
#define rhos 1947.0
#define delhco -140.0
#define delhh -93.4
#define delhh2o 15.9
#define E1 209.2
#define E2 15.4
#define E3 109.4
#define A1 5.922e8
#define A2 6.028e-4
#define A3 1.093e3
#define delHr1 -206100000.0
#define delHr2 41150000.0
#define delHr3 -165000000.0
#define AKco 5.127e-13
#define AKh 5.68e-10
#define AKh2o 9.251
#define Pco 1.0795
#define Ph2 10.795
#define Ph2o 1462.7225
#define Pch4 516.4326
#define Pco2 167.5383
#define cut 0.97

DEFINE_SOURCE(q_tdep_2, cell, thread, dS, eqn)
{
 real source;
 real kco, kh, kh2o, DEN, k1, Kp1, r1, k2, Kp2, r2, k3, Kp3, r3;
 real Pkin1, Prev1, Pkin2, Prev2, Pkin3, Prev3;
 real dk1dt, dKp1dt, dk2dt, dKp2dt, dk3dt, dKp3dt, dDENdt, dr1dt, dr2dt, dr3dt;
 real cell_temp, x[ND_ND], cyl_rad, midpellet_dist, p_dist, axis_dist;
 real rc, xc, yc, zc, d, a, b, c, den, xt, yt, zt;
 real delta, rh, rhc;
 real xc_h1, yc_h1, zc_h1, xc_h2, yc_h2, zc_h2, xc_h3, yc_h3, zc_h3;
 real xt_h1, yt_h1, zt_h1, xt_h2, yt_h2, zt_h2, xt_h3, yt_h3, zt_h3;
 real a_h1, b_h1, c_h1, a_h2, b_h2, c_h2, a_h3, b_h3, c_h3;
 real p_dist_h1, p_dist_h2, p_dist_h3, axis_dist_h1, axis_dist_h2, axis_dist_h3;
 real xt_h4, yt_h4, zt_h4, xc_h4, yc_h4, zc_h4, a_h4, b_h4, c_h4, p_dist_h4, axis_dist_h4;

 cell_temp = C_T(cell, thread);

 C_CENTROID(x,cell,thread);

 xc = -1.36*0.0254;
```

```
yc = -0.496*0.0254;
zc = 1.04*0.0254;

xt = -1.484*0.0254;
yt = -0.163*0.0254;
zt = 1.394*0.0254;

a = xt-xc;
b = yt-yc;
c = zt-zc;

    xc_h1 = -1.118*0.0254;
    yc_h1 = -0.407*0.0254;
    zc_h1 = 1.04*0.0254;

    xt_h1 = -1.239*0.0254;
    yt_h1 = -0.075*0.0254;
    zt_h1 = 1.394*0.0254;

    a_h1 = xt_h1-xc_h1;
    b_h1 = yt_h1-yc_h1;
    c_h1 = zt_h1-zc_h1;

    xc_h2 = -1.425*0.0254;
    yc_h2 = -0.323*0.0254;
    zc_h2 = 0.856*0.0254;

    xt_h2 = -1.546*0.0254;
    yt_h2 = 0.009*0.0254;
    zt_h2 = 1.21*0.0254;

    a_h2 = xt_h2-xc_h2;
    b_h2 = yt_h2-yc_h2;
    c_h2 = zt_h2-zc_h2;

    xc_h3 = -1.607*0.0254;
    yc_h3 = -0.585*0.0254;
    zc_h3 = 1.04*0.0254;

    xt_h3 = -1.728*0.0254;
    yt_h3 = -0.253*0.0254;
    zt_h3 = 1.394*0.0254;

    a_h3 = xt_h3-xc_h3;
    b_h3 = yt_h3-yc_h3;
    c_h3 = zt_h3-zc_h3;

    xc_h4 = -1.3*0.0254;
    yc_h4 = -0.669*0.0254;
    zc_h4 = 1.224*0.0254;
```

```
      xt_h4 = -1.421*0.0254;
      yt_h4 = -0.336*0.0254;
      zt_h4 = -1.477*0.0254;

      a_h4 = xt_h4-xc_h4;
      b_h4 = yt_h4-yc_h4;
      c_h4 = zt_h4-zc_h4;

    cyl_rad = 0.5*0.0254;
    rc = cut*cyl_rad;
    rh = 0.1434*0.0254;

    delta = (1-cut)*cyl_rad;
    rhc = rh+delta;

    den = a*a+b*b+c*c;
    d = -a*xc-b*yc-c*zc;
    midpellet_dist = fabs((a*x[0]+b*x[1]+c*x[2]+d)/sqrt(den));

    p_dist = sqrt((x[0]-xc)*(x[0]-xc)+(x[1]-yc)*(x[1]-yc)+(x[2]-zc)*(x[2]-zc));
    axis_dist = sqrt((p_dist*p_dist)-(midpellet_dist*midpellet_dist));

      p_dist_h1 = sqrt((x[0]-xc_h1)*(x[0]-xc_h1)+(x[1]-yc_h1)*(x[1]-yc_h1)+(x[2]-zc_h1)*(x[2]-zc_h1));
      axis_dist_h1 = sqrt((p_dist_h1*p_dist_h1)-(midpellet_dist*midpellet_dist));

      p_dist_h2 = sqrt((x[0]-xc_h2)*(x[0]-xc_h2)+(x[1]-yc_h2)*(x[1]-yc_h2)+(x[2]-zc_h2)*(x[2]-zc_h2));
      axis_dist_h2 = sqrt((p_dist_h2*p_dist_h2)-(midpellet_dist*midpellet_dist));

      p_dist_h3 = sqrt((x[0]-xc_h3)*(x[0]-xc_h3)+(x[1]-yc_h3)*(x[1]-yc_h3)+(x[2]-zc_h3)*(x[2]-zc_h3));
      axis_dist_h3 = sqrt((p_dist_h3*p_dist_h3)-(midpellet_dist*midpellet_dist));

      p_dist_h4 = sqrt((x[0]-xc_h4)*(x[0]-xc_h4)+(x[1]-yc_h4)*(x[1]-yc_h4)+(x[2]-zc_h4)*(x[2]-zc_h4));
      axis_dist_h4 = sqrt((p_dist_h4*p_dist_h4)-(midpellet_dist*midpellet_dist));


    if (cell_temp <= 550)
      source = dS[eqn] = 0.0;
    else if (midpellet_dist < rc && axis_dist < rc && axis_dist_h1 > rhc && axis_dist_h2 > rhc && axis_dist_h3 > rhc && axis_dist_h4 > rhc)
      source = dS[eqn] = 0.0;
    else
     {
      Pkin1 = Pch4*pow(Ph2o,0.5)/pow(Ph2,1.25);
      Prev1 = Pco*pow(Ph2,3.)/Pch4/Ph2o;
      Pkin2 = Pco*pow(Ph2o,0.5)/pow(Ph2,0.5);
      Prev2 = Pco2*Ph2/Pco/Ph2o;
      Pkin3 = Pch4*Ph2o/pow(Ph2,1.75);
```

```
      Prev3 = Pco2*pow(Ph2,4.)/Pch4/pow(Ph2o,2.);

      kco = AKco*exp(-delhco/(rgas*cell_temp));
      kh = AKh*exp(-delhh/(rgas*cell_temp));
      kh2o = AKh2o*exp(-delhh2o/(rgas*cell_temp));
      DEN = 1+Pco*kco+pow(Ph2,0.5)*kh+Ph2o/Ph2*kh2o;
      Kp1 = 1.198e17*exp(-26830/(cell_temp));
      Kp2 = 1.767e-2*exp(4400/(cell_temp));
      Kp3 = 2.117e15*exp(-22430/(cell_temp));

      k1 = A1*exp(-E1/(rgas*cell_temp));
      r1 = k1*Pkin1*(1-Prev1/Kp1)/pow(DEN,2.);

      k2 = A2*exp(-E2/(rgas*cell_temp));
      r2 = k2*Pkin2*(1-Prev2/Kp2)/pow(DEN,2.);

      k3 = A3*exp(-E3/(rgas*cell_temp));
      r3 = k3*Pkin3*(1-Prev3/Kp3)/pow(DEN,2.);

      source = rhos*(delHr1*r1+delHr2*r2+delHr3*r3);

      dDENdt = Pco*kco*delhco/rgas/cell_temp/cell_temp
          +pow(Ph2,0.5)*kh*delhh/rgas/cell_temp/cell_temp
          +Ph2o/Ph2*kh2o*delhh2o/rgas/cell_temp/cell_temp;

      dk1dt = k1*E1/rgas/cell_temp/cell_temp;
      dk2dt = k2*E2/rgas/cell_temp/cell_temp;
      dk3dt = k3*E3/rgas/cell_temp/cell_temp;

      dKp1dt = Kp1*26830/cell_temp/cell_temp;
      dKp2dt = Kp2*(-4400)/cell_temp/cell_temp;
      dKp3dt = Kp3*22430/cell_temp/cell_temp;

      dr1dt = dk1dt*Pkin1*(1-Prev1/Kp1)/pow(DEN,2.)
         +k1*Pkin1*(Prev1/Kp1/Kp1)*dKp1dt/pow(DEN,2.)
         -2*k1*Pkin1*(1-Prev1/Kp1)/pow(DEN,3.)*dDENdt;

      dr2dt = dk2dt*Pkin2*(1-Prev2/Kp2)/pow(DEN,2.)
         +k2*Pkin2*(Prev2/Kp2/Kp2)*dKp2dt/pow(DEN,2.)
         -2*k2*Pkin2*(1-Prev2/Kp2)/pow(DEN,3.)*dDENdt;

      dr3dt = dk3dt*Pkin3*(1-Prev3/Kp3)/pow(DEN,2.)
         +k3*Pkin3*(Prev3/Kp3/Kp3)*dKp3dt/pow(DEN,2.)
         -2*k3*Pkin3*(1-Prev3/Kp3)/pow(DEN,3.)*dDENdt;
      dS[eqn] = rhos*(delHr1*dr1dt+delHr2*dr2dt+delHr3*dr3dt);
    }
  return source;
}
```

(c) for the diffusion/reaction application of MSR

```
#include "udf.h"

#define rgas 0.0083144
#define rhos 1947.0
#define delhco -140.0
#define delhh -93.4
#define delhh2o 15.9
#define E1 209.2
#define E2 15.4
#define E3 109.4
#define A1 5.922e8
#define A2 6.028e-4
#define A3 1.093e3
#define delHr1 -206100000.0
#define delHr2 41150000.0
#define delHr3 -165000000.0
#define AKco 5.127e-13
#define AKh 5.68e-10
#define AKh2o 9.251
#define Mco 28.0
#define Mh2 2.0
#define Mh2o 18.0
#define Mch4 16.0
#define Mco2 44.0
#define Totpress 2159000.0


DEFINE_SOURCE(spe_ch4, cell, thread, dS, eqn)
{
  real source;
  real kco, kh, kh2o, DEN, k1, Kp1, r1, k2, Kp2, r2, k3, Kp3, r3;
  real Pkin1, Prev1, Pkin2, Prev2, Pkin3, Prev3;
  real dPch4dych4, dr1dPch4, dr2dPch4, dr3dPch4;
  real cell_temp, cell_press;
  real ych4, yh2, yco, yco2, yh2o, Ysum, Pch4, Ph2, Pco, Pco2, Ph2o;
  real alph1, alph2, alph3;

  cell_temp = C_T(cell, thread);
  cell_press = (Totpress+C_P(cell, thread))/1000.0;

  ych4 = C_YI(cell, thread, 0);
  yh2 = C_YI(cell, thread, 1);
  yco = C_YI(cell, thread, 2);
  yco2 = C_YI(cell, thread, 3);
  yh2o = 1.0-ych4-yh2-yco-yco2;
  Ysum = ych4/Mch4+yco/Mco+yco2/Mco2+yh2/Mh2+yh2o/Mh2o;
  Pch4 = cell_press*ych4/Mch4/Ysum;
  Ph2 = cell_press*yh2/Mh2/Ysum;
  Pco = cell_press*yco/Mco/Ysum;
```

```
Pco2 = cell_press*yco2/Mco2/Ysum;
Ph2o = cell_press*yh2o/Mh2o/Ysum;

alph1 = -1.0;
alph2 = 0.0;
alph3 = -1.0;

if (cell_temp <= 550)
   source = dS[eqn] = 0.0;
else
  {
   Pkin1 = Pch4*pow(Ph2o,0.5)/pow(Ph2,1.25);
   Prev1 = Pco*pow(Ph2,3.)/Pch4/Ph2o;
   Pkin2 = Pco*pow(Ph2o,0.5)/pow(Ph2,0.5);
   Prev2 = Pco2*Ph2/Pco/Ph2o;
   Pkin3 = Pch4*Ph2o/pow(Ph2,1.75);
   Prev3 = Pco2*pow(Ph2,4.)/Pch4/pow(Ph2o,2.);

   kco = AKco*exp(-delhco/(rgas*cell_temp));
   kh = AKh*exp(-delhh/(rgas*cell_temp));
   kh2o = AKh2o*exp(-delhh2o/(rgas*cell_temp));

   DEN = 1+Pco*kco+pow(Ph2,0.5)*kh+Ph2o/Ph2*kh2o;

   Kp1 = 1.198e17*exp(-26830/(cell_temp));
   Kp2 = 1.767e-2*exp(4400/(cell_temp));
   Kp3 = 2.117e15*exp(-22430/(cell_temp));

   k1 = A1*exp(-E1/(rgas*cell_temp));
   r1 = k1*Pkin1*(1-Prev1/Kp1)/pow(DEN,2.);

   k2 = A2*exp(-E2/(rgas*cell_temp));
   r2 = k2*Pkin2*(1-Prev2/Kp2)/pow(DEN,2.);

   k3 = A3*exp(-E3/(rgas*cell_temp));
   r3 = k3*Pkin3*(1-Prev3/Kp3)/pow(DEN,2.);

   source = rhos*(alph1*r1+alph2*r2+alph3*r3)*Mch4;

   dPch4dych4 = cell_press*(Ysum/Mch4-(ych4/Mch4)/Mch4)/Ysum/Ysum;

   dr1dPch4 = k1*pow(Ph2o,0.5)/pow(Ph2,1.25)*(1-Prev1/Kp1)/pow(DEN,2.)
        +k1*Pkin1*(Pco*pow(Ph2,3.)/Kp1/pow(Pch4,2.)/Ph2o)/pow(DEN,2.);

   dr2dPch4 = 0;

   dr3dPch4 = k3*Ph2o/pow(Ph2,1.75)*(1-Prev3/Kp3)/pow(DEN,2.)
        +k3*Pkin3*(Pco2*pow(Ph2,4.)/Kp3/pow(Pch4,2.)/pow(Ph2o,2.))/pow(DEN,2.);

   dS[eqn] = rhos*Mch4*(alph1*dr1dPch4+alph2*dr2dPch4+alph3*dr3dPch4)*dPch4dych4;
  }
```

```
  return source;
}

DEFINE_SOURCE(spe_h2, cell, thread, dS, eqn)
{
  real source;
  real kco, kh, kh2o, DEN, k1, Kp1, r1, k2, Kp2, r2, k3, Kp3, r3;
  real Pkin1, Prev1, Pkin2, Prev2, Pkin3, Prev3;
  real dPh2dyh2, dDENdPh2, dr1dPh2, dr2dPh2, dr3dPh2;
  real cell_temp, cell_press;
  real ych4, yh2, yco, yco2, yh2o, Ysum, Pch4, Ph2, Pco, Pco2, Ph2o;
  real alph1, alph2, alph3;

  cell_temp = C_T(cell, thread);
  cell_press = (Totpress+C_P(cell, thread))/1000.0;
  ych4 = C_YI(cell, thread, 0);
  yh2 = C_YI(cell, thread, 1);
  yco = C_YI(cell, thread, 2);
  yco2 = C_YI(cell, thread, 3);
  yh2o = 1.0-ych4-yh2-yco-yco2;
  Ysum = ych4/Mch4+yco/Mco+yco2/Mco2+yh2/Mh2+yh2o/Mh2o;
  Pch4 = cell_press*ych4/Mch4/Ysum;
  Ph2 = cell_press*yh2/Mh2/Ysum;
  Pco = cell_press*yco/Mco/Ysum;
  Pco2 = cell_press*yco2/Mco2/Ysum;
  Ph2o = cell_press*yh2o/Mh2o/Ysum;

  alph1 = 3.0;
  alph2 = 1.0;
  alph3 = 4.0;

  if (cell_temp <= 550)
     source = dS[eqn] = 0.0;
  else
    {
     Pkin1 = Pch4*pow(Ph2o,0.5)/pow(Ph2,1.25);
     Prev1 = Pco*pow(Ph2,3.)/Pch4/Ph2o;
     Pkin2 = Pco*pow(Ph2o,0.5)/pow(Ph2,0.5);
     Prev2 = Pco2*Ph2/Pco/Ph2o;
     Pkin3 = Pch4*Ph2o/pow(Ph2,1.75);
     Prev3 = Pco2*pow(Ph2,4.)/Pch4/pow(Ph2o,2.);

     kco = AKco*exp(-delhco/(rgas*cell_temp));
     kh = AKh*exp(-delhh/(rgas*cell_temp));
     kh2o = AKh2o*exp(-delhh2o/(rgas*cell_temp));

     DEN = 1+Pco*kco+pow(Ph2,0.5)*kh+Ph2o/Ph2*kh2o;

     Kp1 = 1.198e17*exp(-26830/(cell_temp));
     Kp2 = 1.767e-2*exp(4400/(cell_temp));
```

```
    Kp3 = 2.117e15*exp(-22430/(cell_temp));

    k1 = A1*exp(-E1/(rgas*cell_temp));
    r1 = k1*Pkin1*(1-Prev1/Kp1)/pow(DEN,2.);

    k2 = A2*exp(-E2/(rgas*cell_temp));
    r2 = k2*Pkin2*(1-Prev2/Kp2)/pow(DEN,2.);

    k3 = A3*exp(-E3/(rgas*cell_temp));
    r3 = k3*Pkin3*(1-Prev3/Kp3)/pow(DEN,2.);

    source = rhos*(alph1*r1+alph2*r2+alph3*r3)*Mh2;

    dPh2dyh2 = cell_press*(Ysum/Mh2-(yh2/Mh2)/Mh2)/Ysum/Ysum;

    dDENdPh2 = 0.5*kh/pow(Ph2,0.5)-kh2o*Ph2o/pow(Ph2,2.);

    dr1dPh2 = k1*(-1.25*Pch4*pow(Ph2o,0.5)/pow(Ph2,2.25))*(1-Prev1/Kp1)/pow(DEN,2.)
        +k1*Pkin1*(-3.0*Pco*pow(Ph2,3.)/Kp1/Pch4/Ph2o)/pow(DEN,2.)
        -2.0*k1*Pkin1*(1-Prev1/Kp1)/pow(DEN,3.)*dDENdPh2;

    dr2dPh2 = k2*(-0.25*Pco*pow(Ph2o,0.5)/pow(Ph2,1.5))*(1-Prev2/Kp2)/pow(DEN,2.)
        +k2*Pkin2*(-1.0*Pco2)/Kp2/Pco/Ph2o/pow(DEN,2.)
        -2.0*k2*Pkin2*(1-Prev2/Kp2)/pow(DEN,3.)*dDENdPh2;

    dr3dPh2 = k3*(-1.75*Pch4*Ph2o)/pow(Ph2,2.75)*(1-Prev3/Kp3)/pow(DEN,2.)
        +k3*Pkin3*(-4.0*Pco2*pow(Ph2,3.))/Kp3/Pch4/pow(Ph2o,2.)/pow(DEN,2.)
        -2.0*k3*Pkin3*(1-Prev3/Kp3)/pow(DEN,3.)*dDENdPh2;

    dS[eqn] = rhos*Mh2*(alph1*dr1dPh2+alph2*dr2dPh2+alph3*dr3dPh2)*dPh2dyh2;
   }

  return source;
}

DEFINE_SOURCE(spe_co, cell, thread, dS, eqn)
{
  real source;
  real kco, kh, kh2o, DEN, k1, Kp1, r1, k2, Kp2, r2, k3, Kp3, r3;
  real Pkin1, Prev1, Pkin2, Prev2, Pkin3, Prev3;
  real dPcodyco, dDENdPco, dr1dPco, dr2dPco, dr3dPco;
  real cell_temp, cell_press;
  real ych4, yh2, yco, yco2, yh2o, Ysum, Pch4, Ph2, Pco, Pco2, Ph2o;
  real alph1, alph2, alph3;

  cell_temp = C_T(cell, thread);
  cell_press = (Totpress+C_P(cell, thread))/1000.0;
  ych4 = C_YI(cell, thread, 0);
  yh2 = C_YI(cell, thread, 1);
  yco = C_YI(cell, thread, 2);
  yco2 = C_YI(cell, thread, 3);
```

```
yh2o = 1.0-ych4-yh2-yco-yco2;
Ysum = ych4/Mch4+yco/Mco+yco2/Mco2+yh2/Mh2+yh2o/Mh2o;
Pch4 = cell_press*ych4/Mch4/Ysum;
Ph2 = cell_press*yh2/Mh2/Ysum;
Pco = cell_press*yco/Mco/Ysum;
Pco2 = cell_press*yco2/Mco2/Ysum;
Ph2o = cell_press*yh2o/Mh2o/Ysum;

alph1 = 1.0;
alph2 = -1.0;
alph3 = 0.0;

if (cell_temp <= 550)
   source = dS[eqn] = 0.0;
else
  {
   Pkin1 = Pch4*pow(Ph2o,0.5)/pow(Ph2,1.25);
   Prev1 = Pco*pow(Ph2,3.)/Pch4/Ph2o;
   Pkin2 = Pco*pow(Ph2o,0.5)/pow(Ph2,0.5);
   Prev2 = Pco2*Ph2/Pco/Ph2o;
   Pkin3 = Pch4*Ph2o/pow(Ph2,1.75);
   Prev3 = Pco2*pow(Ph2,4.)/Pch4/pow(Ph2o,2.);

   kco = AKco*exp(-delhco/(rgas*cell_temp));
   kh = AKh*exp(-delhh/(rgas*cell_temp));
   kh2o = AKh2o*exp(-delhh2o/(rgas*cell_temp));

   DEN = 1+Pco*kco+pow(Ph2,0.5)*kh+Ph2o/Ph2*kh2o;

   Kp1 = 1.198e17*exp(-26830/(cell_temp));
   Kp2 = 1.767e-2*exp(4400/(cell_temp));
   Kp3 = 2.117e15*exp(-22430/(cell_temp));


   k1 = A1*exp(-E1/(rgas*cell_temp));
   r1 = k1*Pkin1*(1-Prev1/Kp1)/pow(DEN,2.);

   k2 = A2*exp(-E2/(rgas*cell_temp));
   r2 = k2*Pkin2*(1-Prev2/Kp2)/pow(DEN,2.);

   k3 = A3*exp(-E3/(rgas*cell_temp));
   r3 = k3*Pkin3*(1-Prev3/Kp3)/pow(DEN,2.);

   source = rhos*(alph1*r1+alph2*r2+alph3*r3)*Mco;

   dPcodyco = cell_press*(Ysum/Mco-(yco/Mco)/Mco)/Ysum/Ysum;

   dDENdPco = kco;

   dr1dPco = k1*Pkin1*(-1.0*pow(Ph2,3.)/Kp1/Pch4/Ph2o)/pow(DEN,2.)
        -2.0*k1*Pkin1*(1-Prev1/Kp1)/pow(DEN,3.)*dDENdPco;
```

```
      dr2dPco = k2*pow(Ph2o,0.5)/pow(Ph2,0.5)*(1-Prev2/Kp2)/pow(DEN,2.)
            +k2*Pkin2*(Ph2*Pco2)/Kp2/pow(Pco,2.)/Ph2o/pow(DEN,2.)
            -2.0*k2*Pkin2*(1-Prev2/Kp2)/pow(DEN,3.)*dDENdPco;

      dr3dPco = -2.0*k3*Pkin3*(1-Prev3/Kp3)/pow(DEN,3.)*dDENdPco;

      dS[eqn] = rhos*Mco*(alph1*dr1dPco+alph2*dr2dPco+alph3*dr3dPco)*dPcodyco;
    }

  return source;
}

DEFINE_SOURCE(spe_co2, cell, thread, dS, eqn)
{
  real source;
  real kco, kh, kh2o, DEN, k1, Kp1, r1, k2, Kp2, r2, k3, Kp3, r3;
  real Pkin1, Prev1, Pkin2, Prev2, Pkin3, Prev3;
  real dPco2dyco2, dr1dPco2, dr2dPco2, dr3dPco2;
  real cell_temp, cell_press;
  real ych4, yh2, yco, yco2, yh2o, Ysum, Pch4, Ph2, Pco, Pco2, Ph2o;
  real alph1, alph2, alph3;

  cell_temp = C_T(cell, thread);
  cell_press = (Totpress+C_P(cell, thread))/1000.0;
  ych4 = C_YI(cell, thread, 0);
  yh2 = C_YI(cell, thread, 1);
  yco = C_YI(cell, thread, 2);
  yco2 = C_YI(cell, thread, 3);
  yh2o = 1.0-ych4-yh2-yco-yco2;
  Ysum = ych4/Mch4+yco/Mco+yco2/Mco2+yh2/Mh2+yh2o/Mh2o;
  Pch4 = cell_press*ych4/Mch4/Ysum;
  Ph2 = cell_press*yh2/Mh2/Ysum;
  Pco = cell_press*yco/Mco/Ysum;
  Pco2 = cell_press*yco2/Mco2/Ysum;
  Ph2o = cell_press*yh2o/Mh2o/Ysum;

  alph1 = 0.0;
  alph2 = 1.0;
  alph3 = 1.0;

  if (cell_temp <= 550)
      source = dS[eqn] = 0.0;
  else
    {
      Pkin1 = Pch4*pow(Ph2o,0.5)/pow(Ph2,1.25);
      Prev1 = Pco*pow(Ph2,3.)/Pch4/Ph2o;
      Pkin2 = Pco*pow(Ph2o,0.5)/pow(Ph2,0.5);
      Prev2 = Pco2*Ph2/Pco/Ph2o;
      Pkin3 = Pch4*Ph2o/pow(Ph2,1.75);
      Prev3 = Pco2*pow(Ph2,4.)/Pch4/pow(Ph2o,2.);
```

```
    kco = AKco*exp(-delhco/(rgas*cell_temp));
    kh = AKh*exp(-delhh/(rgas*cell_temp));
    kh2o = AKh2o*exp(-delhh2o/(rgas*cell_temp));

    DEN = 1+Pco*kco+pow(Ph2,0.5)*kh+Ph2o/Ph2*kh2o;

    Kp1 = 1.198e17*exp(-26830/(cell_temp));
    Kp2 = 1.767e-2*exp(4400/(cell_temp));
    Kp3 = 2.117e15*exp(-22430/(cell_temp));

    k1 = A1*exp(-E1/(rgas*cell_temp));
    r1 = k1*Pkin1*(1-Prev1/Kp1)/pow(DEN,2.);

    k2 = A2*exp(-E2/(rgas*cell_temp));
    r2 = k2*Pkin2*(1-Prev2/Kp2)/pow(DEN,2.);

    k3 = A3*exp(-E3/(rgas*cell_temp));
    r3 = k3*Pkin3*(1-Prev3/Kp3)/pow(DEN,2.);

    source = rhos*(alph1*r1+alph2*r2+alph3*r3)*Mco2;

    dPco2dyco2 = cell_press*(Ysum/Mco2-(yco2/Mco2)/Mco2)/Ysum/Ysum;

    dr1dPco2 = 0;

    dr2dPco2 = k2*Pkin2*(-1.0*Ph2)/Kp2/Pco/Ph2o/pow(DEN,2.);

    dr3dPco2 = k3*Pkin3*(-1.0*pow(Ph2,4.)/Kp3/Pch4/pow(Ph2o,2.))/pow(DEN,2.);

    dS[eqn] = rhos*Mco2*(alph1*dr1dPco2+alph2*dr2dPco2+alph3*dr3dPco2)*dPco2dyco2;
   }

  return source;
}

DEFINE_SOURCE(q_tdep, cell, thread, dS, eqn)
{
  real source;
  real kco, kh, kh2o, DEN, k1, Kp1, r1, k2, Kp2, r2, k3, Kp3, r3;
  real Pkin1, Prev1, Pkin2, Prev2, Pkin3, Prev3;
  real dk1dt, dKp1dt, dk2dt, dKp2dt, dk3dt, dKp3dt, dDENdt, dr1dt, dr2dt, dr3dt;
  real cell_temp, cell_press;
  real ych4, yh2, yco, yco2, yh2o, Ysum, Pch4, Ph2, Pco, Pco2, Ph2o;

  cell_temp = C_T(cell, thread);
  cell_press = (Totpress+C_P(cell, thread))/1000.0;
  ych4 = C_YI(cell, thread, 0);
  yh2 = C_YI(cell, thread, 1);
  yco = C_YI(cell, thread, 2);
  yco2 = C_YI(cell, thread, 3);
```

```
yh2o = 1.0-ych4-yh2-yco-yco2;
Ysum = ych4/Mch4+yco/Mco+yco2/Mco2+yh2/Mh2+yh2o/Mh2o;
Pch4 = cell_press*ych4/Mch4/Ysum;
Ph2 = cell_press*yh2/Mh2/Ysum;
Pco = cell_press*yco/Mco/Ysum;
Pco2 = cell_press*yco2/Mco2/Ysum;
Ph2o = cell_press*yh2o/Mh2o/Ysum;

if (cell_temp <= 550)
   source = dS[eqn] = 0.0;
else
  {
   Pkin1 = Pch4*pow(Ph2o,0.5)/pow(Ph2,1.25);
   Prev1 = Pco*pow(Ph2,3.)/Pch4/Ph2o;
   Pkin2 = Pco*pow(Ph2o,0.5)/pow(Ph2,0.5);
   Prev2 = Pco2*Ph2/Pco/Ph2o;
   Pkin3 = Pch4*Ph2o/pow(Ph2,1.75);
   Prev3 = Pco2*pow(Ph2,4.)/Pch4/pow(Ph2o,2.);

   kco = AKco*exp(-delhco/(rgas*cell_temp));
   kh = AKh*exp(-delhh/(rgas*cell_temp));
   kh2o = AKh2o*exp(-delhh2o/(rgas*cell_temp));

   DEN = 1+Pco*kco+pow(Ph2,0.5)*kh+Ph2o/Ph2*kh2o;

   Kp1 = 1.198e17*exp(-26830/(cell_temp));
   Kp2 = 1.767e-2*exp(4400/(cell_temp));
   Kp3 = 2.117e15*exp(-22430/(cell_temp));

   k1 = A1*exp(-E1/(rgas*cell_temp));
   r1 = k1*Pkin1*(1-Prev1/Kp1)/pow(DEN,2.);

   k2 = A2*exp(-E2/(rgas*cell_temp));
   r2 = k2*Pkin2*(1-Prev2/Kp2)/pow(DEN,2.);

   k3 = A3*exp(-E3/(rgas*cell_temp));
   r3 = k3*Pkin3*(1-Prev3/Kp3)/pow(DEN,2.);

   source = rhos*(delHr1*r1+delHr2*r2+delHr3*r3);

   dDENdt = Pco*kco*delhco/rgas/cell_temp/cell_temp
         +pow(Ph2,0.5)*kh*delhh/rgas/cell_temp/cell_temp
         +Ph2o/Ph2*kh2o*delhh2o/rgas/cell_temp/cell_temp;

   dk1dt = k1*E1/rgas/cell_temp/cell_temp;
   dk2dt = k2*E2/rgas/cell_temp/cell_temp;
   dk3dt = k3*E3/rgas/cell_temp/cell_temp;

   dKp1dt = Kp1*26830/cell_temp/cell_temp;
   dKp2dt = Kp2*(-4400)/cell_temp/cell_temp;
   dKp3dt = Kp3*22430/cell_temp/cell_temp;
```

```
      dr1dt = dk1dt*Pkin1*(1-Prev1/Kp1)/pow(DEN,2.)
            +k1*Pkin1*(Prev1/Kp1/Kp1)*dKp1dt/pow(DEN,2.)
            -2*k1*Pkin1*(1-Prev1/Kp1)/pow(DEN,3.)*dDENdt;

      dr2dt = dk2dt*Pkin2*(1-Prev2/Kp2)/pow(DEN,2.)
            +k2*Pkin2*(Prev2/Kp2/Kp2)*dKp2dt/pow(DEN,2.)
            -2*k2*Pkin2*(1-Prev2/Kp2)/pow(DEN,3.)*dDENdt;

      dr3dt = dk3dt*Pkin3*(1-Prev3/Kp3)/pow(DEN,2.)
            +k3*Pkin3*(Prev3/Kp3/Kp3)*dKp3dt/pow(DEN,2.)
            -2*k3*Pkin3*(1-Prev3/Kp3)/pow(DEN,3.)*dDENdt;

      dS[eqn] = rhos*(delHr1*dr1dt+delHr2*dr2dt+delHr3*dr3dt);
    }

  return source;
}
```

(d) for the MSR reaction rate calculation in particle 2

```
include "udf.h"

#define rgas 0.0083144
#define rhos 1947.0
#define delhco -140.0
#define delhh -93.4
#define delhh2o 15.9
#define E1 209.2
#define E2 15.4
#define E3 109.4
#define A1 5.922e8
#define A2 6.028e-4
#define A3 1.093e3
#define delHr1 -206100000.0
#define delHr2 41150000.0
#define delHr3 -165000000.0
#define AKco 5.127e-13
#define AKh 5.68e-10
#define AKh2o 9.251
#define Mco 28.0
#define Mh2 2.0
#define Mh2o 18.0
#define Mch4 16.0
#define Mco2 44.0
#define Totpress 2159000.0

FILE *fp = NULL;

DEFINE_ON_DEMAND(part2)
{
 Domain *d;
 int ID = 13;

 real kco, kh, kh2o, DEN, k1, Kp1, r1, k2, Kp2, r2, k3, Kp3, r3;
 real Pkin1, Prev1, Pkin2, Prev2, Pkin3, Prev3;
 real dPch4dych4, dr1dPch4, dr2dPch4, dr3dPch4;
 real cell_temp, cell_press, cell_vol;
 real ych4, yh2, yco, yco2, yh2o, Ysum, Pch4, Ph2, Pco, Pco2, Ph2o;
 real alph1, alph2, alph3;
 real r1ave, r2ave, r3ave, rch4, vol_tot;
 real x[ND_ND];

 Thread *t;
 cell_t c;

 d = Get_Domain(1);
 t = Lookup_Thread(d, ID);

fp = fopen("data.txt","w");
```

```
begin_c_loop(c,t)

  {
cell_temp = C_T(c, t);
cell_press = (Totpress+C_P(c, t))/1000.0;
C_CENTROID(x,c,t);
cell_vol = C_VOLUME(c, t);

ych4 = C_YI(c, t, 0);
yh2 = C_YI(c, t, 1);
yco = C_YI(c, t, 2);
yco2 = C_YI(c, t, 3);
yh2o = 1.0-ych4-yh2-yco-yco2;
Ysum = ych4/Mch4+yco/Mco+yco2/Mco2+yh2/Mh2+yh2o/Mh2o;
Pch4 = cell_press*ych4/Mch4/Ysum;
Ph2 = cell_press*yh2/Mh2/Ysum;
Pco = cell_press*yco/Mco/Ysum;
Pco2 = cell_press*yco2/Mco2/Ysum;
Ph2o = cell_press*yh2o/Mh2o/Ysum;

alph1 = -1.0;
alph2 = 0.0;
alph3 = -1.0;

   Pkin1 = Pch4*pow(Ph2o,0.5)/pow(Ph2,1.25);
   Prev1 = Pco*pow(Ph2,3.)/Pch4/Ph2o;
   Pkin2 = Pco*pow(Ph2o,0.5)/pow(Ph2,0.5);
   Prev2 = Pco2*Ph2/Pco/Ph2o;
   Pkin3 = Pch4*Ph2o/pow(Ph2,1.75);
   Prev3 = Pco2*pow(Ph2,4.)/Pch4/pow(Ph2o,2.);

   kco = AKco*exp(-delhco/(rgas*cell_temp));
   kh = AKh*exp(-delhh/(rgas*cell_temp));
   kh2o = AKh2o*exp(-delhh2o/(rgas*cell_temp));

   DEN = 1+Pco*kco+pow(Ph2,0.5)*kh+Ph2o/Ph2*kh2o;

   Kp1 = 1.198e17*exp(-26830/(cell_temp));
   Kp2 = 1.767e-2*exp(4400/(cell_temp));
   Kp3 = 2.117e15*exp(-22430/(cell_temp));

   k1 = A1*exp(-E1/(rgas*cell_temp));
   r1 = k1*Pkin1*(1-Prev1/Kp1)/pow(DEN,2.);

   k2 = A2*exp(-E2/(rgas*cell_temp));
   r2 = k2*Pkin2*(1-Prev2/Kp2)/pow(DEN,2.);

   k3 = A3*exp(-E3/(rgas*cell_temp));
   r3 = k3*Pkin3*(1-Prev3/Kp3)/pow(DEN,2.);
```

```
    vol_tot += C_VOLUME(c,t);

    r1ave += r1*cell_vol;
    r2ave += r2*cell_vol;
    r3ave += r3*cell_vol;
    }
  end_c_loop(c,t)
  fclose(fp);

    r1ave /= vol_tot;
    r2ave /= vol_tot;
    r3ave /= vol_tot;

    rch4 = r1ave+r3ave;
   printf("%15e %15e %15e\n", r3ave, r2ave, r1ave);
}
```

(e) for the diffusion/reaction application of PDH

```
#include "udf.h"

#define rgas 8.3144
#define rhos 1000.0
#define ka 9.94
#define kb 72000
#define KA 16.749
#define KB 130000
#define delH -124300000.0
#define Mc3h8 44.0
#define Mc3h6 42.0
#define Mh2 2.0
#define Totpress 101500.0



DEFINE_SOURCE(spe_c3h6, cell, thread, dS, eqn)
{
  real source;
  real k, Ke, r;
  real dPc3h6dyc3h6, drdPc3h6;
  real cell_temp, cell_press;
  real yc3h8, yc3h6, yh2, Ysum, Pc3h8, Pc3h6, Ph2;

  cell_temp = C_T(cell, thread);
  cell_press = (Totpress+C_P(cell, thread))/1000.0;

  yc3h6 = C_YI(cell, thread, 0);
  yh2 = C_YI(cell, thread, 1);
  yc3h8 = C_YI(cell, thread, 2);
  Ysum = yc3h6/Mc3h6+yh2/Mh2+yc3h8/Mc3h8;

  Pc3h6 = cell_press*yc3h6/Mc3h6/Ysum;
  Ph2 = cell_press*yh2/Mh2/Ysum;
  Pc3h8 = cell_press*yc3h8/Mc3h8/Ysum;

  if (cell_temp <= 550)
      source = dS[eqn] = 0.0;
  else
    {
      k = exp(ka - kb/(rgas*cell_temp));
      Ke = cell_press/(rgas*cell_temp)*exp(KA - KB/(rgas*cell_temp));

      r = k*(Pc3h8/rgas/cell_temp - Pc3h6*Ph2/(rgas*rgas*cell_temp*cell_temp*Ke));

       source = r*Mc3h6;

      dPc3h6dyc3h6 = cell_press*(Ysum/Mc3h6-(yc3h6/Mc3h6)/Mc3h6)/Ysum/Ysum;
```

```
    drdPc3h6 = -k*Ph2/(Ke*rgas*rgas*cell_temp*cell_temp);

    dS[eqn] = Mc3h6*drdPc3h6*dPc3h6dyc3h6;
   }

 return source;
}

DEFINE_SOURCE(spe_h2, cell, thread, dS, eqn)
{
 real source;
 real k, Ke, r;
 real dPh2dyh2, drdPh2;
 real cell_temp, cell_press;
 real yc3h8, yc3h6, yh2, Ysum, Pc3h8, Pc3h6, Ph2;

 cell_temp = C_T(cell, thread);
 cell_press = (Totpress+C_P(cell, thread))/1000.0;

 yc3h6 = C_YI(cell, thread, 0);
 yh2 = C_YI(cell, thread, 1);
 yc3h8 = C_YI(cell, thread, 2);
 Ysum = yc3h6/Mc3h6+yh2/Mh2+yc3h8/Mc3h8;

 Pc3h6 = cell_press*yc3h6/Mc3h6/Ysum;
 Ph2 = cell_press*yh2/Mh2/Ysum;
 Pc3h8 = cell_press*yc3h8/Mc3h8/Ysum;

 if (cell_temp <= 550)
    source = dS[eqn] = 0.0;
 else
   {
    k = exp(ka - kb/(rgas*cell_temp));
    Ke = cell_press/(rgas*cell_temp)*exp(KA - KB/(rgas*cell_temp));

    r = k*(Pc3h8/rgas/cell_temp - Pc3h6*Ph2/(rgas*rgas*cell_temp*cell_temp*Ke));

     source = r*Mh2;

    dPh2dyh2 = cell_press*(Ysum/Mh2-(yh2/Mh2)/Mh2)/Ysum/Ysum;

    drdPh2 = -k*Pc3h6/(Ke*rgas*rgas*cell_temp*cell_temp);

    dS[eqn] = Mh2*drdPh2*dPh2dyh2;
   }

 return source;
}


DEFINE_SOURCE(q_tdep, cell, thread, dS, eqn)
```

```
{
  real source;
  real k, Ke, r;
  real dkdt, dKedt, drdt;
  real cell_temp, cell_press;
  real yc3h8, yc3h6, yh2, Ysum, Pc3h8, Pc3h6, Ph2;
  real rgs, cts;

  cell_temp = C_T(cell, thread);
  cell_press = (Totpress+C_P(cell, thread))/1000.0;

  yc3h6 = C_YI(cell, thread, 0);
  yh2 = C_YI(cell, thread, 1);
  yc3h8 = C_YI(cell, thread, 2);
  Ysum = yc3h6/Mc3h6+yh2/Mh2+yc3h8/Mc3h8;

  Pc3h6 = cell_press*yc3h6/Mc3h6/Ysum;
  Ph2 = cell_press*yh2/Mh2/Ysum;
  Pc3h8 = cell_press*yc3h8/Mc3h8/Ysum;

   if (cell_temp <= 550)
     source = dS[eqn] = 0.0;
  else
    {
      k = exp(ka - kb/(rgas*cell_temp));
     Ke = cell_press/(rgas*cell_temp)*exp(KA - KB/(rgas*cell_temp));

     r = k*(Pc3h8/rgas/cell_temp - Pc3h6*Ph2/(rgas*rgas*cell_temp*cell_temp*Ke));

      source = delH*r;

     dkdt = k*kb/rgas/cell_temp/cell_temp;

     dKedt = Ke*(KB/rgas/cell_temp/cell_temp-1/cell_temp);

     rgs = rgas*rgas;
     cts = cell_temp*cell_temp;

    drdt = dkdt*(Pc3h8/rgas/cell_temp - Pc3h6*Ph2/(rgs*cts*Ke))-k*(Pc3h8/(rgas*cts)-
2*Pc3h6*Ph2/(rgs*cts*cell_temp*Ke)+Pc3h6*Ph2/(rgs*cts*Ke*Ke)*dKedt);

     dS[eqn] = delH*drdt;
    }

  return source;
}
```

Appendix 4: Mesh structures of the WS models used in diffusion /reaction application

Table A.3 full cylinders packing grid details

	1st prism height x10^3 (m)	b/a*	Number of layers	Total prism height x10^3 (m)	UNS x10^3 (m)
Fluid side					0.7620
Particle 1	0.0254	1.2	3	0.09246	
Particle 2	0.0254	1.2	3	0.09246	
Particle 3	0.0254	1.2	3	0.09246	
Particle 4	0.0254	1.2	3	0.09246	
Particle 5	0.0254	1.2	3	0.09246	
Particle 6	0.0254	1.0	3	0.07620	
Particle 7	0.0254	1.0	3	0.07620	
Particle 8	0.0254	1.2	2	0.05588	
Particle 9	0.0254	1.2	3	0.09246	
Particle 10	0.0254	1.0	3	0.07620	
Particle 11	0.0254	1.0	3	0.07620	
Particle 12	0.0254	1.0	3	0.07620	
Tube wall	0.0254	1.2	4	0.13635	
Solid side (all particles)	0.0762	1.2	4	0.40904	0.7620

* The *b/a* represents the growth factor where *b* is the distance between the first and second rows at a given edge node, and *a* is the height of the first row at the node. The distance between any two rows in the boundary layer at a given edge node is equal to the distance between the preceding two rows times the growth factor.

Table A.4 4-holel cylinders packing grid details

	1st prism height x10^3 (m)	*b/a*	Number of layers	Total prism height x10^3 (m)	UNS x10^3 (m)
Fluid side					0.7620
Particle 1	0.0254	1.0	2	0.05080	
Particle 2	0.0254	1.0	3	0.07620	
Particle 3	0.0254	1.0	2	0.05080	
Particle 4	0.0254	1.0	2	0.05080	
Particle 5	0.0254	1.0	2	0.05080	
Particle 6	0.0254	1.0	1	0.02540	
Particle 7	0.0254	1.0	1	0.02540	
Particle 8	0.0254	1.0	1	0.02540	
Particle 9	0.0254	1.0	3	0.09246	
Particle 10	-	-	-	-	
Particle 11	-	-	-	-	
Particle 12	0.0254	1.0	2	0.07620	
Tube wall	0.0254	1.2	4	0.13635	
Solid side					
Particle 2	0.127	1.0	6	0.762	0.5588
Particle 10	-	-	-	-	0.3302
Particle 11	-	-	-	-	0.3302
All others	-	-	-	-	0.7620

Appendix 5: Effective diffusivity calculations

(a) Methane steam reforming reaction:

Mole fractions:

$y_{CH4} = 0.2392$ $y_{H2} = 0.005$ $y_{CO} = 0.0005$ $y_{CO2} = 0.0776$ $y_{CH4} = 0.6777$

For the inlet operating conditions, the dominant reaction is:

$$CH_4 + 2H_2O \Leftrightarrow CO_2 + 4H_2 \qquad \text{(A-5. 1)}$$

Binary diffusivities may be calculated by the expression introduced by Fuller, Schettler, and Giddings (1966):

$$D_{AB} = \frac{0.001T^{1.75}[(M_A + M_B)/(M_A M_B)]^{0.5}}{P[(\sum v)_A^{1/3} + (\sum v)_B^{1/3}]^2} \quad \text{cm}^2/\text{s} \qquad \text{(A-5. 2)}$$

where T = 824.15 K, and P = 21.3 atm. The molecular weight of components, M_A, and, the molecular volumes of the components, $(\sum v)_A$, are given in Table A.5.

Table A.5 Molecular volumes, and molecular weights of components, MSR reaction

Species	$(\sum v)_i$	M_i
CH_4	24.42	16
H_2	7.07	2
CO	18.9	28
CO_2	26.9	44
H_2O	12.7	18

The calculated binary diffusivities according to equation (A.2) are given in Table A.6.

Table A.6 Binary diffusivities for MRS reaction (cm^2/s)

	H_2	CO	CO_2	H_2O
CH_4	0.192	0.060	0.050	0.075
H_2		0.208	0.178	0.246
CO			0.045	0.072
CO_2				0.059

The Knudsen diffusivity can be calculated with the following equation:

$$D_{K,A} = 9.70 \times 10^3 \overline{r_p} \left(\frac{T}{M_A} \right)^{0.5} \qquad \text{cm}^2/\text{s} \qquad \text{(A-5. 3)}$$

where the average pore radius, $\overline{r_p}$, was taken as 10^3 $\overset{o}{A}$ (Hou and Hughes, 2001). The calculated Knudsen diffusivities were:

$D_{K,CH4} = 0.696$ $D_{K,H2} = 1.969$ $D_{K,CO} = 0.526$ $D_{K,CO2} = 0.420$ $D_{K,H2O} = 0.656$

Molecular diffusivities can be calculated with the following equation:

$$\frac{1}{D_{A,md}} = \frac{\sum_{K=1}^{N} \frac{1}{D_{A,K}} (y_K - y_A \frac{N_K}{N_A})}{1 - y_A \sum_{K=1}^{N} \frac{N_K}{N_A}} \qquad \text{(A-5. 4)}$$

The calculated molecular diffusivities were:

$D_{CH4,md} = 0.123$ cm^2/s [$N_{H2}/N_{CH4} = -4$, $N_{CO}/N_{CH4} = 0$, $N_{CO2}/N_{CH4} = -1$, $N_{H20}/N_{CH4} = 2$]

$D_{H2,md} = 0.225$ cm^2/s [$N_{CH4}/N_{H2} = -1/4$, $N_{CO}/N_{H2} = 0$, $N_{CO2}/N_{H2} = 1/4$, $N_{H20}/N_{H2} = -1/2$]

$D_{CO2,md} = 0.049$ cm^2/s [$N_{CH4}/N_{CO2} = -1$, $N_{CO}/N_{CH4} = 0$, $N_{H2}/N_{CO2} = 4$, $N_{H20}/N_{CO2} = -2$]

$D_{H2O,md} = 0.209$ cm^2/s [$N_{CH4}/N_{H2O} = -4$, $N_{CO}/N_{H2O} = 0$, $N_{CO2}/N_{H2O} = -1/2$, $N_{H2}/N_{H2O} = -2$]

CO is not in the reaction. Therefore, $N_{CO} = 0$. So, $D_{CO,H20} = 0.072$ was used for $D_{CO,md.}$

Effective diffusivities were calculated by : $1/D_A = 1/D_{A,md} + 1/D_{K,A}$, and corrected using the pellet tortuosity and porosity as:

$$D_{A,eff} = \frac{\varepsilon}{\tau} D_A \qquad \text{cm}^2/\text{s} \qquad \text{(A-5. 5)}$$

where $\varepsilon = 0.44$ (Hou and Hughes, 2001), and $\tau = 3.54$ (Xu and Froment, 1989b). The effective diffusivities were:

$D_{CH4,eff} = 1.3 \text{ x } 10^{-6}\ \text{m}^2/\text{s}$
$D_{H2,eff} = 2.5 \text{ x } 10^{-6}\ \text{m}^2/\text{s}$
$D_{CO,eff} = 8.0 \text{ x } 10^{-7}\ \text{m}^2/\text{s}$
$D_{CO2,eff} = 5.0 \text{ x } 10^{-7}\ \text{m}^2/\text{s}$
$D_{H2O,eff} = 2.0 \text{ x } 10^{-6}\ \text{m}^2/\text{s}$

(b) Propane dehydrogenation reaction:

Mole fractions:

$y_{C3H8} = 0.4385$ $y_{H2} = 0.5360$ $y_{C3H6} = 0.0255$

The reaction is:

$$C_3H_8 \Leftrightarrow C_3H_6 + H_2 \tag{A-5. 6 }$$

The molecular volumes and molecular weights of the compounds are given in Table A.7.

Table A.7 Molecular volumes, and molecular weights of components, PDH reaction

Species	$(\sum v)_i$	M_i
C_3H_8	65.34	44
H_2	7.07	2
C_3H_6	61.38	42

Operating T = 874.15 K, and P = 1.0 atm. The calculated binary diffusivities according to equation (A.2) are given in Table A.8.

Table A.8 Binary diffusivities for PDH reaction (cm^2/s)

	H_2	C_3H_6
C_3H_8	2.873	0.477
H_2	▨	2.958

The Knudsen diffusivities were calculated with equation (A.3) with the average pore radius, $\overline{r_p} = 10^3\ \overset{o}{A}$ (Hou and Hughes, 2001). The calculated Knudsen diffusivities were:

$D_{K,C3H8} = 0.432$ $D_{K,H2} = 2.028$ $D_{K,C3H6} = 0.443$ (cm^2/s)

Molecular diffusivities were be calculated with equation (A.4) and found to be:
$D_{C3H8,md} = 1.431$ cm^2/s [$N_{C3H8}/N_{C3H6} = -1$, $N_{C3H8}/N_{H2} = -1$]
$D_{H2,md} = 6.002$ cm^2/s [$N_{H2}/N_{C3H8} = -1$, $N_{H2}/N_{C3H6} = 1$]
$D_{C3H6,md} = 0.873$ cm^2/s [$N_{C3H6}/N_{C3H8} = -1$, $N_{C3H6}/N_{H2} = 1$]

Effective diffusivities were calculated by: $1/D_A = 1/D_{A,md} + 1/D_{K,A}$, and corrected equation (A.5) using the same pellet tortuosity and porosity values as used for MRS reaction. The effective diffusivities were:

$D_{C3H8,eff} = 4.127 \times 10^{-6}$ m^2/s
$D_{H2,eff} = 1.884 \times 10^{-5}$ m^2/s
$D_{C3H6,eff} = 3.650 \times 10^{-6}$ m^2/s

Appendix 6: Monitoring the convergence in diffusion/reaction simulations

(a) MSR reaction full cylinders model

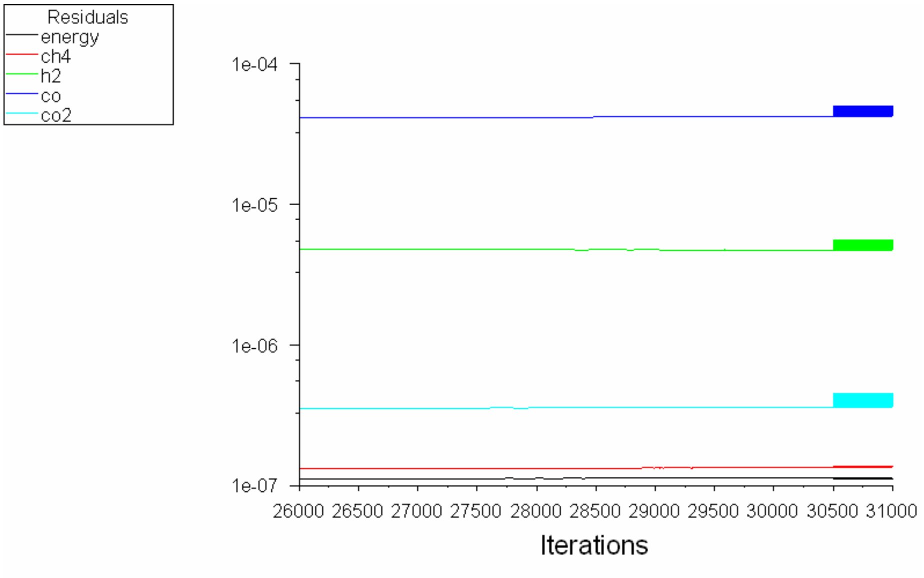

Figure A.1 MRS, full cylinders model residuals plot

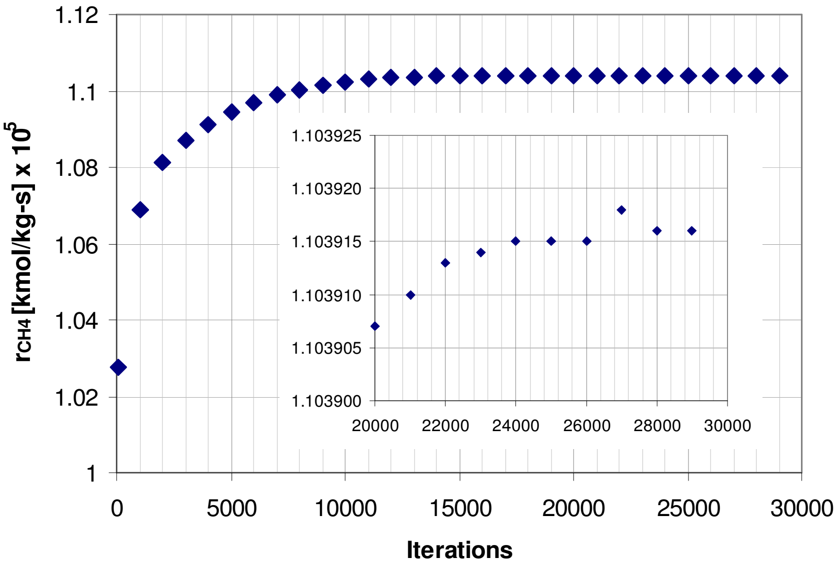

Figure A.2 MSR, full cylinders model CH_4 consumption rate plot

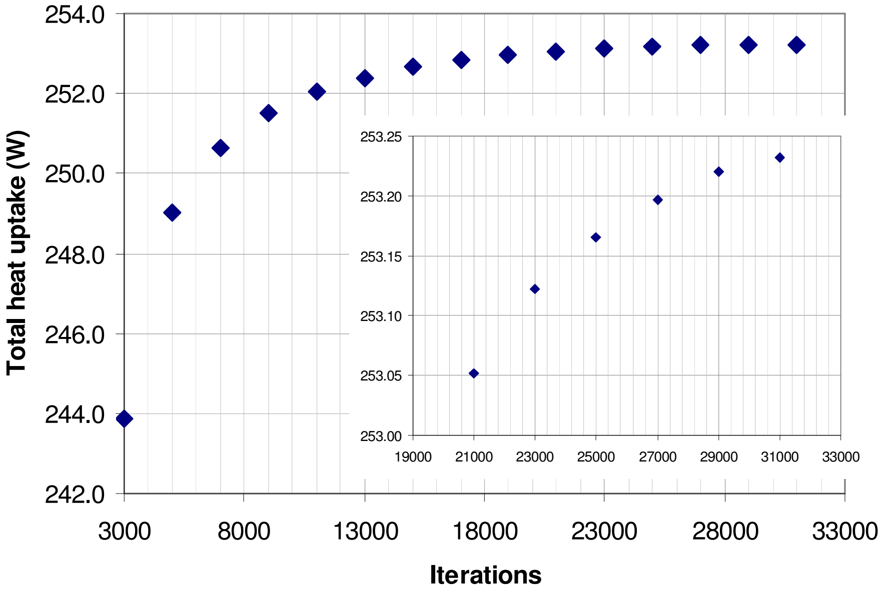

Figure A.3 MSR, full cylinders model total heat uptake plot

(b) MSR reaction, 4-hole cylinders model

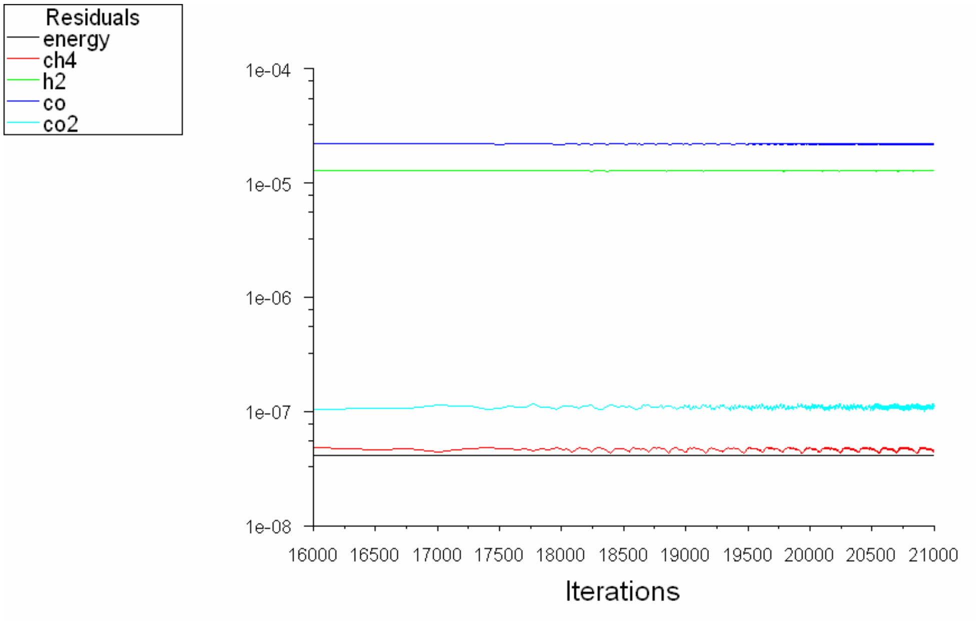

Figure A.4 MRS, 4-hole cylinders model residuals plot

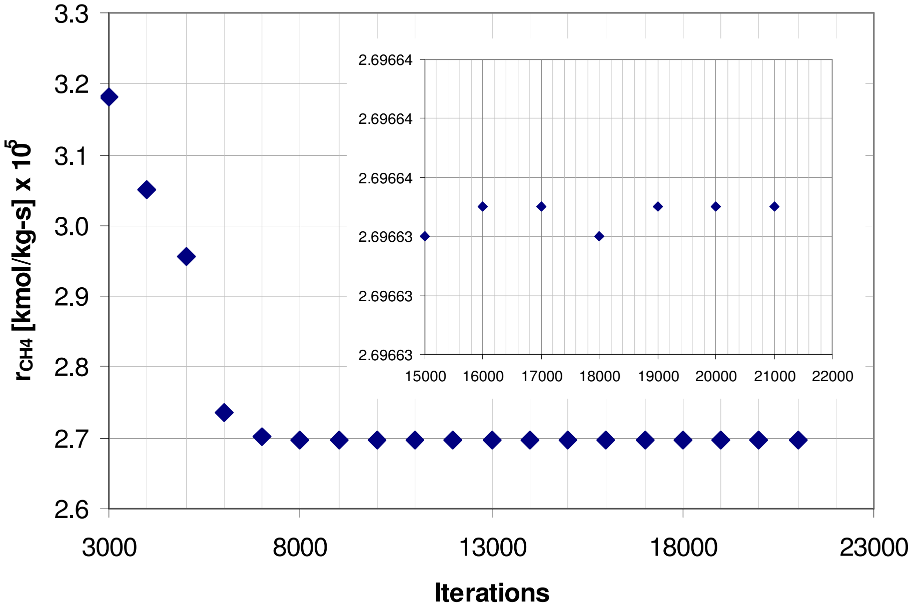

Figure A.5 MSR, 4-hole cylinders model CH_4 consumption rate plot

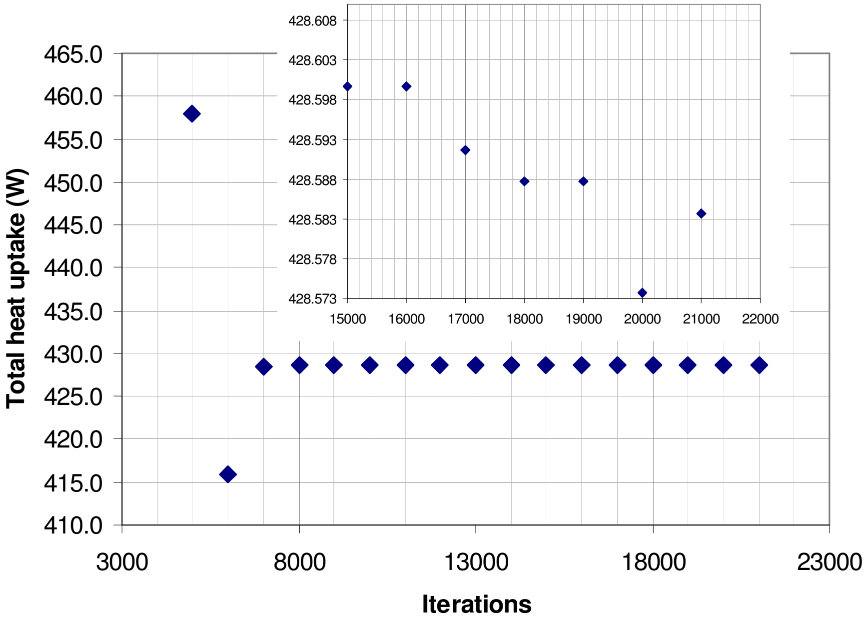

Figure A.6 MSR, 4-hole cylinders model total heat uptake plot

Appendix 7: Correlations

(a) Axial velocity, v_z:

Tsotsas and Schlunder (1988)

$$\frac{u}{u_0} = \beta\left\{1 - \exp\left[aR^*\left(1-\frac{r}{r_t}\right)\right]\left[1 - nR^*\left(1-\frac{r}{r_t}\right)\right]\right\} \qquad \text{(A-7. 1)}$$

)

$$\beta = \frac{R^{*2}}{2}\left[\frac{R^{*2}}{2} - \frac{(nR^*-1)(aR^*+1)}{a^2} + n\left(\frac{R^{*2}}{a} + \frac{2R^*}{a^2} + \frac{2}{a^3}\right) - \frac{\exp(aR^*)}{a^2}\left(1 - nR^* + \frac{2n}{a}\right)\right]^{-1}$$

(A-7. 2)

$$R^* = d_t / d_p \qquad \text{(A-7. 3)}$$

$$a = 4n/(4-n) \qquad \text{(A-7. 4)}$$

n = 27 for Re > 1000.

u is the superficial velocity at a radial position r, u_0 is the average superficial velocity, r_t is tube radius, d_t is tube diameter, and d_p is particle diameter.

The above equations were obtained from the extended Brinkman expression which is in the highly nonlinear 2D partial differential form, by minimizing an integral in the region of interest rather than solving the differential equation. The details can be found in the above reference as well as Vortmeyer and Schuster (1983).

User-defined code

```
DEFINE_PROFILE(w_correlation, t, i)
{
   cell_t c;
   real x[ND_ND], r, a, n, beta, Rstar;
   n = 27.0;
   a = -4.696;
   beta = 0.691;
   Rstar = 4.0;
   begin_c_loop(c, t)
```

```
    {
     C_CENTROID(x, c, t);
     r = sqrt(pow(x[0],2)+pow(x[1],2));
     F_PROFILE(c, t, i) = 1.6135*beta*(1-exp(a*Rstar*(1-r/0.0508))*(1-n*Rstar*(1-r/0.0508)));
     }
     end_c_loop(c, t)
}
```

DPM-fitted v_z profile

User-defined code

```
DEFINE_PROFILE(w_vel, t, i)
{
  cell_t c;
  real x[ND_ND], r;
  begin_c_loop(c, t)
    {
     C_CENTROID(x, c, t);
     r = sqrt(pow(x[0],2)+pow(x[1],2));

     if (r < 0.024 && r > 0.0)
         F_PROFILE(c, t, i) = 0.06519580821 - 107.5259898 * r + 39974.32809 * pow(r,2) - 1511078.848 * pow(r,3) + 17341425.55 * pow(r,4);
    else if (r < 0.049 && r > 0.024)
   F_PROFILE(c, t, i) = 2899.277922 - 476087.7234 * r + 32533409.72 * pow(r,2) - 1183163544 * pow(r,3) + 2.413565553E+010 * pow(r,4) - 2.617091926E+011 * pow(r,5) + 1.178111244E+012 * pow(r,6);
  else if (r < 0.05064 && r > 0.049)
     F_PROFILE(c, t, i) = 58650.66725 - 3550922.107 * r + 71641034.24 * pow(r,2) - 481623231.5 * pow(r,3);
  else if (r < 0.0507 && r > 0.05064)
     F_PROFILE(c, t, i) = -19821.86269 * r + 1008.305437;
  else if (r < 0.05072 && r > 0.0507)
     F_PROFILE(c, t, i) = -34180.53712 * r + 1736.29023;
  else if (r < 0.05076 && r > 0.05072)
```

```
        F_PROFILE(c, t, i) = -24857.55232 * r + 1263.428442;
    else
        F_PROFILE(c, t, i) =   -41477.14193 * r + 2107.03881;
        }
        end_c_loop(c, t)
}
```

(b) Thermal conductivity, *k_{er}*:

Dixon correlation (Dixon and Cresswell, 1979; Dixon, 1988)

$$k_{er} = \frac{d_p u_s \rho c_p}{Pe_{er}} \tag{A-7. 5}$$

$$\frac{1}{Pe_{er}} = \frac{1}{Pe_{fr}} + \frac{k_{rs}/k_f}{\mathrm{Re}\cdot\mathrm{Pr}}\left[\frac{Bi_f+4}{Bi_f}\right]\left[\frac{8}{N_s}+\frac{Bi_s+4}{Bi_s}\right]^{-1} \quad (\mathrm{Re}>50) \tag{A-7. 6}$$

$$\frac{1}{Pe_{er}} = \frac{1}{Pe_{fr}}\left[\frac{Bi_s+4}{Bi_s}\right]\left[\frac{8}{N_F}+\frac{Bi_f+4}{Bi_f}\right]^{-1} + \frac{k_{rs}/k_f}{\mathrm{Re}\cdot\mathrm{Pr}} \quad (\mathrm{Re}<50) \tag{A-7. 7}$$

$$\frac{1}{Pe_{rf}} = \frac{1}{Pe_{rf(\infty)}} + \frac{0.74\varepsilon}{\mathrm{Re}\cdot\mathrm{Pr}} \tag{A-7. 8}$$

$$Pe_{rf(\infty)} = \begin{cases} 12 & spheres \\ 7 & cylinders \\ 6 & hollow\ cylinders \end{cases} \tag{A-7. 9}$$

$$\frac{k_{rs}}{k_f} = \sqrt{1-\varepsilon}\,\frac{2}{M}\left[\frac{B(k_s-1)}{M^2 k_s}\ln\left(\frac{k_s}{B}\right) - \frac{B+1}{2} - \frac{B-1}{M}\right] \tag{A-7. 10}$$

$$M = \frac{k_s - B}{k_s} \qquad k_s = \frac{k_{solid}}{k_f} \qquad B = C\left(\frac{1-\varepsilon}{\varepsilon}\right)^{10/9} \tag{A-7. 11}$$

$$Bi_f = Nu_{wf}\,(d_t / d_{pv})(Pe_{rf} /(\mathrm{Re}\,\mathrm{Pr})) \tag{A-7. 12}$$

$$Nu_{fs} = \frac{0.225}{\varepsilon}\mathrm{Pr}^{1/3}\,\mathrm{Re}^{0.67} \tag{A-7. 13}$$

$$Nu_{wf} = 0.523(1 - d_{pv} / d_t)\,\mathrm{Pr}^{1/3}\,\mathrm{Re}^{0.738} \tag{A-7. 14}$$

$$Bi_s = \begin{cases} 2.41 + 0.156(d_t / d_{pv} - 1)^2 & spheres \\ 0.48 + 0.192(d_t / d_{pv} - 1)^2 & cylinders \end{cases} \tag{A-7. 15}$$

$$\beta_s = \frac{k_{rs} / k_f}{\dfrac{8}{N_s} + \dfrac{Bi_s + 4}{Bi_s}} \tag{A-7. 16}$$

$$N_s = \frac{0.25(1-\varepsilon)\dfrac{A_p}{V_p}\dfrac{d_t^2}{d_{pv}}}{k_{rs} / k_f\left[\dfrac{1}{Nu_{fs}} + \dfrac{1}{\beta}\dfrac{k_f}{k_{solid}}\right]} \tag{A-7. 17}$$

$$N_F = \frac{0.25(1-\varepsilon)\dfrac{A_p}{V_p}\dfrac{d_t^2}{d_{pv}}}{\dfrac{\mathrm{Re}\,\mathrm{Pr}}{Pe_{rf}}\left[\dfrac{1}{Nu_{fs}} + \dfrac{1}{\beta}\dfrac{k_f}{k_{solid}}\right]} \tag{A-7. 18}$$

$$\beta = \begin{cases} 10 & spheres \\ 8 & cylinders \end{cases} \tag{A-7. 19}$$

$$C = \begin{cases} 1.25 & spheres \\ 2.5 & cylinders \end{cases} \tag{A-7. 20}$$

Bauer and Schlunder correlation (1978a, 1978b)

$$\frac{k_{er}}{k_f} = \frac{k_{convection}}{k_f} + \frac{k_{conduction,radiation}}{k_f} \tag{A-7. 21}$$

$$\frac{k_{convection}}{k_f} = \frac{\rho u_s c_p}{k_f} \frac{X_F}{8\left[2-\left(1-2d_{pv}/d_t\right)^2\right]} \tag{A-7. 22}$$

$$\frac{k_{conduction,radiation}}{k_f} = (1-\sqrt{1-\varepsilon})\left(1+\varepsilon\frac{k_{radiation}}{k_f}\right) + \sqrt{1-\varepsilon}\left(\frac{k_{rs}}{k_f}\right) \tag{A-7. 23}$$

$$\frac{k_{radiation}}{k_f} = 2.27\times10^{-7}\,\frac{e}{2-e}T^3\,\frac{d_{pv}}{k_f} \tag{A-7. 24}$$

$$\frac{k_{rs}}{k_f} = \frac{2}{N}\left[\frac{B(k_s+k_r-1)}{N^2k_s}\ln\left(\frac{k_s+k_r}{B}\right) + \frac{B+1}{2B}(k_r-B) - \frac{B-1}{N}\right] \tag{A-7. 25}$$

$$N = \frac{k_s+k_r-B}{k_s} \qquad B = C\left(\frac{1-\varepsilon}{\varepsilon}\right)^{10/9} \tag{A-7. 26}$$

$$k_s = \frac{k_{solid}}{k_f} \qquad k_s = \frac{k_{radiation}}{k_f} \tag{A-7. 27}$$

X_F is the effective mixing length, $X_F = Fd_{pv}$

e is emmisivity

$$F = \begin{cases} 1.15 & spheres \\ 1.75 & cylinders \end{cases} \tag{A-7. 28}$$

$$C = \begin{cases} 1.25 & spheres \\ 2.5 & cylinders \end{cases} \tag{A-7. 29}$$

Winterberg and Tsotsas correlation (2000)

$$k_{er}(r) = k_{bed}(r) + K_1 Pe_0 \frac{u_c}{u_0} f(r_t - r) k_f \qquad \text{(A-7. 30)}$$

$$f(r_t - r) = \begin{cases} \left(\dfrac{r_t - r}{K_2 dp}\right)^2 & for\ 0 \le r_t - r \le K_2 dp \\ 1 & for\ K_2 dp < r_t - r \le r_t \end{cases} \qquad \text{(A-7. 31)}$$

u_c is the superficial velocity at the core of the bed, and k_{bed} is the effective thermal conductivity without fluid flow. $k_{bed}(r)$ was obtained from full cylinders WS model averaging the thermal conductivity vales of fluid and solid regions on the radial planes. By the polynomial functions, k_{bed} was re-produced, and utilized.

Recommended $K_1 = 0.16$, $K_2 \approx 0.40$ for high Re.

The used K_1 and K_2 values:

Section 6.2,	Case-3(a)	$K_1 = 0.16$, $K_2 = 0.40$
	Case-3(b)	$K_1 = 0.10$, $K_2 = 0.50$
	Case-3(c)	$K_1 = 0.20$, $K_2 = 0.10$
	Case-4(a)	$K_1 = 0.16$, $K_2 = 0.40$
	Case-4(b)	$K_1 = 0.10$, $K_2 = 0.40$
	Case-4(c)	$K_1 = 0.20$, $K_2 = 0.20$
Section 6.3,	P-C (1)	$K_1 = 0.16$, $K_2 = 0.13$
	P-C (2)	$K_1 = 0.16$, $K_2 = 0.70$
	P-C (3)	$K_1 = 0.16$, $K_2 = 0.01$

User-defined code

```
DEFINE_PROPERTY(k_eff_corr, c, t)
{
  real lambda, epsilon, lambda_bed;
  real x[ND_ND], r, K1, K2, fRr, B;
```

```
 C_CENTROID(x, c, t);
 r = sqrt(pow(x[0],2)+pow(x[1],2));
if (r < 0.0225 && r > 0.0)
        lambda_bed  =  0.8909162768+8.085091273*r-2782.777489*pow(r,2)+74084.89133*pow(r,3)-
1207081.61*pow(r,4);
      else if (r < 0.0505 && r > 0.0225)
        lambda_bed = 2.455137547-1289.139629*r+124089.7465*pow(r,2)-
4726488.002*pow(r,3)+81043504.61*pow(r,4)-523908173.5*pow(r,5);
      else
        lambda_bed = 0.0876;
      K1 = 0.16;
      K2 = 0.05;
      fRr = (0.0508-r)/(K2*0.029);
      B = 0.0508-K2*0.029;
      if (r <= 0.0508 && r>= B)
        lambda = lambda_bed+K1*7883.7*0.33/1.6135*fRr*0.0876;
      else
        lambda = lambda_bed+K1*7883.7*0.33/1.6135*1*0.0876;
      return lambda;
}
```

(c) Effective diffusivity, D_{er} :

Specia et al. correlation (1980)

$$D_{er} = \frac{u_s dp}{8.65\left[1 + 19.4\left(\frac{dp}{d_t}\right)^2\right]} \tag{A-7. 32}$$

Bauer and Schlunder correlation (1978)

$$D_{er} = \frac{u_s X_F}{8\left[2 - (1 - 2d_{pv} / d_t)^2\right]} \tag{A-7. 33}$$

X_F is the effective mixing length, $X_F = Fd_{pv}$

$$F = \begin{cases} 1.15 & spheres \\ 1.75 & cylinders \end{cases} \tag{A-7. 34}$$

Rase correlation (1990)

$$D_{er} = \frac{u_s dp}{\varepsilon}\left(\frac{1}{m} + \frac{0.38}{\text{Re}}\right) \qquad \text{for } dp/d_t > 0.1 \tag{A-7.35}$$

$$D_{er} = \frac{u_s dp}{\varepsilon}\left(\frac{1}{m} + \frac{0.38}{\text{Re}}\right) / \left[1 + 19.4\left(\frac{dp}{d_t}\right)^2\right] \qquad \text{for } dp/d_t < 0.1 \tag{A-7. 36}$$

$$m = \begin{cases} 11 \quad \text{Re} > 400 \\ 57.85 - 35.36 \log \text{Re} + 6.68(\log \text{Re})2 \quad 20 < \text{Re} < 400 \end{cases} \tag{A-7. 37}$$

DPM-fitted D_{er}

User-defined code

```
DEFINE_PROPERTY(D_effective, c, t)
{
 real D;
 real x[ND_ND], r;
```

```
    C_CENTROID(x, c, t);
    r = sqrt(pow(x[0],2)+pow(x[1],2));
       if (r < 0.015 && r > 0.0)
          D = 1.196112713E-005 - 0.001466495288 * r - 0.4915808717 * pow(r,2) + 91.48866752 *
pow(r,3) - 2476.890131 * pow(r,4) - 26135.46626 * pow(r,5);
         else if (r < 0.0275 && r > 0.015)
          D = 0.0008337534968 - 0.1783691592 * r + 14.49173144 * pow(r,2) - 500.293758 * pow(r,3) +
6176.32268 * pow(r,4);
         else if (r < 0.046 && r > 0.0275)
          D = 0.00360563988 - 0.4129531021 * r + 17.74026682 * pow(r,2) - 338.0363024 * pow(r,3) +
2414.242821 * pow(r,4);
         else if (r < 0.05 && r > 0.046)
          D = 0.2597300077 - 15.95463436 * r + 325.8040534 * pow(r,2) - 2210.511931 * pow(r,3);
         else if (r < 0.0504 && r > 0.05)
         D =  1.735095509 - 68.86031822 * r + 683.2454095 * pow(r,2);
       else if (r < 0.0506 && r > 0.0504)
        D =  -0.1447889841 * r + 0.007385494923;
        else if (r < 0.05072 && r > 0.0506)
          D = -0.4564763148 * r + 0.0231567335;
        else if (r < 0.05074 && r > 0.05072)
          D = 4.96e-6;
        else if (r < 0.05076 && r > 0.05074)
          D = -0.1463608966 * r + 0.00743130848;
        else if (r < 0.05078 && r > 0.05076)
          D = -0.02155790996 * r + 0.00109630888;
        else
          D = 1.6e-6;
      return D;}
```

(d) Bed voidage profile, $\varepsilon(r)$:

Winterberg and Tsotsas correlation (2000)

$$\varepsilon(r) = \varepsilon_{\infty}\left(1 + A\exp\left[-B\frac{r_t - r}{d_{pv}}\right]\right) \qquad \text{(A-7. 38)}$$

$$A = \frac{0.65}{\varepsilon_{\infty}} - 1 \text{ and } B = 6.0 \qquad \text{(A-7. 39)}$$

ε_{∞} is voidage of the infinitely extended bed which was set to 0.1 based on the observations in DPM.

Bey and Eigenberger (2000)

Two different expressions have used for near wall region and bed core.

$$\varepsilon_{wall}(r) = \varepsilon_{\min,C} + (1 - \varepsilon_{\min,C})(r')^4 \qquad \text{for } r' < 0 \qquad \text{(A-7. 40)}$$

$$\varepsilon_{core}(r) = \varepsilon_{0,C} + (\varepsilon_{\min,C} - \varepsilon_{0,C})\exp\left(-\frac{r'}{c}\right)\cos\left(\frac{\pi}{b}r'\right) \quad \text{for } r' \geq 0 \qquad \text{(A-7. 41)}$$

$$r' = a_0\frac{r_t - r}{dp_{eq}} - 1, \qquad a_0 = 1.8 - 2\frac{dp}{dt} - 1, \qquad \text{b} = 0.876, \qquad \text{c} = 2 \quad \text{(A-7. 42)}$$

DPM-fitted $\varepsilon(r)$

User-defined code

```
if (r < 0.0504 && r > 0.0225)
    epsilon = -225.073+40524.003*r-2939272.509*pow(r,2)+110717936.25*pow(r,3)-2293882086.17*pow(r,4)+24853102253.985*pow(r,5)-110180930973.904*pow(r,6);
 else if (r < 0.0225 && r > 0.0)
    epsilon = 0.052463+28.00127*r-23580.3522*pow(r,2)+5594741.763*pow(r,3)-475768235.634*pow(r,4)+17863076450.73*pow(r,5)-251062548976.676*pow(r,6);
 else
    epsilon = 1.0;
```